Femtosecond high power Tm : Ho fiber laser at 2050 nm

Adrian Grande

THÈSE PRÉSENTÉE

POUR OBTENIR LE GRADE DE

DOCTEUR
DE L'UNIVERSITÉ DE BORDEAUX

ECOLE DOCTORALE DE SCIENCES PHYSIQUES ET DE L'INGÉNIEUR

SPÉCIALITÉ: LASER, MATIÈRE ET NANOSCIENCES

Par **Adrian Grande**

Laser à fibres Tm:Ho de haute puissance à femtoseconde à 2050 nm

Sous la direction d'**Eric Cormier**

Soutenue le 15/02/2024

Membres du jury :

Mme. Clara Saraceno	Professeur	Ruhr-Universität, Bochum	Rapporteur
M. Philippe Roy	Directeur de Recherche	X-LIM, Limoges	Rapporteur
M. Marwan Abdou Ahmed	Directeur de Recherche	IFSW, Stuttgart	Président du Jury
Mme. Véronique Jubera	Professeur des Universités	ICMCB, Bordeaux	Examinatrice
M. Eric Cormier	Professeur des Universités	LP2N, Bordeaux	Directeur
M. Valerian Freysz	Ingénieur de Recherche	Alphanov, Bordeaux	Invitée
M. Marc Castaing	Ingénieur de Recherche	Alphanov, Bordeaux	Invitée

Abstract

Résumé :
La technique d'amplification à dérive de fréquence "chirped pulse amplification" (CPA) a été développée pour augmenter la puissance des impulsions issues d'oscillateurs à verrouillage de mode, car l'énergie des impulsions n'étaient pas suffisantes pour des applications telles que la physique des champs forts et l'accélération de particules. Depuis son développement en 1985, elle a été utilisée dans une grande variété de systèmes laser industriels et dans des installations laser à ultra-haute puissance. Cette technique permet d'une part de s'affranchir de l'accumulation de phase non linéaire qui entrave la compression d'impulsions et d'autre part de maintenir la fluence des impulsions en dessous des seuils de dommages induits par laser aux composants. Dans cette thèse, nous développons des systèmes laser CPA à la longueurs d'onde de $2.05\,\mu m$ avec une puissance moyenne élevée et une énergie élevée, en commençant par le développement du laser à $2050\,nm$ jusqu'à la conception et la mise en œuvre de l'étireur, des amplificateurs et du compresseur d'impulsions.

Dans la première section de la thèse, nous introduisons les principaux concepts de physique et les phénomènes nécessaires à la compréhension de la technique d'amplification par dérive de fréquence et au développement du laser à fibre à $2050\,nm$. Cela inclut la dispersion, l'automodulation de phase et la diffusion Raman.

Dans la deuxième section de la thèse, nous présentons le développement d'un laser entièrement fibré à maintien de polarisation et accordable sur plus de $170\,nm$, de $1880\,nm$ à $2050\,nm$, via le phénomene de décalage de fréquence solitonique (Raman soliton self-frequency shift, SSFS). Notre systéme est basé exclusivement sur des fibres disponibles commercialement. Nous avons caractérisé le laser en termes de puissance, de spectre et de durée d'impulsion, et nous avons inclus une étape de post-compression qui repose sur des effets non linéaires pour atteindre une durée inférieure à $100\,fs$ sur toute la plage d¡accordabilité. Les simulations sur la post-compression de solitons montrent la polyvalence du laser, qui permet de personnaliser la durée de l'impulsion sur une plage spectrale donnée, ou alternativement à une longueur d'onde particulière.

Dans la troisième section, nous avons testé le laser accordable dans une grande variété d'architectures d'étirement et de compression adaptées au CPA. Nous avons examiné les fibres et les réseaux de Bragg en volume étiré (CVBG) en tant que dispositifs d'étirement d'impulsions, ainsi que les paires de réseaux de diffraction et les CVBG en tant que compresseurs d'impulsions. Nous discutons la manière de dimensionner une paire d'étireur-compresseur en tenant compte de la phase non linéaire et de l'effet de rétrécissement du gain qui se produit pendant l'amplification d'impulsions, ainsi que de l'évaluation des performances de l'étireur-compresseur. Deux systèmes laser d'amplification à dérive de fréquence ont été conçus et présentés, le premier visant des impulsions fs à large bande avec une puissance moyenne élevée, et le second système visant des impulsions ps à haute énergie. La technologie peu mature dans la région spectrale de $2\,\mu m$ et la faible disponibilité de dispositifs d'étirement adaptés entravent la compression d'impulsions à cette longueur d'onde.

Dans la dernière section de la thèse, nous avons étudié les performances des fibres co-dopées Tm:Ho en configuration d'amplification. Nous discutons des principaux défis de ces fibres, notamment les effets de transfert d'énergie, la disponibilité des sources de pompage qui donnent lieu à deux schémas de pompage principaux : le pompage par diode

et le pompage intra-bande, ainsi que les limitations en termes de taille de fibre. Nous avons testé les fibres dopées Tm:Ho, y compris les fibres à cœur large pour l'amplification d'impulsions à bande étroite et à large bande.

Keywords: laser à fibre, amplification d'impulsions à la dérive de fréquence, optique non linéaire, auto-décalage solitonic , thulium-holmium fibers

---

Abstract:
The chirped pulse amplification (CPA) technique was developed to power scale the pulses from mode-locked oscillators as the pulse energy was not sufficient to target applications such as strong field physics and particle acceleration. Since its development in 1985 it has been applied in a wide variety of commercially available laser systems and ultra-high power laser facilities. The technique allows to circumvent the accumulation of non-linear phase which hampers pulse compression and allows to maintain the fluence of the pulses below the laser induced damage thresholds (LIDT) of components. In this thesis we develop CPA laser systems operating at $2.05\,\mu m$ wavelengths with high average power and high energy starting from the development of the seed laser up to the design and implementation of the pulse stretcher, amplifiers and pulse compressor.

In the first section of the thesis we introduce the physics background and phenomena required for understanding the chirped pulse amplification technique and the development of the seed laser. This includes dispersion, self-phase modulation and Raman scattering.

In the second section of the thesis we present the development of an all-fiber polarization maintaining laser tunable over $170\,nm$, from $1880\,nm$ up to $2050\,nm$ via Raman soliton self-frequency shift (SSFS). The system is based on exclusively commercially available standard fibers. We have characterised the laser in terms of power, spectrum and pulse duration and we have included a post-compression stage that relies on non-linear effects to reach the sub-100 fs duration across the whole tunability range. Simulations of the soliton post-compression shows the versatility of the laser which allows to customise the pulse duration over a spectral range or for a particular wavelength. We believe that the laser is a versatile and robust alternative to Tm and Tm:Ho oscillators.

In the third section we have tested the tunable laser in a wide variety of stretching and compression architectures suitable for CPA. We have investigated fibers and chirped volume Bragg gratings (CVBG) as pulse stretching devices and grating pairs and CVBGs as pulse compressors. We discuss how to dimension a stretching-compressor pair taking into account the non-linear phase and gain narrowing effect that takes place during pulse amplification and how to evaluate the stretching-compressor performance. Two different chirped pulse amplification laser systems have been designed and presented, the first one targets broadband fs pulses with high average power and the second system targets high energetic ps pulses. The non-mature technology in the $2\,\mu m$ spectral region and the weak availability of suitable stretching devices hinders pulse compression at this wavelength.

In the last section of the thesis we investigated the performance of Tm:Ho co-doped fibers in amplification configuration. We discuss the main challenges of these fibers including the cross-relaxation effects, the availability of pump sources which gives rise to two main pumping schemes: diode pumping and in-band pumping and the limitations in terms of fiber size. We tested Tm:Ho doped fibers, including LMA for narrowband and broadband pulse amplification.

Keywords: fiber laser, chirped pulse amplification, non-linear optics, soliton self-frequency shift, thulium-holmium fibers

---

LP2N - Laboratoire photonique, numérique et nanosciences
UMR 5298 - UBx, IOGS, CNRS, 33400 Talence, France.

Contents

Acknowledgements

I would like to thanks Valerian Freysz and Florian Leroy who took care of me at the work place and outside of it. They were always supportive and tried to cheer me up during the hard times. They were always available for me and taught me a lot. Thanks to them I got to know the best places around Bordeaux and made the whole PhD experience and living in France way more enjoyable. I am definitely going to miss them both. I want to thanks Michaël Berisset who always freed some time to splice LMA fibers for me and produce connectors for the specialty fibers used. I enjoyed working with him as is someone you would definitely like to learn from. I want to thanks as well Johan Boullet and Marc Castaing for their advice.

I would like to thanks all the colleagues and fellow researches at the LP2N side as well for their camaraderie and collaborative spirit. The stimulating discussions and shared experiences have enriched the journey. Special thanks to Lilia Pontagnier the one and only who had to share office with me and suffer my complaints in a wide variety of languages, to Esther Szmygel and to Roopa Prakash, they are somehow always smiling and they bring loads of good vibes. In addition, Roopa is a wonderful cooker and she's always happy to bring delicious indian food to share. I want to thank as well all the other members that are or have been part the team: Hussein Tofaili, Paolo Paris, Kentin Poncelet, Ruizhe Gu, Esther Szmygel, Gilles Dalla Barba, Hanyu Ye, Dia Darwich, Abdelkrim Bendahmane, Alejandro Giacomotti, Nicolas Dubreuil, Adèle Hilico, Giorgio Santarelli and Eric Cormier. Many thanks to Prof. Eric Cormier for supervising me for these 3 years. I know I did not make it easy with my beyond optimistic attitude and zero complaining policy but somehow we managed to pull through the thesis which would have been impossible without his guidance, advice, invaluable experience and endless patience.

I want to thanks all the early stage researchers in the GREAT project: Danish Bashir, Ratish Rao, Giovanna Capraro, Marina Fetisova, Fangfang Li, Janis Zideluns, Goby Govindassamy, Anton Savchenko, Georgia Mourkioti, Marek Stehlik, Ayoub Boubekraoui, Muhammad Ghawas and Sayed Muhammad Baker. They have been exceptional and very supporting colleagues. I am very grateful to the organizers of the project because of their effort and specially because of their patience: Marwan Abdou Ahmed, Petri Karvinen, Laurent Gallais, Jacob Mackenzie, Yves Jourlin, Christian Röhrer and Marijana Totic. I wish them all the best and hopefully we may work once again in the future.

I extend my sincere appreciation to the members of my thesis Clara Saraceno, Philippe Roy, Marwan Abdou and Véronique Jubera for their constructive feedback and thoughtful suggestions that improved the quality of this thesis.

My heartfelt thanks to my family for their unconditional love, support and understanding throughout the thesis. Their encouragement provided the emotional sustenance needed to overcome the difficulties and to keep me motivated. They have celebrated the achievements more than me as I am sure they have suffered during the hard times as I

did. They have always been available when I needed them and have been a source of motivation, strength and guidance.

I want to thanks all my friends, those that have been around here in Bordeaux such as Olivia "Adelita" Zurita, Habiba Lharti, Ilse Urquia, Nicolas Cassin, David Tílvez and Rosa Moreno and those that are in Spain and surroundings: Ariadna Sanglas, Alba Alcañiz, Ignasi Pique and Fran Tugores. They have filled these 3 years with loads of joy, laughter and unforgettable memories. Your friendship is a treasure I never take from granted.

This thesis is the result of the collective effort of those who have been a part of my academic and personal journey. Thank you all for your invaluable contributions.

List of Figures

List of Tables

Introduction

Ultrafast fiber lasers have developed very rapidly over the last decades thanks to several breakthrough technologies causing a revolution on the laser industry. The increasing demand of Ytterbium (Yb) and Erbium (Er) high power fiber lasers caused an improvement on the fiber drawing processes and favoured the developing of all type of fibered components being at present the most mature and widely established technology. It was not until the last years that the $2\,\mu m$ spectral region attracted attention and fiber lasers around $2\,\mu m$ wavelength started to be developed and studied. This was motivated by the potential of these sources to surpass in power $1\,\mu m$ Yb lasers and the numerous applications they find in science, medicine and industry. This includes driving high efficiency non-linear crystals such as ZGP, opaque to light below $2\,\mu m$ in optical parametric oscillator (OPO) and amplifier (OPA) architectures [1]. In medicine they are suitable for surgery and for two- or three-photon microscopy via frequency conversion providing a tunable driving laser [2, 3]. In industry they are used for material processing of polymers (drilling, cutting...) which can only be achieved with such long emission wavelengths due to polymers' optical properties.

At present, the generation of fs pulses in the $2\,\mu m$ spectral region mostly relies on fiber mode-locked oscillators due to their versatility and robustness with a wide variety of mode-locking techniques such as the use of saturable absorbers, SESAMs or non-linear polarization evolution (NPE). These oscillators produce either pulses in the picojoule energy level or pulses with higher energies that require further pulse compression outside of the cavity and/or intracavity free-space components. As active medium, mainly Tm, Tm-Ho and Ho doped fibers are employed providing different discrete emissions wavelength ($\sim 1.8\,\mu m - 2.05\,\mu m$, $\sim 2 - 2.2\,\mu m$ and $\sim 2.05 - 2.2\,\mu m$ respectively) but such broad emission spectra can be exploited not only to achieve ultrashort fs pulses but also to build tunable mode-locked oscillators. This is accomplished by spectrally selecting the emission wavelength of the laser by adding a tunable spectral filter within the modelocked laser cavity [4, 5, 6]. Some filters include gratings [7], fiber tapers, interferometric filters or NPE based filters [8] among others. Those systems deliver low output powers and relatively long pulse durations due to a lack of dispersion control as the wavelength is tuned. In addition, they are not truly tunable as intracavity components need to be manually adjusted.

An alternative to femtosecond mode-locked oscillators allowing continuous wavelength tunability relies on Raman scattering through soliton self-frequency shift (SSFS). The generated soliton pulses are spectrally tunable with transform limited pulse duration at the nanojoule energy level. In addition, soliton pulse energies and durations can be predicted as they are strongly dependent on the fiber properties such as dispersion and nonlinear coefficient which is why a large amount of work has been reported on the control and tailoring of specialty fiber properties leading to specific solitonic pulses. One can cite for instance, custom photonic crystal fibers (PCF), tellurite fibers, GeO2-doped fibers,

dispersion managed fibers and even Bragg fibers. PCF fibers allow for high non-linearities and anomalous dispersion in very small fiber cores making them the ideal candidates to achieve SSFS in short pieces of fiber. A tunable laser from 1700 nm up to 2100 nm based on custom-made PCF and a dispersion compensating fiber delivering sub-100 fs pulse duration has already been demonstrated [9]. However, to reach such short pulse durations, the fiber lengths needs to be adjusted depending on the operating wavelength which in the end makes the system not truly tunable. If longer operation wavelengths are desired, changing the fiber matrix from fused silica to tellurite can be beneficial to reduce the losses as wavelength increases. Sub-100 fs pulses tunable from 1560 nm up to 2400 nm have already been demonstrated in suspended core tellurite fibers thanks to their higher transparency and high non-linearities achieving large shifts in wavelength [10]. Those fibers allow for large wavelength shifts with ultrashort pulse durations however, if higher energetic pulses are required, large mode area fibers are a must and Bragg fibers can be used for that purpose. In custom Bragg fibers, MW peak powers have already been demonstrated with sub-100 fs pulses and energies as high as 250 nJ with good beam quality [11]. The SSFS technique allows for continuous tunability of the pulses in spectral regions were there are no available gain media to build fiber lasers and the only way to generate light at those particular wavelengths is by relying on non-linear effects such as frequency conversion techniques and SSFS (see Fig.1a).

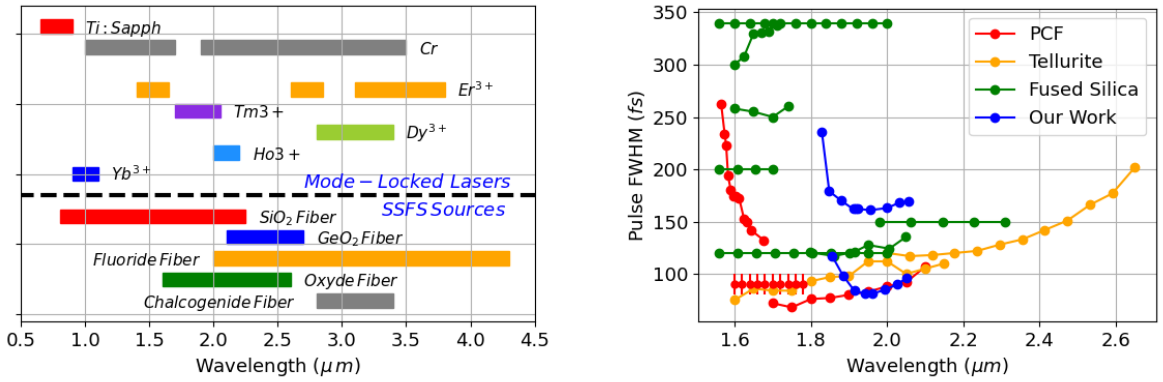

(a) Emission bandwidth of main active ions and spectral coverage of optical fibers in near infrared spectral region.

(b) Pulse FWHM as function of wavelength for SSFS laser sources in the 2 μm spectral range.

Figure 1: Spectral coverage of mode-locked oscillators and laser sources based on the SSFS and pulse duration of SSFS laser sources for different fiber technologies (PCF, Tellurite and fused silica). Data extracted from [12, 13, 14, 15, 16, 17, 18, 19, 20]

Even though such fibers have led to impressive performances in terms of tunability, energy or power, and pulse duration, they are also associated with severe practical challenges. First of all, availability remains restricted to laboratories with specialty fiber drawing capabilities. Specific soliton pulses need adjusted fiber dispersion and non-linearities which yields to an optimization of the fiber drawing process. Then, splicing to commercial fused silica fiber components might be complex, not only because of the geometry, but also because of the material which eventually yields to partially fibered architectures with free-space sections. At the same time, they may not necessarily be polarization maintaining and for most of the applications, especially those that require frequency conversion, polarization control is a must. Therefore, what it is proposed in the first part of this the-

sis, is the development of an all-fiber polarization maintaining (PM) tunable laser which based on exclusively commercially available standard fused silica fibers and components. This approach to generate light in the $2\,\mu m$ region is advantageous as it is based on $1.5\,\mu m$ fiber laser technology which is more mature, there is a wider variety of fibers and components therefore is a more reliable laser than Tm, Ho or Tm:Ho mode-locked oscillators. Since SSFS in standard fused silica fibers delivers tunable pulses with duration above

$$100\,fs$$

(see Fig.1b), a post-compression stage to broaden the spectrum and compress the pulses allowed to reach sub-100 fs pulses over the $1880\,nm$ up to $2050\,nm$ wavelength without the need of adjusting the length of the non-linear or dispersion compensating fibers [21]. This simple architecture is an appealing alternative to mode locked oscillators and a potential seed laser for amplified laser systems in the $2\,\mu m$ spectral region.

In Chapter 1, the different physical phenomena related to ultrashort pulse propagation in Kerr and dispersive mediua are introduced. Then, in Chapter 2, the development and characterization of the tunable laser system is presented and results are supported with simulations.

The present state of the art in modelocked laser oscillators at around $2\,\mu m$ wavelength in terms of pulse duration and pulse energy is shown in Fig.2a and Fig. 2b. From $1.85\,\mu m$ up to $2\,\mu m$, Tm based fiber lasers are well established with pulse durations well beyond $100\,fs$ except for the work of Biao Sun et all which consisted of a fiber oscillator with dispersion control outside of the cavity, an amplifier and a NL compression stage afterwards to reach $65\,fs$ pulses at $1.98\,\mu m$ making the system quite complex even though it was all-fibered [22]. The approach of employing passive fibers for SSFS and NL pulse compression turns to be superior when it comes to achieve ultrashort pulses compared to non-linear polarization evolution (NPE), saturable absorvers (SA), saturable absorver mirrors (SAM) and semiconductor SAM mirrors (SESAM) modelocking techniques which are the most widely employed in Tm fiber oscillators. Pulse energies of such oscillators is limited by the core size of the fibers and the required non-linear phase to achieve modelocking therefore, it is common to obtain higher energies with longer pulses yet the energies obtained with our laser system is quite high taking into account the pulse duration and the fibers employed as can be seen in Fig.2b. For wavelengths from $2\,\mu m$ up to $2.1\,\mu m$, lasers based on bulk technology offer pulse durations below those obtained with our tunable system reaching durations and as short as sub-50 fs long pulses. This is attributed to the fact that dispersion control in the cavity can be adjusted at will by the use of chirped mirrors allowing the operation of the laser in the solitonic regime. In addition, bulk lasers have the possibility to implement Kerr-lens modelocking (KLM) as modelocking technique which has proven to be one of the most efficient techniques to achieve ultrashort pulses. This combined together with new host materials such as CALGO [23, 24, 25, 26], CNGG [27] and LCLNGG [28] among others [29, 30, 31, 32] offering broadband emission bandwiths when Tm:Ho co-doped is applied allows for ultrashort pulse durations. The beam size can be adjusted within the cavity of the system which results in lower fluences on SAMs and SESAMs which offers the possibilities for alternative materials and in principle allowing for higher pulse energies out of the oscillators and in particular for thin disk lasers. Such systems offer impressive performances yet they have some drawbacks. For instance the fact that they need to be realigned from time to time and that they are quite expensive as those systems based on Tm, Tm:Ho and Ho are usually pumped by either Ti:Sapph CW lasers or Tm fiber laser systems except for the work of Anna Suzuki et all in which they achieve $88\,fs$ pulses in a diode-pumped Tm,Ho:CLNG laser at $2090\,nm$ [30].

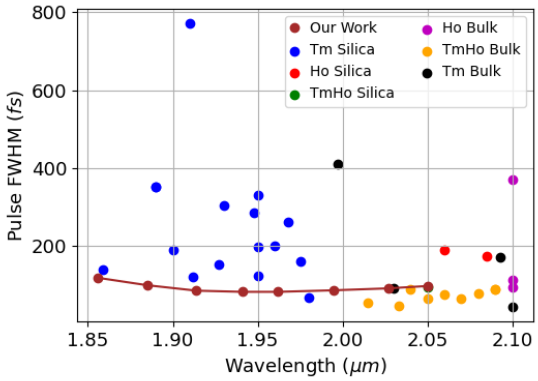

(a) Pulse FWHM as function of wavelength for different oscillator laser technologies around $2\,\mu m$ wavelength.

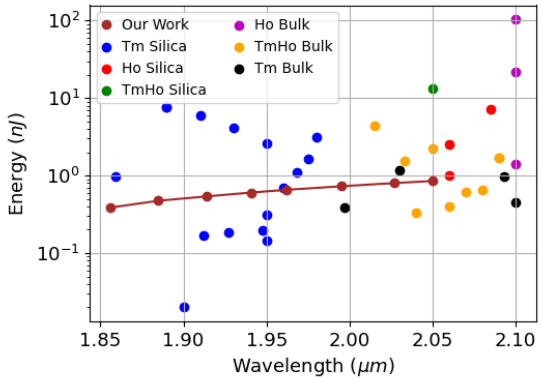

(b) Pulse energy as function of wavelength for different oscillator laser technologies around $2\,\mu m$ wavelength.

Figure 2: Pulse duration and pulse energies of oscillator laser sources at $2\,\mu m$ wavelength for different technologies including fiber and bulk. Data extracted from: [22, 23, 24, 25, 26, 27, 28, 29, 30, 31, 32, 33, 34, 35, 36, 37, 38, 39, 40, 41, 42, 43, 44, 45, 46, 47, 48, 49, 50, 51, 52]

Unfortunately, the generated pulses from mode-locked oscillators or from SSFS laser systems don't have high enough energies or intensities for certain applications and pulse amplification is required. For instance, the generation of pulses in the mid IR requires high power fs pulses to achieve substantial amount of light from difference frequency generation in non-linear crystals or for efficient amplification with high conversion efficiencies in OPA. The generation of supercontinuum in the mid IR also requires high intensities and this can only be achieved by strongly seeding highly non-linear specialty fibers. By amplifying the fs pulses either on fiber or bulk amplifiers higher output powers and energies can be obtained rapidly reaching the onset of non-linear effects such as self-focusing or to such high intensities that can damage the gain medium and optical components in the laser chain limiting the output power of amplified fs pulses. To surpass these limitations, the chirped pulse amplification (CPA) [53] technique was developed in which the fs pulses are stretched in time to hundreds of ps or even to ns duration reducing the peak power by several orders of magnitude. Afterwards pulses can be safely amplified and later re-compressed to recover the initial pulse duration. This technique has been widely used in Yb fiber lasers and in bulk Ti:sapphire lasers and amplifiers however, applying it to laser systems in the $2\,\mu m$ region has several advantages for power scaling.

There has already been work around the development of CPA systems at $2\,\mu m$ using usually a mix of fiber and bulk technology (see Fig.3. Below $2\,\mu m$ wavelength we find Tm fiber based systems most of them operating at high repetition rates ($\sim MHz$) reaching powers as high as $1\,kW$ with hundred to few hundred fs pulse durations [54]. As soon as high subsequent amplification stages are employed to achieve either high average power or high energies with low repetition rate, pulse durations start to increase due to gain narrowing increasing the transform limited duration unless NL compression or multipass cells are employed to further reduce the pulse duration after amplification. Those Tm based systems are limited to wavelengths below $2\,\mu m$ and to relatively low energies of tenths to hundreds of μJ except for regenerative amplifiers based on Tm:YAP technology capable of reaching the mJ energy level [55]. Beyond the $2\,\mu m$ wavelength we find CPA

systems based on Ho:YLF and Ho:YAG emitting at $2.05\,\mu m$ and $2.09\,\mu m$ wavelength respectively. These materials offer long lifetimes of few ms, high gain, low quantum defects and relatively broad spectral BW. The systems mostly consist of a low energy high repetition rate seeder whose repetition rate is reduced and pulses are amplified in bulk amplifiers, usually regenerative amplifiers. Thanks to the high gain obtained at low repetition rates energies as high $260\,mJ$ can be achieved with Ho:YLF based system at kHz repetition rate [56]. There are very few or none laser systems operating at around $1\,MHz$ or even higher. That is why we target such regimes by exploring CPA based on Tm:Ho co-doped fibers as they can be a potential alternative to bulk systems at a relatively high repetition rate. The target performance of our Tm:Ho doped fiber CPA laser systems have been included in Fig. 3 with the present state or the art in terms of energy as function of the repetition rate.

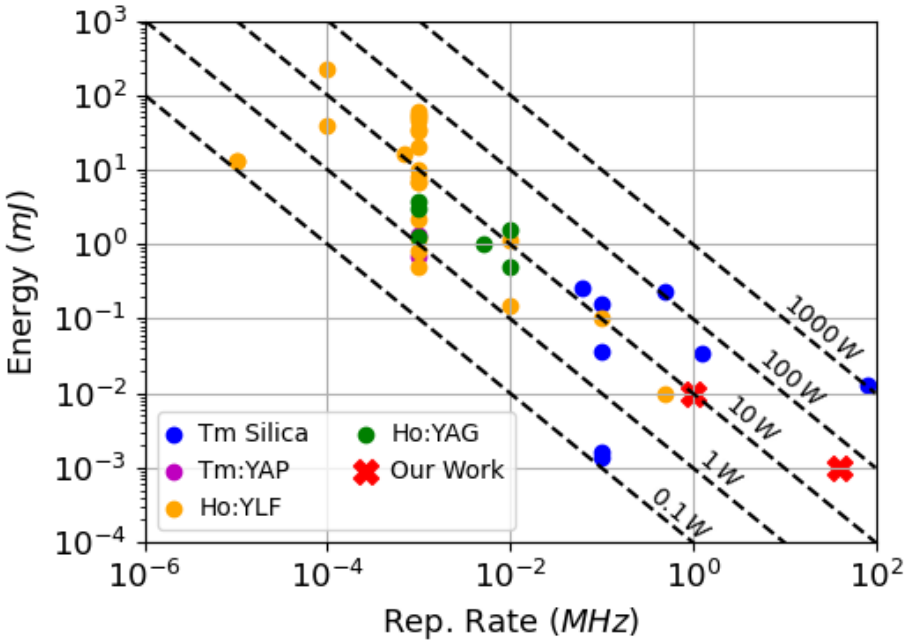

Figure 3: Pulse energy as function of the laser system repetition rate including the target performances in this work. Data extracted from: [54, 55, 56, 57, 58, 59, 60, 61, 62, 63, 64, 65, 66, 67, 68, 69, 70, 71, 72, 73, 74, 75, 76, 77, 78, 79, 80, 81, 82, 83, 84, 85, 86, 87, 88, 89, 90, 91]

Compared to $1\,\mu m$ technology, the long emission wavelength allows for the use of bigger fiber cores, which is of paramount importance for power scaling, while ensuring single-mode operation, a must for most of the applications. CPA lasers are limited by non-linear effects such as self-phase modulation (SPM) which degrades pulse compression, self-focusing which cause damage of the optical components and transverse mode instability (TMI) which degrades the beam mode in optical fibers. All these mentioned effects are wavelength dependent and by doubling the emission wavelength to $\sim 2\,\mu m$, SPM is reduced by a factor 2, self focusing limit increases by a factor 4, and TMI threshold increases by more than a factor 2 compared to $\sim 1\,\mu m$ technology [92]. This means that $2\,\mu m$ lasers have the potential to overcome the peak powers of Yb doped fiber amplifiers. In this thesis, two different CPA architectures have been designed and studied.

In Chapter 3, a high repetition rate, high average power CPA laser at $2050\,nm$ is

designed to target sub-350 fs pulses with $\sim 40\,W$ average power (see Fig. 3.17). Several stretching-compression systems are tested including fiber stretchers, chirped volume Bragg gratings (CVBGs) and grating pairs. Matching the dispersion of the stretcher and compressor is of paramount importance to achieve optimal pulse compression specially those that are grating based as high-order dispersion terms become more and more important as the wavelength increases. Results on pulse stretching and compression are presented and supported with simulations.

High repetition rate systems can deliver high average power however, the energy contained on each pulse is relatively low. To achieve highly energetic pulses, the repetition rate of the system needs to be reduced before amplification. This is quite challenging in all-fiber CPA laser systems because high energy pulses are prone to accumulate a large amount of non-linear phase worsening pulse compression. This takes place even for $\sim ns$ pulses due to being confined in fibers whose mode field diameter is between $7\,\mu m$ up to $\sim 40\,\mu m$ in single mode operation and therefore, very high intensities are quickly reached. That is why, most of low repetition rate systems at $2\,\mu m$ wavelength are based on solid state amplifiers either Ho:YLF or Ho:YAG. They are seeded by fiber lasers (mode-locked oscillators, SSFS lasers or supercontinuum souces) with reduced repetition rate and stretched pulses to be then amplified in regenerative amplifiers before further power scaling in single or double pass bulk amplifiers [67, 59]. Overall, very low energies in the $\sim nJ$ range are seeded into the regenerative amplifier however this is compensated by a large number of passes through the gain medium reaching high gain up to $\sim mJ$ levels. The main inconvenience of regenerative amplifiers is that they can operate in two regimes, in single pulse operation and in two-pulse operation [78, 74]. This is due to the long upper-state life-times of the gain media which yields to a phenomena known as bifurcation instability between these two regimes [71]. Depending on the configuration of the regenerative amplifier (repetition rate, number of round-trips...) the equilibrium in single pulse operation, while achieving high gain and low noise, can be very complex to reach. Therefore, an alternative to avoid regenerative amplifiers is the use of fiber CPA font end delivering high energy pulses capable of directly seeding single and multi pass bulk amplifiers avoiding the use of regenerative amplifiers

In Chapter 3 we also present a low repetition rate, high energy fiber CPA laser at $2050\,nm$ as an alternative to the regenerative amplifier configuration for further power scaling in Ho:YLF solid state amplifiers. Pulse stretching and compression is achieved with the use of large aperture CVBGs and the repetition rate of the system is reduced by pulse picking using an AOM. The system has been designed to achieve $10\,W$ output power at $1\,MHz$ repetition rate which corresponds to $10\,\mu J$ pulse energies with compressed pulses in the $1-2\,ps$ long duration (see Fig. 3.17). The laser would serve as seed for further energy scaling in Ho:YLF bulk amplifiers, as pump source for optical parametric chirped pulse amplification (OPCPA) using non-oxyde crystals [56, 87, 88] and for high harmonic generation.

High average powers and energies are only possible when efficient pulse amplification is achieved. In the $1\,\mu m$ spectral region, Yb fiber technology allows for high power scaling due the availability of high power, high brightness multi-mode diodes at $940\,nm$ and $976\,nm$. High efficiencies are achieved due to the low quantum defect Yb lasers and amplifiers have which, combined with the wide variety of doped standard and large mode areas (LMA) fibers, $\sim kW$ powers can be achieved from single emitter lasers. In the $2\,\mu m$ spectral region, the main active ions include Tm and Ho emitting light from $\sim 1.8\,\mu m - 2.05\,\mu m$, and $\sim 2.05 - 2.2\,\mu m$ respectively. Both Tm and Ho can be used to amplify light at $2.05\,\mu m$ however the limited availability of high power pump laser

sources and PM doped fibers reduces the efficiencies of lasers and amplifiers. Tm fibers can be pumped with either high power multi-mode diodes at $793\,nm$ or fiber lasers from $1.5\,\mu m - 1.85\,\mu m$ while Ho can only be pumped with Tm lasers. Low efficiencies with high thermal loads are expected for Tm lasers limited to the stokes limit of 33 % when pumped at $793\,nm$ however, thanks to the 2 for 1 cross-relaxation process, efficiencies above 60 % can be achieved which is of paramount importance for power scaling. Unfortunately, amplification in Tm fibers at $2.05\,\mu m$ is difficult due to the low emission cross-section at such long wavelengths. To circumvent this problem, Tm:Ho co-doped fibers are employed taking advantage of the pumping schemes for Tm fibers including the cross-relaxation effect and the long emission wavelength of Ho doped fibers.

In the last chapter of the thesis, Chapter 4, the amplification of pulses at $2.05\,\mu m$ employing Tm:Ho co-doped fused silica fibers is presented and discussed. Particular attention is paid to the cross-relaxation effect as function of the input power in amplifiers as it can improve the efficiency almost by a factor 2. Other effects such as the fiber amplifier and pump diode temperatures were also investigated. A wide variety of pulses (fs, few ps and hundreds ps) were amplified in several configurations (co-propagation, contra-propagation and free space) focusing on the temporal and spectral quality of the pulses to asses if Tm:Ho co-doped fibers are suitable for broadband pulse amplification.

Finally, the conclusions recalling the main achievements and results during this thesis are presented with a discussion on future perspectives.

The GREAT Project

This thesis is part of an European project known as the GREAT (Grating Reflectors Enabled laser Application and Training) project. It focuses on the conception, fabrication, characterization up to the implementation of grating waveguide structures (GWS) for tayloring the spectral, temporal and spatial properties of light.

Compared to traditional diffraction gratings, a GWS is a combination of sub-wavelength gratings into a planar waveguide (see Fig.4) and they offer improved diffraction efficiencies theoretically as high as 99.9% and higher induced damage thresholds provided that they are well designed. Their working principle is based on resonant diffraction effects in which the grating couples the light into the waveguide according to the Eq.1:

$$n_{eff} = sin(\theta) + \frac{\lambda}{\Delta} m \tag{1}$$

Where n_{eff} is the effective refractive index of the coupled mode, θ is the angle of incidence into the GWS, λ is the wavelength of the light, Δ is the period of the sub-wavelength grating and m is the diffraction order. Due to the nature of the coupling condition which depends on wavelength, polarization, refractive index and geometrical parameters of the GWS those devices can be implemented in laser systems enabling applications such as: wavelength division multiplexing and laser diode stabilization, pulse compression and stretching taking advantage of the dispersive effects of GWS and polarization shaping of light including radial and azimultal polarization that can be obtained by adjusting the geometry of the GWS.

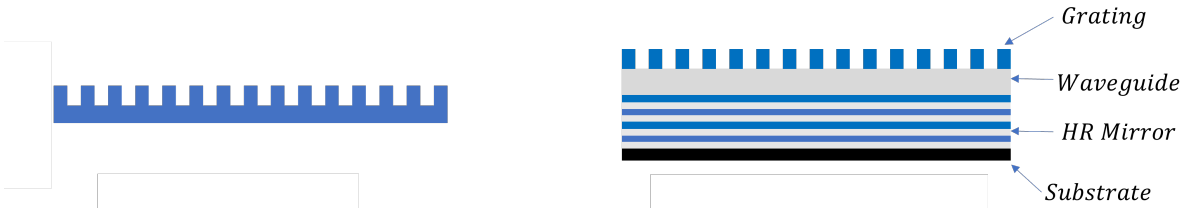

(a) Diffraction grating.

(b) Grating Waveguide Structure (GWS).

Figure 4: Schematics of diffraction gratings and grating waveguide structures.

The mentioned applications are challenging and the laser systems involved are complex therefore, to be able to control all the steps from the design up to the implementation of GWS in laser systems, a consortium of scientific institutions including academic and industrial partners was formed each of them having expertise in a particular area of the GWS production chain (design, fabrication, characterization or implementation). In addition, a group of 15 early stage researchers (ESR) located in 4 different countries including Germany, France, United Kingdom and Findland associated to the institutions of the GREAT project worked jointly to complete their PhDs and to successfully produce and

implement GWS in laser systems targeting the mentioned applications. More information about the partners and the project can be found at http://itn-great.eu/.

My role in the GREAT project was the implementation of GWS for pulses compression in chirped pulse amplified laser systems at $2.05\,\mu m$ wavelength. In most CPA lasers, the gratings implemented in the laser chain are the most sensitive elements as the beam needs to go through them 4 times therefore diffraction efficiencies above 95% are required to achieve an overall compressor efficiency above 80%. In addition, the grating needs to sustain high powers and/or energies as ultrashort femtosecond pulses with either high average power or energy are incident on them which is why those are the most commonly damaged elements in CPA systems. Developing GWS with diffraction efficiencies as high as 99% with improved laser induced damage thresholds is of paramount importance for scaling laser systems at $2.05\mu m$. The objective of the thesis is the development of CPA laser systems at $2.05\,\mu m$ wavelength with either high average power or high energy in which we can implement GWS for pulse compression.

Chapter 1

Pulse Propagation in Optical Fibers

In this chapter the conventions and formalisms used to describe ultrashort pulses and their propagation in optical fibers and dispersive media are presented. Ultrashort pulses are usually considered to be optical pulses within few picoseconds ($10^{-12}\,s$) down to femtoseconds ($10^{-15}s$). In order to have such short pulses, large bandwidths are required hence the spectral domain plays an important role through the amplitude and the phase of all the spectral components contained in the pulse as the amplitude and relative phase between each single wavelength affects the pulse temporal shape and therefore duration. Ultrashort pulses allow to reach very high peak powers and intensities as all the energy of the pulse is contained in a short period of time. When those pulses are focused or confined in a tiny space, which is the case for optical fibers, non-linear (NL) effects can take place allowing to drive a large variety of phenomena such as the generation of new frequencies, to generate solitonic pulses or to continuously shift the pulses in wavelength among others.
In this chapter the physical phenomena related to ultrashort pulse propagation in a dispersive and in NL Kerr media are introduced with the basic notions and equations to describe ultrashort pulses used all along the thesis.

1.1 Ultrashort Pulses: Temporal and Spectral Representations

An optical pulse is an electromagnetic wave that can be described by its electric field. The real electric field of an optical pulse propagating along the z axis reads in cylindrical coordinates as:

$$\vec{E}(r,z,t) = A_0(r,z,t)cos(w_0 t - \beta z + \phi(r,z,t))\vec{i} \tag{1.1}$$

Where $A_0(r,z,t)$ is the amplitude which contains the temporal and spatial information, w_0 is the carrier wave frequency and $\vec{\beta}$ the wave vector. In the absence of spatio-temporal coupling, the temporal dependence can be separated from the spatial one. Optical fibers exhibit cylindrical symmetry and it is common to work with the complex amplitude of the electric field:

$$\mathcal{A}(r,z,t) = A_0 F(r,z,t)e^{\phi_s(r,z)}H(t)e^{j\phi_t(t)}e^{-j\beta z} \tag{1.2}$$

The complex electric field can be then decomposed in three different contributions:

- The transverse spatial component: $\mathcal{F}(r,z) = F(r,z)e^{j\phi_s(r,z)}$

- The temporal component $\mathcal{H}(t) = H(t)e^{j\phi_t(t)}$
- The propagation constant $\mathcal{P}(z) = e^{-j\beta z}$

In single mode optical fibers, which are the optical fibers used all along the thesis unless specified, the spatial mode is the LP_{01} and can be approximated by a Gaussian mode with high accuracy [93]. Taking this into account, the spatial dependence will be ignored to work exclusively with the temporal component that, for convenience, will be written as:

$$\mathcal{E}(t) = \mathcal{E}_0(t)e^{j\phi(t)} \tag{1.3}$$

This expression is more convenient for pulse manipulation and in case the electric field is required, it can be obtained by taking the real port of the complex amplitude of the field $E(t) = Re[\mathcal{E}(t)]$. Ultrashort pulses' duration is strongly linked to their spectral content, not only in terms of amplitude also in phase. The temporal and spectral domain are related to each other through the Fourier transform:

$$\mathcal{E}(w) = \mathcal{F}^{-1}[\mathcal{E}(t)] = \int_{-\infty}^{\infty} \mathcal{E}(t)e^{jwt}dt \tag{1.4}$$

$$\mathcal{E}(t) = \mathcal{F}[\mathcal{E}(w)] = \frac{1}{2\pi}\int_{-\infty}^{\infty} \mathcal{E}(w)e^{-jwt}dw \tag{1.5}$$

Hence in the spectral domain and by analogy to the electric field description in time, the complex amplitude reads:

$$\mathcal{E}(w) = \mathcal{E}_0(w)e^{j\phi(w)} \tag{1.6}$$

The complex amplitude in the temporal and in the spectral domain will be used along the thesis and will always be expressed as an amplitude $\mathcal{E}_0(t)$ and $\mathcal{E}_0(w)$ and its respective temporal and spectral phase $\phi(t)$ and $\phi(w)$.

It is also important to remind that what is most frequently measured in the lab are the temporal intensity $I(t) = |\mathcal{E}(t)|^2$ using either FROG [94] through the recovery of the field or Autocorrelation techniques among others and the spectral intensity $I(w) = |\mathcal{E}(w)|^2$ using an optical spectrum analyzer. The spectral content of the pulse determines how short the pulse can be and the spectral phase is a measure of the delays between the spectral components, it contains the information of where a given spectral component is located within the pulse in time. On the other hand the temporal phase contains the information of the instantaneous frequency, that is the frequency of the pulse at a certain time within the pulse temporal extent. The importance of the temporal and spectral phase will be further discussed in the next section.

1.2 Dispersion in Ultrashort Pulses

The effect of dispersion comes from the fact that materials have a refractive index whose value is wavelength dependent, this means that every wavelength propagating in a dispersive medium propagates at a different velocity which yields to frequency dependent propagation delays affecting the pulse duration. The effect of dispersion becomes more and more important as the spectral content of the pulses increases. For a nanosecond pulse which has a very narrow spectrum, even though it suffers from dispersion, the effect

is negligible as the change in refractive index is very small across the spectral bandwidth. However, for ultrashort pulses with spectra spanning tenths of nanometers, dispersion plays a very important role during propagation. The propagation delay or group delay indicates at which time within the pulse the frequency w is "located" and is linked to the spectral phase by the following expression:

$$\mathcal{T}(w) = \frac{d\phi(w)}{dw} \tag{1.7}$$

Usually, the spectral phase $\phi(w)$ is treated as a Taylor expansion around the carrier frequency w_0 as:

$$\phi(w) = \phi(w_0) + \left(\frac{d\phi}{dw}\right)_{w_0}(w - w_0) + \frac{1}{2}\left(\frac{d^2\phi}{dw^2}\right)_{w_0}(w - w_0)^2 + \frac{1}{6}\left(\frac{d^3\phi}{dw^3}\right)_{w_0}(w - w_0)^3 + ... \tag{1.8}$$

The expansion can be rewritten in a more compact way by substituting the derivative terms $\phi_n = \left(\frac{d^n\phi}{dw^n}\right)_{w_0}$:

$$\phi(w) = \phi_0 + \phi_1(w - w_0) + \frac{1}{2}\phi_2(w - w_0)^2 + \frac{1}{6}\phi_3(w - w_0)^3 + \frac{1}{24}\phi_4(w - w_0)^4 + ... \tag{1.9}$$

The zero order term ϕ_0 is known as the carrier envelope phase or carrier envelope offset phase (CEP) and it is related to the delay between the optical phase and the pulse envelope. The CEP is relevant for few cycle pulses however such short pulse durations are not reached within this work and CEP term will be ignored. The first order term ϕ_1 is known as the group delay and is the time delay linked to pulse propagation, the time it takes a pulse to travel from one location to another. The GD does not affect the pulse duration itself. The following expansion coefficients ϕ_2, the group delay dispersion (GDD), ϕ_3 the third order delay dispersion (TOD), ϕ_4 the fourth order delay dispersion (FOD) and so on are known as dispersive terms and they affect the pulse shape and duration. GDD broadens the pulse as it is a frequency dependent linear delay. TOD is responsible for producing a tail of pre or past pulses. Even terms have symmetric effects in the pulse while odd terms are asymmetric. In this work, up to fourth order dispersion coefficient has been taken into account for the study of dispersion in optical pulses. Before treating the dispersive terms one by one it's important to make few clarifications when it comes to deal with dispersion in optical fibers.

An alternative description for the dispersion usually used in fibers, is to work with the spectral phase per unit of length [95]. This is equivalent to do a Taylor expansion on the propagation constant:

$$\beta(w) = \beta(w_0) + \left(\frac{d\beta}{dw}\right)_{w_0}(w - w_0) + \frac{1}{2}\left(\frac{d^2\beta}{dw^2}\right)_{w_0}(w - w_0)^2 + \frac{1}{6}\left(\frac{d^3\beta}{dw^3}\right)_{w_0}(w - w_0)^3 + ... \tag{1.10}$$

Again, the expansion can be rewritten by substituting the derivative terms $\beta_n = \left(\frac{d^n\beta}{dw^n}\right)_{w_0}$:

$$\beta(w) = \beta_0 + \beta_1(w - w_0) + \frac{1}{2}\beta_2(w - w_0)^2 + \frac{1}{6}\beta_3(w - w_0)^3 + \frac{1}{24}\beta_4(w - w_0)^4 + ... \tag{1.11}$$

The spectral phase can be then obtained by multiplying the propagation constant β by the propagation length or fiber length L, $\phi(w) = \beta(w)L$. The first order term β_1 is the inverse of the group velocity v_G:

$$\beta_1 = \left(\frac{d\beta}{dw}\right)_{w_0} = \frac{1}{v_G} \tag{1.12}$$

$$v_G = \left(\frac{d\beta}{dw}\right)^{-1}_{w_0} = \frac{c}{n - \left(\frac{dn}{d\lambda}\right)} = \frac{c}{n}\left(\frac{1}{1 + \frac{w}{n}\frac{dn}{dw}}\right) \tag{1.13}$$

Where the propagation constant is $\beta = w\frac{n(w)}{c}$, c is the speed of light in vacuum and $n(w)$ is the effective refractive index. It's important to remark that the effective refractive index is due to the material refractive index, usually expressed using the Selmeier equation [96] (see Eq.1.14), which takes into account material resonances in the ultraviolet (UV) and IR for three different wavelengths (λ_1,λ_2 and λ_3) and the waveguiding contribution to the refractive index which comes from light propagation in waveguides (optical fiber).

$$n^2(\lambda) = 1 + \frac{A\lambda^2}{\lambda^2 - \lambda_1^2} + \frac{B\lambda^2}{\lambda^2 - \lambda_2^2} + \frac{C\lambda^2}{\lambda^2 - \lambda_3^2} \tag{1.14}$$

This implies that there are dispersive effects due to the material (material dispersion) and dispersion due to the waveguide (waveguiding dispersion). The second term β_2 is known as group velocity dispersion (GVD) yet in practice, in optical fibers the dispersion value D is commonly used:

$$D = \frac{d\beta_1}{d\lambda} = \frac{-2\pi c\beta_2}{\lambda^2} \tag{1.15}$$

The dispersion value D is expressed in $ps/(nm\,km)$ and it tells what would be the delay in time between two different wavelengths when propagated over an optical fiber of length L. As an example, if a transform limited pulse with a bandwidth of $10\,nm$ at full width half maximum (FWHM) in intensity propagates in a $100\,m$ long optical fiber with dispersion $D = 25\,ps/(nm\,km)$, the pulse will stretch and by the end of the fiber it will be $2.5\,ps$ long at FWHM. The higher order terms β_3, β_4 and so on are also known as TOD and FOD per unit length.

All the components within the laser chain can modify the spectral phase of the pulses affecting its temporal properties. In fact, the manipulation of ultrashort pulses consists of properly manipulating the spectral phase with the suitable dispersive elements and this is the core and main idea of the CPA technique as it will be seen in the second part of the thesis.

1.2.1 Group Velocity Dispersion (GVD)

The GVD is the first dispersive coefficient in the Taylor expansion and is linked to the dispersion parameter D by Eq.1.15. In fused silica optical fibers, two different dispersion regimes can be distinguished, the normal dispersion regime ($\beta_2 > 0$ and $D < 0$) where low frequency (red-shifted) components travel faster than high frequency (blue-shifted) spectral components and the anomalous dispersion regime ($\beta_2 < 0$ and $D > 0$) which is the other way around. The change from normal to anomalous dispersion takes place at the zero dispersion wavelength λ_{ZD} which is usually around $1.3\,\mu m$. Since the dispersion

experienced by pulses in an optical fiber comes from the material (D_m) and the wave-guiding dispersion (D_w), which is always normal for single mode optical fibers [97], the fibers can be engineered in order to taylor its properties and shift the zero dispersion wavelength to longer values (dispersion shifted fibers) or flatten the dispersion curve (dispersion flattened fibers) (see Fig.1.1a). The sum of the material and wave-guiding dispersion is known as chromatic dispersion D_C (see Fig.1.1b and Eq.1.16).

$$D_C = D_m + D_w \tag{1.16}$$

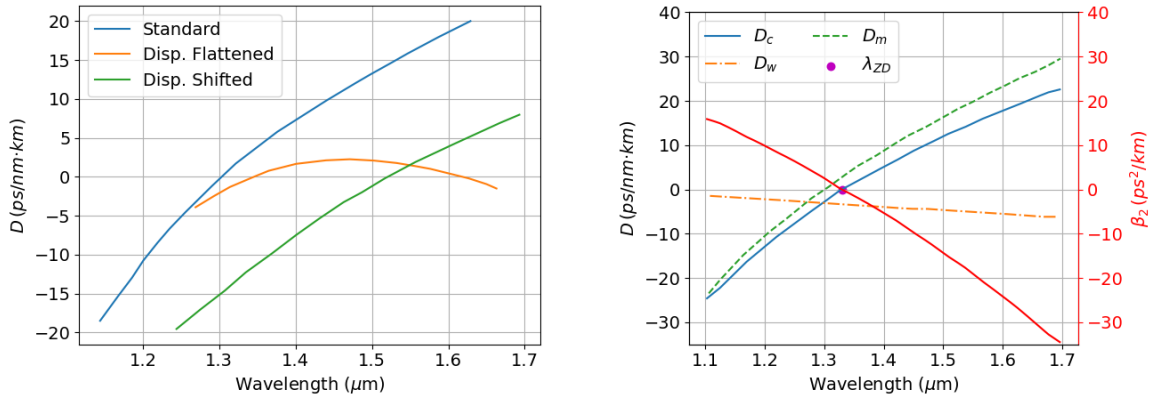

(a) Dispersion for standard, dispersion flattened and dispersion shifted optical fibers

(b) Chromatic dispersion D_c, material dispersion D_m, waveguide dispersion D_w and GVD for a standard telecom optical fiber

Figure 1.1: Fiber dispersion parameter D for different optical fibers and material, waveguide and chromatic dispersion in standard telecom optical fiber.

Before analysing the effects of the GVD, it is important to introduce the instantaneous frequency $w_{inst}(t)$ which gives the carrier frequency at a time t within the pulse and is linked to the temporal phase $\phi(t)$ by the following expression:

$$w_{inst}(t) = w_0 - \frac{\partial\phi(t)}{\partial t} \tag{1.17}$$

To illustrate the effects of GVD, the propagation of a Gaussian pulse with pulse duration τ_0 in a dispersive media is used as an example. Before propagation, the pulse in the time and in the frequency domain read:

$$\mathcal{E}(t) = e^{-\left(\frac{t}{2\tau_0}\right)^2} e^{j\phi(t)} \tag{1.18}$$

$$\mathcal{E}(w) = e^{-\left(\frac{w}{2\Delta w}\right)^2} e^{j\phi(w)} \tag{1.19}$$

Initially the pulse is transform limited $\phi(t) = \phi(w) = 0$. After propagating in a dispersive medium of length L with only β_2 ($\phi(w) = \frac{1}{2}\beta_2 L(w - w_0)^2$) the pulse in the time domain can be calculated by Fourier transform and it becomes:

$$\mathcal{E}(t) = e^{-\left(\frac{t}{2\tau}\right)^2} e^{j(a+(w_0-bt)t)} \tag{1.20}$$

$$b = \frac{4\beta_2 L}{\tau_0^4 + 4\beta_2^2 L^2} \tag{1.21}$$

It can be seen from the equations that the instantaneous frequency of the the pulse after propagation exhibits a linear chirp contribution $w(t) = w_0 - \frac{\partial\phi(w)}{\partial w} = (w_0 + bt)$ and that the pulse duration has changed to τ:

$$\tau = \tau_0\sqrt{1 + \left(\frac{4log2\phi_2}{\tau_0^2}\right)^2} \tag{1.22}$$

The pulse duration has increased in time due to the GDD acquired during propagation. Please note that τ and τ_0 refer to the field at $1/e^2$ in intensity, and it is only used for the development of the equations. In practice, the pulse intensity at full width half maximum τ_{FWHM} will always be used in the examples and measurements unless specified. Both values are related by the following relation: $\tau_{FWHM} = \sqrt{(2ln2)}\tau$. For a $100\,fs$ pulse at $1560\,nm$, $35.6\,nm$ BW that has propagated in a dispersive medium and acquired a total GDD of $\phi_2 = \pm 5000\,fs^2$ (Fig.1.2b, 1.2d) the pulse shape changes according to Fig.1.2a, and Fig.1.2c.

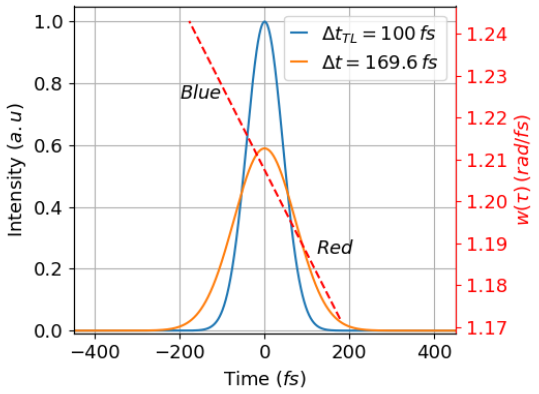

(a) Anomalous dispersion with $\phi_2(w) = -5000\,fs^2$. Blue spectral components travel faster than red.

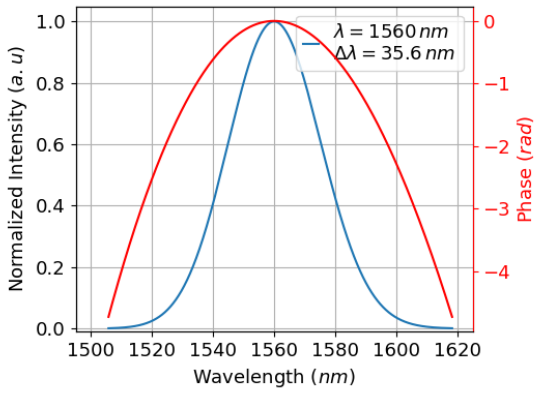

(b) Anomalous dispersion with $\phi_2 = -5000\,fs^2$, $\lambda_0 = 1560\,nm$ and $\Delta\lambda = 35\,nm$.

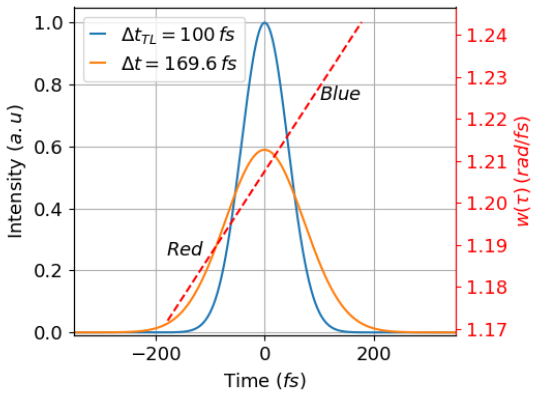

(c) Normal dispersion with $\phi_2(w) = +5000\,fs^2$. Red spectral components travel faster than blue.

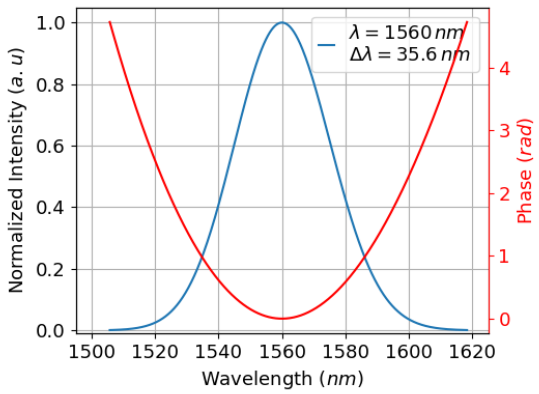

(d) Normal dispersion with $\phi_2 = +5000\,fs^2$, $\lambda_0 = 1560\,nm$ and $\Delta\lambda = 35\,nm$.

Figure 1.2: Pulse intensity and spectra of chirped Gaussian pulses due to negative and positive GDD.

The pulse stretched in time from $100\,fs$ to $169.6\,fs$ at FWHM independently of the sign of the GDD. The main difference from positive to negative GDD (normal or anoma-

lous dispersion) is the frequency variation across the pulse $w_{inst}(t)$ which is either linearly increasing or decreasing. If the instantaneous frequency increases across the pulse, the pulse is said to be up-chirped, this means that the low frequency components are leading the pulse therefore red spectral components travel faster than blue ones (see Fig.1.3a). This is the case for normal dispersion media. In the anomalous dispersion regime, the instantaneous frequency across the pulse decreases and the pulse is said to be down-chirped. The high frequency components are leading the pulse therefore blue spectral components travel faster than the red ones (see Fig.1.3b). Hence the difference between Fig.1.2a and Fig.1.2c is the time at which a particular wavelength is contained within the pulse and this information can be obtained from the group delay $\tau(w)$. For the same amount of GDD, the pulse duration of broadband pulses will be more affected than for narrowband pulses.

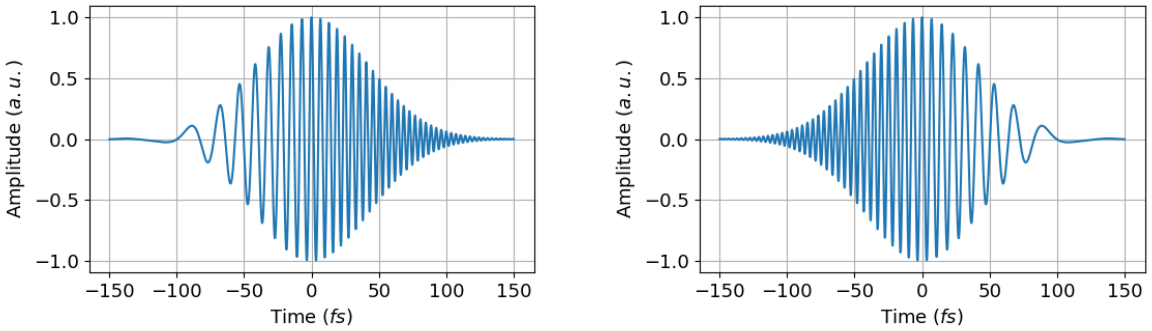

(a) Up-chirped.

(b) Down-chirped.

Figure 1.3: Electric field of a chirped Gaussian pulse.

Adding GDD stretches the pulses and this is solely achieved by modifying pulses' spectral phase using dispersive elements. If pulse compression is required after stretching, this can be achieved by adding GDD with the opposite sign used to stretch. If normal dispersive elements have been used to stretch the pulses, anomalous dispersive components will compress them and the other way around.

1.2.2 Third Order Dispersion (TOD)

Third order dispersion (TOD) is the second dispersion term in the Taylor development and is asymmetric as it has a cubic dependence with respect to the angular frequency w. Pulse propagation in a fiber that has TOD affects the pulse shape and width. TOD broadens the pulse in time and it also creates a set of secondary pulses with decreasing energy as they walk away from the main pulse. It is a very detrimental term because not only it broadens the pulse, decreasing its peak power, but also creates a series of side pulses distributing the total energy between them.

For a $100\,fs$ pulse at $1560\,nm$, $\Delta\lambda = 35.6\,nm$ bandwidth that has acquired a total TOD of $\phi_3 = \pm 10^6\,fs^3$ ($\phi(w) = \frac{1}{6}\phi_3(w - w_0)^3$) the pulse shape is obtained by Fourier transform and it changes according to Fig.1.4a and Fig.1.4c.

As can be seen in Fig.1.4b and Fig.1.4d, when the TOD signed is reversed, the tail of the pulses generated are at the trailing edge of the pulse ($\phi_3 > 0$) or at the leading edge ($\phi_3 < 0$).

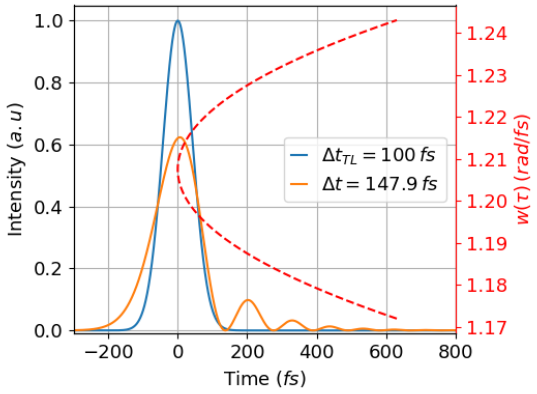

(a) $\phi_3(w) = +10^6\, fs^3$.

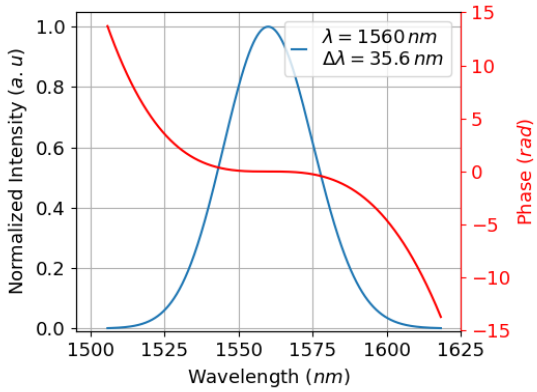

(b) $\phi_3 = +10^6\, fs^3$, $\lambda_0 = 1560\, nm$ and $\Delta\lambda = 35\, nm$.

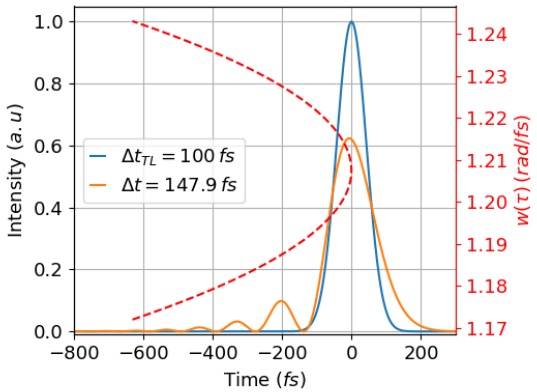

(c) $\phi_3(w) = -10^6\, fs^3$.

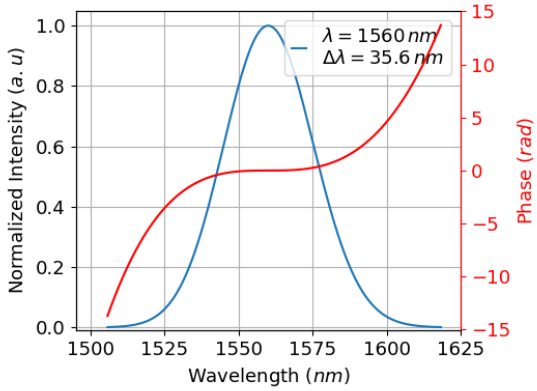

(d) $\phi_3 = -10^6\, fs^3$, $\lambda_0 = 1560\, nm$ and $\Delta\lambda = 35\, nm$.

Figure 1.4: Pulse intensity and spectra of chirped Gaussian pulses due to positive and negative TOD.

1.2.3 Fourth order dispersion (FOD)

The last dispersive term that is taken into account in this work is the fourth order dispersion term FOD (ϕ_4). FOD creates a pedestal around the pulse, increasing its duration and reducing the peak power. If a $100\,fs$ pulse at $1560\,nm$, $\Delta\lambda = 35\,nm$ bandwidth that has acquired a total FOD of $\phi_4 = \pm 1.5 \cdot 10^8\,fs^4$ ($\phi(w) = \frac{1}{24}\phi_4(w - w_0)^4$), the pulse shape is obtained by Fourier transform and it changes according to Fig.1.5a and Fig.1.5c.

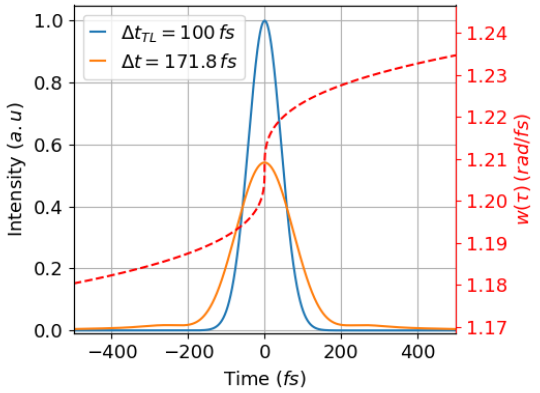

(a) $\phi_4(w) = +1.5 \cdot 10^8\,fs^4$.

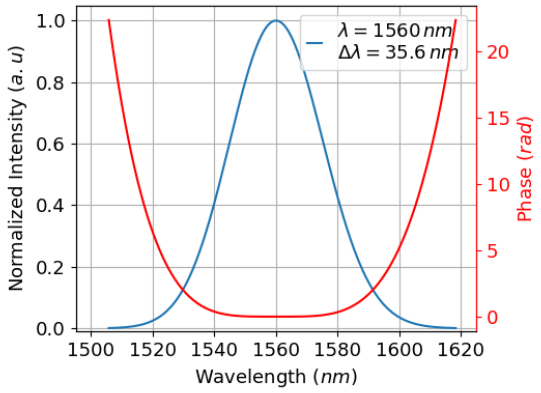

(b) $\phi_4(w) = +1.5 \cdot 10^8\,fs^4$., $\lambda_0 = 1560\,nm$ and $\Delta\lambda = 35\,nm$.

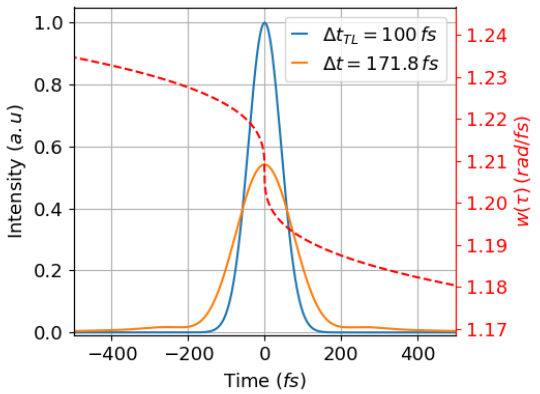

(c) $\phi_4(w) = -1.5 \cdot 10^8\,fs^4$.

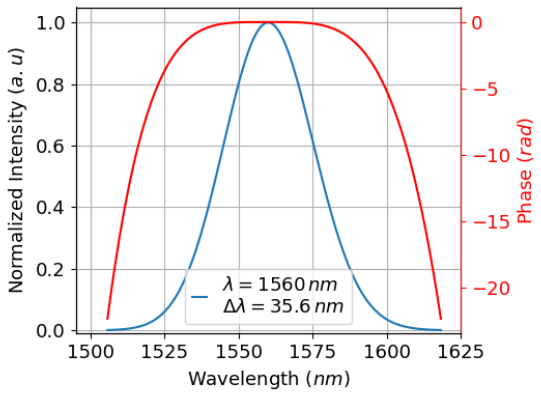

(d) $\phi_4(w) = -1.5 \cdot 10^8\,fs^4$., $\lambda_0 = 1560\,nm$ and $\Delta\lambda = 35\,nm$.

Figure 1.5: Pulse intensity and spectra of chirped Gaussian pulses due to positive and negative FOD.

The pulse has stretched from $100\,fs$ to $171.8\,fs$ duration regardless of the sign of the phase and a small pedestal has appeared extending few hundreds of fs on both sides of the pulse. As for the case of GDD, the main difference from Fig.1.5a and Fig.1.5c is whether the low frequency or high frequency components are leading the pulse. Since the effect of FOD is symmetric, it can be partially compensated with GDD slightly shortening the pulse duration however the pedestal originated from FOD can't be removed second order dispersion.

1.3 Ultrashort Pulse Propagation in a Kerr Medium

The optical Kerr effect or AC Kerr effect is a phenomena by which a material exhibits a refractive index variation which is intensity dependent:

$$n(w, I) = n(w) + n_2 I(t) \tag{1.23}$$

$$n_2 = \frac{3}{8}\frac{\chi^{(3)}}{n(w)^2 c\epsilon_0} \tag{1.24}$$

with ϵ_0 the vacuum electric permittivity, c the speed of light and $\chi^{(3)}$ the real part of the third order susceptibility of the material [95, 98]. In general, this refractive index variation is very small and in fused silica fibers is approximately $n_2 \sim 2.7{\cdot}10^{-16} cm^2/W$ [99]. For glass materials such as fused silica, n_2 is always positive provided that multi-photon absorption is avoided by using wide bandgap materials [100] or limited intensities. If a substantial refractive index variation is desired, high intensities are a must, that means that high energetic ultrashort pulses confined in a tiny region are required, and to this end optical fibers are ideal due to its long interaction lengths and small mode areas.

The Kerr effect is a NL process responsible of several NL phenomena such as self-phase modulation (SPM), self-focusing and four-wave mixing among others. Some of these NL phenomena such as four-wave mixing are very weak and can be ignored unless phase matching conditions are met [98]. The only NL effects that will be considered along the thesis are SPM, which originates from an intensity dependent phase shift, and Raman Scattering [101], which is a process in which the photons interact with the medium transferring part of its energy to a phonon. Both effects will be introduced and discussed in the following sections ignoring dispersion effects unless specified.

1.3.1 Self-Phase Modulation (SPM)

Self-phase modulation is the consequence of having a time dependent refractive index due to the Kerr effect. To describe this phenomena a Gaussian pulse with amplitude $\mathcal{E}_0$ propagating along the z direction is used as example:

$$\mathcal{E}(t, z) = \mathcal{E}_0 e^{-\left(\frac{t}{2\tau}\right)^2} e^{j(w_0 t - \beta z)} \tag{1.25}$$

Then its temporal intensity $I(t) = |\mathcal{E}(t)|^2$:

$$I(t) = |\mathcal{E}(t)|^2 = |\mathcal{E}_0|^2 e^{-\frac{t^2}{\tau^2}} = I_0 e^{-\frac{t^2}{\tau^2}} \tag{1.26}$$

By direct substitution of Eq.1.26 into Eq.1.23 a time dependent refractive index is obtained:

$$n(w, I(t)) = n(w) + n_2 I(t) = n(w) + n_2 I_0 e^{-\frac{t^2}{\tau^2}} \tag{1.27}$$

The phase acquired during pulse propagation in the NL medium is also intensity dependent:

$$\phi(t, z) = -\frac{w_0}{c} n(I(t)) z = -\frac{w_0}{c} n(w) z - \frac{w_0}{c} n_2 I(t) z \tag{1.28}$$

Where the first term is a linear contributions to the phase and the intensity dependent term is the NL phase contribution ($\phi_{NL} = \frac{w_0}{c} n_2 I(t) z$). The intensity dependent refractive index results in a time dependent phase change and this is known as self-phase modulation.

Thus the intensity dependent refractive index changes the phase of the wave itself as function of time (see Fig.1.6a). The instantaneous frequency of the pulse after propagation over a distance $z = L$ is then:

$$w_{inst}(t) = \frac{\partial\phi(t)}{\partial t} = w_0 - \frac{w_0}{c}L\frac{\partial n(t)}{\partial t} = w_0 + \frac{2w_0 n_2 I_0}{c\tau^2}Lte^{-\frac{t^2}{\tau^2}} \tag{1.29}$$

Eq.1.29 shows that the instantaneous frequency across the pulse is changing with respect to the carrier frequency w_0 which yields to up-chirped pulses. For $t \sim 0$ the frequency variation is linear with time $w(t) - w_0 \propto t$ (linear chirp) while for $t >> \tau$ the instantaneous frequency is the carrier frequency w_0. Between those limits there are two turning points such that $\frac{\partial^2\phi(t)}{\partial t^2} = 0$. This takes place at $t_T = \pm\frac{\tau}{\sqrt{2}}$ (see Fig.1.6b). Then, the maximum broadening due to SPM (Δw_{SPM}) defined as the instantaneous frequency variation between these two turning points is:

$$\Delta w_{SPM} = w_{inst}\left(\frac{\tau}{\sqrt{2}}\right) - w_{inst}\left(\frac{-\tau}{\sqrt{2}}\right) = \frac{2\sqrt{(2)}w_0 n_2 I_0 L}{c\tau\sqrt{e}} \propto \frac{n_2 I L}{\tau} \tag{1.30}$$

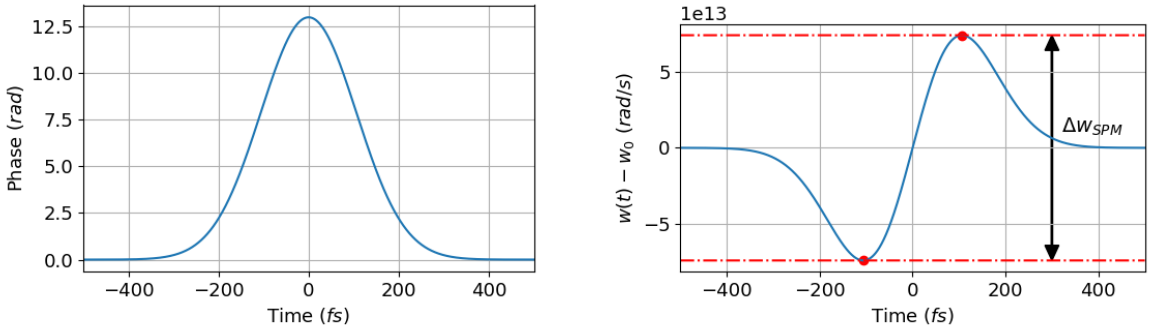

(a) Temporal phase $\phi(t)$.

(b) Instantaneous frequency.

Figure 1.6: Temporal phase and instantaneous frequency of a Gaussian pulse after propagation in a Kerr medium (fused silica) over $10\,m$.

The newly generated frequencies can also be observed on the spectrum of the pulse. SPM was simulated by propagating a Gaussian pulse ($250\,fs$, $\Delta\lambda_0 = 14.3\,nm$ and $\lambda_0 = 1560\,nm$) in a Kerr medium (fused silica fiber) over $L = 10\,m$. The evolution of the pulse spectrum has been plotted every $2\,m$ of fiber in Fig.1.7.

As the pulse propagates more and more frequencies are being generated and the new spectral components start to appear in the spectra. It can be seen that the spectra is modulated and this is because there is always delay between two identical generated frequencies in time (see Fig.1.6b). The interference depends on the phase difference and as the BW increases more wavelengths are interfering with each other increasing the modulations. SPM is increasing the bandwidth of the pulse potentially leading to shorter pulses. SPM does not modify the temporal pulse shape or duration and since dispersion effects are being ignored so far, the input and output pulses have the same duration but the spectral content has changed. The input pulse was transform limited while output pulse is up-chirped yet both having same pulse duration. The newly generated spectral content is obviously spread in time and therefore dispersed. Dispersion compensation will shorten the pulse duration and this can be achieved by propagating the pulses in an anomalous dispersive medium. For instance, SPM is a technique that allows the

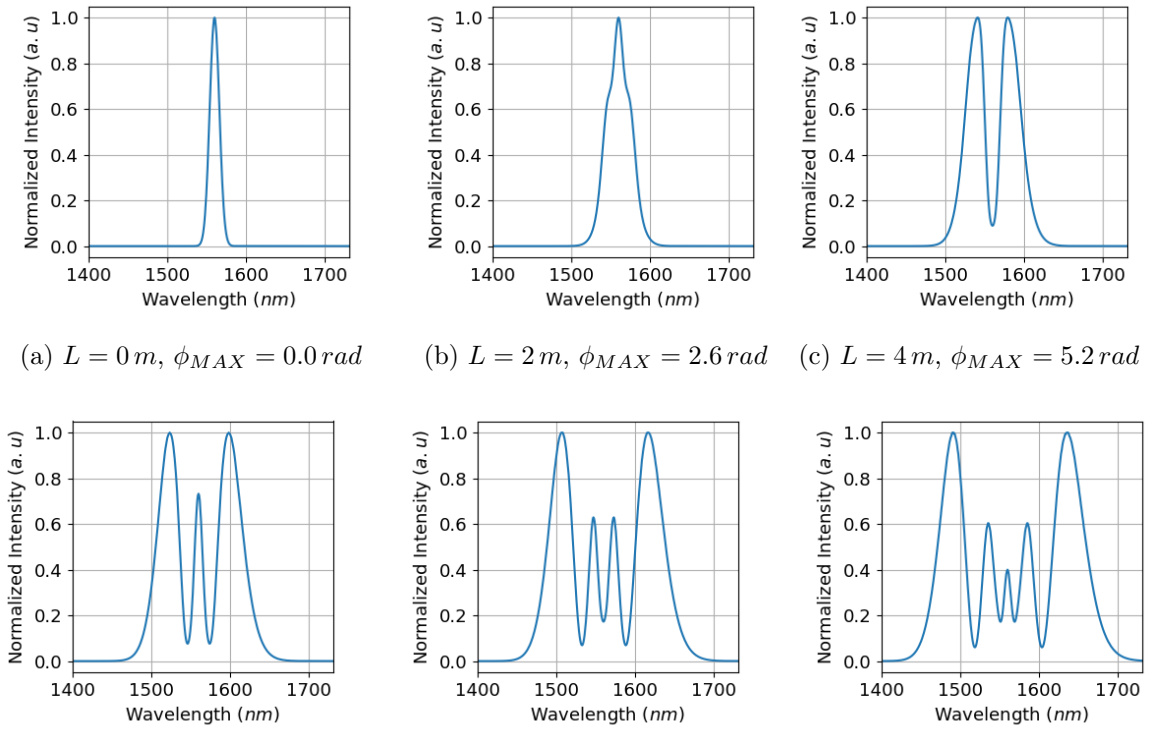

(a) $L = 0\,m$, $\phi_{MAX} = 0.0\,rad$ (b) $L = 2\,m$, $\phi_{MAX} = 2.6\,rad$ (c) $L = 4\,m$, $\phi_{MAX} = 5.2\,rad$

(d) $L = 6\,m$, $\phi_{MAX} = 7.8\,rad$ (e) $L = 8\,m$, $\phi_{MAX} = 10.41\,rad$ (f) $L = 10\,m$, $\phi_{MAX} = 13.0\,rad$

Figure 1.7: Spectral evolution of a Gaussian Pulse in a Kerr medium (fused silica fiber) for different fiber lengths L

generation of new frequencies that, combined with dispersion, can yield to ultrashort pulses [81, 102, 103, 104].

It is important to remark that the generated bandwidth is proportional to L, the length of the NL material which for optical fibers can be very long. Therefore the limitation for SPM are losses and dispersion. Losses reduce the pulse intensity as it propagates and eventually stop SPM. However, standard telecom fused silica fibers have losses below $1db/km$ in the near IR region and as low as $0.2dB/km$ at $1.56\,\mu m$ [105]. This means that the main limiting phenomena is dispersion. Dispersion will temporally stretch the pulse as it propagates at rate that will increase as new frequencies are generated (increasing bandwidth). On the other hand, as the pulse extends in time, the intensity of the pulses reduces until SPM ceases. In the absence of SPM only dispersive effects will remain during pulse propagation. It is very useful then to define two quantities, the dispersion length L_D and the NL length L_{NL}:

$$L_D = \frac{\tau_0^2}{|\beta_2|} \tag{1.31}$$

$$L_{NL} = \frac{1}{\gamma P_0} \tag{1.32}$$

$$\gamma(w_0) = \frac{w_0 n_2}{c A_{eff}} \tag{1.33}$$

Where τ_0 is the field half width half maximum $(1/e)$ pulse duration, P_0 is peak power, γ is the NL coefficient and A_{eff} is the effective mode area of the fiber. As the frequency

increases, the NL coefficient γ increases due to a higher photon energy while a higher effective area A_{eff} decreases the energy density and the NL coefficient. These quantities can be used to know whether dispersive or NL effects play a dominant role during pulse propagation over a length L. Four different cases can be distinguished:

- $L << Z_{NL}$ and $L << L_D$ Neither dispersive nor NL effects play a significant role, the pulse remains unchanged both in time and frequency.
- $L << Z_{NL}$ and $L \sim L_D$ Pulse propagation is governed by dispersion and NL effects are negligible.
- $L \sim Z_{NL}$ and $L << L_D$ NL effects dominate and SPM will modify the optical spectrum of the pulses with negligible temporal shape change.
- $L \geq Z_{NL}$ and $L \geq L_D$ Dispersion and NL effects act together.

The most interesting regime is when dispersion and NL effects act together. In this situation is it possible to potentially spectrally broaden and compress the pulses simultaneously, this is known as NL pulse compression and this technique is used later in the thesis to generate sub-100 fs pulses [64, 106, 107]. It can also happen that dispersion and NL effects balance each other. In such case, pulses propagate without changing its duration or spectrum. This is known as solitonic propagation and cooperation between dispersion and SPM can only happen in the anomalous dispersion regime. The resulting pulses are known as solitons and have a set of properties and characteristics that make them very interesting [108].

1.4 Solitonic Propagation

A soliton is a pulse that propagates without changing neither its temporal or spectral properties in a lossless fiber as a result of the perfect balance between dispersion in the anomalous regime and non-linearities (SPM). SPM broadens the spectrum producing up-chirped pulses while dispersion in the anomalous regime ($D > 0$) yields to down-chirped pulses. SPM and anomalous dispersion compensate each other when the non-linear length (Eq.1.32) and the dispersion length (Eq.1.31) are equal. The soliton order N is defined as:

$$N^2 = \frac{L_D}{L_{NL}} = \frac{\gamma \tau_0^2 P_0}{|\beta_2|} \tag{1.34}$$

For $N = 1$ there is perfect balance between dispersion and non-linearities and fundamental soliton pulses are obtained. The condition $L_D = L_{NL}$ sets the soliton energy ($E_{SOL} = P_0 \tau_{FWHM}/0.88$) and pulse duration according to the fiber properties (n_2, β_2, A_{eff}) as can be seen on Eq.1.35:

$$E_{SOL} = \frac{2|\beta_2|}{\gamma \tau} = \frac{|\beta_2| \lambda A_{eff}}{\pi n_2 \tau} \tag{1.35}$$

The soliton energy is proportional to the mode area A_{eff}, the wavelength λ and the group velocity dispersion β_2. For a fixed pulse duration, if high energy solitons are desired fibers with a large mode area and large anomalous dispersion must be used. It is the other way around to generate ultrashort solitons. For a fixed pulse energy, small mode areas

and small anomalous dispersion is required. Ultrashort and high energy solitons can also be obtained. As pulse duration decreases, the bandwidth of the pulses increases and the dispersion effects become more and more important. To balance out dispersion, SPM has to increase by increasing the energy of the pulses [108, 109]. According to Eq.1.35, it should be possible to taylor the soliton energy and duration by selecting the optical fiber with the right properties (n_2, β_2, A_{eff}). At the same time, the properties of the soliton are also dependent on the initial pump pulses as they need to evolve as they propagate to adjust its energy and duration such that $L_D = L_{NL}$.

The temporal shape of soliton pulses can be expressed as:

$$\mathcal{E}(t) = \mathcal{E}_0 sech\left(\frac{t}{\tau_0}\right) e^{i\frac{\tau_0^2 t}{2|\beta_2|}} \tag{1.36}$$

Where $\mathcal{E}_0$ is the amplitude, τ_0 is field half width half maximum $(1/e)$ and β_2 is the GVD. For the soliton pulses, the intensity FWHM is $\tau_{FWHM} = 1.763\tau_0$. Solitons are transformed limited as long as dispersion and SPM balance each other. For *sech* pulses, the time bandwidth product is $\Delta\tau_{FWHM}\Delta w_{FWHM} = 0.315$. The pulse duration is inversely proportional to the bandwidth and since the target pulse duration is sub-100 fs pulses, large bandwidths are expected (tenths of nm). Such short pulse durations and large bandwidths give rise to an additional non-linear phenomena which is of particular particular importance for soliton pulses which is Raman Scattering and manifests as a continuous shift in wavelength known as soliton self-frequency shift (SSFS).

1.4.1 Soliton Self-Frequency Shift

Raman Scattering is an inelastic NL process where there is an exchange of energy between the photons and the NL medium. In this process, a signal photon will interact with the medium transferring part of its energy to generate a phonon and a photon that has been downshifted in frequency. The downshift is determined by the vibrational modes of the medium and is known as Raman shift. In fused silica fibers, which is an amorphous material, the vibrational modes are very broad and the Raman gain extends up to $40\,THz$ with a peak at $13.1\,THz$ as depicted in Fig. 1.8 [101, 110]. The Raman gain can be expressed as:

$$g_R(w - w_0) = \frac{f_R w_0}{cn(w_0)}\chi^{(3)} Im[h(w - w_0)] \tag{1.37}$$

Where f_r is the Raman material contribution and $h(w - w_0)$ is the Fourier transform of the Raman response $h(t)$. The Raman gain g_R and the Raman response $h(t)$ for fused silica are shown in Fig.1.8.

Raman Scattering is a very fast process in the fs range and exhibits a threshold-like behaviour. It takes place provided that the pulses have a high enough peak power, otherwise it can be ignored. As the pulse propagates, Raman scattering takes place generating photons $\sim 13\,THz$ away from each frequency contained in the pulse. Since pulse are very broad, the generated photons $13\,THz$ away by the high frequency components of the pulse, still fall within the pulse bandwidth which makes the process stimulated. The high frequency components act as pump for the low frequency ones which results in a continuous red-shift in wavelength as the pulse propagates [95, 111].

As the soliton frequency shifts and reaches longer wavelengths, the rate at which the shift takes place slows down. There are several mechanisms that slow down SSFS

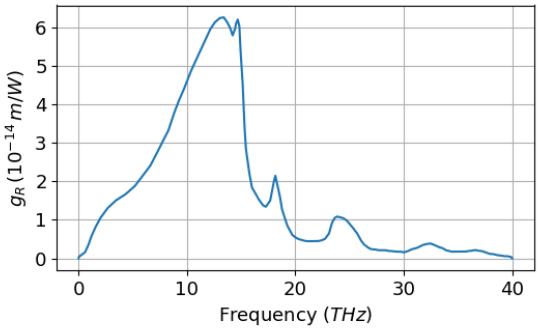

(a) Raman gain spectrum.

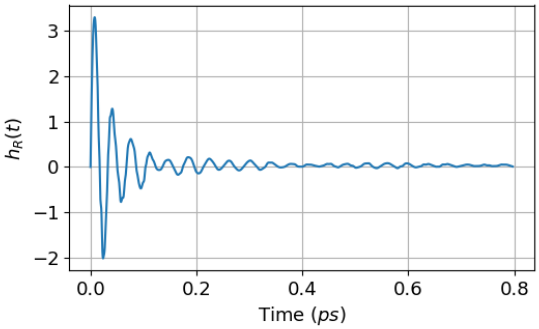

(b) Raman response $h(t)$.

Figure 1.8: Raman gain spectrum and Raman response. Data taken from [101].

such as propagation losses and the intrinsic losses due to Raman scattering which is an inelastic process. As the wavelength shifts, there is an increase of the mode field (MFD) in fibers with wavelength, further reducing the pulse intensity, and an increase in the pulse dispersion (becoming more anomalous). All this phenomena combined reduce SSFS until it stops. If propagation continues, eventually SPM won't be able to balance an increasing dispersion and the pulse will start to chirp loosing its soliton pulse shape. The rate at which SSFS initially takes place is proportional to:

$$\frac{dv}{dz} \propto \frac{1}{\tau_0^4} \tag{1.38}$$

This means that the shorter the input pulse, the larger wavelength shift [112]. As the bandwidth of the pulses increases, the spectra will further overlap with the Raman gain g_R increasing Raman scattering and consequently SSFS. At the same time, a shorter pulse means higher NL effects and enhanced Raman scattering. This is illustrated in Fig.1.9 were the the propagation of a 120 fs and 60 fs soliton pulses in fused silica fiber has been simulated.

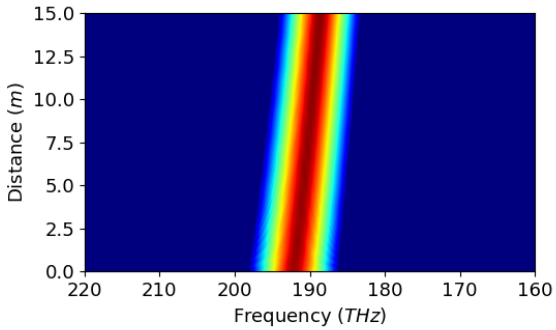

(a) Spectra of a 120 fs soliton pulse as a function of length.

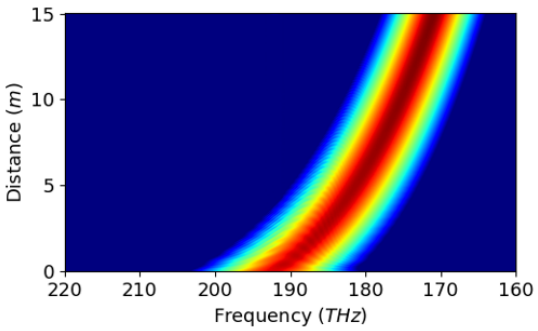

(b) Spectra of a 60 fs soliton pulse as a function of length.

Figure 1.9: Spectrum of a soliton pulse undergoing SSFS in fused silica fiber.

In Fig.1.9a it can be seen that the 120 fs soliton barely shifts in 15 m of fused silica fiber while the 60 fs soliton pulse has shifted almost 30 THz as depicted in Fig.1.9b.

1.4.2 Soliton Generation and High Order Solitons

Higher order solitons are generated when $N > 1$. In this situation dispersive effects dominate over NL effects ($L_D > L_{NL}$) and competition between dispersion and non-linearities takes place as the soliton propagates. Due to the competition between dispersion and non-linearities, higher order solitons temporal and spectral properties change periodically. When the NL effects dominate, the pulse broadens spectrally as new frequencies are being generated by SPM and is compressed in the temporal domain until dispersion dominates. When dispersion dominates, the pulse stretches in time and the spectra narrows due to spectral narrowing until NL takes over. This takes place periodically provided that the high order soliton is not perturbed. This has been illustrated in Fig.1.10 where a $N = 2$ soliton ($1.56\,\mu m$, $100\,fs$) propagates in fused silica fiber to illustrate the balance between dispersion and NL effects.

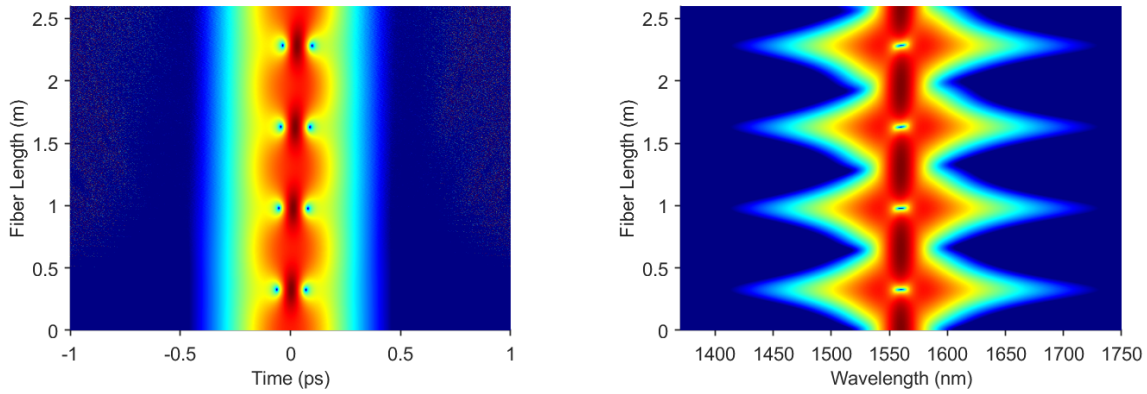

(a) Pulse shape as function of propagation length. (b) Spectrum as a function of propagation length.

Figure 1.10: Pulse shape and spectrum of a $N = 2$ soliton ($1.56\,\mu m$ and $100\,fs$) as function of propagation distance in fused silica fiber.

This periodic behaviour doesn't last long and the high order soliton fissions into fundamental solitons and a residual pulse [95, 113]. As the high order soliton propagates, Raman scattering and β_3, which have an asymmetric behaviour, perturb the pulse producing soliton fission. Each of the generated fundamental solitons will Raman shift and behave accordingly to fundamental solitons properties. Just before soliton fission which takes place at a distance of $L_F \sim L_D/N$, the pulse reaches its shortest duration and peak power propelling the first ejected soliton to longer wavelengths compared to subsequent generated solitons. This is because the pulse duration of the subsequent generated solitons increases and their energy decreases [113]. This has been illustrated in Fig.1.11 where the propagation of a high order soliton ($600\,fs$ $1.56\,\mu m$ and $5\,nJ$) in fused silica fiber is shown in time and frequency.

Fig.1.11a shows temporal evolution of the pump pulse and the generated solitons. As the soliton shifts in wavelength, the refractive index changes and so does the group velocity of the pulse. This is why the fundamental solitons generated have a delay with respect to the input pulse at $1.56\,\mu m$. On Fig.1.11b there is the spectral evolution of the pump pulse were it can be seen the two fundamental solitons generated an the residual pump pulse.

Fundamental soliton pulses are very robust and stable, specially when it comes to their generation. If the pump pulse is far away from fulfilling the condition $L_D = L_{NL}$

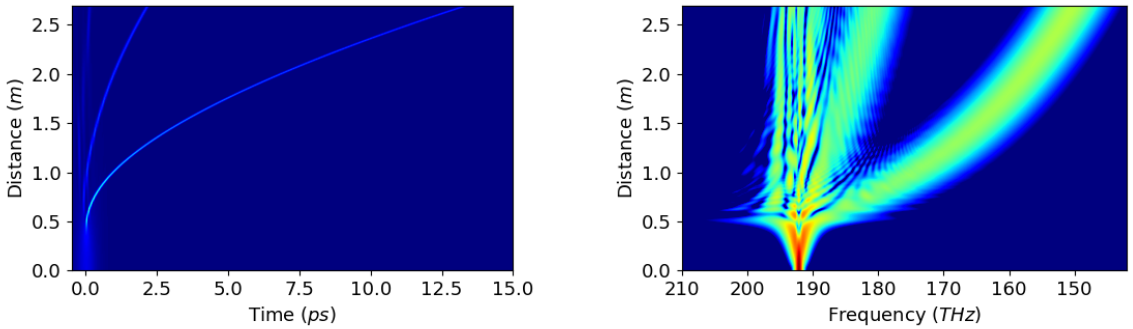

(a) Pulse shape as function of propagation length. (b) Spectrum as a function of propagation length.

Figure 1.11: Temporal and spectrum evolution as function of propagation length for a $600\,fs$, $5\,nJ$ at $\lambda_0 = 1.56\,\mu m\,(192.17\,THz)$. in fuse silica fiber.

which means that $N > 1$, the pulse will adapt its energy and pulse duration until the soliton is formed or it will eventually fission in one or more fundamental solitons that can then be separated using filters or dichroic mirrors. Optical pulses will always evolve into a soliton in the anomalous regime provided that their peak power is enough to trigger SPM. The generation of soliton pulses is a simple process that allows to generate pulses in the $100-300\,fs$ pulse durations or even shorter provided that the fiber has been wisely chosen [18, 114, 115, 116]. In addition, SSFS process is dependent on the energy and duration of the pump pulse which can be controlled by adjusting the laser parameters. This means that it is possible to generate transform limited widely tunable ultrashort pulses at wavelengths not accessible by the known gain media. In the next chapter of the thesis the development of a tunable laser source exploiting the SSFS is effect presented.

Chapter 2

Sub-100 fs all-Fiber Polarization Maintaining Tunable Laser

The generation of light pulses in the $2\,\mu m$ spectral region usually rely on fiber-mode-locked oscillators using saturable absorbers, SESAMs or non-linear polarisation rotation. They are based on Tm, Tm:Ho or Ho doped fibers and produce either pulses in the picojoule energy level or pulses with higher energies that require further compression outside the cavity and/or free-space intracavity optical components.

An alternative to femtosecond mode-locked oscillators is to rely on Raman scattering through SSFS. As it has been shown in the previous chapter, fundamental soliton pulses are spectrally tunable, with transform limited pulse duration and they have nanojoule energy levels in standard telecom fibers. They are very easy to generate and their properties can be taylored and predicted by adjusting the fiber parameters.

The objective of this chapter is to present the different elements and experiments that yielded to the development of a seed laser for CPA laser architectures in the $2\,\mu m$ spectral region and how to further shorten the pulse duration below $100\,fs$ by balancing NL effects and dispersion in optical fibers.

2.1 The Er Modelocked Oscillator

A 40 MHz, SESAM modelocked Er-doped fiber ring laser oscillator was used as pulse seeder. The gain medium is a fused silica Er-doped fiber core pumped by a frequency stabilised pump laser diode at $976\,nm$. The oscillator exclusively contains polarization maintaining (PM) components. In this work the oscillator is considered as a black box (schematics are not presented) that has been characterised in terms of power, pulse duration and spectrum.

The average power of the oscillator has been measured and is presented in Fig.2.1a and goes from $1.3\,mW$ up to $2\,mW$. Usually, the output power of SESAM modelocked oscillators is low due to the low damage threshold of SESAMs with pulses in the pJ energy level. As the oscillator output power increases the spectrum is also changing and this is illustrated in Fig.2.1b. The laser operates at $1558\,nm$ wavelength and the bandwidth measured at FWHM increases with pump power from $5.74\,nm$ up to $7.79\,nm$. The oscillator is working in the solitonic regime, that means that the total net dispersion in the cavity is zero and that the output pulses are soliton pulses. As the pump power increases, the energy of the pulses and output power increase and according to Eq.1.35, the pulse duration has to shorten which imply larger bandwidths. On Fig.2.1b a set of

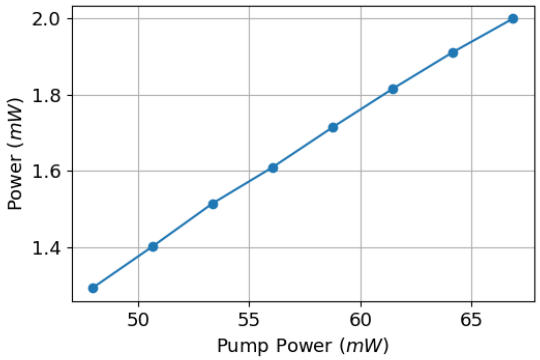

(a) Output power of the Er oscillator.

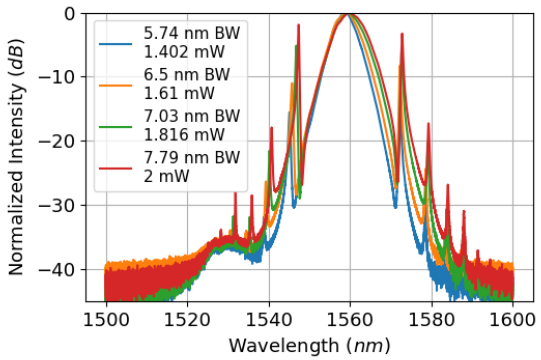

(b) Spectrum of the Er oscillator for different output powers.

Figure 2.1: Power and spectrum out of the Er oscillator as function of pump power.

narrow peaks can be observed on the soliton spectra known as Kelly sidebands. They are the result of the interaction between the soliton and the dispersive wave generated by the circulating soliton [117, 118]. As the soliton energy increases so does the non-linearities in the cavity. The Kelly sidebands become more pronounced as the variations on the pulse spectrum and shape along the cavity increase due to dispersion, increased NL effects and gain in the cavity [119].

The oscillator output power is limited between 1.29 and 2 mW. When power is decreased the oscillator is not modelocking anymore and it operates in Q-switched regime while beyond 2 mW output power, it becomes unstable and switches between one and two pulses operation at 40 MHz and 80 MHz. Two different working points were set for the oscillator at 1.61 mW and 1.91 mW output power. The pulse shape was characterized using an Autocorrelator (APE Pulse Check) and the spectrum using an optical spectrum analyser (Yokogawa AQ6375 OSA). Pulse durations and spectras along the thesis have been measured using those devices unless specified. The measured optical spectrum and pulse durations are illustrated in Fig.2.2 and Fig.2.3 for 1.61 mW and 1.91 mW output power.

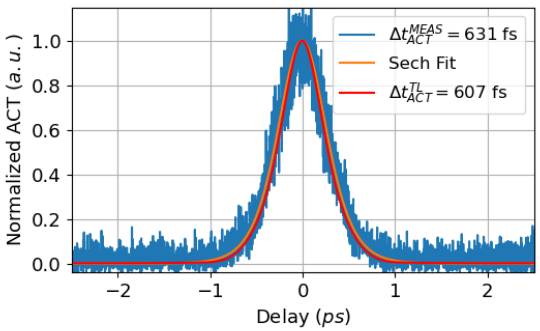

(a) Measured autocorrelation trace. $\Delta t_{FWHM}^{SECH} = 402\,fs$

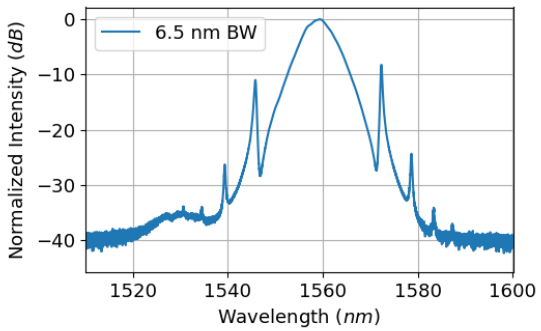

(b) Measured optical spectrum.

Figure 2.2: Autocorrelation trace and spectrum out of the Er oscillator at 1.61 mW output power. In orange, the ACT fit for sech pulses and in red the TL ACT.

The oscillator delivers almost transform limited pulses 400 fs and 349 fs for the mea-

sured bandwidths of 6.5 nm and 7.5 nm respectively. It is important to recall the different relative amplitude of the Kelly sidebands compared to the main peak at 1558 nm, $\sim 11\,dB$ and $\sim 3.5\,dB$. This makes a difference when it comes to amplification as they can substract an important amount of gain from the soliton pulse and influence the SSFS in laser systems [120].

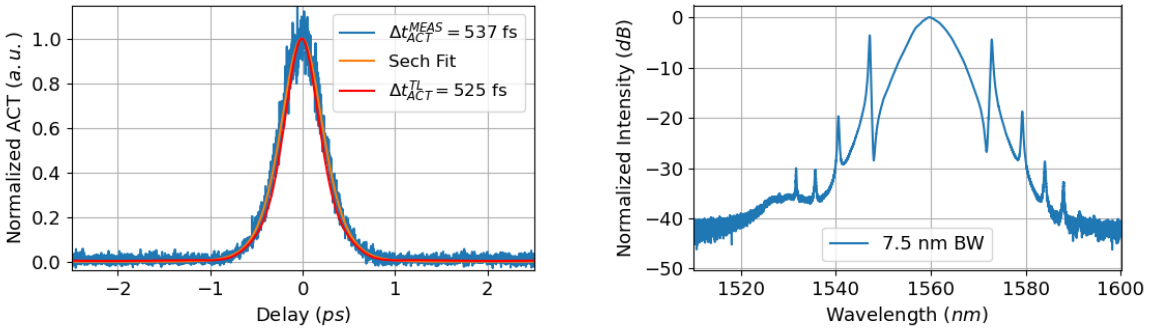

(a) Measured autocorrelation trace. $\Delta t_{FWHM}^{SECH} = 349\,fs$

(b) Measured optical spectrum.

Figure 2.3: Autocorrelation trace and spectrum out of the Er oscillator at 1.91 mW output power. In orange, the ACT fit for sech pulses and in red the TL ACT.

2.2 The Er Amplifier

Pulse amplification is a must before addressing the SSFS stage as the amplifier will be used to adjust the pulse parameters in terms of energy and control the wavelength shift of the pulses. To this end, an Er-doped fiber amplifier was developed. The gain medium consists of an Er-doped fused silica fiber (Er110-4/125-PM LIEKKI, 6.5 μm MFD, $-22\,ps/nm\,km$ and 0.2 NA). The fiber has normal dispersion and is highly doped which is suitable for ultra-fast pulse amplification as high gain can be achieved with short fibers for minimal non-linear effects. The amplifier is core pumped with two single mode laser pump diodes at 976 nm either in co-propagation, contra-propagation or in both ends.

2.2.1 Single Mode Pump Diodes for Er Amplifier Core Pumping

Three different single mode pump diodes have been tested and characterised in terms of power and spectra, and they are referred as CHP, CVB and G&H pump diodes. The power and spectra as a function of the pump current is presented in Fig.2.4.

The measured powers are shown in Fig.2.4a and the maximum powers obtained are 1 W for the CVB, 860 mW for the G&H and 750 mW for the CHP pump diodes. The optical spectra of the CVB and G&H diodes are illustrated in Fig.2.4b and Fig.2.4c respectively for different output powers. As the output power of the diodes is increased, the wavelength is shifting for the G&H while is kept stable for the CVB diode. This is because the CVB and CHP pump diodes are fiber Bragg gratings (FBG) stabilised while the G&H pump diode is not. The lack of FBG allows for the wavelength to drift and is accompanied by a higher sensitivity of the diode to temperature variations which reduces the output stability in terms of power and wavelength potentially affecting the Er amplifier. The CVB pump diode was chosen because of a more stable performance

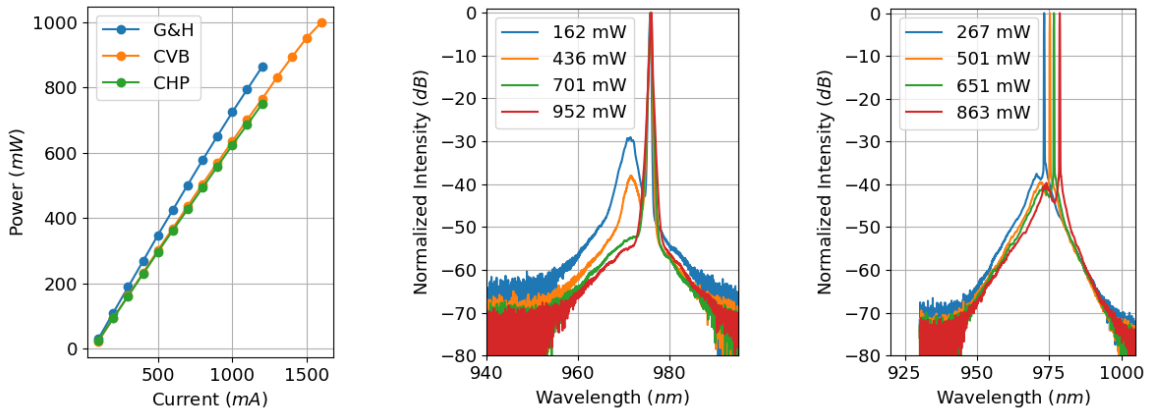

(a) Pump power as function of current.

(b) Optical spectrum of CVB pump diode.

(c) Optical spectrum of G&H diode.

Figure 2.4: Pump diodes' output power and optical spectrum.

and a higher output power compared to the CHP and G&H pump diodes. The available pump power is then $2\,W$ equally split to pump the Er amplifier in co-propagation and contra-propagation.

2.2.2 Single Side Pumping Er Amplifier

The amplifier gain medium was studied in terms of output power for different fiber lengths in both configurations co and contra-propagation by splicing two wavelength division multiplexers (WDM) at the input and output of the doped fiber and by performing a cutback on the active fiber. The oscillator was set at $2\,mW$ output power ($340\,fs$ pulses). Results are summarised in Fig.2.5.

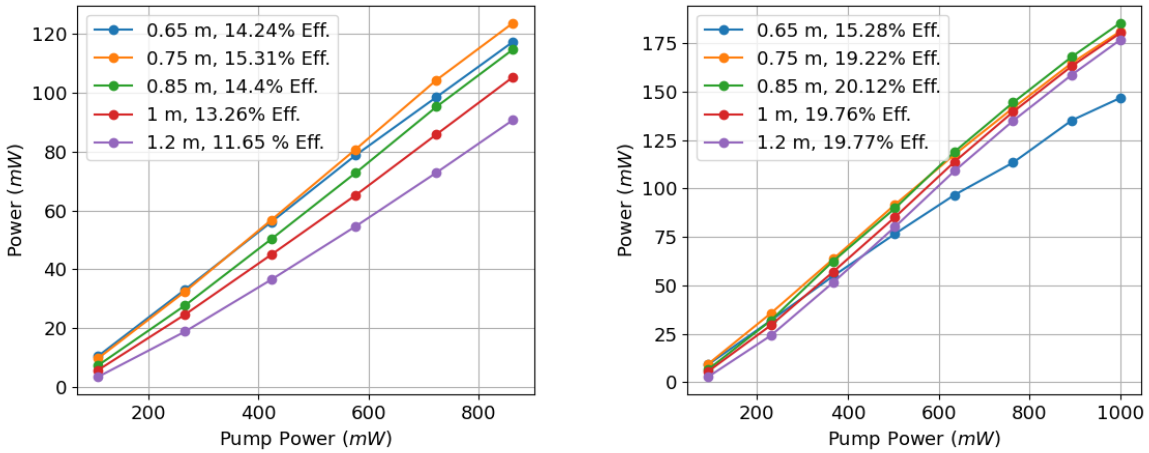

(a) Co-propagation.

(b) Contra-propagation.

Figure 2.5: Output power out of the Er amplifier in co and contra-propagation configurations as function of the pump power.

Depending on the pumping scheme, for the same pump power different fiber lengths are optimal for each configuration due to the population inversion distribution along the

fiber. In a co-propagation pumping scheme, the population of atoms in the excited state is high at the beginning and decreases along the fiber due to pump absorption. The exact opposite situation takes place in contra-propagation scheme, high inversion at the end of the fiber while low inversion at the beginning. The different output powers for the same amount of fiber length comes from the gain the input pulses can extract from the fiber. In a co-propagation scheme, the majority of the gain is situated at the beginning of the fiber where there is more population inversion however, the input signal power is low and it cannot extract all the available gain. On the other hand, for the contra-propagation scheme, at the beginning of the fiber the input signal is low but at the same time the available gain is low and the signal grows slowly. By the end of the fiber where there is the maximum available gain, the signal power is higher and efficient energy extraction is achieved. An optimal doped fiber length of $0.75\,m$ was obtained in co-propagation which yielded to a $15.31\,\%$ slope efficiency. In contra-propagation, a maximum slope efficiency of $20.12\,\%$ versus the pump power was obtained for a fiber length of $0.85\,m$. It is important to note that best performances are obtained when there is some residual pump light that has not been absorbed and this is because of re-absorption. Active gain mediums and more specifically glasses such as fused silica, due to the Stark effect and homogeneous broadening, the discrete emission and absorption lines broaden yielding to a continuum allowing amplification of ultrashort pulses due to large emission bandwidths. In quasi three level systems such as (Er, Yb and Tm), absorption and emission cross sections overlap to some extend and this means that the active medium can absorb light at the signal wavelength. This absorption is proportional to the population of atoms in the ground state which decreases as the active medium is pumped. If re-absorption takes place the efficiency of the amplifier will reduce as the amplified signal is being re-absorbed. This affects particularly the pulses as they are being slowly red shifted in wavelength if re-absorption becomes important. By adjusting the fiber length for a given pump level, the wavelength at which the amplifier has maximum gain and efficiency can be adjusted. For a fixed pump power, a short piece of fiber will have maximum gain and efficiency for wavelengths in the blue side of the emission spectra while a long piece of fiber will have it on the red side. This is why a cut-back on the active fiber allows for the maximization of the output power for a given configuration.

Overall, the contra propagation scheme is usually better in terms of efficiency and reduced non-linear effects. This is because the pulse intensity is low over the amplification fiber and very high in the very last section while in co-propagation signal peak power is high all along the fiber. However, co-propagation is more practical specially when clad pumped. Optimisation of the amplifier is performed in an easy way by cut-back method while in contra-propagation, clad pumping requires implementing a pump stripper after each cutback measurement performed. Also for very high power lasers, high power combiners are required with ideally short fiber lengths to reduce non-linearities in passive fibers. The effect of non-linearities in amplifiers and its effects are of paramount importance for CPA laser systems and will be discussed later in the thesis.

The amplifier has to be designed to match powers compatible with a SSFS stage capable of shifting the pulses from $1560\,nm$ up to $2100\,nm$. The higher the average power reached for a given pulse duration, the longer in wavelength the pulse will shift. To achieve such performance a double side pumping configuration was chosen.

2.2.3 Double Side Pumping Er Amplifier

The two side pumping scheme was adopted for the final configuration of the Er amplifier with $1.2\,m$ active fiber length. The fiber is slightly longer for either co or contra propagation however, by pumping on both sides simultaneously the maximum output power compared to co and contra-propagation individually can be surpassed if required. At the same time, the gain distribution along the fiber and the non-linearities during amplification can be adjusted by modifying the pump powers on both sides. This is beneficial to adjust the pulse parameters before the SSFS stage in terms of power and pulse duration. The same output power can be achieved with several configurations for both pump diodes which would be beneficial to fine tune the pulse duration before SSFS. With the knowledge acquired a second amplifier was prepared, which was optimised in terms of splicing. The schematics are presented in Fig.2.6a.

The Er amplifier consists of two WDMs, two $1\,W$ pump diodes (CVB) and an isolator (ISO) which has been included compared to the previous study of the Er doped fiber to correct for any polarization issues derived from the Er amplifier. The average power obtained out of the amplifier is shown in Fig.2.6b.

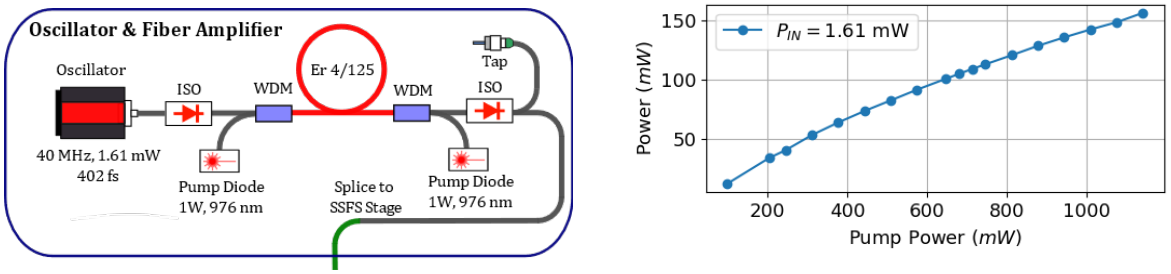

(a) Er amplifier architecture.

(b) Power out of Er amplifier isolator as function of total pump power.

Figure 2.6: Er amplifier architecture and amplifier output power.

In Fig.2.6b the output power as a function of the total pump power (this means pump power in co and contra-propagation) is shown. What it has been done to distribute the power is first pump up to $215\,mW$ in contra-propagation and then start increasing the co-propagation pump diode up to $931\,mW$. This choice was based on the results that were obtained later on in terms of the maximum wavelength that could be achieved in the SSFS stage. The amplifier allows to reach same output power with different pump diodes configurations however the resulting pulse duration is different due to dynamics (gain and NL effects along the doped fiber) which can yield to different shifts in wavelength. Based on the results obtained in Fig.2.5, it is clear that the amplifier is saturated and linear behaviour in terms of output power as function of pump power should be obtained and that not having a suitable fiber length just reduces the efficiency. However, a roll-over effect in power can be observed due to the fact that an ISO has been included in the setup which has losses and a recommended operation bandwidth of $\pm 15\,nm$. If it is used outside the operation bandwidth the losses start to increase and its isolating properties decrease and this is what is happening in the amplifier. Ultrashort pulse amplification quickly gives rise to SPM and as the bandwidths become larger ($> 30\,nm$ at FWHM, see Fig.2.7) the losses at the isolator increase.

The SSFS rate is $dv/dz \propto 1/\tau^4$ therefore, it would be of interest to achieve pulse durations below the $400\,fs$ provided by the oscillator. To shorten the pulses, SPM and

non-linear pulse compression is combined. Amplification of the 400 fs pulses in the normal dispersion Er fiber yields to SPM and to pulse stretching due to dispersion. SPM is beneficial as potentially shorter pulses can be obtained however, the dispersion needs to be compensated and pulses compressed. Pulse compression takes place in the WDM and ISO passive fibers, the PM1550XP, which has anomalous dispersion. As the pulse is being compressed, SPM is taking place simultaneously due to an increase in intensity allowing for further pulse compression. This process stops when a soliton is generated and the SSFS process starts. It is important to note that the passive fibers used to compress the pulses have been shortened as much as possible so that the generation of the soliton pulse and SSFS effect takes places after the isolator and as close as possible to the non-linear fiber included for that purpose. The spectra of the pulses after the amplifier measured at the isolator TAP (see Fig.2.6a) are shown in Fig.2.7 for different powers. The SPM modulation effect can be observed on the measured spectra without any signal of SSFS.

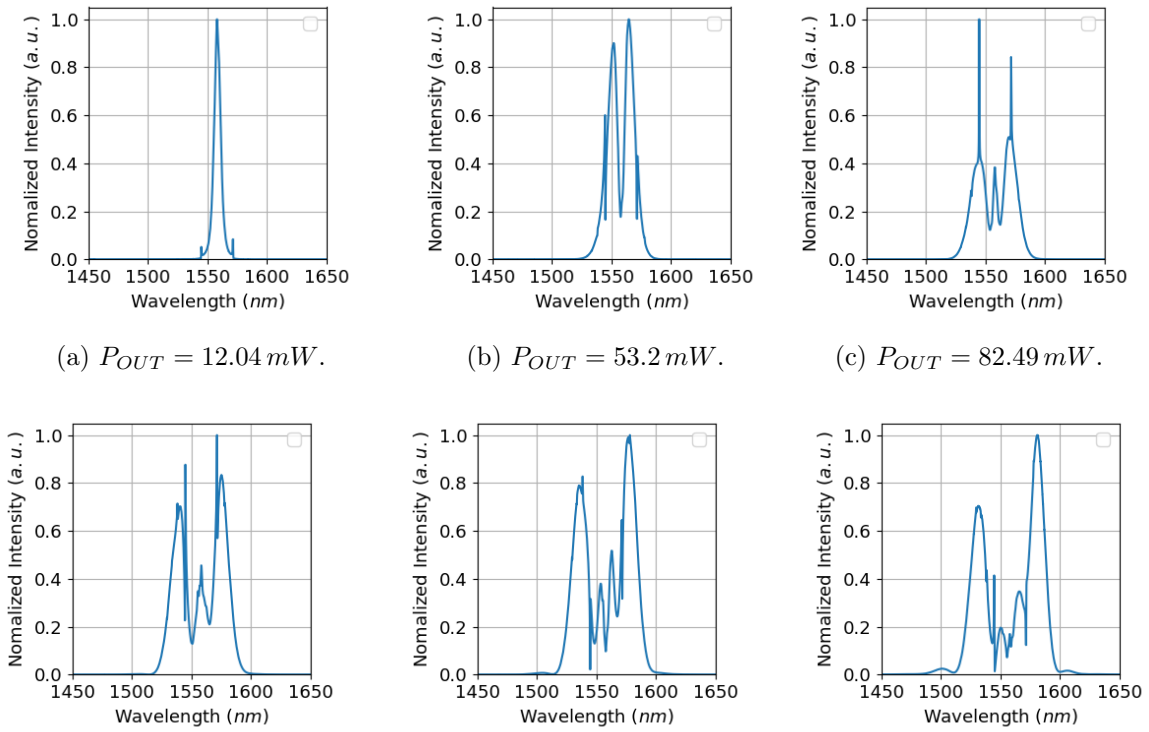

(a) $P_{OUT} = 12.04\,mW$. (b) $P_{OUT} = 53.2\,mW$. (c) $P_{OUT} = 82.49\,mW$.

(d) $P_{OUT} = 104.95\,mW$. (e) $P_{OUT} = 120.67\,mW$. (f) $P_{OUT} = 142.44\,mW$.

Figure 2.7: Spectrum out of the Er amplifier for different output powers showing the development of SPM.

The amplifier delivers a maximum average power up to $160\,mW$ using slightly more than 50% of the available pump power. It was decided not to keep increasing the pump power to avoid developing a soliton before the isolator as its energy would be substantially decreased due to having a wavelength far beyond the operation wavelength of the isolator. In order to improve the stability of the whole system, a $50:50$ PM coupler between the WDM and the contra-propagating pump diode was added. This is done to increase the pump power by a factor 2 allowing the diode to work closer to its designed operation power of $1\,W$ output. Half of the pump power of the diode is dumped at the $50:50$ PM coupler.

The pulse durations have not been measured because at the output of the isolator

there are already 2 pulses, the soliton and the residual pump at $1.56\,\mu m$ which are too close in wavelength to separate them properly by means of filters or dichroic mirrors. Pulse durations can be measured at the tap however they cannot be compared to the pulses at the output of the isolator. This is because the propagation at the output of the isolator depends on dispersion and non-linearities while at the tap, only about 1.1% of the power is picked thus only dispersion plays a role. In addition the fiber length from the ISO to the SSFS stage is different to that of the tap.

2.3 Soliton Self-Frequency Shift Stage

To develop the SSFS stage, a set of experiments were carried out to estimate and find the suitable optical fiber and length to reach the target wavelength of $2.1\,\mu m$. This wavelength was chosen because the laser can then seed the main active gain mediums in the $2\,\mu m$ spectral region which are Thulium and Holmium.

An all-fibered PM tunable laser system based on exclusively commercially available components would be of interest because of its versatility, robustness and accessibility. Within the available telecom fibers in this particular spectral region, the most commonly known and used are the PM1550XP and the PM1950. The PM1550XP from Coherent has a $8.5\,\mu m$ core, a $10.1\,\mu m$ MFD @$1550\,nm$ and a $0.125\,NA$. It is a PM single mode optical fiber and has a panda structure. The second fiber is the PM1950 fiber from Coherent as well which has been specifically design for the $2\,\mu m$ spectral region. It is single mode PM fiber with panda structure and a $7\,\mu m$ core, a $8\,\mu m$ MFD @$1950\,nm$ and a $0.2\,NA$. These two fibers were chosen for the study mainly because of practical reasons. The PM1550XP is widely used when it comes to producing all type of fibered components in the $1.5-2\,\mu m$ wavelength which makes it attractive for splicing. It has been produced to operate around the $1.5\,\mu m$ wavelength and therefore should be suitable for the generation of solitons in the vicinity of the operation wavelength. There are wide variety of providers for this particular fiber therefore its properties can change from one to another. On the other hand, the PM1950 has smaller core size and the core doping makes this passive fiber suitable for non-linear processes and reduced losses at longer wavelengths, therefore optimal for the generation of solitons between $1.9\,\mu m$ and $2.1\,\mu m$. Both fibers have a small core size which should be beneficial for SSFS as it is usually a must among the specialty fibers used to achieve large shifts in wavelength. They operate at two different wavelengths, $1.5\,\mu m$ and $2\,\mu m$ which opens the possibility for SSFS combining the two fibers. Bigger fibers can as well be used however, they offer reduced non-linearities and more energetic input pulses are required to achieve substantial SSFS. The use of panda fibers is preferred compared to the use of specialty fibers such as PCF to avoid splicing of specialty fibers with complex geometry to the panda structure of telecom fibers. Since the fiber parameters play an important role on the SSFS, both fibers were simulated before experimentally testing them.

2.3.1 Simulation of PM1550XP and PM1950 fibers

To further understand the SSFS in optical fibers, the fiber properties involved in the SSFS process were simulated, that is the MFD which is linked to the NL effects, the GVD β_2 and the mode overlap with the core which is linked to losses in the fiber. To this end, the fiber cross section geometry was measured. This included the core size, the boron stress rods size and their relative position from one to another (see Fig.2.8a and 2.8b). Then

COMSOL was used to compute the waveguide eigen-modes to obtain the parameters mentioned above by solving the propagation equations. The simulations provide the effective refractive index of the fiber which is then used to calculate its properties. Based on the obtained results, the parameters were slightly adjusted (core size and/or NA) of the fiber to match with the datasheet and provider's information [121]. The results for the PM1550XP and PM1950 fibers are shown in Fig.2.9.

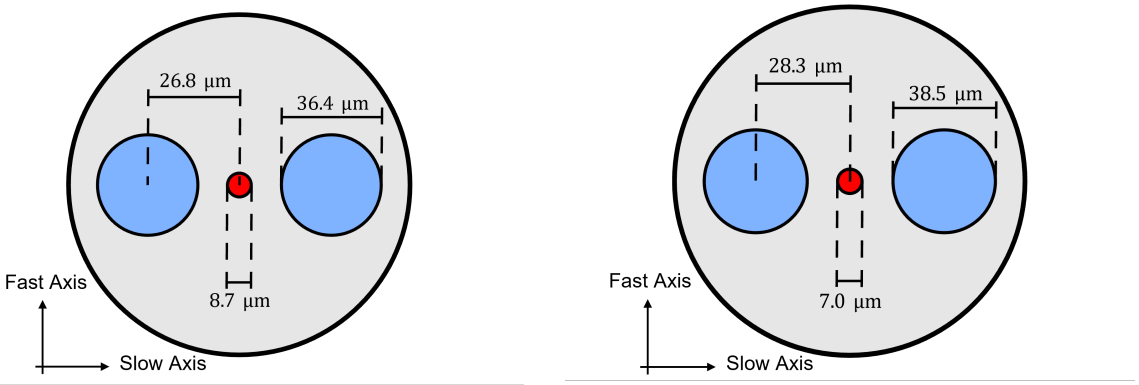

(a) Measured fiber cross-section geometry for the PM1550XP fiber. Fiber clad is 125 μm diameter.

(b) Measured fiber cross-section geometry for the PM1950 fiber. Fiber clad is 125 μm diameter.

Figure 2.8: Measured cross-section geometries for the PM1550XP and PM1950 fibers.

The MFD, GVD and field to core overlap were computed for the fast and slow axis of the fibers. Fast or slow axis can be selected by setting the polarization of the light aligned with either one or the other yet the slow axis, which is the one were the polarization of the light is aligned with the boron stress rods, is the commonly used one. In terms of MFD, the PM1550XP is substantially bigger compared to the PM1950 fiber and it goes from $\sim 9.9\,\mu m$ at $1.5\,\mu m$ to $\sim 12.9\,\mu m$ at $2.1\,\mu m$. For the PM1950 the MFD increases from $\sim 6.9\,\mu m$ at $1.5\mu m$ to $\sim 8.7\,\mu m$ at $2.1\,\mu m$. The increase in MFD is only of $2\,\mu m$ compared to the $3\,\mu m$ of the PM1550XP and this is of paramount importance specially taking into account that the main parameter is the mode effective area $A_{eff} \propto MFD^2$. Higher MFD implies that the energies of the generated pulses will be higher and that the SSFS rate will be smaller. This is because when the seed pulse is injected into the SSFS fiber, way higher intensities are achieved propelling the generated soliton further away. At the same time, the increase of the MFD with wavelength will slow down the SSFS as the non-linearities decrease. Therefore longer shifts in wavelength should be obtained with the PM1950 fiber and higher energetic solitons with the PM1550XP. From slow to fast axis the trend is the same and bigger MFDs are obtained so a reduced shift rate should be expected in the fast axis and solitons with slightly higher energy [14].

The GVD β_2 of both fibers is similar, the PM1950 is slightly less dispersive (less negative dispersion) therefore shorter solitons in pulse duration are expected compared to the PM1550XP. High non-linearities (SPM) can be compensated with dispersion however, if dispersion is low, large BW are required to balance out SPM and efficiently compress the pulse. In any of the fibers, the dispersion is not changing much from one axis to the other therefore there is no benefit from using fast axis instead of the slow axis.

The fourth parameter calculated is the mode overlap and is the ratio between the A_{eff} of the mode, the LP_{01} and the core area. The higher the mode overlap the less losses the fiber will experience due to bending [122]. The overlap for the PM1550XP at long wavelengths such as $2.1\,\mu m$ is $\sim 60.9\,\%$, almost 10% lower compared to PM1950 fiber

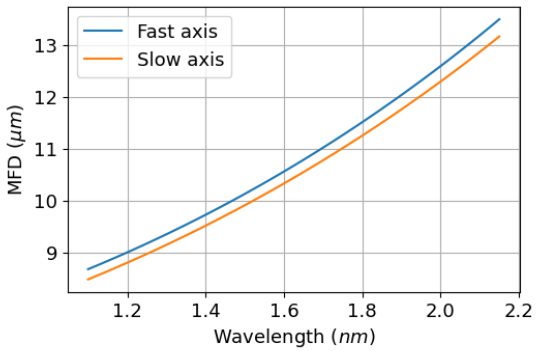

(a) Mode field diameter (MFD) of the PM1550XP fiber.

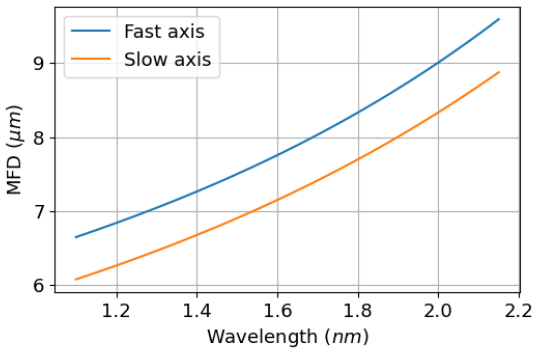

(b) Mode field diameter (MFD) of the PM1950 fiber.

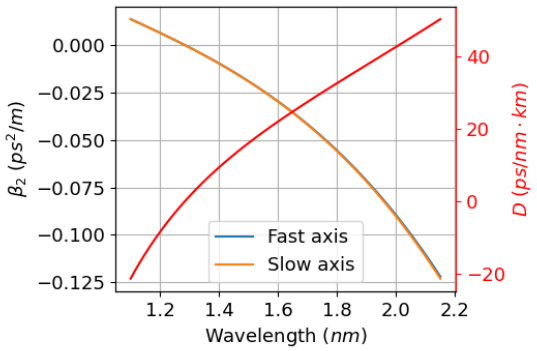

(c) Group velocity dispersion β_2 of the PM1550XP fiber.

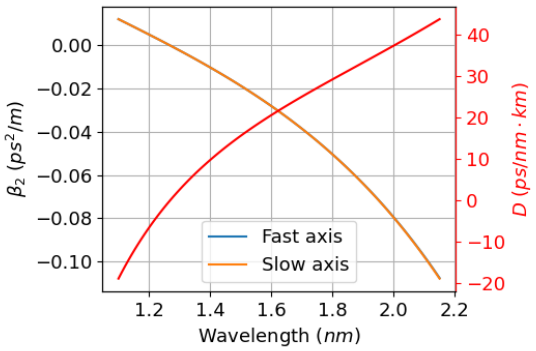

(d) Group velocity dispersion β_2 of the PM1950 fiber.

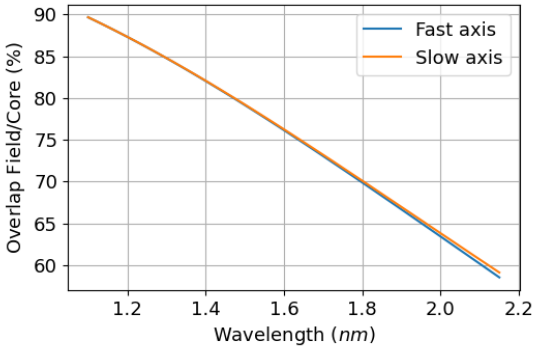

(e) Overlap of the fundamental mode and core area of the PM1550XP fiber.

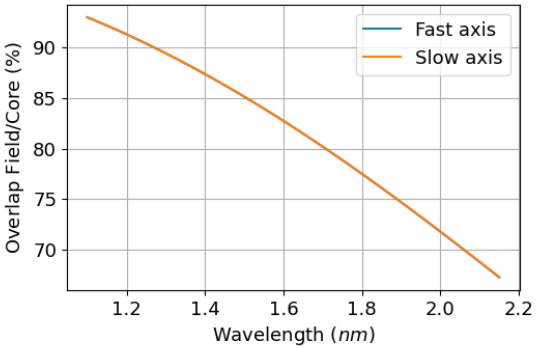

(f) Overlap of the fundamental mode and core area of the PM1950 fiber.

Figure 2.9: Simulated fiber properties (MFD, GVD and moe overlap) based on fiber cross-section geometry for the PM1550XP (left), and the PM1950 (right) fibers.

with a 68.8 %. Therefore, if the PM1550XP fiber is used, larger bending radius have to be applied compared to the PM1950 to reduce the losses. This is important as tenths of meters of fiber may be required to shift from 1.56 μm up to 2.1 μm.

In principle, the simulations confirm that the PM1950 fiber is more suitable to achieve large shifts in wavelengths through SSFS with fs pulses. In addition, due to being designed at 2 μm, reduced losses are expected in the fiber allowing for larger shifts in wavelength. The main benefit of using the PM1550XP fiber is the higher energy of the solitons. To confirm the simulations, the fibers were tested and the solitons characterized.

2.3.2 SSFS in PM1550XP and in PM1950 Fibers

In order to determine which fiber or combination of fibers is more suitable for the laser, they were tested for the generation of soliton pulses that were characterised in terms of power, wavelength tunability, and pulse duration while performing a cutback on the fibers. The experimental setup used to perform the study is shown in Fig.2.10.

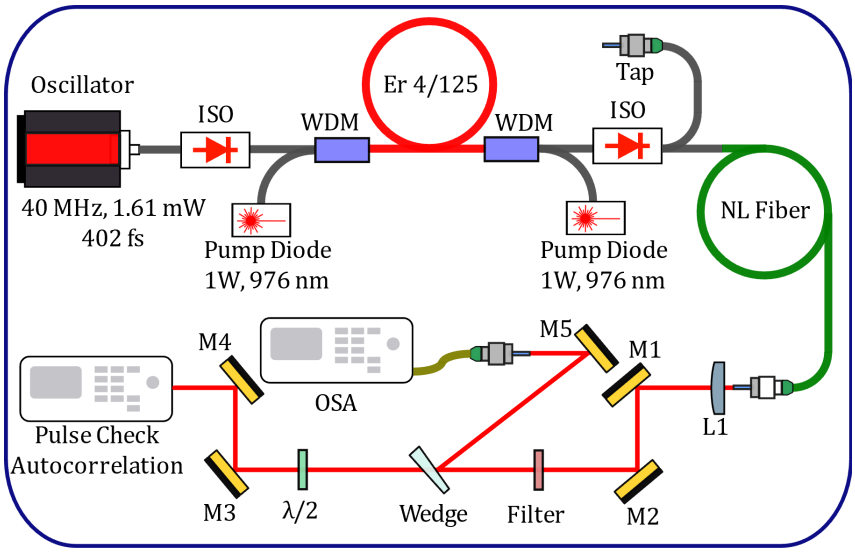

Figure 2.10: Experimental setup for studying the SSFS in an optical fiber.

The OSA was used to record the spectrum of the solitons from which the solitons' central wavelength was calculated for different powers out of the Er amplifier. The soliton power and the pulse duration as function of the wavelength was measured with the help of a free space filter to remove all residual light from the Er amplifier and select only the soliton. Once all the data was gathered, a piece of fiber was removed and we repeated the process until a total length of about $\sim 5\,m$ was cut. By doing this, the trend the soliton pulses have in terms of power, pulse duration and how fast they shift in wavelength per meter of optical fiber could be observed. This tells how suitable the fiber is to target long wavelengths and how many meters of fiber are required to reach 2.1 μm wavelength. The first fiber studied was the PM1550XP and $\sim 8.7\,m$ were spliced right after the Er amplifier isolator. The summarised results for the PM1550XP fiber are shown in Fig.2.11.

In Fig.2.11a the mean wavelength of the solitons is shown for different input powers and the rate at which they shift per meter of PM1550XP optical fiber. As it can be seen, as the power of the Er amplifier increases, the shift rate increases from 6.2 nm/m up to 9 nm/m. As the soliton shifts, the dispersion, the MFD and the losses increases (inelastic process). Therefore, the intensity is slowly decreasing until SSFS stops. If propagation

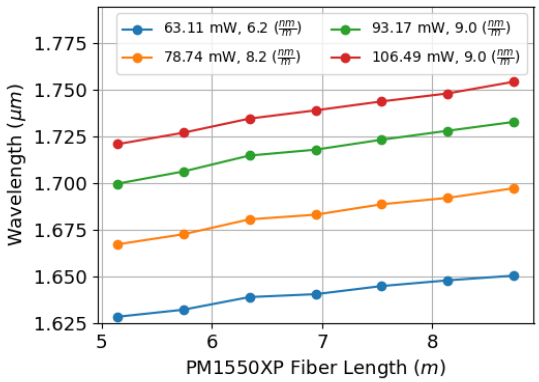

(a) Soliton wavelength as function of fiber length. On the legend there is the input power and rate at which the soliton shifts in wavelength per meter of fiber.

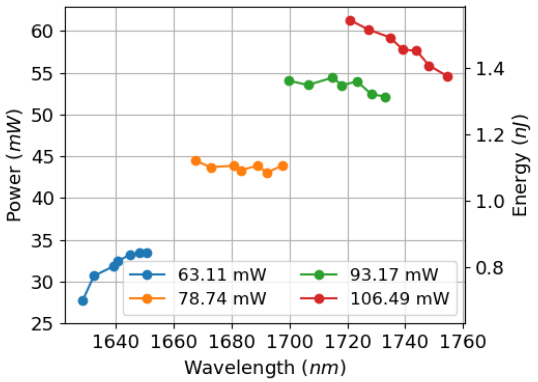

(b) Soliton power as function of wavelength for the different input powers. The soliton wavelength increases with the fiber length.

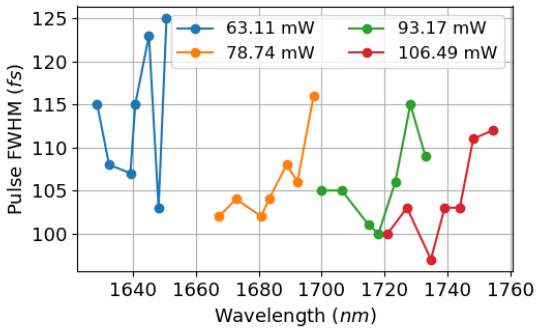

(c) Pulse FWHM as function of wavelength for the different input powers. The soliton wavelength increases with the fiber length.

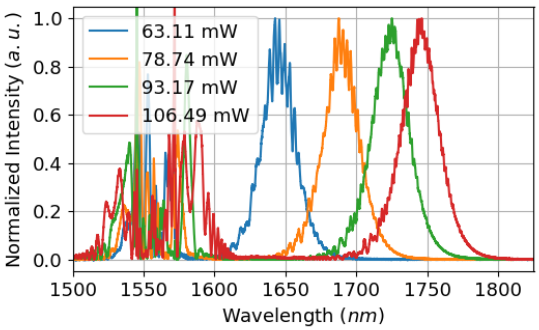

(d) Typical spectra of the generated solitons after $7.54\,m$ of PM1550XP fiber for different input powers.

Figure 2.11: Summarised results on SSFS using PM1550XP optical fiber.

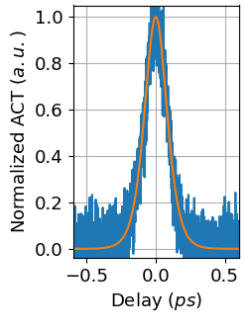

(a) $P_{IN} = 63.11\,mW$
$\Delta t_{ACT} = 202.0\,fs$
$\Delta t_{sech} = 123.0\,fs$

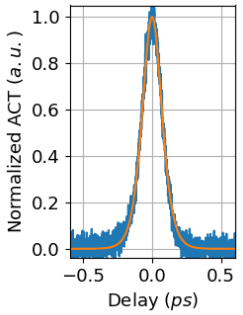

(b) $P_{IN} = 78.74\,mW$
$\Delta t_{ACT} = 162.0\,fs$
$\Delta t_{sech} = 108.0\,fs$

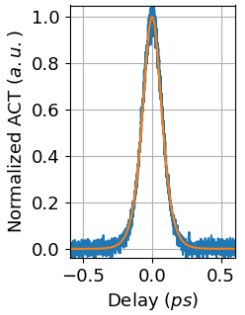

(c) $P_{IN} = 93.17\,mW$
$\Delta t_{ACT} = 167.0\,fs$
$\Delta t_{sech} = 106\,fs$

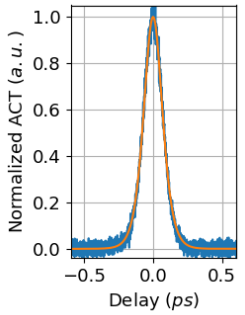

(d) $P_{IN} = 106.49\,mW$
$\Delta t_{ACT} = 160.0\,fs$
$\Delta t_{sech} = 103.0\,fs$

Figure 2.12: Measured ACT for the generated solitons with $7.54\,m$ of PM1550XP fiber for the different input powers P_{IN}.

continues, the TL duration is eventually lost as SPM cannot sustain dispersion and the pulses stretch in time. Higher powers allows the soliton to shift further away in the fiber reaching longer wavelengths for the same amount of optical fiber [95]. In Fig.2.11b the soliton power and energy is plotted as function of the wavelength. For a given input power, shorter wavelengths correspond to shorter fiber lengths. The power of the soliton increases with wavelength and the measured energies range from $\sim 0.7\,nJ$ at $\sim 1625\,nm$ up to $\sim 1.545\,nJ$ at $\sim 1720\,nm$ which is 2 orders of magnitude higher compared to the pulse energy delivered by the Er oscillator. The pulse duration (FWHM) is deducted from an ACT assuming a sech pulse shape. Except for the low power solitons, the SSFS mechanism produces pulses with a stable duration around $105\,fs$ in the range $1660\,nm$ up to $1760\,nm$ as depicted in Fig.2.11c. To illustrate some of the spectras recorded and the pulses measured, the measured optical spectrum for the solitons after $7.5\,m$ of fiber have been included in Fig.2.11d, where the four generated solitons and the residual light at $1560\,nm$ from the Er amplifier can be distinguished. Fig.2.12 shows the ACT of the solitons for $7.5\,m$ of NL fiber.

Simulations on SSFS in fibers can also be performed to cross-check the results. By using the simulated dispersion parameters β_2 and β_3, the MFD and the measured input soliton pulses (spectrum, power and ACT) the evolution of the pulses in the PM1550XP fiber can be predicted with great accuracy. This was tested for the soliton pulses generated for $93.17\,mW$ out of the Er amplifier. As input pulse the measured data for the solitons at $1.7\,\mu m$ was used. The results are shown in Fig.2.13

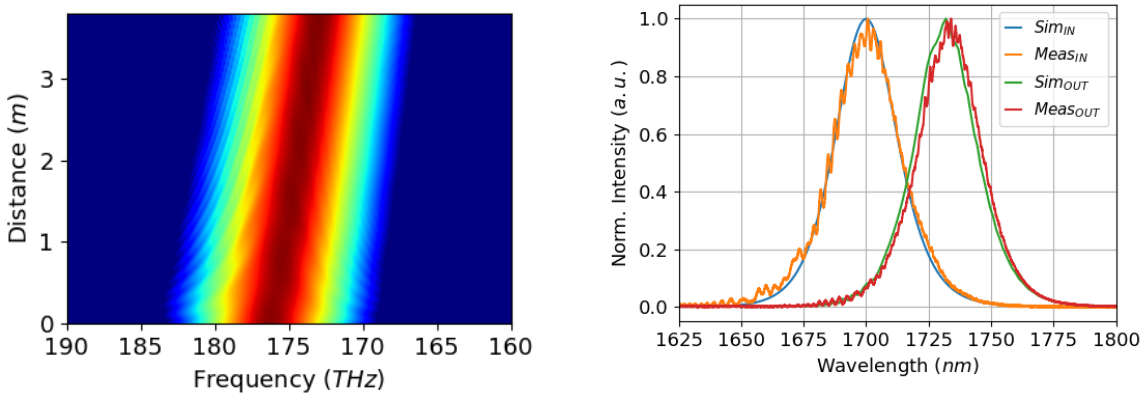

(a) Simulated spectrum as function of the fiber length.

(b) Input and output measured (Meas) and simulated (Sim) spectrum after propagation over $3.8\,m$ of PM1550XP fiber.

Figure 2.13: SSFS simulation in PM1550XP fiber for input $105\,fs$ pulses at FWHM, centered at $1700\,nm$ and $1.376\,nJ$. This corresponds to the measured solitons for $93.17\,mW$ power out of the Er Amplifier.

In Fig.2.13a the spectrum of the soliton pulses is shown as function of the PM1550XP fiber length. To compare the input and output measured spectra with the simulated ones, they have been plotted in Fig.2.13b. As can be seen, the simulations are very accurate such that over $3.8\,m$ the shift in wavelength is almost exact. The pulse ACT is not shown but is maintained constant due to the solitonic propagation.

Based on the presented results, reaching $2.1\,\mu m$ will require to add at least $20\,m$ of fiber assuming a constant rate of $9\,nm/m$ which is not realistic. Specially taking into account that losses in fused silica increase with wavelength. Increasing the input power

up to 160 mW will certainly will help but the N^{th} order generated soliton will fission in 2 or 3 fundamental solitons whose isolation would be difficult therefore, a different strategy was adopted.

Splicing 4.58 m of PM1550XP to $\sim$ 6.8 m of PM1950 was chosen to test the later fiber in the high loss spectral region and long wavelength side. A combination of both fibers seems a good approach as each fiber would operate in the spectral region they were designed for. By doing this, the SSFS in the PM1950 can be evaluated and compared to the PM1550XP fiber to know which one offers a faster SSFS and choose whether to use a combination of both fibers or just one of them. The optical spectrum, power and pulse shape were measured for different input powers and fiber lengths following the same procedure as before. The results obtained are summarised in Fig.2.14.

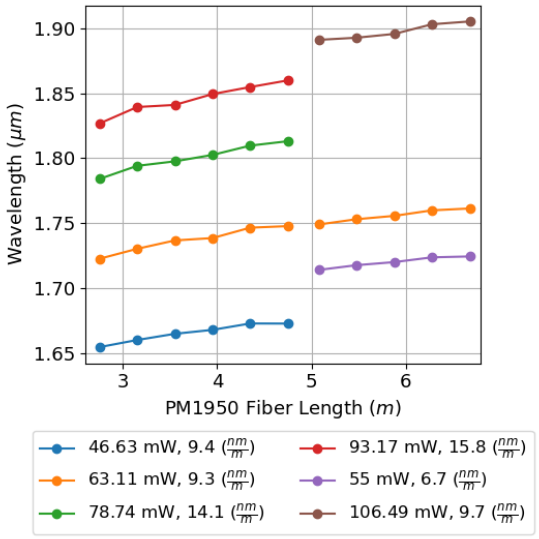

(a) Soliton wavelengths as function of fiber length. On the legend there is the input power and soliton shift rate per meter of fiber.

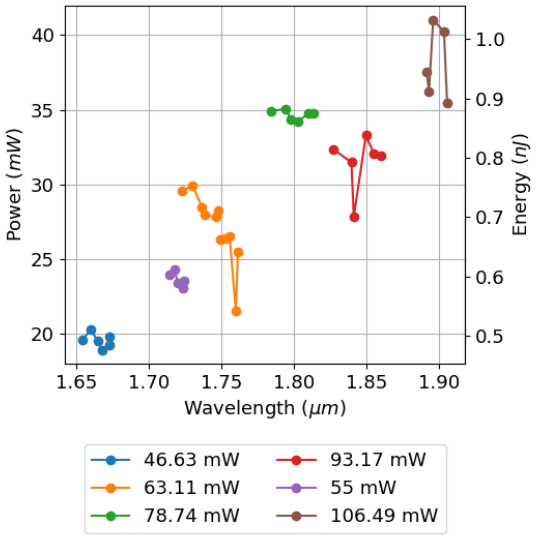

(b) Soliton power as function of wavelength for the different input powers.

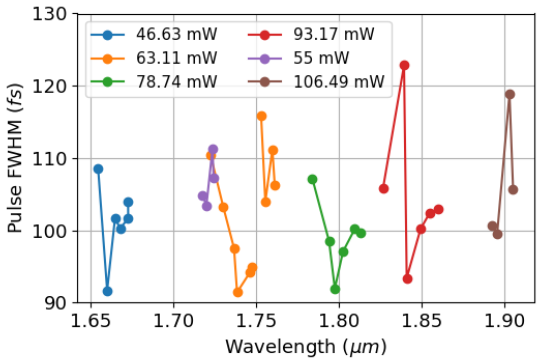

(c) Pulse FWHM as function of wavelength for the different input powers.

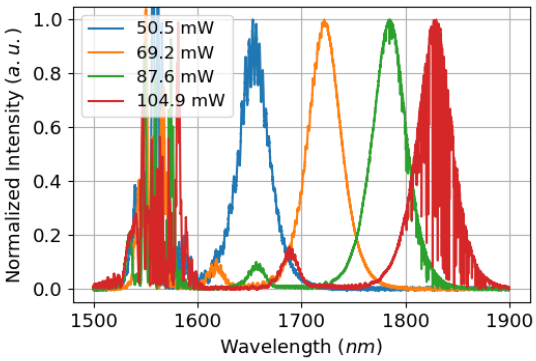

(d) Spectrum of the generated solitons after 2.75 m, of PM1950 fiber.

Figure 2.14: Summarised results on SSFS using PM1950 optical fiber. The fiber lengths used are 4.58 m of PM1550XP fiber and the cutback was done to $\sim$ 6.8 m of PM1950 fiber spliced to the PM1550XP fiber.

In Fig.2.14a the solitons' wavelength for the different input powers as function of the

fiber length and the rate at which they shift per meter of fiber is presented. Compared to the previous case, with the PM1950 fiber the SSFS rate is higher even though there are losses due to splicing two different fibers. Up to $15.8\,nm/m$ and what is more important, higher shift rates at the same wavelengths for lower input powers from the amplifier. That is $9.4\,nm/m$ between 1.65 and $1.68\,\mu m$ with the PM1950 for $46.63\,mW$ from the Er amplifier compared to the $8.2\,nm/m$ within the same spectral region for $63.11\,mW$ from the amplifier for the PM1550XP. For fiber lengths beyond the $5\,m$ long, the SSFS rate is reduced due to the splicing of two pieces of PM1950, that is why the SSFS rate for $63.11\,mW$ input power is smaller than expected. If the measured data for that particular input power for lengths longer than $5\,m$ is ignored, the value $12.6\,nm/m$ is obtained. As predicted by the simulations of the fiber parameters, SSFS in the PM1950 fiber allows to reach longer wavelengths compared to the PM1550XP. In Fig.2.14b the soliton power as function of the wavelength and input power are depicted. Compared to the PM1550XP, the powers are substantially lower for the same wavelength, almost by a factor of ~ 1.7 which is linked to the reduction of the mode field area by a factor ~ 2. In Fig.2.14c the pulse FWHM was measured using an autocorrelator. On average, $100\,fs$ pulses are obtained which are shorter than those obtained with the PM1550XP fiber. This can further explain the larger shift in frequency according to Eq.1.38. As predicted by the simulations, the pulse durations in the PM1950 fiber are slightly shorter compared to the PM1550XP and is attributed to a reduced dispersion. To illustrate some of the spectra, the measured optical spectrum for the solitons half way through the cutback in Fig.2.14d have been included, where three contributions can be distinguished: the evolving solitons, the residual light at $1560\,nm$ from the Er amplifier and a small amount of light $150\,nm$ on the blue side of the solitons. This light is due to the soliton in the PM1550XP fiber and the generated soliton in the PM1950. Due to the splicing, there is a discontinuity in MFD, β_2 and n_2 hence the soliton needs to adjust its energy and pulse duration. For completeness, the measured ACT in Fig.2.15 have been included for the solitons whose spectra were shown in Fig.2.14d.

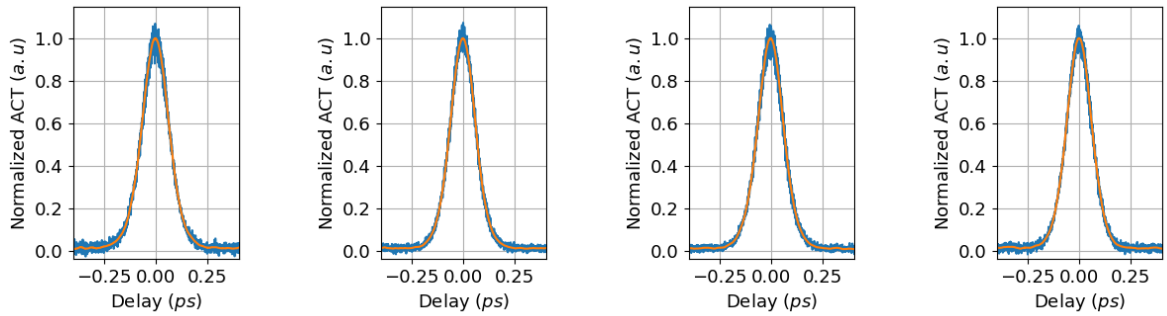

(a) $P_{IN} = 50.5\,mW$
$\Delta t_{ACT} = 150.73\,fs$
$\Delta t_{sech} = 97.52\,fs$

(b) $P_{IN} = 69.2\,mW$
$\Delta t_{ACT} = 142.09\,fs$
$\Delta t_{sech} = 91.39\,fs$

(c) $P_{IN} = 87.6\,mW$
$\Delta t_{ACT} = 144.31\,fs$
$\Delta t_{sech} = 93.37\,fs$

(d) $P_{IN} = 104.9\,mW$
$\Delta t_{ACT} = 141.67\,fs$
$\Delta t_{sech} = 91.67\,fs$

Figure 2.15: Measured ACT for the generated solitons after $4.58\,m$ of PM1550XP and $2.75\,m$ of PM1950 fiber for the different input powers P_{IN}.

To evaluate the accuracy of the simulated parameters for the fibers to some extend, the equation Eq.1.35 can be evaluated for both fibers for the characterised solitons. By substituting the measured pulse durations and energies and the simulated dispersion β_2 and MFD, the non-linear refractive index n_2 can be obtained which for fused silica fibers

should be between, $n_2 \sim 2.7 - 3.2 \cdot 10^{-20} m^2/W$. For both fibers the non-linear refractive index obtained was $n_2 \sim 3.3 \cdot 10^{-20} m^2/W$ which is slightly higher than expected but still reasonably accurate and therefore accurate simulated values for the dispersion and MFD.

The PM1950 fiber has some advantages compared to the PM1550XP. It offers enhanced SSFS rate and shorter pulse durations however, the power of the solitons is smaller (see Eq.1.35). Using exclusively the PM1950 fiber would allow to reach longer wavelengths within a shorter fiber length. Therefore, for the final configuration, the PM1950 fiber was used exclusively.

2.4 SSFS Tunable Laser

The architecture of the tunable laser system is depicted in Fig.2.16a. A $40\,MHz$ Er-doped SESAM modelocked oscillator generates $1.61\,mW$, $400\,fs$ transform limited pulses at $1.56\,\mu m$. The oscillator working conditions are different compared to the previous section ($2\,mW$, $340\,fs$) to decrease the influence of Kelly sidebands on the SSFS which allows us to slightly increase the Raman shift [119]. To increase the pulse energy, an Er-doped amplifier ($1.2\,m$ LIEKKI Er110-4/125) bi-directionally core-pumped is used. The amplifier output power is set by adjusting the co-directional pump laser diode current while keeping the other pump fixed. The variable power ranges from $100\,mW$ to $160\,mW$ out of the amplifier as estimated via a tap power measurement. The soliton self-frequency shift takes place in two pieces of PM1950 fiber ($7\,\mu m$ core, $8\,\mu m$ MFD @$1950\,nm$, 0.2 NA, $36\,ps/nm\,km$) separated by a WDM filter. The pulses out of the Er amplifier can generate two solitons and the WDM filter has been set at a particular position within the two pieces of fiber to ensure that only the long wavelength shifted soliton goes through the WDM filter while the short wavelength soliton is rejected with the residual pump through the reflected port.

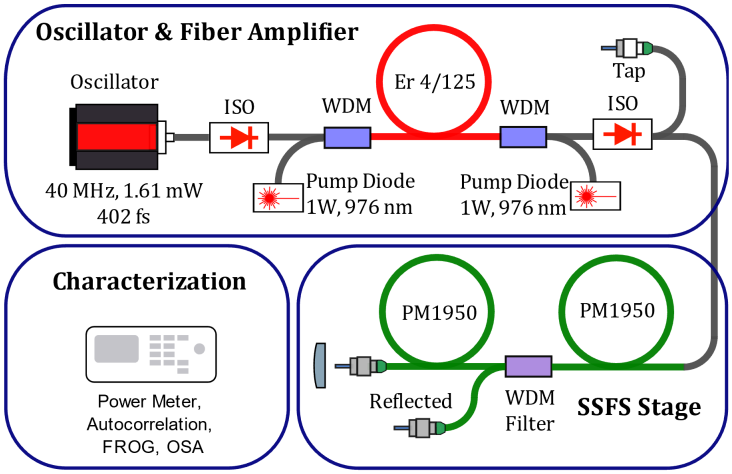

(a) SSFS tunable laser architecture.

Figure 2.16: SSFS tunable laser architecture

The SSFS spectra have been measured with the optical spectrum analyzer and are displayed on Fig.2.17a for different input powers out of the Er amplifier. Water absorption lines can be observed between $1.8\,\mu m$ and $1.92\,\mu m$. As the WDM filter rejects all radiation below $\sim 1.80\,\mu m$, the pulse wavelength tunability extends from $1.8\,\mu m$ up to $2055\,nm$ simply by adjusting the pump power of the Er amplifier. Longer wavelengths are out of

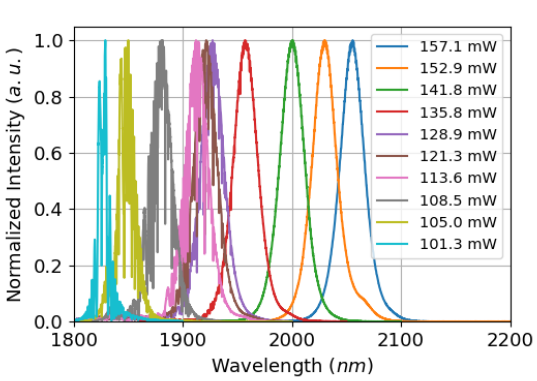

(a) Optical spectrum out of the SSFS tunable laser.

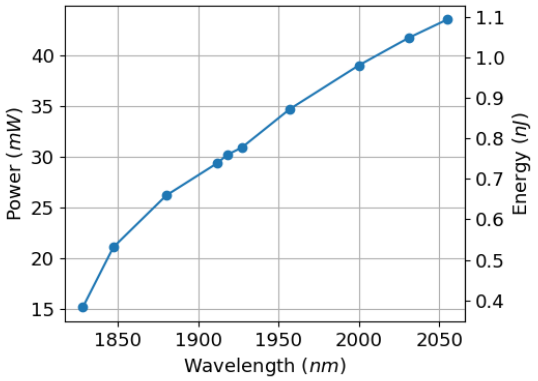

(b) Soliton power and energy.

Figure 2.17: Measured optical spectrum of the soliton pulses as function of Er amplifier output power and average power of the solitons as function of wavelength

reach with this configuration due to excessive losses of fused silica above $2\,\mu m$. Note that pulses with wavelengths below $1.8\,\mu m$ are available at the reflected port.

The average power of the solitons is displayed on Fig.2.17b as a function of the central wavelength and varies from $21\,mW$ up to $43.5\,mW$. As shown in the previous section, the energy of the solitons and hence the power, is well defined and depends on the fiber properties (β_2,n_2,A_{eff}) according to Eq.1.35. As the wavelength shifts, β_2 increases and so does the mode area hence the energy of the soliton increases.

The laser architecture is based on exclusively polarization maintaining components and the polarization was evaluated by measuring the polarization extinction ration (PER) which is defined as the ratio between the power in the slow axis and the fast axis, which in dB is expressed as:

$$PER(dB) = 10log_{10}\left(\frac{P_S}{P_F}\right) \tag{2.1}$$

Where P_S and P_F are the power in the slow and fast axis respectively. In order to measure the amount of power on each axis a polarizer or half-waveplate and polarization beam splitter (PBS) is used to separate both polarizations. The measured PER as a function of the soliton wavelength is shown in Fig.2.18a. The PER is above $19\,dB$ for wavelengths below $2\,\mu m$ decreasing slightly with $15.5\,dB$ at $2033\,nm$ and $17.5\,dB$ for $2055\,nm$. Characterising the PER of fibers is complex as it depends on the input light properties, the alignment with the fiber axis, the fiber length, the coiling or even the environmental conditions which can add some stress induced birefringence but, in the end, the output light polarization is what matters [123]. The PER of the light out of the isolator sets the input quality in terms of PER which is $\sim 22\,dB$. The alignment of the input light with the PM1950 fiber slow axis is as accurate as the fiber splicing machine is (Fujikura FSM 100-P or Fujikura FSM 100-P+). Slight miss-alignments on the fiber stress rods from one fiber to another degrade the polarization. Splicing fibers designed for the $2\,\mu m$ spectral region becomes more complex due to the dopants included in the fused silica matrix. This is because the alignment procedure of the splicing machines use cameras and imaging systems to observe the contrast between the core, the clad and the stress rods and based on the images the alignment is performed. This ultimately

yields to angle mismatch $0.2 - 1.3^o$ from fiber to fiber that has always been maintained below 0.8^o. The polarization maintaining properties of the fiber are strongly linked to the fiber birefringence Δn_B and the beat length defined as $L_B = \lambda/\Delta n_B$. The higher the birefringence, the shorter the beat length and the better the polarization maintaining properties of the fiber. Typically, telecom fibers in the $2\,\mu m$ spectral region have a beat length which is longer compared to the well established $1\,\mu m$ fiber technology. For the PM980XP ($@1\,\mu m$) fiber the beat length is $2.7\,mm$, for the PM1550XP ($@1.56\,\mu m$) is $5\,mm$ and PM1950 ($@1.95\,\mu m$) is $5.2\,mm$. The variation in the PER is a combination of the mentioned factors and due to the polarisation maintaining properties of the WDM filter used.

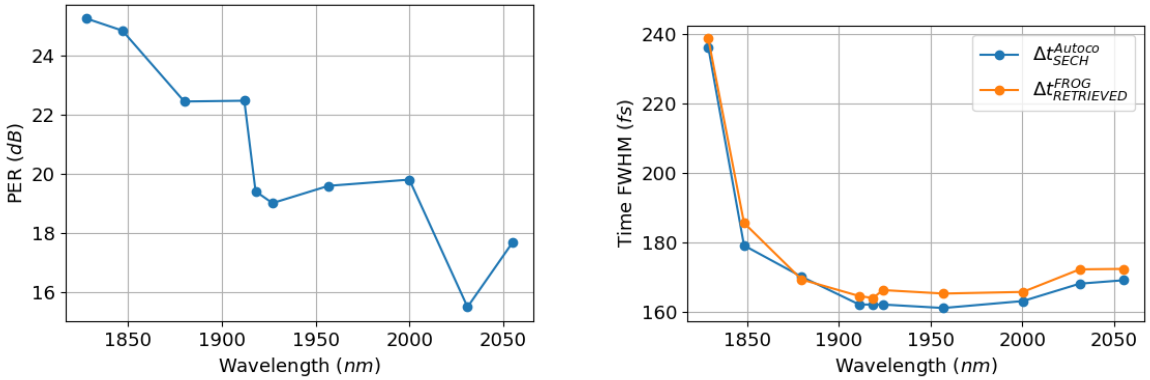

(a) Polarization extinction ratio (PER).

(b) Soliton pulse FWHM as function of wavelength.

Figure 2.18: Measured PER and pulse FWHM of the soliton pulses as function of wavelength.

Pulse durations were estimated from an autocorrelator (APE PulseCheck) measurement assuming a sech pulse which was fit to the measured ACT to obtain the pulse FWHM. To verify the results, measurements were crosschecked with a FROG (MS-FROG, FemtoEasy). The pulse duration as a function of the soliton's wavelength is depicted in Fig.2.18b. The soliton duration remains mostly constant with a minimum pulse duration of 161 fs at $1960\,nm$ and a maximum of 240 fs at $1830\,nm$. The pulse duration increases as the wavelength decreases because of the filter used to reject the pump and the second soliton. The bandwidth of the filter is narrowing and attenuating the soliton pulse at $1830\,nm$ and in the end due to narrowing and losses along propagation, the soliton cannot keep the balance between dispersion and non-linearities and broadens in time. The measured values using an autocorrelator agree quite well with those obtained using FROG. The differences from FROG measurement to autocorrelator was always below $10\,fs$ which corresponds to $10 - 13\%$ deviation. The difference in pulse duration is attributed to the FROG spectrometer resolution ($1\,nm$) which can slightly affect the pulse duration during the acquisition which then is mapped into the reconstruction algorithm. It is important to recall that the measured pulse durations are longer compared to those obtained when studying the properties of the PM1950 fiber (see Fig.2.14). The differences can come from the fact that a different fiber spool was used which may have slightly different parameters (dispersion, MFD and n_2) and the fact that the experimental conditions are different. In the previous case the pump pulse was a soliton generated in the PM1550XP fiber at an already shifted wavelength but now the pulses come directly from the Er amplifier and

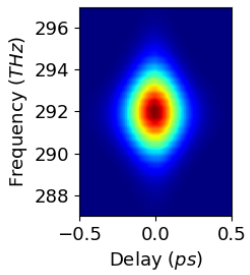

(a) Measured spectrogram. $\lambda_0 = 2055\,nm$

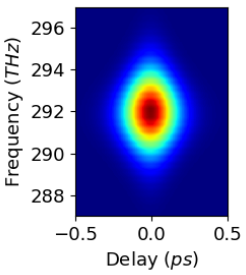

(b) Reconstructed spectrogram. $\lambda_0 = 2055\,nm$

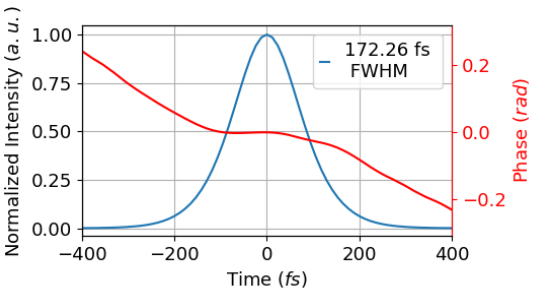

(c) Retrieved pulse shape. $\lambda_0 = 2055\,nm$

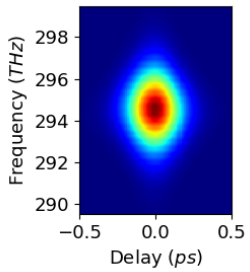

(d) Measured spectrogram. $\lambda_0 = 2033\,nm$

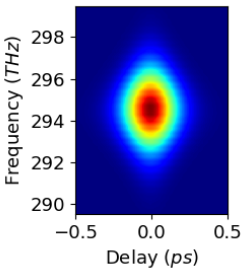

(e) Reconstructed spectrogram. $\lambda_0 = 2033\,nm$

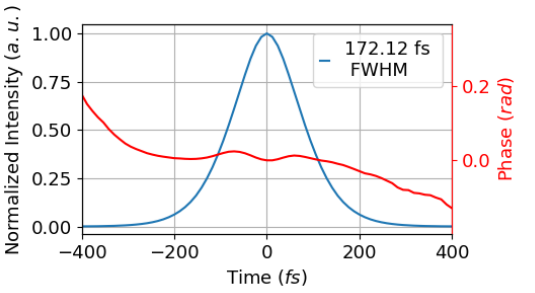

(f) Retrieved pulse shape. $\lambda_0 = 2033\,nm$

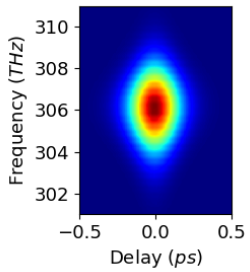

(g) Measured spectrogram. $\lambda_0 = 1960\,nm$

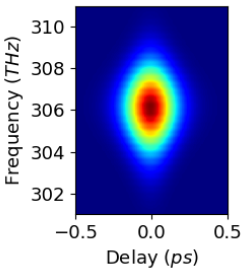

(h) Reconstructed spectrogram. $\lambda_0 = 1960\,nm$

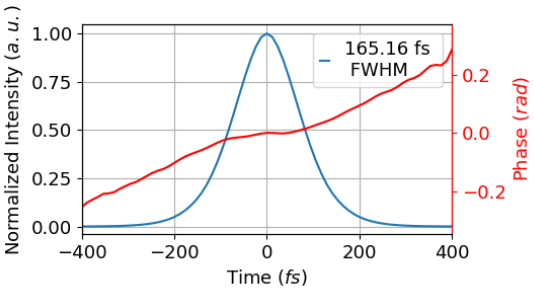

(i) Retrieved pulse shape. $\lambda_0 = 1960\,nm$

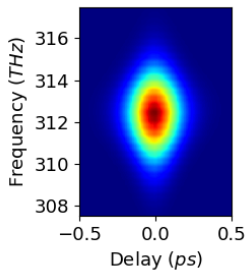

(j) Measured spectrogram. $\lambda_0 = 1920\,nm$

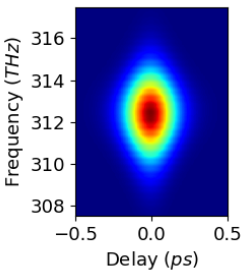

(k) Reconstructed spectrogram. $\lambda_0 = 1920\,nm$

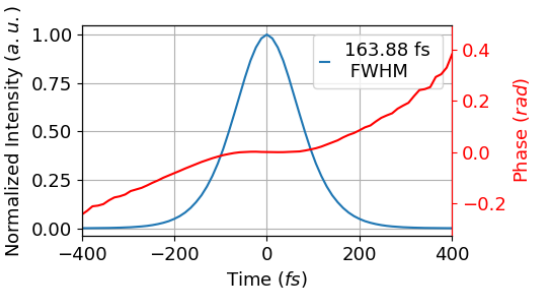

(l) Retrieved pulse shape. $\lambda_0 = 1920\,nm$

Figure 2.19: Measured and reconstructed spectrograms and retrieved pulse shapes for soliton pulses at 2050 nm, 2033 nm, 1960 nm and 1920 nm.

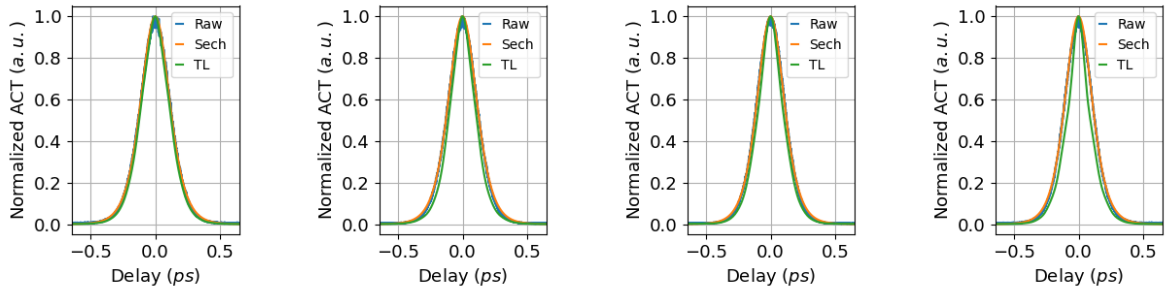

(a) ACT $\lambda_0 = 2050\,nm$
$\Delta t_{ACT} = 265\,fs$
$\Delta t^{sech}_{PULSE} = 171\,fs$

(b) ACT $\lambda_0 = 2033\,nm$
$\Delta t_{ACT} = 261\,fs$
$\Delta t^{sech}_{PULSE} = 168\,fs$

(c) ACT $\lambda_0 = 1960\,nm$
$\Delta t_{ACT} = 254\,fs$
$\Delta t^{sech}_{PULSE} = 161\,fs$

(d) ACT $\lambda_0 = 1918\,nm$
$\Delta t_{ACT} = 256\,fs$
$\Delta t^{sech}_{PULSE} = 162\,fs$

Figure 2.20: Measured ACT for soliton pulses at $2050\,nm$, $2033\,nm$, $1960\,nm$ and $1918\,nm$.. In blue the measured ACT, in orange the ACT for the sech fit and in green, the transform limited (TL) ACT.

the added PM WDM filter to reject the second generated soliton also plays a role in the SSFS by adding losses.

In Fig.2.19 the measured and reconstructed spectrograms have been included with the retrieved pulse shape for the solitons at $2050\,nm$, $2033\,nm$, $1960\,nm$ and $1920\,nm$ wavelength. To compare, the measured ACT for the same pulses measured with the APE autocorrelator are depicted in Fig.2.20. As it can be seen in Fig.2.19, measured and retrieved spectrogram are identical and the retrieved pulse shapes are almost transform limited as it can be deduced by the residual phase which is mostly flat within the pulse. It can be seen how close to the TL duration the pulses are in Fig.2.20 where the measured ACT is almost identical to the TL pulse depicted in green.

Pulse durations for SSFS in standard telecom fibers are usually above the $100\,fs$ and cannot reach $2.1\,\mu m$ wavelength in a single SSFS stage due to increasing losses in fused silica fibers. In order to overcome the limitations different approaches can be used. Longer wavelengths can be achieved provided that an extra amplifier (Tm or Tm:Ho) is included half way the SSFS stage to boost the energy of the pulses to overcome the losses and further shift in wavelength. If the amplifier is properly set and adjusted in terms of dispersion, highly efficient SSFS can be achieved reaching up to $2.4\,\mu m$ wavelength [13, 124, 125, 126, 127]. If a single SSFS stage is desired, specialty fibers can be used with taylored properties such as increased Raman scattering [128], controlled dispersion and non-linearities to shorten the pulse duration and increase rate at which SSFS takes place. This approach has been widely used and studied and large amounts of work have been done around photonic crystals (PCF), tellurite fibers, GeO_2-doped fibers [129, 130], dispersion managed fibers and even Bragg fibers. PCF allows to reach very high non-linearities by reducing the core size while still having an anomalous dispersion [2, 9, 116, 131]. Tunable pulses from $1700\,nm$ up to $2100\,nm$ with durations below $100\,fs$ pulses have been demonstrated in custom-made and commercially available PCF fibers . The only inconvenience for this approach is that the fiber lengths needed to be adjusted depending on the operation wavelength for optimal performance [9]. Tellurite fibers are also of interest because they offer high transparency in the near IR up to mid IR and high non-linearities. Tunable pulses from $1560\,nm$ up to $2400\,nm$ with durations below $100\,fs$ have been demonstrated [10]. PCF and tellurite fibers are good alternatives but they have the inconvenience that fiber splicing is very complex and sometimes require free space injection

and may not be polarization maintaining fibers. This is also the issue with Bragg fibers, they allows to reach MW peak powers with highly energetic pulses due to their large mode areas with durations below $100\,fs$ in non-PM fibers provided that they are seeded with CPA laser systems [11]. If specialty fibers are not an option, a higher power Er laser can be used. Er CPA laser systems can produce highly energetic ultrashort pulses that when injected in fused silica fibers can yield to large SSFS tunability [3, 132]. The approach chosen to further reduce the pulse duration of the solitons while maintaining the tunability and the commercially available components was to rely on non-linear effects, SPM for spectral broadening and non-linear pulse compression (SPM and dispersion) to compress the pulses.

2.5 NL Spectral Broadening and Compression

In order to reach the sub-$100\,fs$ pulse duration a spectral broadening and compression stage consisting of two fibers with opposite dispersion was included. The first fiber is the PM2000D ($\sim 8\,cm$ long, $2.1\,\mu m$ core diameter, $4\,\mu m$ MFD @$2\,\mu m$, 0.4 NA and $-55 \pm 10\,ps/nm \cdot km$). The fiber has a large normal dispersion due to its small core which is dominated by the waveguide dispersion overcompensating the fused silica material contribution to dispersion. Due to the small MFD, the short pulse durations and high intensities, SPM will occur and spectrally broaden the spectra. The second fiber is a $17.5\,cm$ of PM1950 with high anomalous dispersion compressing the pulse while further broadening as the pulse gets shorter (NL pulse compression). Taking this into account, the fiber laser architecture is depicted in Fig.2.21. The pulses have been characterised once again after the spectral broadening and compression stage. The measured spectra are shown in Fig.2.22a.

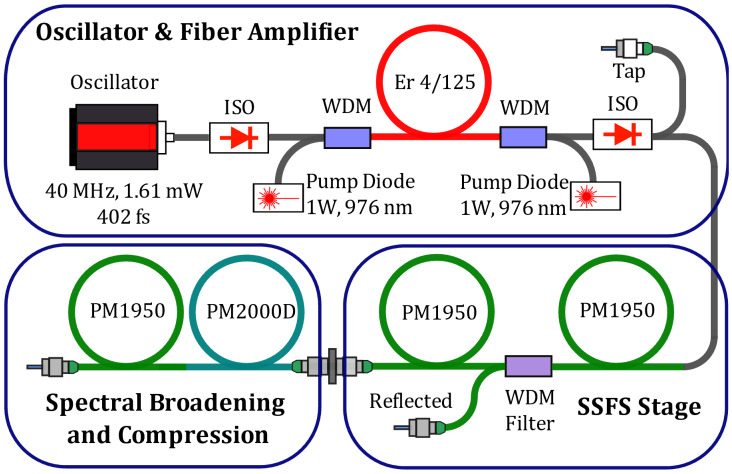

Figure 2.21: Architecture of the $sub-100\,fs$ tunable laser.

The spectra of the pulses have substantially broadened compared to the soliton pulses in Fig.2.17a. The spectra FWHM as a function of wavelength for the soliton and post-compressed pulses are shown in Fig.2.22b. For the soliton pulses at $2055\,nm$ they have spectrally broadened from $26.3\,nm$ up to $71.4\,nm$ after post-compression which is 2.7 times larger at FWHM. Such large bandwidths allows to sustain pulses whose duration is below $100\,fs$.

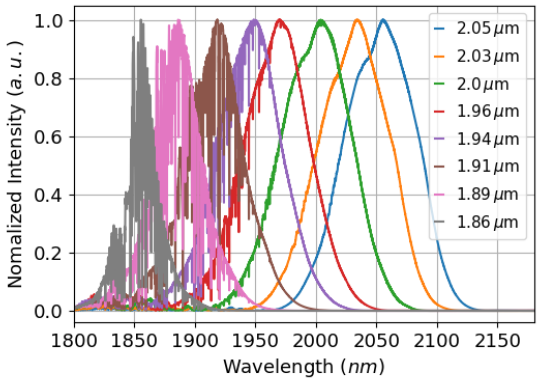

(a) Measured optical spectrum.

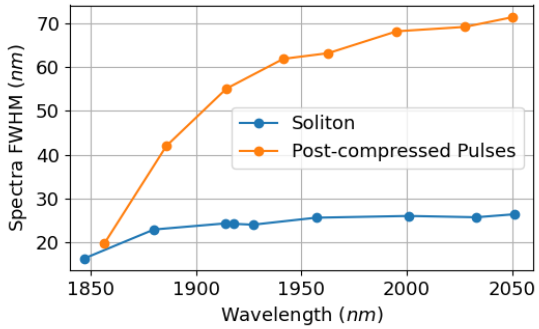

(b) Spectrum FWHM.

Figure 2.22: Measured Optical spectrum and spectrum FWHM as function of wavelength for the post-compressed and soliton pulses.

The pulse output powers of the spectral broadening and compression stages are plotted in Fig.2.23a. As it can be seen, the powers have dropped substantially and only 77% of the soliton power remains at the output of the spectral broadening and compression stages. Due to a large mismatch between the PM1950 and PM2000D fibers in terms of core size, MFD and NA, splicing losses reduce the power transmitted from the PM1950 to the PM2000D fiber. At the same time, the mating sleeves used to connect the fibers further reduce the power transmitted. The measured power varies from $15\,mW$ up to $33.8\,mW$ with the wavelength following the same trend as the solitons' power.

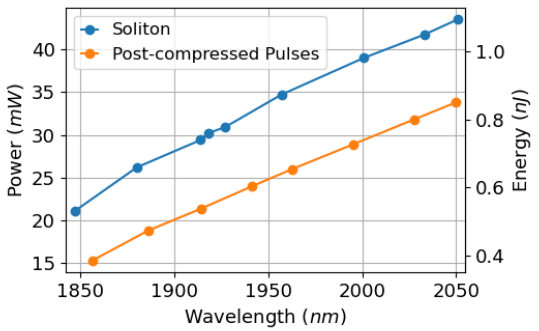

(a) Measured average power.

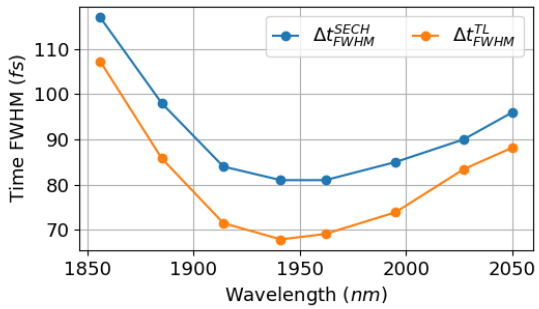

(b) Measured pulse FWHM for deconvoluted sech pulse shape and transform limited FWHM.

Figure 2.23: Measured average power of the post-compressed pulses and pulse ACT, TL ACT and pulse FWHM for sech pulse shape as function of wavelength.

The pulse duration of the post-compressed pulses have been measured using an auto-correlator. In Fig.2.23b the transform limited duration Δt^{TL}_{FWHM} and the pulse FWHM assuming a sech shape Δt^{SECH}_{FWHM} are shown as function of the wavelength. Assuming a sech pulse shape pulse durations below the $100\,fs$ are obtained from $1886\,nm$ up to $2050\,nm$ with a minimum of $81\,fs$ for pulses at $1940\,nm$ and $1960\,nm$. The measured ACT of the post-compressed pulses are shown in Fig.2.24. In this situation, the pulses are far away from being TL as the ACT measured values are $20\,fs$ to $30\,fs$ longer in time. This can be because the lengths of the PM2000D and PM1950 fibers, are not matched in length to perfectly balance dispersion and/or because the non-linearities that generated

the BW required to sustain such short pulses, have produced a NL phase that cannot be compressed using fibers. Fiber lengths can be adjusted provided that the residual phase can be measured shortening the pulse duration however, residual non-linear phase to get to the transform limited duration cannot be compensated.

The main issues with ACT measurements is that the measured pulse duration can be obtained assuming the pulse shape is known (Gaussian, sech, Lorentzian...). To avoid under estimation of the duration, alternative measurement techniques such as FROG have to be used. FROG measurements were tried for the post-compressed pulses and the results for the shortest pulse 81 fs pulses at 1960 nm are shown in Fig.2.25.

As it can be seen, the measured and reconstructed spectrogram do agree quite well and so does the measured and reconstructed ACT and the measured and reconstructed $2w$ optical spectrum. It must be noted that even though they match any discrepancy can have an important impact on the reconstructed pulse shape, specially when pulses are that short. The retrieved pulse duration was $\Delta t_{FWHM} = 92.2\, fs$ which is slightly longer than what expected for sech pulses (81 fs) and for Gaussian pulses (88 fs) according to the measurements taken with the autocorrelator which corresponds to discrepancies between $5 - 12\%$. The main issue observed is that the reconstructed optical spectrum of the pulses has shifted in wavelength and become narrower compared to the one measured with the optical spectrum analyser (see Fig.2.25). This doesn't necessarily mean that the measurement is wrong, it can be that the spectral components that have not been measured or retrieved are contained in a long pedestal that cannot be resolved due to limited resolution of the spectrometer or that there is an important amount of light that is not contributing to the pulse duration. Another reason can be that the FROG is mainly analysing the doubled light at $2w$ to reconstruct the pulse. For the pulses analysed at 1960 nm, an important part of the spectrum suffers from water absorption which may have an impact on the frequency doubling slightly shifting the mean wavelength of the frequency doubled pulses. Any of the mentioned explanations are valid yet very hard to verify or measure with the commercial device. Ideally, alternative measurement techniques that can retrieve pulse shape and duration such as D-scan could be used to cross-check the results [133]. When the FROG measurements were performed for the SSFS laser, the spectral BW was accurate to $\pm 1\, nm$ and $\pm 2\, nm$ for the measured main wavelength. When the post-compressed pulses were characterized at other wavelengths the same issue was observed. The reconstructed pulses were longer than those measured with autocorrelator (it gets worse as wavelength decreases as we get into the water absorption spectral region) and the measured BW were substantially narrower compared to measurements with the OSA. The FROG trace was measured twice and the same results were obtained for all the measured wavelengths. The Autocorrelation measurements were as well repeated with a different device and no change was observed hence we are confident on the measured values using the autocorrelator as it's a much simpler and robust technique. In addition, the measured ACT using FROG agreed very well with the one using APE autocorrelator. So in the end it is complex to identify whether the discrepancy on the FROG measurements come from a physical phenomena such a long pedestal in the pulse or from the reconstructed algorithm which usually gives longer retrieved ACT and narrower BW.

To further understand the dynamics that take place in the spectral broadening and pulse compression stage and to cross-check the measurements and results obtained with FROG, simulations were performed using the commercially available FiberDesk software.

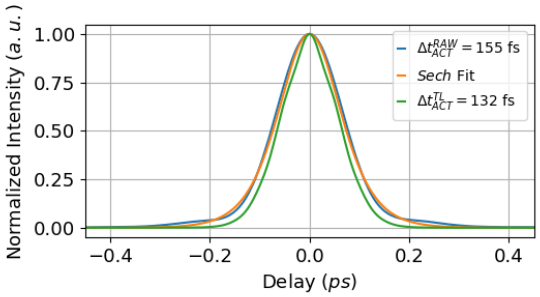

(a) ACT $\lambda_0 = 2050\,nm$
$\Delta t_{FWHM}^{sech} = 96\,fs$

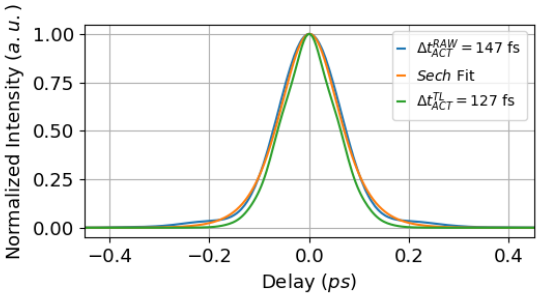

(b) ACT $\lambda_0 = 2028\,nm$
$\Delta t_{FWHM}^{sech} = 90\,fs$

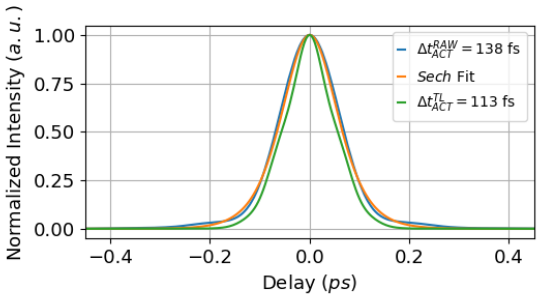

(c) ACT $\lambda_0 = 1995\,nm$
$\Delta t_{FWHM}^{sech} = 85\,fs$

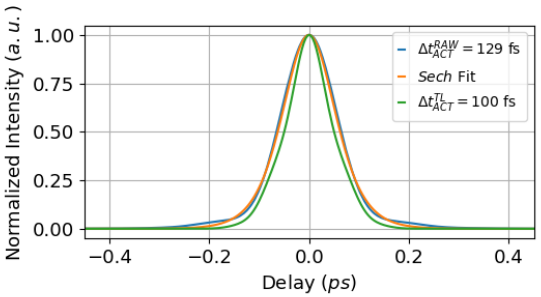

(d) ACT $\lambda_0 = 1963\,nm$
$\Delta t_{FWHM}^{sech} = 81\,fs$

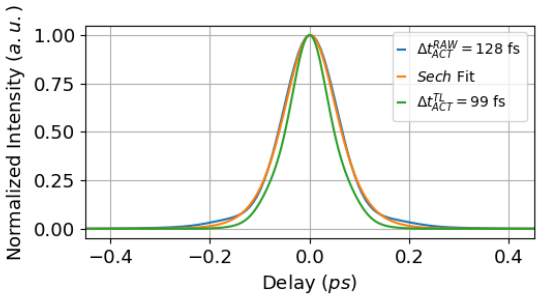

(e) ACT $\lambda_0 = 1941\,nm$
$\Delta t_{FWHM}^{sech} = 81\,fs$

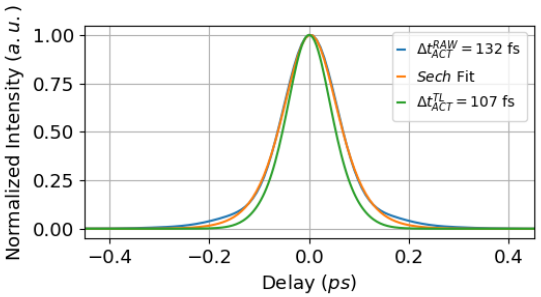

(f) ACT $\lambda_0 = 1914\,nm$
$\Delta t_{FWHM}^{sech} = 84\,fs$

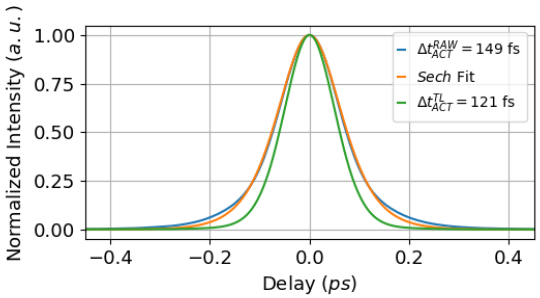

(g) ACT $\lambda_0 = 1886\,nm$
$\Delta t_{FWHM}^{sech} = 98\,fs$

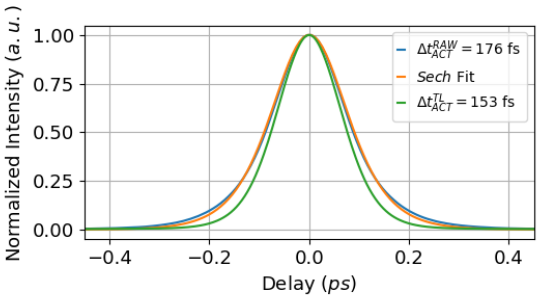

(h) ACT $\lambda_0 = 1856\,nm$
$\Delta t_{FWHM}^{sech} = 117\,fs$

Figure 2.24: Measured ACT of the post-compressed pulses. Δt_{ACT}^{RAW} is measured the ACT at FWHM, Δt_{ACT}^{TL} is the ACT of the transform limited pulse at FWHM and Δt_{FWHM}^{sech} is the pulse FWHM for sech pulses.

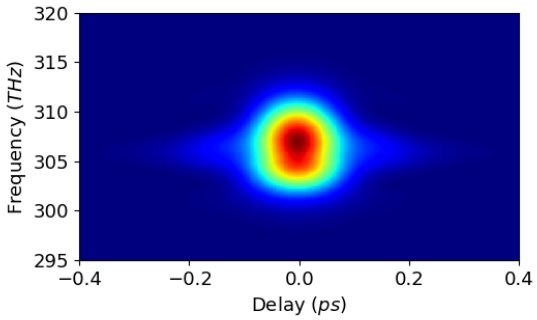

(a) Measured spectrogram.

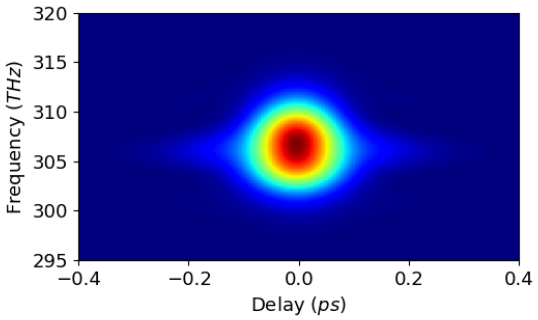

(b) Reconstructed spectrogram.

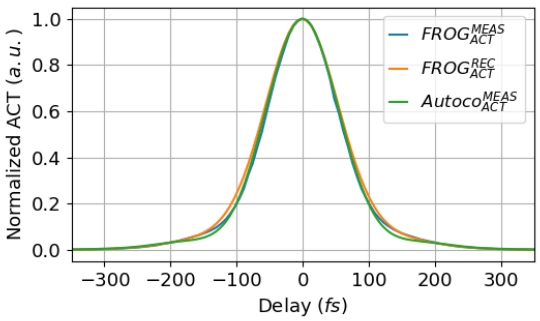

(c) Measured (MEAS) and reconstructed (REC) ACT. $\Delta t_{FROG}^{MEAS} = 126\,fs$ $\Delta t_{FROG}^{REC} = 135\,fs$ and $\Delta t_{ACT}^{MEAS} = 129\,fs$.

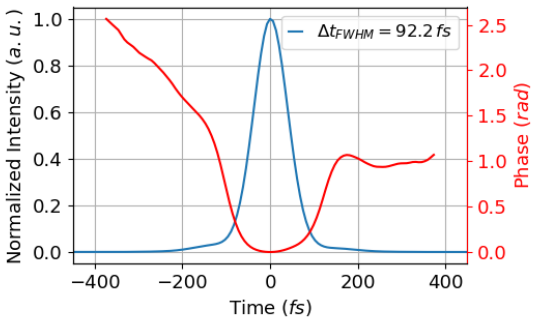

(d) Retrieved pulse shape.

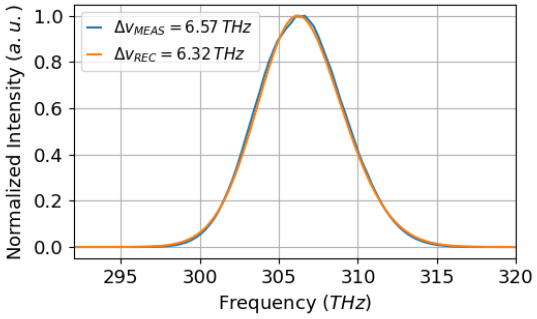

(e) Measured (MEAS) and retrieved (REC) $2w$ spectrum.

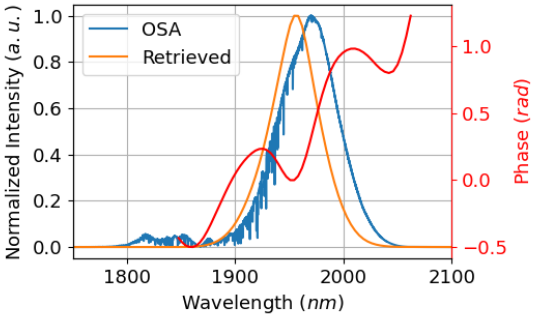

(f) Measured and retrieved spectrogram.

Figure 2.25: FROG measurements of the post-compressed pulses at $\lambda = 1960\,nm$.

2.5.1 Modelling the PM2000D and PM1950 Fiber Parameters

To perform the simulations, the physical properties (MFD, β_2, β_3 and n_2) of both fibers, the PM2000D and PM1950 fibers, had to be modelled.

The dispersion and MFD of the PM2000D fiber could not be estimated based on fiber geometry as done in the previous section because it was not possible to observe and measure the size and relative position of the core and the boron stress rods on the microscope due to their small sizes. Hence, the MFD value was taken from the datasheet and slightly adjusted for the simulations. The dispersion of the fiber was measured to first order (β_2) by performing a cutback on a $120\,m$ spool of PM2000D fiber and β_3 was taken from literature, where the dispersion of the fiber had already been measured. By measuring the pulse duration and spectrum of the pulses the dispersion parameter D could be measured and β_2 could be calculated according to Eq.1.15. The results and the experimental setup are show in Fig.2.26.

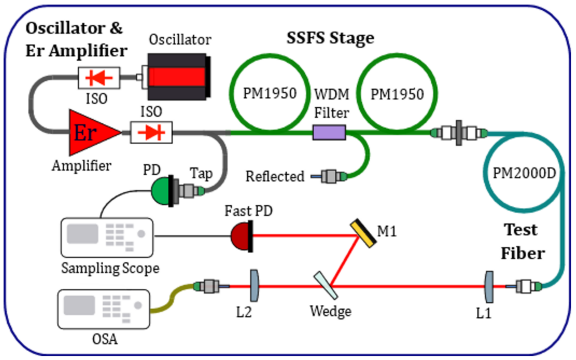

(a) Dispersion measurement setup. PD: photodiode, L1 and L2: lens, M1: mirror and OSA: optical spectrum analyser.

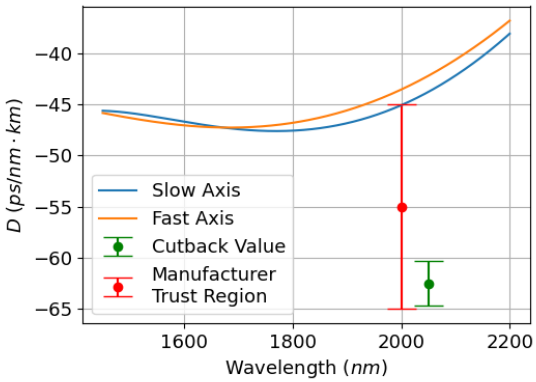

(b) Dispersion parameter D.

Figure 2.26: Setup to measure fiber dispersion parameter D at $\lambda_0 = 2050\,nm$ for the PM2000D fiber and PM2000D dispersion parameter D values. Dispersion data taken from [134].

Pulse durations in the hundreds of ps regime can be measured using a fast photodiode (ET-4000, BW$> 12\,GHz$) and a fast oscilloscope or a triggered sampling scope. A sampling scope was used to measure the pulse which was triggered with the Er amplifier's isolator tap directly connected to a fast enough photodiode to measure the repetition rate of the laser ($40\,MHz$). The soliton pulses at $2050\,nm$ ($43.5\,mW$, $26.6\,nm$ BW and $172\,fs$) were used to measure dispersion at that particular wavelength. The spectra of the pulses was measured with the OSA and the dispersion as function of the cut fiber can be obtained by dividing the pulse FWHM and the spectrum FWHM for the different fiber lengths and performing a linear fit to recover $D\,(ps/nm\,km)$. In Fig.2.27, the measured pulse shape and spectrum is shown after removing $20\,m$ of fiber together with the linear fit for the dispersion parameter D.

As can be seen in Fig.2.27, the spectra of the pulses broadened from $\sim 26.6\,nm$ up to almost $80\,nm$ BW and in time the pulses have stretched up to $\sim 435\,ps$. The propagation is non-linear which means that the rate at which the pulses stretch in time increases as they propagate due to an increase of BW. Due to the small MFD, the non-linearities take place over the first few meters of fiber. To make sure that the dispersion is measured

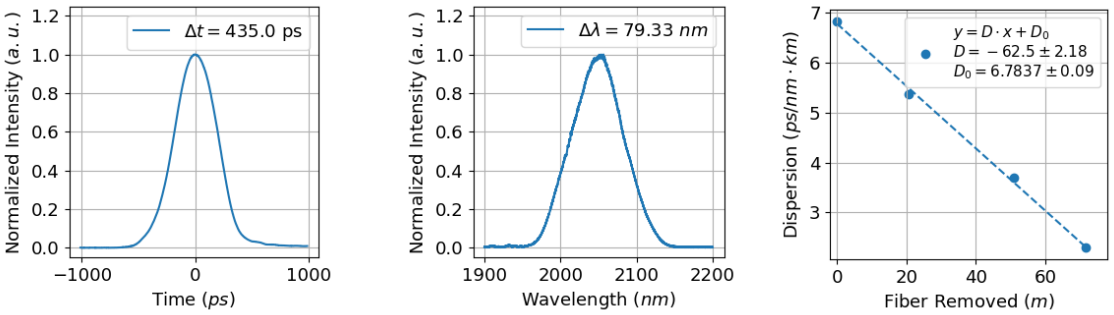

(a) Pulse shape.

(b) Optical spectrum.

(c) Calculated dispersion parameter $D(ps/nm \cdot km)$.

Figure 2.27: Measured pulse shape and optical spectrum after cut-back of $20\,m$ of fiber and calculated dispersion parameter D

PM2000D		PM1950	
$\beta_2\ \left(\frac{ps^2}{m}\right)$	0.139	$\beta_2\ \left(\frac{ps^2}{m}\right)$	-0.08841
$\beta_3\ \left(\frac{ps^3}{m}\right)$	-0.000174	$\beta_3\ \left(\frac{ps^3}{m}\right)$	0.00040464
$MFD\,(\mu m)$	4.1	$MFD\,(\mu m)$	8.5
$n_2\,(cm^2/W)$	$2.7 \cdot 10^{-16}$	$n_2\,(cm^2/W)$	$2.7 \cdot 10^{-16}$

Table 2.1: Simulation parameters for pulse propagation in PM2000D and PM1950 optical fibers.

in the linear regime in which non-linear effects are avoided, the cut-back was performed ensuring that the spectrum FWHM was constant, otherwise the measurement would loose accuracy. The measured dispersion parameter value was $D = -62.5 \pm 2.2\,\frac{ps}{nm \cdot km}$ which compared to literature is well below for pulses propagating in the slow axis of the fiber, $D_{LIT} \sim -45\,\frac{ps}{nm \cdot km}$ [134]. Although a large discrepancy in the dispersion parameter, it still falls within the manufacturer trust region (see Fig.2.26b) and the measured value was used for the simulations. TOD (β_3) was calculated from the literature dispersion curve by calculating $\beta_2(w)$ and its first derivative (see Eq.1.15 and Eq.1.10).

It is worth mentioning that even though scanning the SSFS laser would provide the dispersion parameter D as function of the wavelength and therefore β_3 by derivation of β_2, some limitations on the technique and equipment would have made it difficult to obtain accurate results. In the end, the main issue would have been the accuracy to measure pulse durations and this is linked to the BW of the photodiode $12.5\,GHz$ which yields to resolutions of up to $\sim 30\,ps$. If precise fiber dispersion values are required, alternative and more accurate techniques that rely on supercontinuum laser sources [113, 135] that can scan the whole spectral region at once in combination with interferometers can lead to very accurate dispersion data [134, 136]. The summarised values used to simulate the PM2000D fiber can be found in Table.2.1 which also includes the parameters for the PM1950 fiber taken from COMSOL simulations (see Fig.2.9 in the previous section 2.3.1).

2.5.2 Simulation on Spectral Broadening and non-linear Pulse Compression

The pulse shape and spectral evolution along the spectral broadening and compression stages for the soliton pulses at $2050\,nm$ ($43.5\,mW$, $26\,nm$ BW and $172\,fs$) is show in Fig.2.28a and Fig.2.28b respectively. As it can be seen, in the PM2000D fiber, there is spectral broadening due to SPM which combined with dispersion leads to pulse stretching up to $460\,fs$ at FWHM. The simulated bandwidth at the end of the PM2000D fiber is $\sim 40\,nm$. Pulse FWHM and spectrum FWHM as function of fiber length has also been computed and is shown in Fig.2.29a and Fig.2.29b.

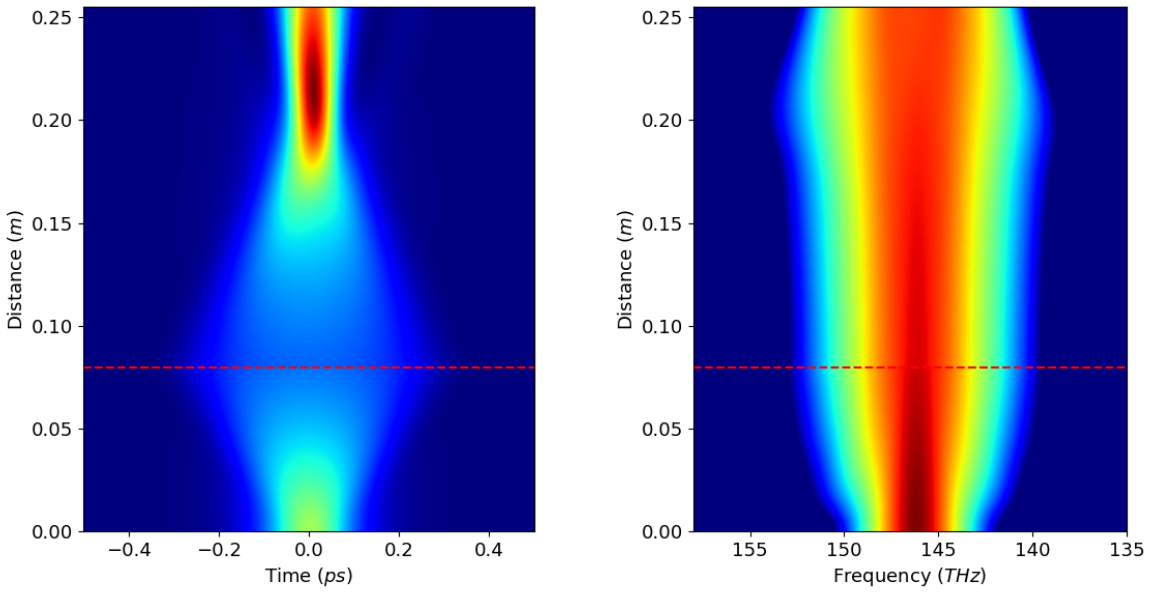

(a) Pulse shape.

(b) Optical Spectrum.

Figure 2.28: Simulated temporal and spectral pulses at $2050\,nm$ along the spectral broadening and compression stage. Fiber splice location is dashed in red.

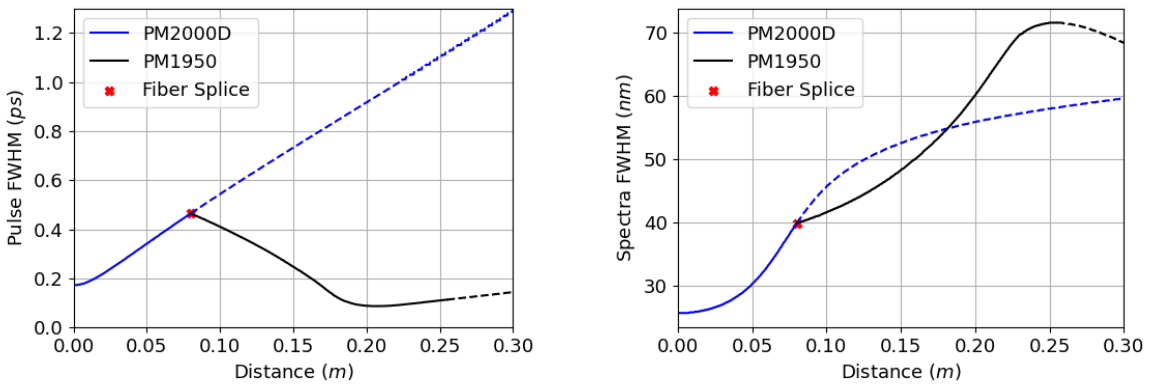

(a) Simulated pulse FWHM.

(b) Simulated optical spectrum FWHM.

Figure 2.29: Simulated pulse and optical spectrum FWHM along the spectral broadening and compression stage for $2050\,nm$ pulses.

It can be observed that for a longer piece of PM2000D, besides further pulse stretching, the bandwidth would keep increasing at a reduced rate as the peak power decreases and it would eventually reach a maximum value of $\sim 80\,nm$ as observed when measuring the PM2000D fiber dispersion over $120\,m$ (see Fig.2.27). On the second fiber, the PM1950, pulse compression occurs in combination with further spectral broadening until the fiber end in a process known as non-linear pulse compression. The pulse reaches a minimum in duration few centimeters before the end of the fiber which means that there is margin for improvement and that the dispersion between the PM2000D and PM1950 fiber is not perfectly balanced. Adjusting the fiber length would definitely improve the performance at $2050\,nm$ however, the system is tunable and what is won in pulse duration on one side of the tunability range is lost on the other. This is because dispersion is wavelength dependent hence what is usually done is to optimise the system taking into account dispersion and NL effects around the center wavelength within the tunability range obtaining a short pulse over a broad spectral range. PM2000D fiber has a quite flat dispersion which makes it suitable for ultrashort pulse stretching (see Fig.2.26b) but this is not the case for the PM1950 fiber (see Fig.2.9d) which means that it is not possible to minimize pulse duration all along the spectral tunability range. In Fig.2.30 the measured and simulated autocorrelation traces (ACT) and spectrum respectively are illustrated showing a good agreement.

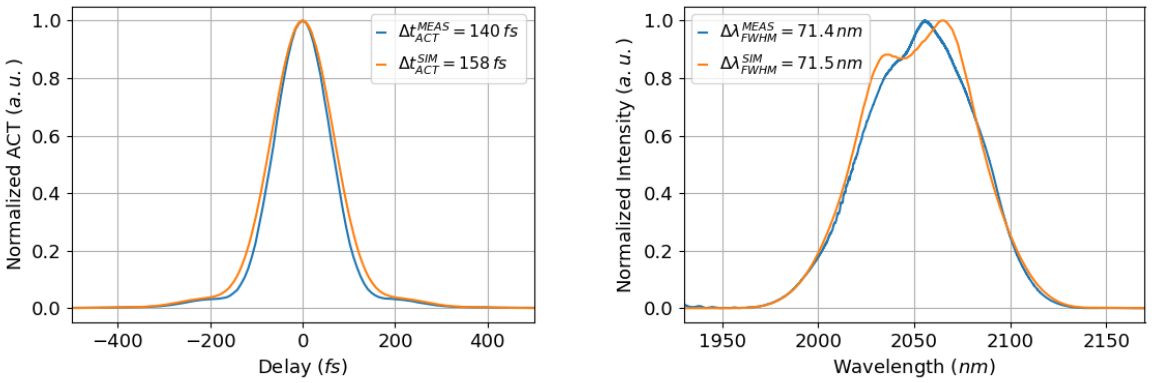

(a) Simulated and measured autocorrelation trace.

(b) Simulated and measured optical spectrum.

Figure 2.30: Simulated and measured autocorrelation trace and spectrum for compressed optical pulses at $2050\,nm$.

In Fig.2.30 a dip starts to develop in the simulated spectrum at the mean wavelength of $2050\,nm$ which is due to the accumulated non-linear phase. This marks the onset of typical modulations observed due to self-phase modulation. The onset of SPM dip is the main difference in the simulated and measured spectrum as in terms of FWHM they are almost identical. Regarding the pulse duration, a slightly longer pulse was obtained compared to the measured values. Discrepancies are mainly due to the fact that fiber properties for both fibers have been simulated or partially characterised instead of performing a full characterization of the parameters involved in pulse propagation. The behaviour observed for pulses at $2050\,nm$ can be extrapolated to pulses all along the tunability range from $1850\,nm$ up to $2050\,nm$. Due to different powers, pulse durations, bandwidths and fiber parameters, the results will differ from one to another but they will obey the same trend and physics in terms of spectral broadening, pulse stretching and non-linear pulse compression.

Taking into account the simulated pulse dynamics, one can argue that even shorter pulses can be obtained if the PM2000D fiber is used exclusively provided the pulses are compressed externally by other means using a grating compressor or a prism compressor for instance. If a $\sim 1.3\,m$ of PM2000D optical fiber is used, $71.4\,nm$ BW and $5.7\,ps$ stretched pulses should be obtained that then can be compressed using a Treacy compressor at Littrow incidence angle down to $90\,fs$. Pulse propagation and pulse compression were simulated and the results are summarised in Fig.2.31.

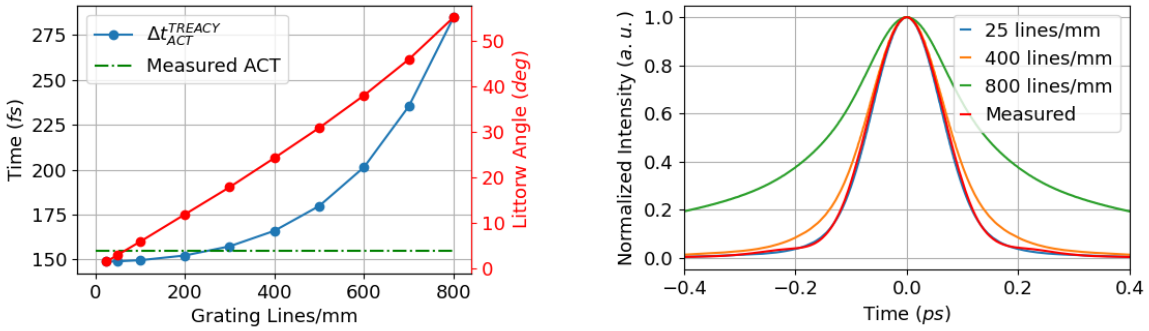

(a) Simulated ACT of the post-compressed pulses using a Treacy compressor with custom grating lines/mm.

(b) Simulated post-compressed pulses using a Treacy compressor.

Figure 2.31: Simulated post-compressed pulses using a Treacy compressor with custom grating lines/mm.

As the grating lines/mm decreases, better pulse compression is achieved. This is because the ratio of $\frac{\phi_3}{\phi_2}$ in the compressor approaches the $\frac{\phi_3}{\phi_2}$ ratio of the PM2000D leading to optimal phase compensation. At the same time, as the lines/mm decrease, so does the Littrow angle of the gratings and for few lines/mm the incidence on the gratings is almost at 90^o (see Fig.2.31a). For a Treacy compressor with 25 lines/mm the ACT has been shortened by $6\,fs$ compared to the measured value using fibers for pulse compression. The simulated normalized ACT obtained using a grating compressor with different lines/mm are shown in Fig.2.31b. There is almost no improvement when using a Treacy compressor compared to fiber compression. In addition, for the simulation only dispersion has been considered but not diffraction efficiency and as the lines/mm decrease so does the diffraction efficiency of the gratings as it is proportional to the amount of illuminated lines by the beam.

Typically, grating compressors consist of gratings with few hundreds lines/mm making them highly dispersive. They are used to compress pulses from hundreds of ps to fs pulse durations. For such short stretched pulse durations in the few ps regime they are not convenient and prism compressors are commonly used. They are way less dispersive compared to grating based compressors which makes them particularly useful for intracavity dispersion control in bulk laser or to compress stretched pulses in the $\sim ps$ duration. Compression by means of a prism pair has not been simulated however it's equivalent to compress with gratings with very few lines/mm. It has already been shown that the improvement is not that much compared with fiber compression and that there is a limit in terms of how further pulses can be compressed due to the accumulated non-linear phase as can be seen in Fig.2.31a. In addition, since the dispersion of the fiber is changing with the wavelength, the compressor has to be adjusted as the wavelength is tuned which is not the case when using a fiber to compress the pulses.

The advantage of the system is that it can be customized by adjusting the fiber lengths of the PM2000D and PM1950. If longer pulses are required shorter fibers have to be used reducing the NL effects and the spectral broadening. If shorter pulses are desired this can also be done by increasing the length of PM2000D fiber and by increasing the fiber length of PM1950 fiber accordingly to compensate for the extra dispersion. By doing this higher BW is generated in the PM2000D fibers which yields to stronger non-linear pulse compression generating even more BW and in the end shorter pulses. The only drawback of this approach is that as the BW increases the system becomes more sensitive to dispersion and more precise adjustment is required which in the end means that shorter pulses will be achieved within a smaller tunability range or that the pulse duration will change substantially from one wavelength to the other. If the tunability properties of the laser are not going to be exploited, one can try to adjust fiber lengths to obtain the shortest possible duration for a given wavelength which will be below $80\,fs$ in duration according to the simulations and the measured data. Further spectral broadening can also be achieved by optimising the power injection into the NL spectral broadening and compression stage by splicing instead of using mating sleeves or by improved splicing between the PM1950 and PM2000D fibers which are very dissimilar. Higher powers would be then injected increasing the NL effects generating shorter pulses. It is also important to recall that as soon as the accumulated non-linear phase exceeds $\sim \pi\,rad$ the characteristic spectral modulations from SPM will start to develop such as those shown in simulations in Fig.2.30.

The splicing between the $PM1950$ and $PM2000D$ fibers was improved and the mating sleeves were replaced to improve the power injection into the post-compressed stage. This resulted in reduced losses and therefore higher output powers and increased non-linearities. Since the fiber lengths were kept constant, the balance between dispersion and non-linearities is different which modified the pulse durations all along the tunability range and the wavelength at which minimum pulse duration was obtained. The pulses were characterised and the results are summarised in Fig.2.32.

The measured optical spectrum has broadened for all the post-compressed pulses and a dip characteristic of SPM has developed (see Fig.2.32a). The spectrum of the post-compressed pulses generated by the $2055\,nm$ solitons is now $85.2\,nm$ BW which has increased by $13.8\,nm$ due to an increase in output power of $\sim 4.3\,mW$ compared to the previous values (see Fig.2.32b). The measured ACT has significantly reduced for wavelengths between $1910\,nm$ and $2030\,nm$ (see Fig.2.32b). As an example, the measured ACT for the post-compressed pulses at $2050\,nm$ and $1960\,nm$ have been also included (see Fig.2.32c and Fig.2.32d).

The combination of SSFS with NL spectral broadening and compression is an attractive and versatile approach to generate fs pulses within the tunability range of the laser. Thanks to the non-linear compression stage, pulses between $\sim 170\,fs$ down to $\sim 60\,fs$ have been demonstrated just by adjusting the fiber lengths for spectral broadening and non-linear compression. The system allows for optimization over a certain bandwidth or for a particular wavelength. The system is compact, polarization maintaining and is based on exclusively commercially available fused silica fibers and components making this technology easily accessible. It is an appealing alternative to Tm, Tm:Ho and Ho fiber oscillators in the $2\,\mu m$ spectral region due to its tunability, the short pulses delivered and the higher energies in the $\sim nJ$ level obtained. The laser system will be then used in the next sections as seed laser source for a high average power fs CPA laser at $2.05\,\mu m$ and as seed laser for high energy CPA lasers with ps long pulses and $10\,\mu J$ energies compatible with Ho:YLF crystals for further power scaling.

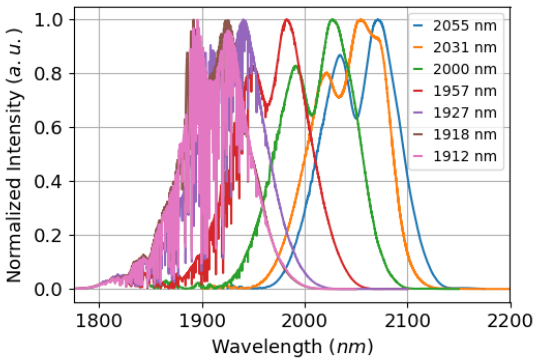

(a) Measured optical spectrum as function of the input soliton wavelength.

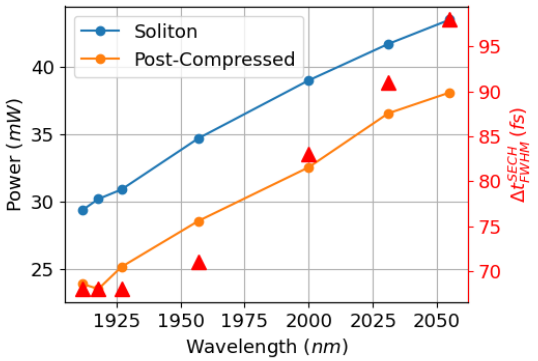

(b) Measured average power and pulse ACT as function of wavelength.

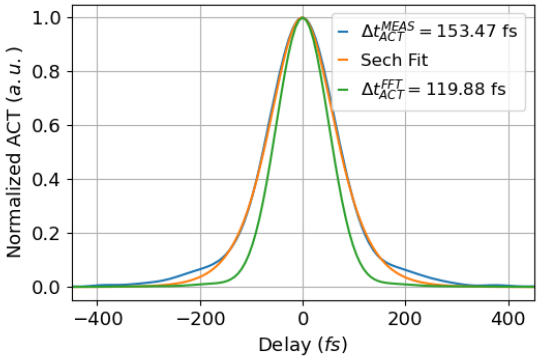

(c) Measured ACT for post-compressed pulses at 2050 nm wavelength.

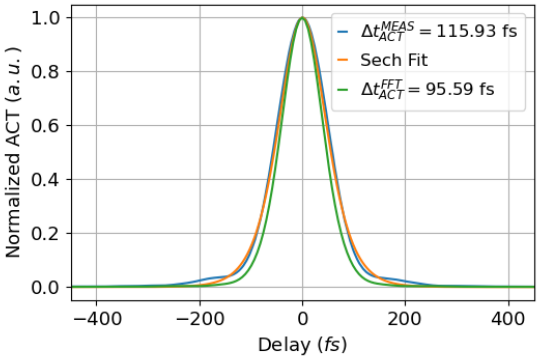

(d) Measured ACT for post-compressed pulses at 1960 nm wavelength.

Figure 2.32: Measured optical spectrum, power and ACT for the post-compressed pulses with improved losses.

Chapter 3

The Chirped Pulse Amplification Technique

The generation of ultrashort pulses from a modelocked laser oscillator, either fibered or bulk, usually produces pulses with not enough energies or intensities for certain applications and pulse amplification is required. At the same time, the amplification of ultrashort pulses rapidly reaches the threshold for NL effects that are undesired or detrimental for the laser such as self-focusing or to such high intensities that can damage the gain medium or optical components in the laser chain. The chirped pulse amplification (CPA) technique was developed to amplify optical pulses circumventing laser induced damage threshold in optical components and NL effects.

At first, one can try to increase the beam size as the peak power of the pulses increases. This means bigger optical fibers, lenses and optical components that need to be scaled accordingly as the amplification process takes place. This has practical limitations in terms of optics size which limits the scalability of the system and the price of the components. Therefore, alternative to reduce the intensity is by stretching the pulses in time and this is the core of the CPA technique.

Given an ultrashort pulse laser, the pulses can be stretched in time using highly dispersive elements such as gratings, chirped Bragg gratings (CBG) or optical fibers. The idea is to add a controlled amount of dispersion stretching the pulses to few hundreds ps up to ns time-scales reducing the peak intensities few orders of magnitude. Once the pulses have been stretched they can be safely amplified up to the desired energy level. Finally, compression takes place using highly dispersive elements compensating the dispersion introduced by the stretcher and amplifiers obtaining ultrashort fs pulses. This is schematically presented in Fig.3.1.

In practice, the CPA technique consists of properly dealing with dispersion and the phase the pulse acquires along the laser chain (the linear and non-linear phase). Given the initial residual phase of the laser oscillator ϕ_o, one has to properly balance the dispersion added by the pulse strecher ϕ_S, the dispersion of the amplification chain ϕ_A and the compressor ϕ_C dispersion so that after compression the net dispersion is as close as possible to zero. The better the dispersion is balanced, the shorter the compressed pulse is. At the same time, as the target pulse duration decreases, more orders in dispersion need to be taken into account ($\phi_2, \phi_3, \phi_4...$). It is then particularly important to design the pulse stretcher and pulse compressor accordingly as their contribution to dispersion (in absolute value) is way more important than the contribution from the oscillator and pulse amplifiers ($\phi_s \sim \phi_C >> \phi_o\,,\, \phi_A$) [137]. The NL effects that will occur along the amplification need to be taken into account as well as they will set the minimum stretched pulse duration

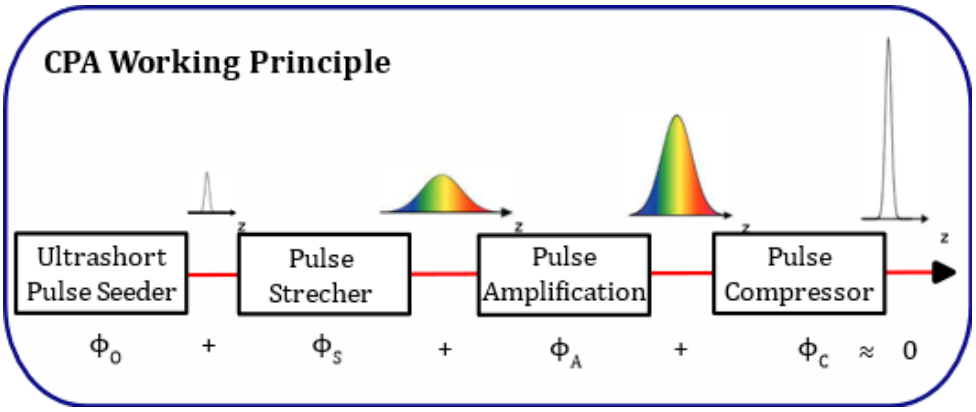

Figure 3.1: Chirped Pulse Amplification (CPA) technique.

which will depend on the target energy or power level of the laser.

This technique has been widely used in large laser facilities where ultra-high intensities are achieved with petawatts peak power levels and also in many commercially available lasers where ultrashort pulses with moderate to low powers are required. The CPA technique has become very popular and relevant such that in 2018, the physics nobel price was given to Gérard Mourou and Donna Strickland for the development of the CPA. In their work they demonstrated the combination of SPM to generate ultrashort pulses with dispersion in optical fibers to achieve pulse stretching. Then the pulses were amplified in Nd:glass amplifiers and re-compressed in a grating-based compressor [53].

In this section of the thesis the aim is to present the design and development of two fiber CPA laser systems at $2.05\,\mu m$ based on Tm:Ho co-doped fibers for either high average power operation with ultrashort fs pulses or for high pulse energy operation with ps pulses.

3.1 High Average Power Tm:Ho CPA Architecture

CPA lasers operating at $2050\,nm$ are of interest for frequency conversion techniques such as parametric amplification which benefits from non-linear crystals with large non-linear coefficients and high damage thresholds. Some of those crystals such as ZGP cannot be used with the well established Yb and Ti:Sapphire technology and laser systems lasing at longer wavelengths are required. As an alternative, Tm and Tm:Ho based lasers have the potential to deliver high powers with high efficiencies thanks to the 2 for 1 cross-relaxation effect which combined with the CPA allows for ultrashort pulses with high average powers. The CPA laser that has been designed is depicted in Fig.3.2.

The system is seeded with the tunable sub-100 fs laser presented in section 2.5 and then pulses are stretched in a highly dispersive stretcher. Several stretching devices have been considered such as fiber Bragg gratings, chirped volume Bragg gratings and optical fibers however, given the limited availability of these components, only optical fibers and chirped volume Bragg gratings have been investigated for pulse stretching. As gain medium in the $2\,\mu m$ spectral region there are only two options which are either Tm or Ho ions. Tm:Ho co-doped fibers were chosen as gain medium as they offer longer emission wavelengths compared to Tm doped fibers and benefit from the Tm pumping schemes involving laser diodes. The drawback however is the weaker availability of PM co-doped Tm:Ho fibers and the core size options. To the best of our knowledge, there is only 6/130 Tm:Ho doped fibers and large mode area (LMA) fibers with either 20/300 or 25/300 sizes. The lack

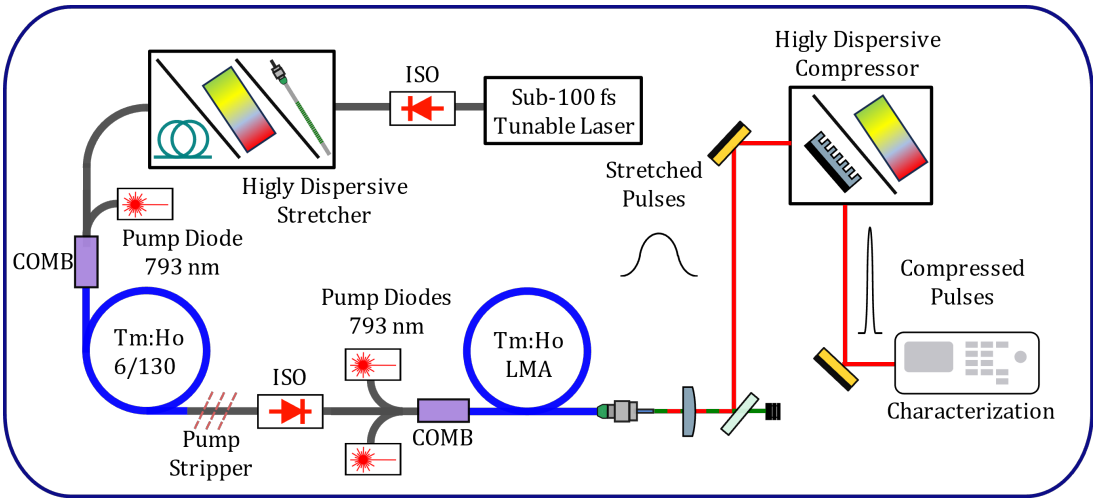

Figure 3.2: Architecture of the high average power CPA laser system.

of intermediate fiber sizes combined with the low efficiencies usually achieved makes gain distribution and power scaling along the system complex therefore, a pre-amplifier and a main LMA fiber amplifier have been included yet alternative options will be discussed along the next sections. Finally, as a highly dispersive compressor two options have been tested, either the use of gratings in the well known Treacy compressor configuration or the use of CVBGs.

In the next subsections the different available highly dispersive systems are presented including their advantages, the drawbacks and how to dimension a stretcher/compressor pair including several practical examples applied to the high average power CPA laser. The high energy CPA laser is presented afterwards followed by the pulse picking technique. The discussion on the gain medium choice and pulse amplification performance is mainly discussed in the last chapter of the thesis.

3.2 Highly Dispersive Optical Systems

Dispersion can be achieved by propagating pulses in a material which has wavelength dependent refractive index such as optical fibers or by propagating each wavelength contained in the pulse through a different optical path. To this end, the fibers, diffraction gratings, prisms and chirped Bragg gratings (CBG) are the most commonly used dispersive elements.

Optical fibers are not a convenient approach when working with short pulses ($> 100\,fs$) because very long lengths are required to stretch up to hundreds of ps. This is because β_2 is fixed and is usually very low compared to other dispersive elements. The ϕ_3/ϕ_2 ratio is quite small compared to the devices used to compress the pulses as they usually rely on dispersion by angular spreading of light that yields to high ϕ_3/ϕ_2 ratios. In addition, as the pulse becomes shorter, higher order terms such as ϕ_4 start to play an important role. The lack of degrees of freedom in the system when stretching using optical fibers makes pulse compression very complex even with custom dispersive optics designed according to the fiber dispersion for pulse compression.

Gratings and prisms rely on diffraction and refraction [138] respectively to angularly disperse the spectral content of the pulses allowing for different optical paths and hence pulse stretching or compression. Gratings are high dispersion components commonly used

to compress or stretch from fs up to hundreds of ps or even more provided that they are geometrically large enough. On the other hand, refraction yields to smaller separation angle between adjacent wavelengths therefore prisms are less dispersive than gratings. They are commonly used in cavities to precisely adjust the net dispersion of modelocked laser oscillators or used for pulse compression from few ps to sub-100 fs duration [139].

Bragg gratings are optical devices which exhibit a periodic refractive index variation that allows for high reflectance of a particular wavelength or BW. If an aperiodic variation is applied instead, a chirped Bragg grating (CBG) is obtained producing large group delays as each wavelength within the BW is being reflected at a different location within the CBG either stretching or compressing the pulses. CBGs are widely used in CPA and have been developed in fibers as chirped fiber Bragg gratings (CFBG) and in bulk photo thermo refractive (PTR) glass as chirped volume Bragg gratings (CVBG).

The mentioned highly dispersive elements are the most widely used in the CPA technique and among them, gratings, fibers and CBG are the ones that have been used in the thesis and the ones that will be presented in the next sections. It is worth mentioning that alternative dispersive elements that rely on different physical phenomena such as spatial light modulators (SLM) [140], dispersive filters that use the acousto-optic effect [141] or chirped mirrors [35], for fine adjustment of GDD can also be used for dispersion control in a wide variety of scenarios.

3.2.1 Chirped Bragg Gratings

The refractive index of fused silica fibers can be modified when exposed to UV light as it exhibits a photo-induced refractive index change known as photosensitivity. The origin of this phenomena is the presence of oxygen deficient bonds Ge-Ge, Si-Si and Ge-Si that can absorb UV light and emit an electron locally modifying the refractive index of the glass. The change in the refractive index is usually low and in order to obtain a substantial refractive index variation, several techniques including Ge doping, B doping, hydrogenation and flame brushing have been developed to enhance photosensitivity. Taking advantage of this phenomena, one can selectively illuminate particular regions along the optical fiber to imprint a permanent periodic grating in the fiber core creating a fiber Bragg grating (FBG) [142].

Given a reflective FBG with a uniform period Λ, reflection takes places for the Bragg wavelength λ_B that satisfies the following equation:

$$\lambda_B = 2n_{AVG}\Lambda \tag{3.1}$$

Where n_{AVG} is the FBG average refractive index. The Bragg condition comes from momentum conservation (phase matching) between the incident wavelength ($k_i = 2\pi n_{AVG}/\lambda$), the reflected wavelength ($k_r = -k_i$) that has the same magnitude but opposite direction, and the FBG periodicity ($K = 2\pi/\Lambda$) such that $k_i + K = k_r$. FBGs can then be used as narrowband reflectors where the reflected wavelength λ_B can be defined by properly selecting the refractive index variation and periodicity of the FBG. Whenever the Bragg condition is satisfied, the corresponding wavelength will be reflected while the rest will be transmitted [95]. The main advantage of FBGs is their versatility as there are plenty of parameters that can be engineered (refractive index variation, periodicity, modulation depth and tilt) along the fiber length. This allows to create uniform FBGs that work either in reflection or transmission, tilted gratings such that the lines are tilted allowing to couple out of the core the refracted light and chirped Bragg gratings (CFBGs) which

offer accurate dispersion control through an aperiodic pitch.

CFBGs are FBGs whose refractive index variation is aperiodic. It changes according the desired dispersion properties. Their working principle can be understood as a superposition of FBGs. Uniform FBGs allow for narrowband reflection hence one can argue that a set of FBGs with different periods Λ placed one after the other will reflect a broadband spectrum and at the same time will add a certain delay between each frequency component due to each wavelength propagating a different distance inside the fiber. In practice what is done is to create a refractive index variation such as:

$$\delta n_{eff} = \delta n_{eff} \left[1 + A(z) cos \left(\frac{2\pi}{\Lambda(z)} z + \phi(z) \right) \right] \tag{3.2}$$

Where $A(z)$ is the modulation depth, $\phi(z)$ is the phase term and $2\pi/\Lambda(z)$ is the frequency term whose value is position dependent [143, 144]. By continuously changing the CFBG period Λ a broad spectrum where each wavelength is reflected at a particular position along the CFBG (see Fig. 3.3) is obtained. This simultaneously introduces a phase delay from one frequency to another. If this period variation is well designed, custom ϕ_2, ϕ_3 and ϕ_4 can be taylored which make these devices the most popular pulse stretching device in CPA laser systems. CFBGs also offer the advantage that their dispersion can be slightly tuned by adjusting the temperature of the device expanding the fiber and changing the period of the CFBG. This allows compensation of phase mismatches along the laser chain adding extra degrees of freedom so that by adjusting the dispersion of the CFBG and compressor, proper pulse compression is achieved. CFBGs have been widely used in CPA as pulse stretcher and not that much in pulse compression configuration due to the high powers of the compressed pulses inside the fiber. To this end, this technology has also been applied to volume Bragg gratings (see Fig.3.3).

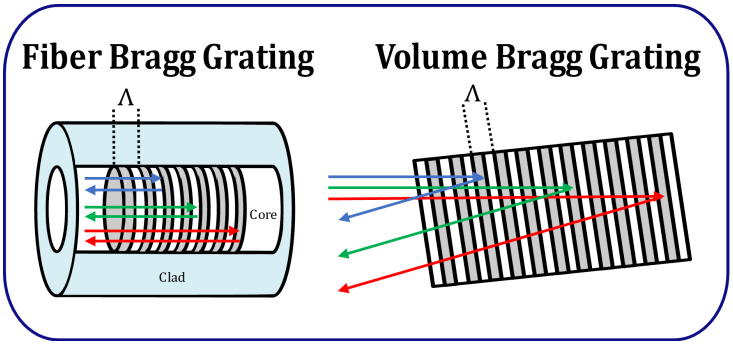

(a) Chirped Fiber Bragg Grating and Chirped Volume Bragg Grating working principle.

Figure 3.3: Chirped Fiber Bragg Grating and Chirped Volume Bragg Grating working principle.

The development of chirped volume Bragg gratings (CVBG) came with the development of PTR which is a photo-thermo-refractive glass that can be manufactured in wide variety of sizes from few mm up to few cm long and wide apertures enabling higher operation powers compared to CFBG. It is a very convenient material particularly in the $2\,\mu m$ spectral region due to low losses as absorption is negligible and scattering losses are below 10% [145, 146]. As with CFBGs, an aperiodic modulation of the refractive index across the PTR glass yields to a stretching or compression device. They can be used either to compress, stretch or both simultaneously provided that stretching is achieved

by propagating light through one side of the CVBG and compression by illumination through the opposite end (same with CFBGs). CVBG and CFBGs are monolitic devices, very robust, insensitive to vibrations and very compact compared to diffraction grating based stretching/compressor devices. The limitations in terms of operation BW and stretching/compression of CVBGs are linked to fabrication challenges yet they can stretch/compress pulses from $\sim 100\,fs$ up to hundreds of ps. The fabrication of large aperture long CVBGs relies on large aperture holographic recording on PTR glass and high uniformity and accuracy is required to achieve precise dispersion which turns out to be complex. Hence an alternative to increase the pulse stretching/compression is to use a two pass configuration by adding a tilt on the CVBG (see Fig.3.3).

In the two pass configuration, the stretching/compression doubles allowing for further pulse stretching and compression. In addition, after the first pass through the CVBG, the beam is elliptical and becomes spatially chirped (see Fig.3.3). This opens new possibilities for pulse shaping through phase masks as the spectral content of the pulse is spread transversely to the propagation direction [147]. The spectral content is put back together after the second pass through the CVBG. The maximum average power and energy of the compressed pulses that the CVBG can sustain is limited by the onset of NL effects and more specifically SPM.

In this thesis, due to the lack CFBG providers with the desired properties in terms of dispersion and BW at $2050\,nm$, CVBGs were chosen as pulse stretchers for high average power and high energy CPA laser systems. For the high average CPA laser, the first CVBG with custom ϕ_3 was produced so that the dispersion could match as close as possible the grating compressor. For the high energy CPA laser that requires stretching to the ns timescale, CVBGs were used for both, stretch and compress the pulses in a two pass configuration.

3.2.2 Diffraction Gratings

A diffraction grating is an optical element which contains a periodic structure that diffracts light depending on the periodicity and the wavelength of the incident light. Given a diffraction grating with G_D the groove density, that is the number of lines per mm, d the grating period ($d = 1/G_D$) and θ_I the incident angle with respect to normal incidence, the diffracted beam θ_D for a given wavelength λ and diffraction order m is:

$$sin\theta_D^m = sin\theta_I + \frac{m\lambda}{d} \tag{3.3}$$

Usually, the diffraction order $m = -1$ is the most commonly used as this configuration yields to maximum diffraction efficiency which takes place for an angle known as Littrow angle (see Fig.3.4a) [148, 149]. At Littrow angle θ_D^L, the incident and diffracted angle are equal ($\theta_I = -\theta_D$) hence:

$$sin\theta_D^L = \frac{\lambda}{2d} \tag{3.4}$$

Whenever an optical pulse (broadband) is sent into a grating, the different spectral components will diffract with a different angle forming a continuum in θ_D. This angle dependence with wavelength is the responsible of dispersion as it produces different optical paths for each wavelength. The dispersion of the grating increases with the number of lines/mm as the diffracted angle increases hence the dispersion of the gratings can be controlled by adjusting the grating period and incident angle. If a second grating, parallel

to the first one, is added at a certain distance G, dispersion stops and a large elliptical beam spatially chirped (spectral content changes across the beam) is obtained. If a second pass through the grating pair is performed, the dispersion introduced is doubled yet a round uniform beam is recovered. This grating pair configuration is known as Treacy compressor [150] and is used to compress pulses in CPA laser architectures. The schematics for the Treacy compressor using transmission gratings is shown in Fig.3.4b.

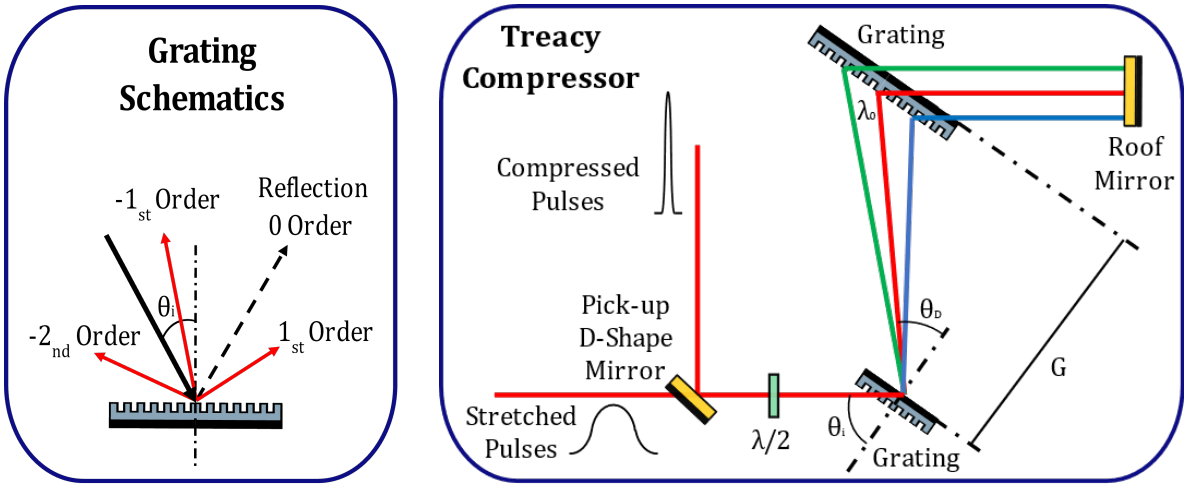

(a) Reflective diffraction grating.

(b) Transmission Treacy Compressor schematics

Figure 3.4: Diffraction grating and Treacy compressor schematics.

As we can see in Fig.3.4b, in a grating based pulse compressor the optical beam goes through the grating pair twice using a roof mirror to slightly shift the height of the beam and a pick-up mirror to extract the pulses. This means that if the diffraction efficiency of the gratings is low, most of the power will be lost during compression. For a 90% diffraction efficiency, after 4 pass through the gratings, only 65% of the input power is recovered. The diffraction efficiency of a grating depends on the pattern used to create the periodicity. The most commonly used or known are the blazed gratings which have a sawtooth profile [151]. Maximization of the diffraction efficiency for a given order mostly consists on minimizing the amount of existing orders m (propagating modes) that verify the grating equation (Eq.3.3) [152, 149]. Hence gratings are usually designed for a particular wavelength and angle of incidence according to the groove density (Littrow angle). As the incident angle moves away from the Littrow angle the diffraction efficiency of the grating decreases. In general, the diffraction efficiency can be calculated by solving the Maxwell equations which depend on the polarization of the beam, the refractive index of the grating and the blazing profile. From a geometrical point of view, it is important to keep the periodicity of the grating constant as any deviation from grating to grating will cause spatial chirp on the beam. This is particularly complex especially as the lasers power increase and the pulse duration shortens (larger BW) which quickly scales the size of the grating due to large stretching factors, broadband pulses and higher fluences. The first grating needs to sustain high power ultrashort pulses after compression and the resulting fluence needs to be reduced by increasing the beam size as gratings are usually the limiting optical component in laser chains in terms of laser induce damage treshdold (LIDT) [153, 154]. At present, available gratings with efficiencies above 95% can be purchased with a wide range of materials (dielectric, metallic and polymer based), working in reflection or transmission with sizes limited to $\sim 1\,m$ long [152, 154].

The Treacy compressor is the most widely used grating based compressor and the dispersion introduced can be calculated according to the following equations [155, 156]:

$$G_c = \frac{G}{cos\theta_D} \tag{3.5}$$

$$\phi_2 = \frac{-G_c\lambda_0^3}{\pi c^2 d^2 cos^2\theta_D} < 0 \tag{3.6}$$

$$\phi_3 = \frac{-3}{w_0}\phi_2(1 + \frac{2\pi c sin\theta_D}{dw_0 cos^2\theta_D}) > 0 \tag{3.7}$$

$$\phi_4 = \frac{3\phi_2}{w_0^2}\left[4 + \frac{16\pi sin\theta_D}{w_0 d cos^2\theta_D} + \left(\frac{2\pi c}{w_0 d}\right)^2 (1 + tan^2\theta_D(6 + 5tan^2\theta_D))\right] < 0 \tag{3.8}$$

$$\frac{\phi 3}{\phi 2} = \frac{-3\lambda_0}{\pi c}\left(1 + \frac{2\lambda_0 sin(\theta_D)}{dcos^2(\theta_D)}\right) < 0 \tag{3.9}$$

$$\frac{\phi_4}{\phi_2} = \frac{3}{w_0^2}\left[4 + \frac{16\pi sin\theta_D}{w_0 d cos^2\theta_D} + \left(\frac{2\pi c}{w_0 d}\right)^2 (1 + tan^2\theta_D(6 + 5tan^2\theta_D))\right] > 0 \tag{3.10}$$

Where G is the distance between gratings, G_c is the distance travelled by the central wavelength λ_0 between the two gratings, θ_I and θ_D are the incident and diffracted angle at the central wavelength, d is the grating period, w_0 is the angular frequency associated to the central wavelength ($w_0 = 2\pi c/\lambda_0$) and c is the speed of light. To illustrate how the different phase orders change with the parameters that can be experimentally adjusted (θ_I and G_C) the phase contribution of a Treacy compressor built with the available transmission diffraction gratings has been calculated. The gratings have 800 lines/mm gratings, a clear apperture of 63 by 25 mm^2 and a diffraction efficiency of $\sim 95\%$ at Littrow angle for $\lambda_0 = 2050\,nm$ which is the central wavelength. This is illustrated in Fig.3.5.

The dispersion introduced by a Treacy compressor always increases (absolute value) with the distance between gratings G_C independently of the dispersion order ϕ_n and regardless of the incident angle as can be seen in Fig.3.5. Increasing the incident angle always results in a reduction of the dispersion (absolute value) regardless of the grating distance G_C and the dispersion order ϕ_n. The ϕ_3/ϕ_2 and ϕ_4/ϕ_2 ratios are always independent of the grating distance G_C and they increase or decrease (absolute value) by reducing or increasing the incident angle respectively. At littrow, $\phi_3/\phi_2 = 16.67\,fs$ and $\phi_4/\phi_2 = 459.7\,fs^2$. These two magnitudes are coupled as ϕ_3 and ϕ_4 depend on ϕ_2 therefore, it is not possible to compensate both of them simultaneously.

When it comes to adjust the pulse compression what is usually done is to set the grating initially at Littrow angle ($\theta_L = 55.08^o$ for this particular case) and then adjust the distance G_C until ϕ_2 of the laser chain is zero which corresponds to the minimum pulse duration. Then, depending on the residual phase of the next high order term ϕ_3, the incident angle is adjusted so that the ratio ϕ_3/ϕ_2 is modified and then G_C is adjusted again. This process is repeated until minimum duration is obtained (see Fig.3.5). If the pulse stretcher is well designed, minimum corrections are required on the incident angle and efficient compression can be achieved. Otherwise, large angle corrections will be required which will lower the overall diffraction efficiency of the compressor as is moved away from the Littrow angle. As it can be deduced by the parameters that can be

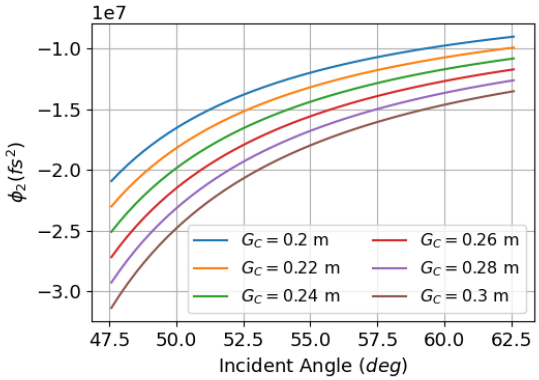

(a) ϕ_2 as function of G_C and incident angle.

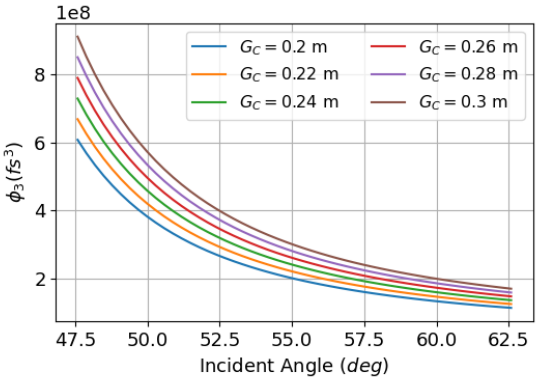

(b) ϕ_3 as function of G_C and incident angle.

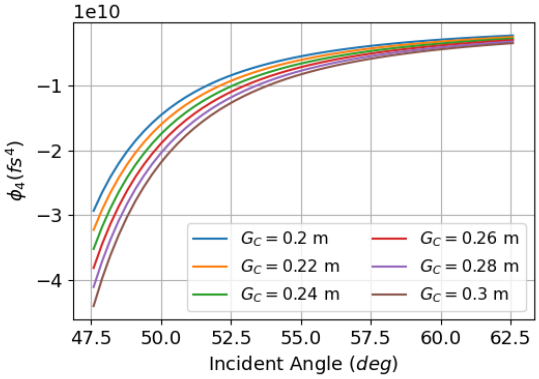

(c) ϕ_4 as function of G_C and incident angle.

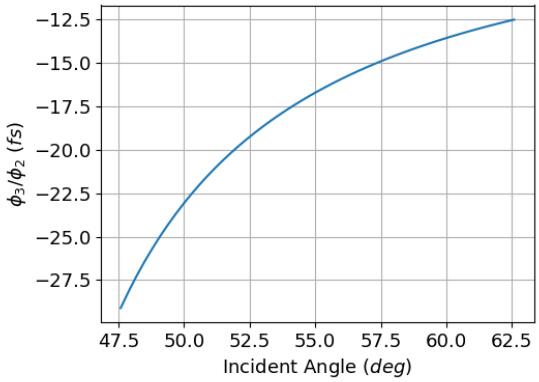

(d) $\frac{\phi_3}{\phi_2}$ as function of incident angle.

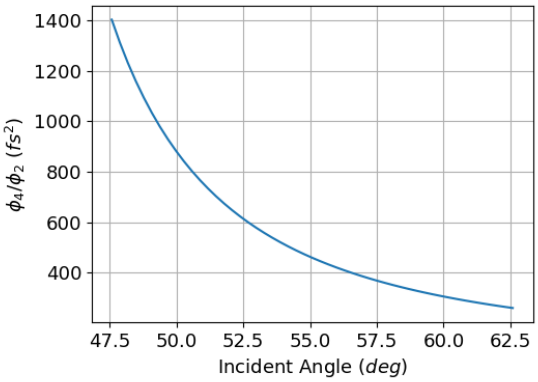

(e) $\frac{\phi_4}{\phi_2}$ as function of incident angle.

Figure 3.5: Treacy compressor phase (ϕ_2,ϕ_3,ϕ_4 and $\frac{\phi_3}{\phi_2}$) as function of the incident angle θ_I and G_C for 800 lines/mm gratings.

modified, it is not possible to adjust ϕ_2, ϕ_3 and ϕ_4 simultaneously so that all orders are zero. If ϕ_4 is also required to be zero, the stretcher needs additional degrees of freedom so that adjusting the pulse stretcher and the compressor accordingly phase compensation up to 4th order or even higher is achieved. As a rule of thumb, high order terms start to become important when $\phi_n \sim (\tau_{TL})^n$ where τ_{TL} is the transform limited pulse duration at FWHM.

Another important factor to take into account when building and designing the stretcher and compressor pair is the BW of operation. In the Treacy compressor, the distance G_C between gratings needs to be adjusted which eventually can yield to spectral clipping of the pulses due to not having a large enough grating pair. This is particularly important for ultrashort pulses as clipping the beam implies losses and can later affect the re-compressed pulse duration and generate side pulses due to having sharp spectral edges. The ACT for for Gaussian pulses ($\lambda = 2050\,nm$, $\Delta\lambda_{FWHM} = 50\,nm$) have been simulated when pulses are clipped due to a filter with BW $\Delta\lambda_f$ which mimics the effect of clipping using diffraction gratings. This is illustrated in Fig.3.6.

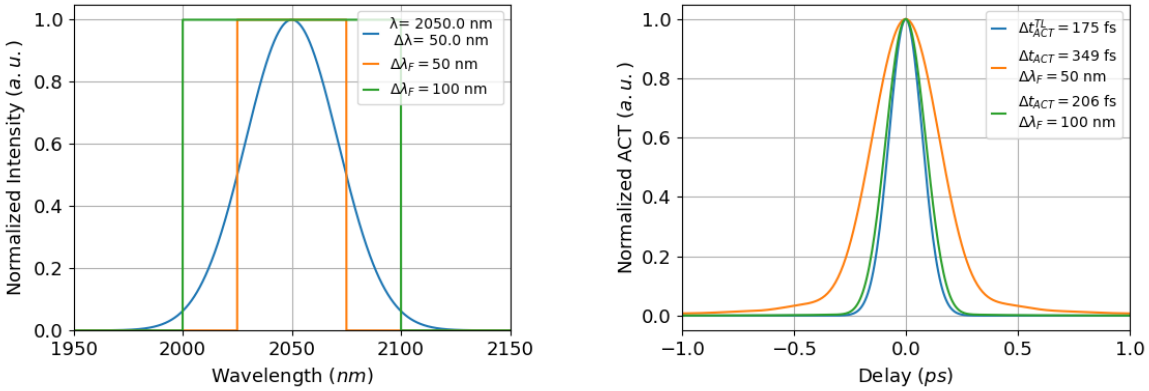

(a) Optical spectrum of the compressed pulses and clipping filters.

(b) ACT of the compressed pulses.

Figure 3.6: Optical spectrum and ACT of the compressed pulses when clipped due to grating size.

The transform limited ACT for the test pulses is $\Delta t_{ACT} = 175\,fs$ assuming perfect dispersion compensation. If clipping of the spectral content takes place at $\Delta\lambda_{FWHM} = 50\,nm$ and $2\Delta\lambda_{FWHM} = 100\,nm$ the resulting ACT broadens to $\Delta t_{ACT} = 349\,fs$ and to $\Delta t_{ACT} = 206\,fs$ respectively. Even with perfect dispersion compensation, clipping the spectral content at $\Delta\lambda_{FWHM}$ broadens the ACT by a factor 2. Therefore, it is important to design the compressor so that at least $2\Delta\lambda_{FWHM}$ can be allocated within the long diffraction grating. The required grating length can be calculated using geometrical ray tracing and the expression is:

$$L = G_C \left(\frac{tg(\theta_{MAX} - \theta_D)}{sin(\pi/2 - \theta_{MAX})} + \frac{tg(\theta_{MIN} - \theta_D)}{sin(\pi/2 - \theta_{MIN})} \right) \tag{3.11}$$

Where θ_{MAX} and θ_{MIN} obey the following equations:

$$sin\theta_{MAX} = \frac{\lambda_{MAX}}{d} - sin\theta_I \tag{3.12}$$

$$sin\theta_{MIN} = \frac{\lambda_{MIN}}{d} - sin\theta_I \tag{3.13}$$

Where λ_{MAX} and λ_{MIN}, according to Fig.3.6, are $\lambda_0 \pm \Delta\lambda_{FWHM}$ to allocate $2\Delta\lambda_{FWHM}$.

Diffraction gratings are of paramount of importance within this thesis and the core of the GREAT project in which grating waveguide structures (GWS) that is, the combination of gratings and waveguides, are designed, build and implemented in laser systems to taylor the temporal, spectral and spatial properties of light. Therefore, gratings will be the main compression element used along the thesis to compress broadband pulses. The objective is to compare the performance of standard diffraction gratings well stablished in CPA architectures with the newly designed and implemented GWS from the project which offer enhanced LIDT and aim for efficiencies as high as 99% for broadband pulses at $2.05\,\mu m$. Hence the stretchers will always be matched or as matched as possible to the grating pairs and GWS to be tested.

Designing a stretcher/compressor pair is complex as there is a compromise between the gratings size, the BW of the pulses to allocate in the gratings, the compressor size as G_C can eventually become big and how much stretching is required to avoid NL effects during amplification. So far the effects that the amplifiers can have on the stretched pulses have been ignored but they can become important through the accumulated NL phase if pulses are not long enough to avoid NL effects while amplification and through an effect known as gain narrowing which reduces the BW of the pulses during amplification shortening them in time. These two effects will be discussed and introduced later on in the thesis.

The dispersion of the grating pair is always negative ($\phi_2 < 0$) in a Treacy compressor which implies that the pulse stretcher must have positive $\phi_2 > 0$. It can be shown that positive ϕ_2 can be achieved with a grating pair provided that an imaging system consisting of two lenses (telescope) is included between the grating pair. This configuration is known as Martinez stretcher [157] and is used to stretch pulses. The Martinez stretcher is a complex configuration which suffers from chromatic aberration (specially in sub-100 fs pulses due to large BWs) as the pulses need to be incident on the lenses off axis to allocate for the 2 pass configuration. An alternative grating based stretcher with reduced chromatic aberrations is the Öffner stretcher which uses convex and concave mirrors instead making it more complex to align [158]. There has been lot of work around pulse stretchers and compressors pairs that allow phase correction up to ϕ_5 [159] or combination of multiple compressor systems, such as a Treacy compressor followed by a prism compressor for fine tuning [160] or even GRISMs which are prisms pairs where a grating has been inscribed in the prism surfaces [137, 155]. In this thesis only the Treacy compressor has been studied.

Finally, it is worth mentioning the impact of material dispersion with particular attention to optical fibers. Fibers chromatic dispersion D_C is the sum of two contributions, the material dispersion D_m and the waveguiding dispersion D_w. The material dispersion contribution in the anomalous dispersion regime for fused silica fibers is such that $\phi_2^{MAT} < 0$ and $\phi_3^{MAT} > 0$ with same signs as the Treacy compressor. Usually, material dispersion contribution is low compared to the stretcher or compressor itself ($\phi_s \sim \phi_C >> \phi_M$) and by slightly adjusting the angle and distance between gratings it can be compensated. If the length of fiber used due to amplifiers and passive fiber components becomes important, its effect needs to be taken into account in the design of the stretcher/compressor pair. In general, material dispersion will always dominate over waveguiding dispersion in standard fibers. The only situation when this is not the case is for high NA fibers

with very tiny cores in which ϕ_2 and ϕ_3 can have any sign depending on the waveguiding dispersion contribution. The stretchers and compressors which are grating based do offer some degrees of freedom and can be adjusted, even the CFBG can be slightly tuned with temperature or stress on the fibers but this is not the case for optical fibers dispersion. The main difficulty is then obtaining accurate dispersion data for all the fibers involved in the fiber CPA laser system.

3.2.3 Pulse Compression with a Fiber Stretcher and Treacy Compressor Pair

The first approach to fully extract the potential of the tunable laser was to use a fiber stretcher and a Treacy compressor. This has the advantage that the stretching device is broadband and can be used to stretch pulses across the whole tunability range of the laser therefore, if dispersion is properly managed, a tunable CPA laser can be in principle achieved where the main limitation will be the amplification BW of the gain medium and the gratings diffraction efficiency as the wavelength is tuned away from the central wavelength. This configuration has some challenges. On one side the gratings need to be adjusted as the wavelength is tuned and on the other side, the PM2000D stretching fiber yields to NL effects as it broadens the spectrum as discussed in the previous chapter. The first approach hence was to verify to what extent the pulses could be compressed after stretching. If the NL phase achieved during pulse stretching and spectral broadening is not significant, ultrashort pulses should be achieved. To perform this test the tunable laser ($40\,MHz$, $43.5\,mW$, $\Delta t_{FWHM} = 170\,fs$, $\lambda_0 = 2050\,nm$) was used as seed laser, the PM2000D fiber as stretcher and a Tm:Ho clad pumped amplifier was included to increase the power up to $0.5\,W$. The residual non-absorbed pump light at $793\,nm$ was removed at the pump stripper. The schematics are presented in Fig.3.7.

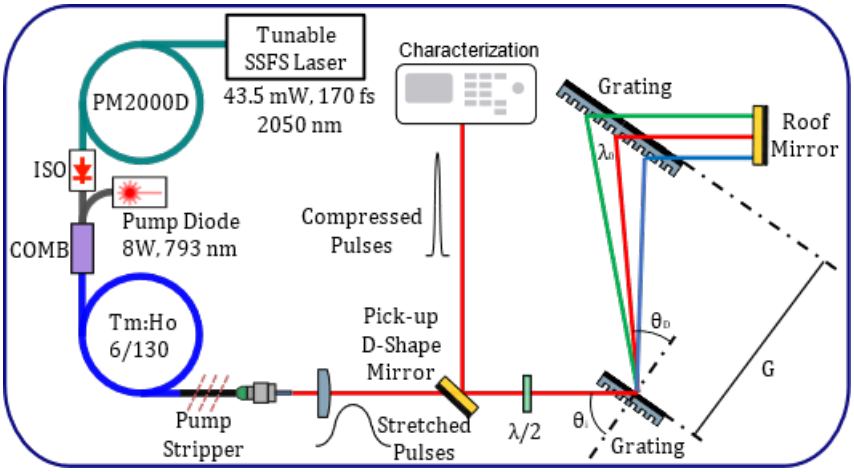

Figure 3.7: Pulse stretching and compression setup for fiber stretcher and grating compressor pair. COMB: signal and pump beam combiner.

The stretched and amplified pulses were characterised in terms of optical spectrum (see Fig.3.8a) and duration. Before amplification, pulses had $\Delta\lambda_{FWHM} \sim 79\,nm$ BW and were $\Delta t_{FWHM} \sim 460\,ps$ long while after amplification the measured BW and pulse duration was $\Delta\lambda_{FWHM} \sim 56\,nm$ BW and $\sim 300\,ps$ respectively. As amplification occurs, gain narrowing takes place in the Tm:Ho amplifier and the BW of the pulses is reduced shortening the stretched pulse duration in time. Whenever a pulse stretcher is designed,

gain narrowing needs to be taken into account as the required stretched duration needs to be increased so that after gain narrowing, the desired stretched pulse duration is obtained. This is sometimes hard to predict and techniques such as spectral beam shaping [161, 72] in grating based stretchers [58, 85] or the use of CBG with sharp spectral edges can help to prevent gain narrowing in amplifiers. The main dispersive term that yields to pulse stretching is ϕ_2 which is a linear chirp therefore, pulse duration will shorten due to gain narrowing approximately by the same ratio as the BW decreases. The stretched pulses went from $\Delta t_{FWHM} \sim 460\,ps$ to $\Delta t_{FWHM} \sim 300\,ps$ which is ~ 1.5 times shorter after amplification and the BW has reduced almost by the same factor, from $79.33\,nm$ to $56.51\,nm$, which is ~ 1.4 times less BW. The slight differences comes from the fact that pulse stretching is taking place simultaneously with non-linearities (SPM) in the fiber increasing stretching as the new frequency components are being generated.

The grating compressor was aligned with the help of thermal cards due to lack of an existing viewing device in the $2\,\mu m$ spectral region and a camera (WinCamD-IR-BB) was used to observe the beam ellipticity after compression as it indicates miss-alignment grating to grating and roof mirror to grating pair [162, 163]. If the compressor is well set, the optical spectrum and pulse duration should be constant (no spatial chirp) across the beam. This was verified using the Mozza which is a free space slit based spectrometer which allows us to scan the beam across the slit.

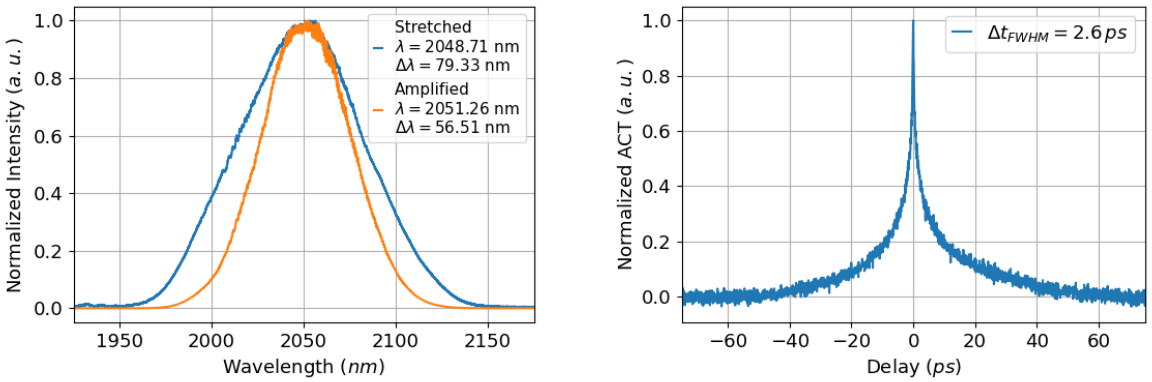

(a) Measured optical spectrum of the stretched and amplified pulses at $0.5\,W$.

(b) Measured ACT of the amplified pulses after compression.

Figure 3.8: Pulse duration and optical spectrum of the fiber stretched pulses after compression.

The compressed pulses are shown in Fig.3.8b and they exhibit the characteristic ACT shape of pulses with large amounts of residual ϕ_3. The Treacy compressor was aligned at Littrow angle ($\sim 55.08^o$ for 800 lines/mm gratings) and showed a diffraction efficiency of 89% after the 2 pass through the grating pair. Before trying to adjust the incident angle on the gratings to improve compression by adjusting ϕ_3/ϕ_2 ratio, calculations on the observed ϕ_3 and the required rotation angle for proper dispersion compensation were performed. Given the measured pulse duration of $\Delta t_{FWHM} \sim 300\,ps$, $56\,nm$ BW at FWHM and assuming that ϕ_2 is the only responsible of pulse stretching, the grating distance should be $G_C = 20\,cm$ at Littrow angle. The resulting ACT taking into account the highe order dispersion terms (ϕ_3 and ϕ_4) was computed as is shown in Fig. 3.9.

In Fig.3.9a the measured ACT and the simulated ACT are depicted assuming there is only ϕ_3 left due to the grating compressor. It can be seen that the measured ACT and

the simulated one agree quite well taking into account that perfect ϕ_2 compensation has been assumed for the distance $G_C = 20\,cm$. In practice, G_C can be slightly different as perfect compensation of ϕ_2 with such amount of residual ϕ_3 is complex which can explain the differences in pulse $FWHM$. The agreement between simulations and experiment show that the grating distances have been quite well adjusted to minimize ϕ_2 and that the measured pulse shape is due to the remaining ϕ_3 of the compressor. This means that the ϕ_3 contribution from the fiber stretcher and amplifier is an order of magnitude smaller compared to that of the grating compressor as it was later confirmed in [134] were the dispersion of the PM2000D fiber was characterized. Even though there is still margin to adjust the grating angle, in Fig.3.5 is shown that the ratio ϕ_3/ϕ_2 which at Littrow angle is $-16.67\,fs$ can be reduced/increased, by a factor ~ 1.5 at expenses on the diffraction efficiency. For the PM2000D fiber $\beta_3/\beta_2 = -1.25\,fs$ as shown in the previous chapter (see Table 2.1) which is 1 order of magnitude below with large uncertainty as ϕ_3 could not be measured and was extracted from literature [134]. Due to the large miss-match, optimal pulse compression will never be achieved using the fiber stretcher and the Treacy compressor. A tunable fiber stretcher based on CFBG would be ideal as the dispersion of the CFBG can be adjusted by temperature tuning but unfortunately this was not available. Even in the best scenario where perfect phase compensation up to third order is achieved, the resulting ACT due to the residual ϕ_4 of the grating compressor (see Fig. 3.9b) gives 416 fs pulses at FWHM ($\Delta t_{ACT} = 692\,fs$), which is still 5 times longer than the expected TL duration. The gratings used are highly dispersive which gives rise to large high order phase terms which forces phase compensation up to ϕ_4. Reducing the lines/mm of the gratings will help to reduce higher order terms (ϕ_3 and ϕ_4) on expenses of using bigger gratings and larger compressors as the distance between gratings needs to be adjusted to make up for the reduced dispersion of the grating pair.

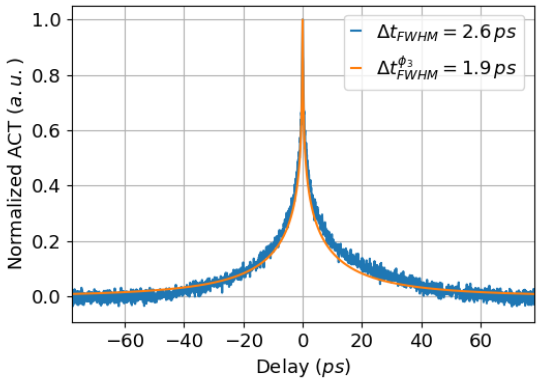

(a) Measured ACT and simulated ACT with phase compensation up to ϕ_2.

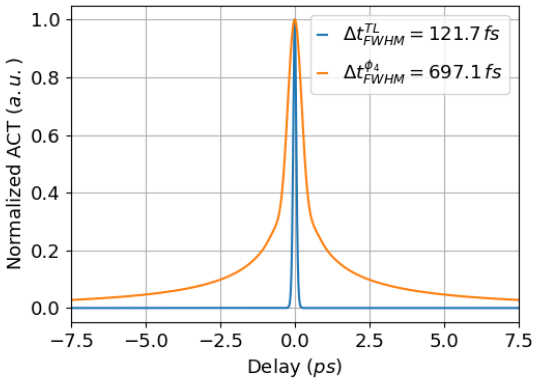

(b) Simulated TL ACT ($\phi(w) = 0$) and ACT with phase compensation up to ϕ_3.

Figure 3.9: Simulated ACT using a Treacy compressor with phase compensation up to third order ($\phi_3 = 0$)

According to the results obtained in terms of pulse compression the stretcher needs to be replaced. To properly design the new stretching device, the phase miss-match ϕ_3/ϕ_2 and potentially ϕ_4/ϕ_2 ratio between the stretcher and compressor has been taken into account together with the gain narrowing effect which results in pulse shortening and the accumulated NL phase. The NL phase plays a crucial role in CPA which can drastically worsen pulse compression as it cannot be properly compensated. The total NL phase

shift accumulated over an optical element with thickness L (length for optical fibers) is calculated with the B integral (β_{IN}) as:

$$\beta_{IN} = \frac{2\pi}{\lambda} \int_0^L n_2 I(z)\, dz \tag{3.14}$$

Where n_2 is the non-linear refractive index, λ is the wavelength of the pulses and $I(z)$ is the intensity. This expression can be applied to any optical medium even those who exhibit gain such as optical amplifiers as the amplification across the gain medium will be reflected in $I(z)$. For pulsed laser systems in active fibers a distributed gain along the fiber can be assumed as first approach. This means that the population inversion is constant along the fiber and that there is no gain depletion. The approach allows for a simplified equation that can be applied to estimate the total NL phase shift:

$$\beta_{IN} \approx \frac{8 n_2 P_0 (G-1)}{a^2 \tau v \lambda log(G/L)} \tag{3.15}$$

Where P_0 is input power, G is the linear gain, λ is the wavelength of the pulses, τ is the pulse duration at FWHM and v is the repetition rate of the laser. The total accumulated NL phase shift is commonly used in bulk laser systems such as regenerative amplifiers to evaluate if there is risk of self-focusing which can damage the optical components. It is always encouraged to maintain β_{IN} as small as possible or at least below $\pi\, rad$ for optimal pulse compression [164].

Both effects, gain narrowing and the NL phase shift are relatively easy to adjust provided that the whole system has been build and characterised which implies at least an iteration on the design of the stretcher/compressor pair to compensate both effects however, an initial estimation can show whether these effects will become important or not. To evaluate the NL phase shift the output power out of each amplifier in the system and the length of active and passive fiber lengths have to be estimated. As first approach, calculation of the NL phase accumulated exclusively due to the optical amplifiers was performed. This sets a minimum pulse duration constrained by the NL phase shift, the grating size and the gain narrowing effect which takes place in both, pre-amplifier (6/130 Tm:Ho co-doped fiber with $7.37\,\mu m\, MFD$) and large mode area (LMA) fiber amplifier. A quick investigation on the 25/300 Tm:Ho co-doped LMA fiber ($21.6\,\mu m\, MFD$) showed further gain narrowing down to $\Delta\lambda_{FWHM} \sim 41\, nm$. Given the grating size ($63\, mm$ by $23\, mm$ clear aperture) required to allocate $41\, nm$ BW pulses, pulse compression of up to $330\, ps$ long pulses while allocating $2\Delta\lambda$ within the grating size can be achieved. Considering that gain narrowing reduces by a factor 2 the input BW (from $\sim 80\, nm$ to $56\, nm$ and then to $41\, nm$), stretching up to $660\, ps$ long is required. Once the pulse duration is known, the accumulated NL phase shift can be computed. With such long pulses the total accumulated NL phase shift calculated with the distributed approach gives for the pre-amplifier $0.356\, rad$ when amplifying $430\, ps$ pulses from $20\, mW$ up to $5\, W$ level, at $2050\, nm$ and $40\, MHz$ repetition rate in $3.5\, m$ of active fiber. In practice, it will be slightly lower ($0.235\, rad$) as amplification up to $\sim 3\, W$ may be enough to seed the LMA amplifier. For the LMA amplifier, $3\, m$ of active fiber with $330\, ps$ pulses and identical repetition rate and wavelength yields to $0.796\, rad$ for amplification from $3\, W$ up to $45\, W$ level. Considering that the available pump power is $100\, W$, $45\, W$ output power is a quite optimistic estimation as efficiencies of the order of $\sim 45\%$ would be required which for Tm:Ho fibers is very high. Therefore the NL phase shift and output power will be smaller. Overall, the accumulated NL phase shift is below $< 1\, rad$ without taking into account

the contribution from the passive fiber components. Stretching up to $660\,ps$ to achieve up to $45\,W$ output power would allow for proper pulse compression after amplification. Nevertheless, it is always better to keep passive fibers short to minimize their contribution to the NL phase.

There exist several mitigation strategies to reduce the NL phase or the gain narrowing effect. Some of them are linked to a redistribution of the gain in the amplifiers, to the use of circular polarization instead of linear polarization [165] but one can always rely on further pulse stretching and replacing the gratings by bigger ones. Gain narrowing can also be prevented or its effects reduced by the use of spectral shaping which can simultaneously compensate the NL phase as well as achieving optimal pulse compression with a higher accumulated NL phase [72, 166]. There have been demonstrations of high quality pulse compression with a NL phase of $\sim 3\,rad$ for high average power CPA laser systems reaching the kW average power level around $2\,\mu m$ [167]. It should be noted that the residual NL phase is effectively an uncompensated phase which will have a more important effect on broadband ultrashort pulses compared to narrowband pulses.

3.2.4 Pulse Compression with a CVBG stretcher and Treacy Compressor Pair

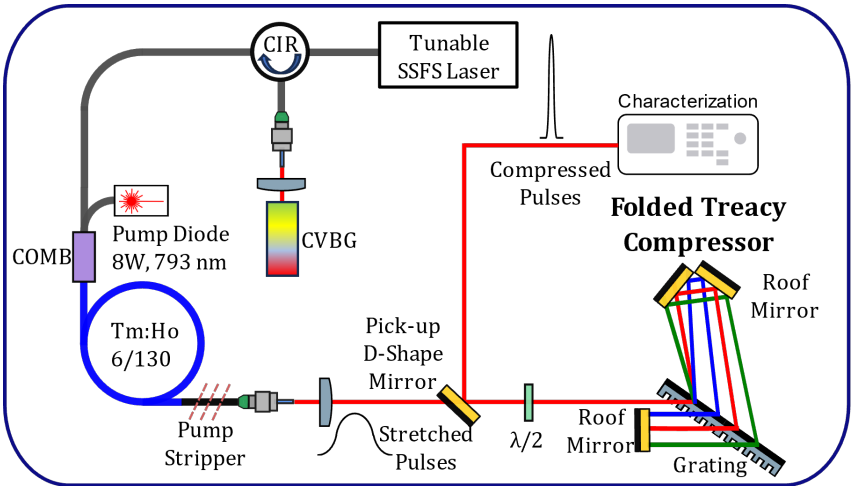

Figure 3.10: Pulse stretching and compression setup for CVBG stretcher and grating compressor pair.

To improve pulse compression the stretching device was replaced by a CVBG due to the lack of a provider capable of producing the matched CFBG to our grating pair. A pair of CVBG from Optigrate were produced for the first time with a custom amount of ϕ_3 trying to match the grating compressor pair. They are centered at $2050\,nm$ wavelength, had a BW of $\sim 62\,nm$, a reflectivity of $\sim 90\,\%$ and stretching factor of $\sim 8\,ps/nm$ and $\phi_3 \sim 0.22\,ps^3$ and $0.23\,ps^3$. They are $5\,cm$ long and had an aperture of 5 by $5\,mm$. In order to make pulse compression easier and less sensitive to uncompensated phase, the SSFS laser which delivers $170\,fs$ pulses and has a narrower BW was used instead. This is important as the different dispersion orders ϕ_n start to become important when $\phi_n \sim \tau_{TL}^n$ hence narrower BW leads to longer pulses and therefore less sensitive to uncompensated phase. This is specially important for higher order dispersion terms decreasing their impact on pulse compression. Since the alignment of the grating pair was complex as it is hard to identify whether miss-alignments come from grating to grating or from grating

pair to roof mirror as both appear as an elliptical beam in the camera after compression, a folded compressor was built. A set of flat mirrors were glued to produce a pair of roof mirrors so that a single grating folded Treacy compressor could be used provided that the beam fits in the grating. Both roof mirrors were aligned using an He-Neon laser before gluing them and pre-aligned in the grating compressor using as well the visible laser. This configuration is illustrated in Fig.3.10 and was chosen because is simpler, more compact and easier to adjust .

A circulator (CIR) was used to get in and out of the CVBG in a free space propagation section and then pulses were amplified in a Tm:Ho amplifier to increase the power to $\sim 0.5\,W$. Due to the losses added by the CIR, the soliton pulses adjusted their pulse duration and spectrum which resulted in narrower bandwidths and slightly longer TL pulses. Out of the CIR the pulses are $\Delta t = 155\,ps$ long with a spectral width of $\Delta\lambda = 17.66\,nm$ as shown in Fig.3.11. Optimization was carried out by adjusting the roof mirror to grating distance and then the incident angle until optimal pulse duration was achieved or substantial loss in the diffraction efficiency was observed (overall compression efficiency below 50%). The measured autocorrelation traces and amplified optical spectrum are shown in Fig.3.12.

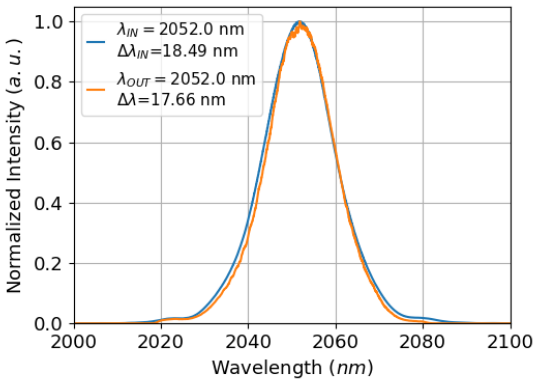

(a) Optical spectrum before and after stretching on CVBG. The small ripples or modulations on the spectrum are due to the non-perfectly flat reflectivity of the CVBG.

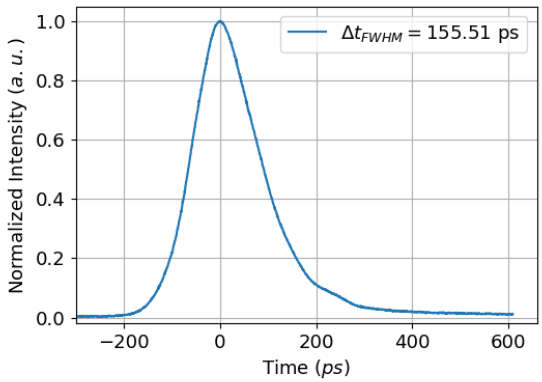

(b) Measured pulse duration after pulse stretching on CVBG.

Figure 3.11: Measured pulse duration and optical spectrum of the stretched pulses using CVBG with custom ϕ_2 andϕ_3.

It can be seen that the measured ACT has a small pedestal spanning from $-10\,ps$ up to $10\,ps$ and that the ACT does not show any substantial variation as the incident angle and the grating distance is adjusted. The measured optical spectrum has developed a set of modulations that may come from the amplification of the small ripples in Fig.3.11 or from a secondary pulse generated in the CIR due parasitic reflections in the components as they were designed to operate at $2000\,nm$ wavelength over a narrow spectral band. According to the calculations, optimal pulse compression in terms of ϕ_2 and ϕ_3 simultaneously is achieved at $\sim 62^o$ provided that the CVBG with the largest amount of ϕ_3 is used. The problem in this configuration is that the angle is quite far away from Littrow and the diffraction efficiency starts to decrease substantially specially taking into account that the grating is designed to have maximum efficiency at $1980\,nm$ and 52.4^o angle of incidence. Due to this, the compressor efficiency beyond 61^o is below $50\,\%$ which is the reason why further optimization of the pulse by increasing the grating angle was not performed.

Even though pulse compression has improved with the use of CVBGs, their dispersion

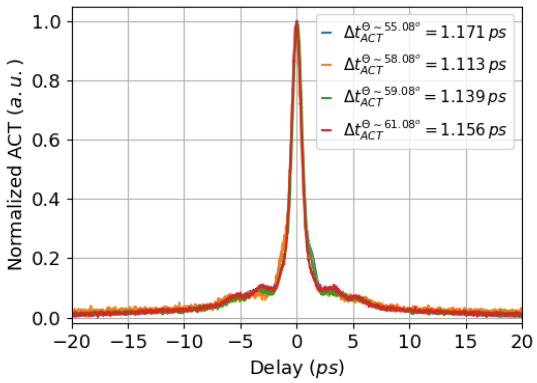

(a) Measured ACT of the compressed pulses for different grating angles.

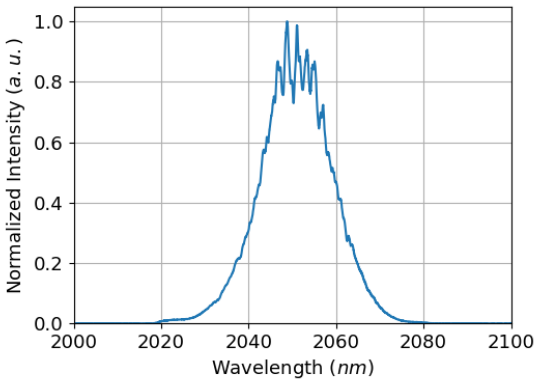

(b) Measured optical spectrum for $0.5\,W$ output power.

Figure 3.12: Measured ACT of the compressed pulses and amplified optical spectrum.

was limited by the fabrication capabilities as it was the first the provider had to monitor and measure ϕ_3 in a quite complicated situation as large spectral BW and stretching was required. A larger amount of ϕ_3 during manufacturing in a accurate way could not be introduced in the design nor measured. For the CVBG with the largest ϕ_3 the ratio $\phi_3/\phi_2 = -12.9\,fs$ calculated with the datasheet information. This means that operation of the grating compressor at $\sim 62^o$ would yield to optimal pulse compression however, based on the measured stretched pulse, the CVBG ϕ_3/ϕ_2 ratio should be $\sim -11.8\,fs$ as the measured stretching factor is $\sim 8.8\,ps/nm$ ($\Delta t = 17.66 * 8.8 = 155\,ps$). In Fig.3.13a we have plotted the ϕ_3 phase difference between the CVBG and the grating compressor as function of the incident angle on the grating. For the particular $\phi_3/\phi_2 \sim 11.8\,fs$ ratio, the grating angle needs to be adjusted even at a more extreme angle of $\sim 65^o$ further reducing the diffraction efficiency. Simulations on pulse compression for TL Gaussian pulses ($\Delta\lambda = 17.6\,nm$, $\lambda = 2050\,nm$) under the same conditions for stretching and compression were carried out and the results are shown in Fig.3.13.

As the incident angle increases the residual ϕ_3 decreases while ϕ_4 increases due to the grating compressor (see Fig.3.13a) improving pulse compression (see Fig.3.13b). For $\theta \sim 65^o$ the TL duration is recovered only limited by ϕ_4 which is already playing a role with relatively narrowband pulses. The main difference observed as the incident angle is adjusted is the improvement in compression at the bottom of the pulse which in the measurements (see Fig.3.12a) is not easy to see due to the pedestal. At the same time, simulations suggest that for the same angles, the measured pulses are a slightly longer than expected which means that further optimization in terms of grating distance could have been done.

Further pulse compression cannot be achieved as the overall Treacy compressor diffraction efficiency is $\sim 50\%$. Pulses as short as $\Delta t_{ACT}^{FWHM} \sim 1.1\,ps$ which corresponds to $777\,fs$ Gaussian pulses have been measured, ~ 2.58 times longer than the TL case of $301\,fs$ assuming Gaussian pulses. The best approach to maintain the use of gratings for pulse compression would be to slightly modify the lines/mm the gratings have by reducing them such that the ϕ_3/ϕ_2 ratio could match the CVBG stretcher dispersion. Alternative, the GWS could be tested in the same configuration hoping for a higher diffraction efficiency at higher incident angles allowing for improved pulse compression with reduced

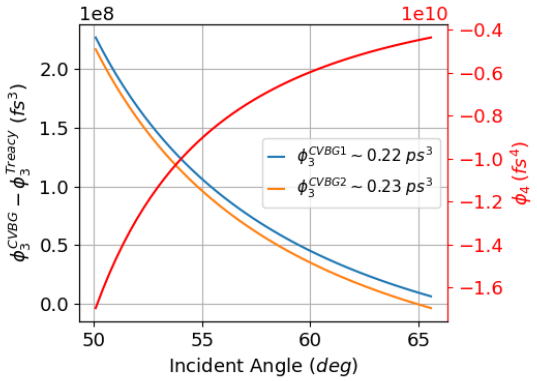

(a) Calculated incident angle for suitable pulse compression and residual ϕ_4 due to the Treacy compressor.

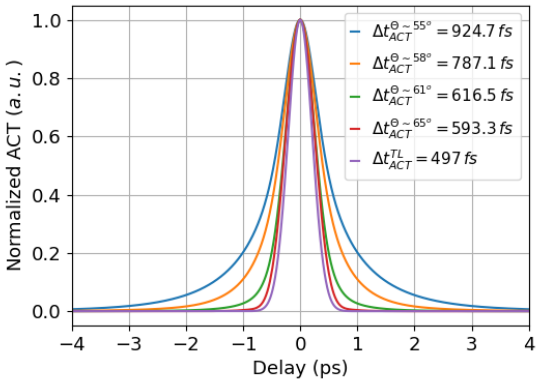

(b) Simulated ACT for different grating angles.

Figure 3.13: Calculated residual ϕ_3 and ϕ_4 for the CVBG and Treacy compressor pair and the resulting simulated ACT.

losses. Otherwise the compressor or stretcher needs to be replaced once again. Since unfortunately GWS for pulse compression at 2.05 μm wavelength were not produced within the GREAT project, pulse stretching and compression was tested with the use of the CVBGs pair.

3.2.5 Pulse Compression with a CVBG stretcher and Compressor Pair.

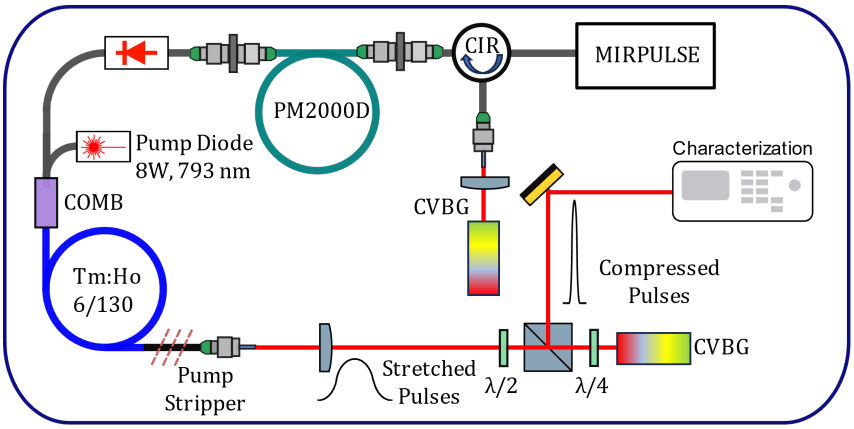

Figure 3.14: Pulse stretching and compression setup for CVBG stretcher and compressor pair.

The approach of using a pair of CVBGs to stretch and compress pulses have been widely used in the past specially when it comes to CPA systems with low repetitions rates, high energies and TL pulses of the order of $\sim 1\,ps$. This is because ps pulses are narrowband which means that they are less sensitive to dispersion and less care needs to be taken into account when it comes to compensate the phase introduced by the subsequent amplification stages, specially for bulk solid state amplifiers [67, 78, 71]. This is very important as in this case there aren't any degrees of freedom to adjust the com-

pressor/stretcher which makes the system more compact, easier to align and thanks to the large apertures of the CVBGs, high energetic pulses with large beams sizes can be used. The setup to test pulse compression using the pair of broadband CVBGs is shown in Fig.3.14.

The SSFS tunable laser was replaced by the MIRPULSE which delivers 120 fs soliton pulses at 2050 nm, $\sim$ 36 nm BW and $\sim$ 48 mW average power. A section of PM2000D fiber was included to compensate the dispersion introduced by the CIR, the isolator, the Tm:Ho fiber amplifier and any dispersion miss-match between the stretching and compressing CVBG. The compressed pulses are extracted out of the system using a combination of a PBS and a quarter waveplate. The optical spectrum and the ACT of the compressed pulses for different output powers out of the Tm:Ho amplifier were measured after optimization of the PM2000D fiber length which was assessed by observation of the pulse duration while cutting back the fiber till a minimum in duration is reached. The results are shown in Fig.3.15.

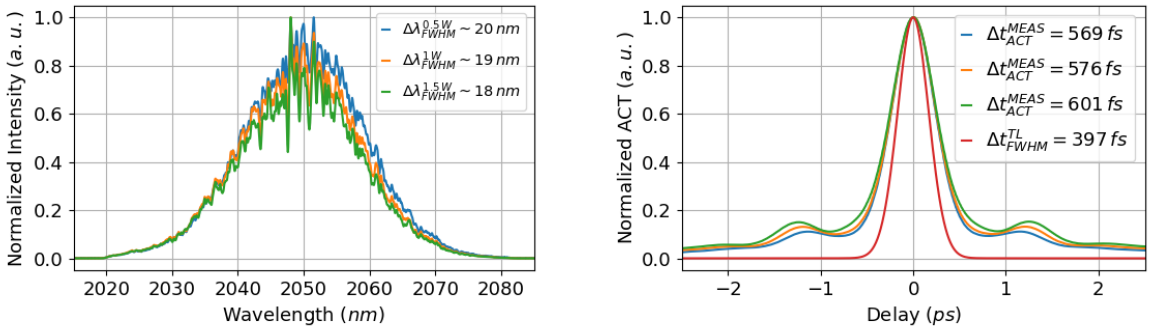

(a) Measured amplified optical spectrum.

(b) Measured ACT for the compressed pulses for different output powers out of the Tm:Ho Amplifier. $P_{OUT} = 0.5\,W$ in blue, $P_{OUT} = 1\,W$ in orange and $P_{OUT} = 1.5\,W$ in green.

Figure 3.15: Measured optical spectrum and ACT for the compressed pulses using a CVBG pair as stretcher and compressor devices.

As the output power increases the modulations on the measured optical spectrum became bigger while in the temporal domain, the increase in the output power shows an increase on the side pulses measured at $\sim \pm 1.2\,ps$ delay slightly increasing the measured Δt^{MEAS}_{ACT} at FWHM. For Gaussian pulses, the deconvoluted pulse durations range from 402 fs at 0.5 W output power up to 425 fs at 1.5 W output power. It must be noted that the optimization of the pulse duration by cut-back of the PM2000D fiber is linked to practical issues because of the fiber core size. The PM2000D fiber (2.1 μm core diameter, 4 μm MFD @2 μm, 0.4 NA and $-55 \pm 10\,ps/nm \cdot km$) has a MFD twice as big as the core size which means that the vast majority of the mode is outside the core of the fiber making it very sensitive to bending and torsion substantially affecting its dispersion. This was not appreciated when used as fiber stretcher as it was kept on the fiber spool however, as the optimization takes place and the fiber is cut and coiled back again, variations in the pulse shape were observed. Different pulse durations and shapes can be measured when bending and more specifically when torsion is applied to the fiber limiting to some extent the minimum pulse duration that can be achieved due to coiling back the fiber. The used CVBGs can have a miss-match in ϕ_2 which has been corrected using the PM2000D fiber but the miss-match in ϕ_3 of 0.01 ps^3 cannot be compensated. Simulations were carried

out to observe the effects in pulse compression for the actual pulses with 23.4 nm BW after the circulator and the expected pulses for which the system was designed (40 nm) as shown in Fig.3.16.

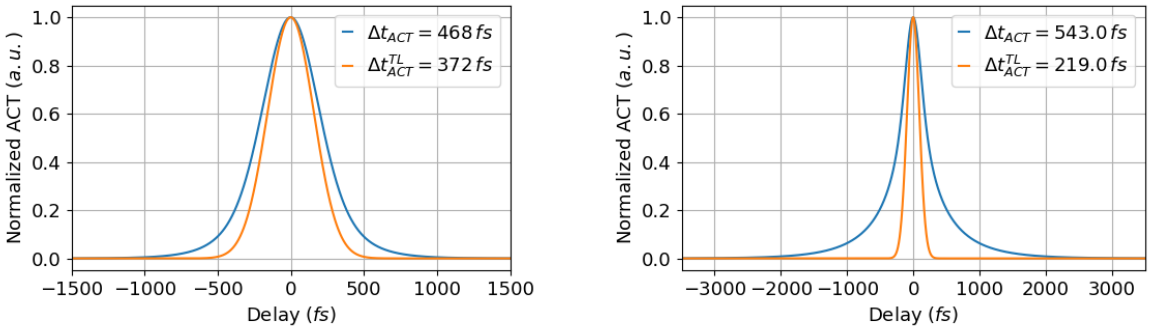

(a) Simulated ACT for compressed Gaussian pulses with $\Delta\lambda = 23.4\,nm$ and residual phase $\phi_3 = 0.01\,ps^3$.

(b) Simulated ACT for compressed Gaussian pulses with $\Delta\lambda = 40\,nm$ and residual phase $\phi_3 = 0.01\,ps^3$.

Figure 3.16: Simulated ACT for Gaussian pulses with $\Delta\lambda = 23.4\,nm$ and $\Delta\lambda = 40\,nm$ with a residual phase of $\phi_3 = 0.01\,ps^3$.

For the 23.4 nm BW pulses, the pulse duration is slightly longer due to ϕ_3 however for the 40 nm BW ones it doubles. The pulse ACT for the 23.4 nm BW Gaussian pulses is about 468 fs due to exclusively ϕ_3 which is very close to the measured ACT duration of 570 fs for slightly narrower pulses ($\sim$ 20 nm) which suggests that optimization of ϕ_2 was quite accurate. The ideal solution would be to use the same CVBG as stretcher and compressor simultaneously however, the aperture is too small to allocate two spatially separated beams as re-injection into the system of the amplified pulses to be compressed must be avoided. The broadband CPA laser system would achieve, in principle, better pulse compression using the 23.4 nm BW pulses however, the stretching factor would not be enough and the pulses would acquire a substantial amount of non-linear phase during amplification which would limit pulse compression in the end. The only option would be to adopt a two pass configuration on the CVBG at the expense of doubling the miss-match introduced by the CVBG pair in terms of ϕ_3 worsening pulse compression as well.

Pulse compression of broadband pulses cannot be further improved with the available stretchers/compressors either because of low diffraction efficiencies when using gratings, due to important miss-match between stretcher and compressor or due to the maturity of the stretching devices at 2 μm when high order dispersion compensation is required. In addition, the spectral modulation phenomena has appeared in all the tested configurations accompanied by small side pulses and a pedestal next to the main pulse in the temporal domain.

The origin of the spectral and temporal pulse degradation is complex and hard to determine. They can come from the main laser which may be generating a main pulse and a small but delayed copy of it that was not observed when characterising the seed lasers. The problem can also be associated to a loss of coherence of the sources (tunable laser and MIRPULSE) during the SSFS process [131, 168] and partially coherent pulses may be not suitable for stretching, amplification and compression. Reflections from the passive components (circulators and isolators) due to being designed at 2 μm, 50 nm away from operating wavelength with broadband pulses can generate a replica of the main pulse. Polarization issues that can come from splicing or from passive components

as they can also generate such behaviour specially with large beat length fibers. If there is a splice with a small angle from one fiber to the other, two pulses can be generated with different group velocities due to propagating in different fiber axis (fast and slow). After propagation along the fiber, they are delayed due to the fiber birefringence and different group veolocities. This also applies to polarizing elements such as circulators and isolators that rely on faraday rotators, waveplates and polarizing beam splitters. Proper polarization rotation takes place for the designed wavelength provided that the used optics are broadband enough and achromatic for the operation bandwidth with the right anti-reflection coating. Splicing can also be the origin, if splicing is not properly done reflections can take place and be amplified later on in the laser chain. The non-mature technology at $2\,\mu m$ can also have an impact for instance on the CVBG stretcher whose use at this wavelength is only used in research. This was investigated later in Chapter 4.

3.3 High Energy Tm:Ho CPA Architecture

High energy lasers in the $2\,\mu m$ spectral region can be used as pump lasers for optical parametric chirped pulse amplification (OPCPA) taking advantage of the long emission wavelength to pump high efficiency NL crystals [88, 87, 56]. In such systems, low repetition rate lasers are employed with very high energy levels that cannot be exclusively achieved with optical fibers and bulk amplifiers based on Ho:YLF or Ho:YAG crystals are employed. The high energy CPA laser designed targets a relatively low repetition rate of $1\,MHz$ and high energy ps long pulses with narrow bandwidths compatible with Ho:YLF amplifiers. It aims to be a robust alternative to systems based on regenerative amplifiers and it will deliver $\sim 10\,\mu J\ ps$ pulses which corresponds to $10\,W$ average power to be further amplified in bulk Ho:YLF multi-pass amplifiers. The architecture of the laser is shown in Fig.3.17.

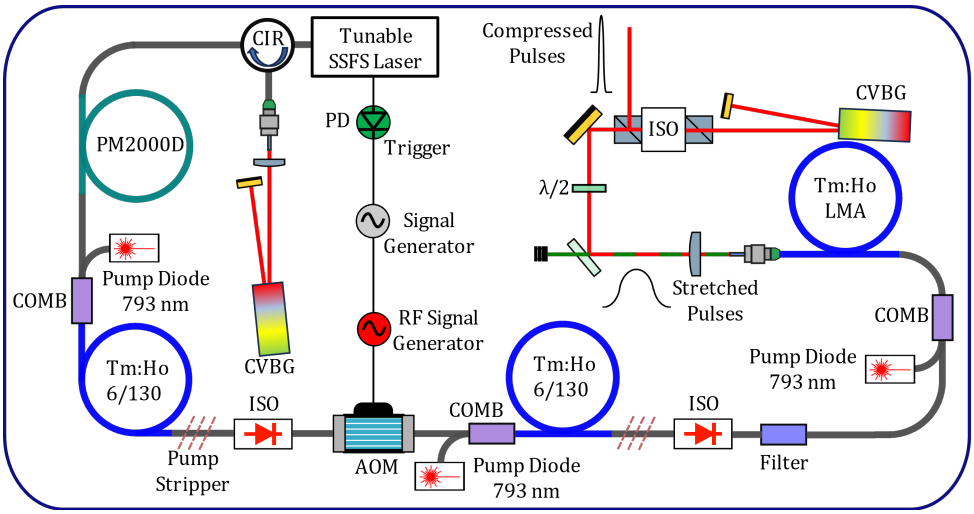

Figure 3.17: Architecture of the high energy CPA laser system.

The system starts with the tunable SSFS laser ($170\,fs$, $43.5\,mW$ average power, $40\,MHz$ and $26.6\,nm$ BW) and then the pulses are stretched in a CVBG. Given the target performance of the system in terms of energy, there aren't many options to achieve enough pulse stretching hence only narrowband CVBGs were investigated. This is because low repetition rate systems, when amplified in optical fibers, can extract substantial amount of energy which yields to high NL phase accumulation therefore very long pulses ($\sim ns$ range) are required. The function of the CVBG is twofold, on one side it will

stretch the pulses in time and on the other it will act as a spectral filter. This is a must for efficient amplification in the crystals as the vast majority of the light has to be contained within the emission bandwidth of the Ho:YLF otherwise it will be absorbed or not amplified. The process of filtering or clipping the optical spectrum is accompanied by losses as an important amount of light is being removed by going from from 26.6 nm BW at 2050 nm down to $\sim$ 6 nm BW imposed by the narrowband CVBG. After pulse stretching a section of PM2000D fiber has been included for fine adjusting of the dispersion along the whole laser chain before the first Tm:Ho clad pumped amplifier. The fiber compensates for any miss-match between CVBGs in dispersion and will make up for the dispersion introduced by the amplifiers and passive optical components. To reduce the repetition rate of the laser, an acousto-optic modulator directly synchronised with the seed laser is used to go from 40 MHz down to 1 MHz by selecting one pulse every 40 pulses within the pulse train. Two Tm:Ho amplifiers separated by an isolator and a filter are used to increase the power to the 10 W level which correspond to 10 μJ pulse energy. Finally, pulse compression takes place in CVBGs and pulses are extracted using a free-space isolator.

3.3.1 Pulse Stretching and Compression of ns Pulses

The narrowband CVBG used for pulse stretching and compression has 6.2 nm BW with sharp edges (no apodization) centered at 2050 nm, 80 ps/nm stretching factor, 95% diffraction efficiency, 10 mm by 8 mm clear aperture and is 5 cm long. When used as spectral filter, the resulting spectrum is pretty much squared as clipping takes place above 90% maximum intensity level (see Fig.3.18a). The advantage of having a flat optical spectrum with sharp edges is that it reduces gain narrowing during amplification but it has an inconvenience in the time domain. The TL pulse corresponds to a sinc pulse shape which consists of a main pulse preceded and followed by a set of small side pulses (see Fig.3.18b). This has also an impact on the ACT which exhibits a small pedestal as can be seen in the same figure. To prevent the sinc pulse shape, a filter was included on the design to shape and apodize the spectrum and filter the ASE just before the LMA amplifier.

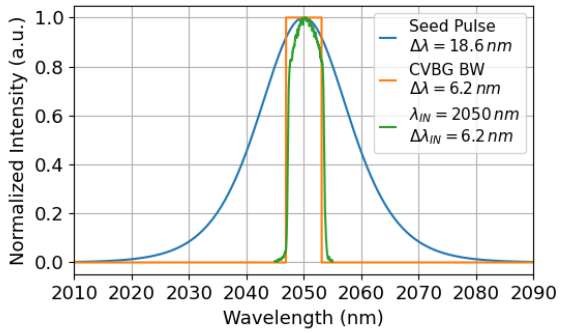

(a) Simulated and measured input pulses spectrum and CVBG bandwidth for spectral clipping.

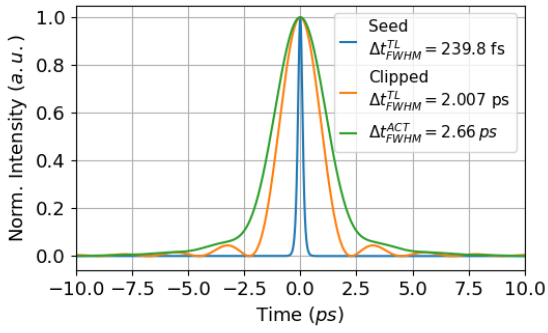

(b) Simulated seed (blue) and spectrally clipped TL pulse duration (orange) and ACT of the clipped pulses (green).

Figure 3.18: Spectrum, ACT and pulse shape of the spectrally clipped pulses used as seed for the narrowband CPA laser.

The high energy CPA architecture has already been presented in Fig.3.17 and the NL phase is estimated as for the high average power CPA laser with the distributed approach

for the β_I (see Eq.3.15). An initial stretched pulse duration of $1\,ns$ pulses were considered given that this was the longest pulse duration achievable by the available CVBGs in a two pass configuration.

The first Tm:Ho amplifier consists of a 6/130 ($7.37\,MFD$) Tm:Ho co-doped fiber and has to amplify up to $\sim 625\,mW$ so that the maximum input power into the AOM of $450\,mW$ is reached just after the isolator. Soliton pulses have a BW of $26.6\,nm$ however, solid state Ho:YLF amplifiers require a BW of $\sim 6\,nm$ and narrowing down the bandwidth would be accompanied by losses of about $\sim 90\%$. They are not only due to spectral narrowing also due to the circulator, the diffraction efficiency of the CVBG in a two pass configuration and the re-injection into the fiber giving about $5\,mW$ of seed power.

The total accumulated NL phase due to the first pre-amplifier was calculated to be $0.022\,rad$ for $1\,ns$ pulses, $40\,MHz$ repetition rate and $3.6\,m$ active fiber length. The first pre-amplifier contribution to the NL phase is negligible even for way shorter pulses due to the high repetition rate with low power. After pulse picking, the expected remaining power is $0.84\,mW$ due to the reduction of the repetition rate (from $40\,MHz$ to $1\,MHz$) and losses of the AOM ($10\,dB$ insertion losses). Pulse picking using an AOM is further described later on in this chapter and for the calculations only the maximum power the device can handle and the insertion losses into the AOM are required. The main problem when designing the high energy CPA comes right after pulse picking and is the power scaling. To increase the power from $0.84\,mW$ up to $10\,W$, $\sim 41\,dB$ of gain has to be allocated (ignoring losses due to passive optical components) within the two available amplifiers. This is quite complicated given the lack of intermediate active fiber sizes, there is only 6/130 and then LMA fibers such as 20/300 or 25/300 and with such low repetition rates a large amount of NL phase is expected. In addition, due to the low power out of the pulse-picking stage, the amplifiers' efficiency will decrease due to low injection, specially in the first one. If amplification is not enough, the same problem may occur on the subsequent LMA fiber amplifier if not seeded with enough power. The fiber length of the pre-amplifier was assumed to be $3.6\,m$, identical to the high repetition rate pre-amplifier given that mW power level is injected. The amplification from $0.81\,mW$ up to $400\,mW$ at $1\,MHz$ repetition rate, $1\,ns$ pulses, in the 6/130 Tm:Ho clad pumped doped fiber gives a total NL phase of $0.45\,rad$. Further pulse amplification can be achieved however the gain is already $26.9\,dB$ which is very high and can be risky to increase it as it increase the chances of Q-switching. For the LMA fiber, the biggest fiber with the largest MFD was chosen minimizing the NL effects. If the 25/300 Tm:Ho LMA ($21.6\,\mu m$ MFD) fiber with a total length of $3\,m$ is used to amplify from $400\,mW$ up to $10\,W$ with $1\,ns$ pulses at $1\,MHz$ the calculated NL phase is $2.02\,rad$. In total the NL phase due to the amplifier fibers is $2.493\,rad$ still below $\pi\,rad$. The gain can be slightly redistributed to obtain $300\,mW$ in the first fiber ($6\,\mu m$) and then increase the power up to the $10\,W$ in the LMA fiber reducing the total NL phase by $0.243\,rad$ to $2.25\,rad$ reducing the NL phase accumulated in both amplifiers. Compared to the high average power CPA laser, the NL phase is substantially higher due to pulses having higher energies. Given the situation the only option to further decrease NL phase is by further stretching of the pulses however, the maximum chirp rate that could be achieved by the manufacturer is $\sim 80\,ps/nm$ which for $6.2\,nm$ BW gives $\sim 496\,ps$ pulses or twice this quantity in double pass configuration reaching the $\sim ns$ pulse duration. This is the limit for single stretching device.

The setup for testing pulse compression is illustrated in Fig.3.19. Compared to the previously used setup using a pair of CVBG, the PBS and quarter waveplate were replaced by a high power narrowband free space isolator used to isolate and extract the pulses after compression. The system has been designed for double pass configuration through the

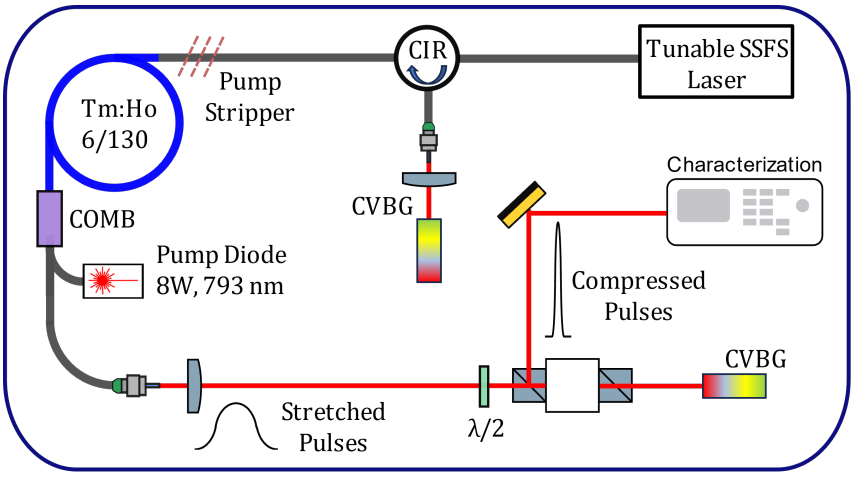

Figure 3.19: Experimental setup used to test pulse compression with narrowband pulses.

stretcher and compressor CVBGs however pulse compression can be validated at first in single pass. One of the things that have been noticed while aligning the system is that the CVBG diffraction efficiency is not uniform across its clear aperture hence scanning of the CVBG surface with the beam was performed to find a proper region with a smooth re-injected optical spectrum as the one shown in blue in Fig.3.20a. As for the amplification of broadband pulses in Tm:Ho fibers, the same modulation phenomena was obtained in the spectrum which develops as the pump power increases (see Fig.3.20a and 3.20b). When pulses are compressed, ACTs with structured pedestals and a main pulse are measured as shown in Fig.3.21a. Proper pulse compression cannot be achieved if the PM2000D fiber is

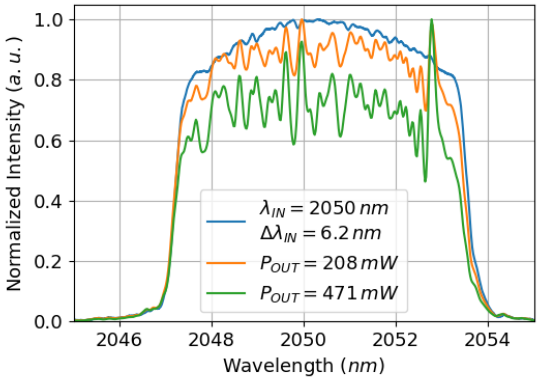

(a) Measured optical spectrum at different output power levels.

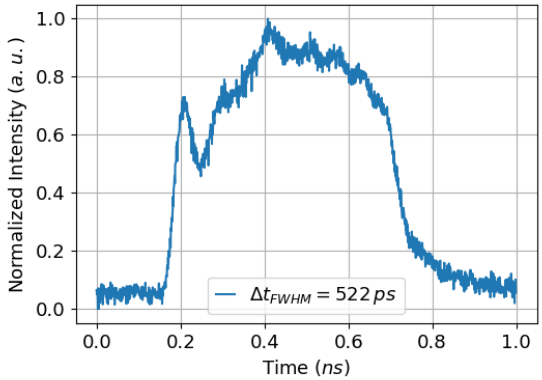

(b) Measured pulse duration of the stretched pulses in single pass configuration.

Figure 3.20: Measured pulse duration and spectrum of the stretched amplified narrowband pulses at 40 MHz

not included to compensate for the dispersion (β_2) introduced by the amplifier, combiners and passive components. For such TL long pulses it is not required to take care of β_3 as pulses are less sensitive to dispersion compared to fs pulses. This can be observed in the measured ACT (Δt_{ACT}^{MEAS}). Even though dispersion due to the fiber amplifier was not compensated, the measured compressed pulse is quite close to the TL pulse duration (Δt_{ACT}^{TL}) and in accordance with the dispersion estimated from the amplifier and passive components. A pedestal spanning up tenths of ps can as well be observed in the measured

ACT. The origin is partially due to the spectrum shape with sharp edges and therefore sinc behaviour as shown in Fig.3.18b. However, the pedestal is spanning several tenths of *ps* which is too long for being exclusively due to the sinc behaviour of the pulse. It can come from large amounts of ϕ_4 from the CVBGs or can be as well related to the modulation observed in the spectrum of the pulses yet the origin is hard to identify.

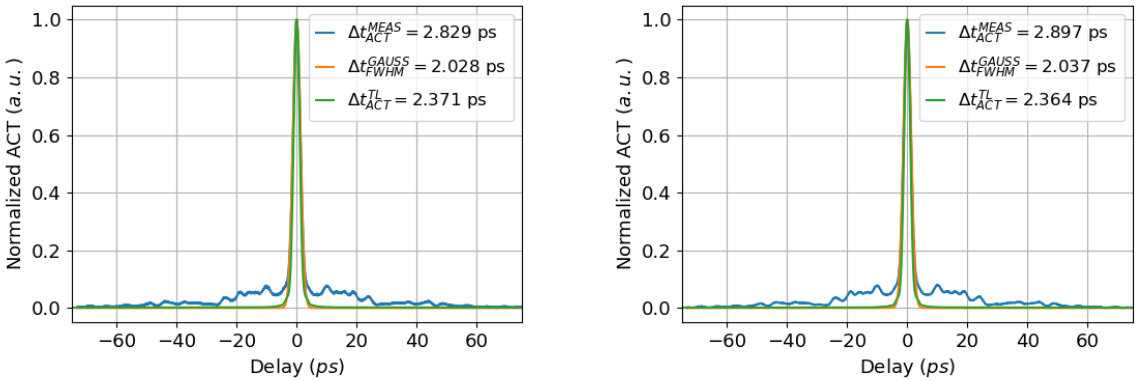

(a) Measured ACT of the compressed pulses after pre-amplification to $P_{OUT} = 208\,mW$.

(b) Measured ACT of the compressed pulses after pre-amplification to $P_{OUT} = 471\,mW$.

Figure 3.21: Measured pulse duration of the compressed amplified narrowband pulses at $40\,MHz$. Δt_{ACT}^{MEAS}: measured ACT at FWHM, Δt_{ACT}^{TL}: TL ACT at FWHM and Δt_{FWHM}^{GAUSS}: pulse FWHM for Gaussian pulse shape.

To achieve highly energetic pulses, the repetition rate of the laser has to be reduced before further amplification by selecting a pulse or pulses within the pulse train. The pulse picking process is accompanied by loses therefore it is better to perform pulse picking before further amplification to minimise the overall losses of the system.

3.3.2 Pulse Picking using an AOM

Pulse picking is the technique of reducing the repetition rate of a laser, that is to pick a certain pulse or pulses within a pulse train while blocking the others. The most common pulse picking devices are electronically controlled optical switches or gates and we distinguish two types, the electro-optical modulators (EOM) usually known as Pockels cells and acousto-optic modulators (AOM). AOMs rely on the acousto-optic effect to generate a refractive index variation in a material by inducing a mechanical strain generated by an acousto-optic wave (radio-frequency wave). The refractive index variation generates a grating across the material that deflects the light (Bragg diffraction) allowing the use of AOMs as optical gates. While the radio-frequency signal is "on", the deflected pulses pass through an aperture and are selected or "picked" and when the RF signal is "off", the pulses are not deflected but blocked (see Fig.3.22). AOMs exhibit a relatively long switching time (rise/fall time) which is the time it takes for the AOM to build the diffraction grating for efficient deflection of the light but they are suitable for fast switching at high repetition rates (MHz to GHz) which is the opposite to EOMs, fast rise/fall times but slow switching. In this work only AOMs have been tested for pulse picking.

There are several considerations when it comes to selecting the suitable AOM for pulse picking such as the repetition rate of the AOM, the rise/fall time, the diffraction efficiency, the losses and the common characteristics associated with optical devices (dispersion,

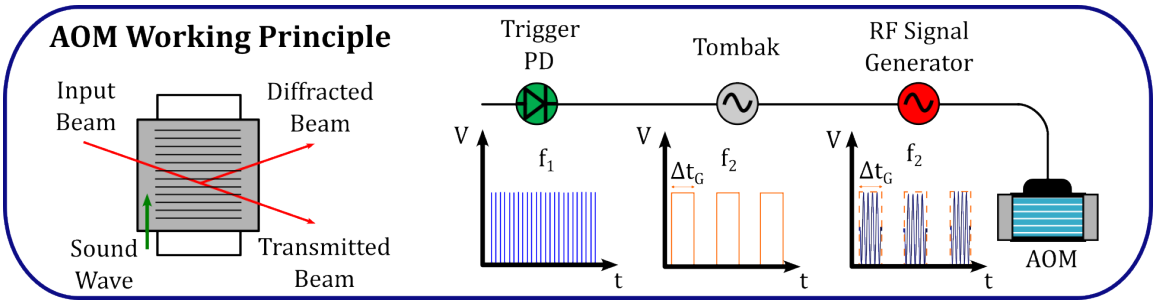

Figure 3.22: AOM working principle and configuration.

LIDT and operating BW). A fiber pigtailed AOM from Brimrose operating at 2050 nm and 500 MHz RF frequency was used. It has an operating BW of $\pm 30\,nm$, a rise time of $5\,ns$, $10\,dB$ insertion losses, can sustain a maximum power of $450\,mW$ and the Bragg angle is $81\,mrad$ which yields to a total deflected angle of $162\,mrad$. The laser and the AOM are synchronised using a photodiode to trigger the pulse delay generator (Tombak electronic card from AeroDiode) which generates an electrical square gate with an adjustable delay, repetition rate, duration and voltage that will enable the RF signal allowing to pulse pick within the train of pulses (see Fig.3.22). The RF signal generated by the matched RF source to the AOM provided by Brimrose was measured for different square gates lengths generated by the Tombak. This is illustrated in Fig.3.23.

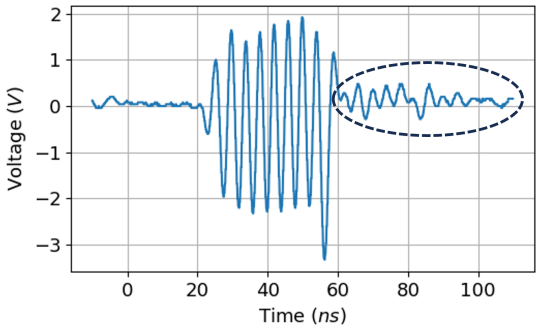

(a) Measured RF signal for a gate $\Delta t = 30.9\,ns$, single acquisition frame.

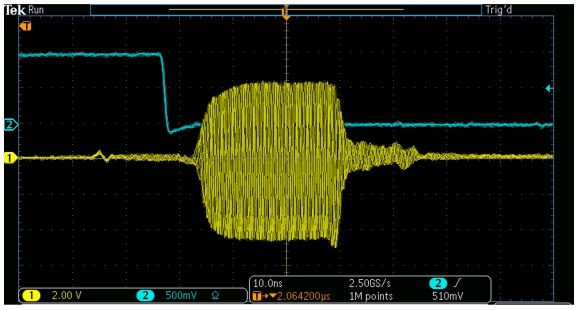

(b) Oscilloscope screen image of the gate (blue) and the RF signal (yellow) for $25\,ns$ long gates.

Figure 3.23: Measured RF signal out of Brimrose RF signal generator for a $30.9\,ns$ gate and oscilloscope screen image of the gate and the delayed RF signal.

No matter the gate length, there was always present a residual signal after the main RF oscillation which extends $\sim 20\,ns$ with a smaller peak to peak voltage. The tiny residual signal limits the suppression of adjacent pulses to the one selected from the pulse train. Without a fast rising and falling time high diffraction efficiency in the AOM cannot be quickly achieved and neither high extinction between adjacent pulses when the RF signal is off. If the repetition rate of the laser is reduced but the extinction is not enough, when amplifying the picked pulses, the adjacent pulses will grow worsening the contrast obtaining a burst of a pair or few pulses with the repetition rate set by the gate switching rate. The laser repetition rate is $\sim 40\,MHz$ and pulses are $\sim 1\,ns$ long. This means that the gate has to be longer than the pulse width otherwise it would temporally clip the pulses and, as rule of thumb, the gate should also be smaller than the period of the laser of $25\,ns$ which automatically eliminates the investigated RF source. This is to

ensure that only one pulse is allocated within the gate to avoid burst operation mode of the laser. At the same time, it is important to center the gate with the pulse to be picked maximizing the diffraction efficiency and the side pulse suppression as shown in Fig.3.24a and 3.24b. In practice, if the gate and the pulse are well centered and synchronised, one can argue that the gate can be almost twice longer however, the resulting transmission window understood as the time the AOM deflects the beam for a given input gate, is the result of the convolution of the time gate generated by the Tombak with the RF signal generator and with the AOM response which always yields to effective longer transmission windows than the initial gate set by the Tombak. That is why the gate has to be shorter than the period of the laser system. The transmission window can be measured with the use of an external continuous wave laser connected to the AOM by measuring the power output with a fast photodiode to obtain the time response of the whole system. Due to the reasons mentioned, the Brimrose RF source was replaced by a custom one that has been characterised in Fig.3.25 allowing for pulse picking from $40\,MHz$ down to $1\,MHz$ with high contrast as shown in Fig.3.24b.

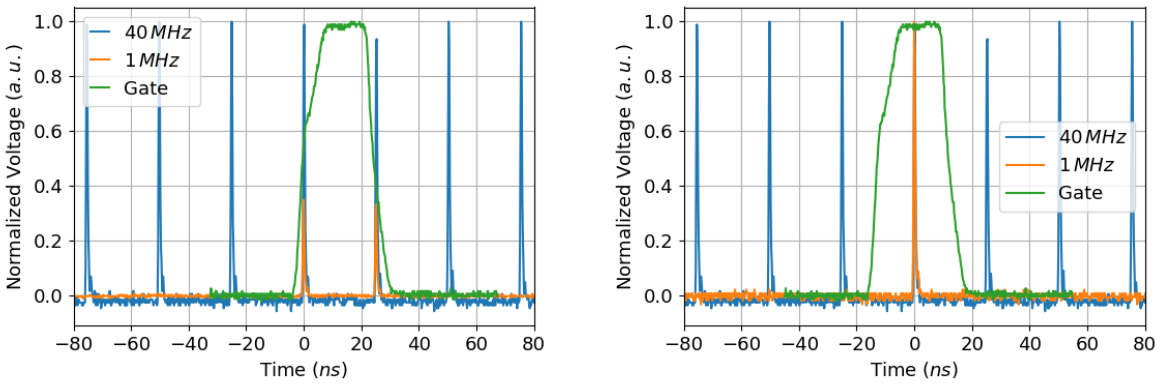

(a) Photodiode signal after pulse picking with gate that is not centered with the picked pulse.

(b) Pulse picked photodiode signal with high adjacent pulse suppression.

Figure 3.24: Measured pulse picked signals with an optimised gate size with and without optimised delay for high adjacent pulse suppression.

In Fig.3.25a the trigger signal from the photodiode, the generated gate by the Tombak and the resulting RF signal have been included. It can be seen that one gate is generated each 40 pulses and that there is always present some delay between the trigger pulse, the gate and the RF signal due to the electronics response. Even though the Tombak does not generate a perfectly squared pulse, the RF signal has fast rise/fall time being suitable for pulse picking with high diffraction efficiency and extinction between adjacent pulses.

The last consideration taken into account was the impact on the power of the laser when reducing the repetition rate from $40\,MHz$ to $1\,MHz$. By selecting 1 pulse out of 40 the average power drops by a factor 40 which added to the insertion losses of $10\,dB$, leads to $1.125\,mW$ output power. The power was further reduced to $\sim 0.84\,mW$ due to the use of PM fiber connectors. This is important as it sets a limit in the amplifier before pulse picking to the maximum power the AOM can sustain and also a maximum in the division factor ($R^{IN}_{RATE}/R^{OUT}_{RATE}$) as it forces to design the amplifier after pulse picking accordingly based on the input power into the amplifier. With $0.84\,mW$ after pulse picking, there is not enough power to saturate the next amplifier which means that it will have low efficiency and will generate ASE. Amplification of the $1\,MHz$, $0.84\,mW$ pulses in $3.6\,m$

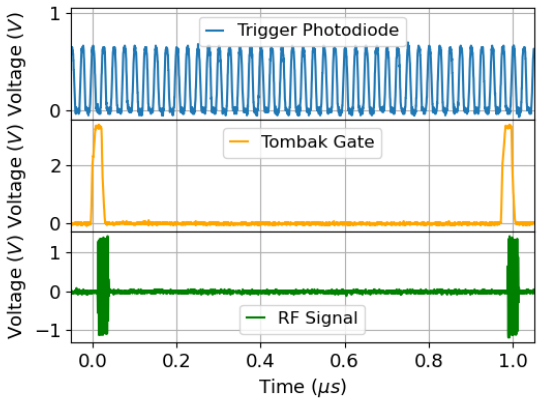

(a) Measured pulse picker trigger signal, generated time gate and RF signal to go from $40\,MHz$ to $1\,MHz$.

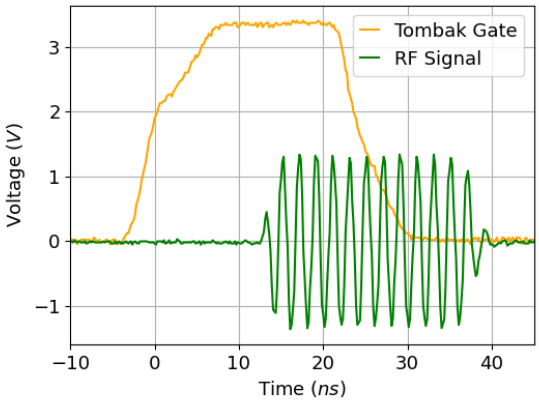

(b) Measured gate and RF signal.

Figure 3.25: Pulse piking trigger signal, time gate and RF signal for $1\,MHz$ repetition rate.

of clad pumped Tm:Ho co-doped active fiber was performed as shown in Fig.3.26a. The results are summarised in Fig.3.26b, 3.27a and 3.27b.

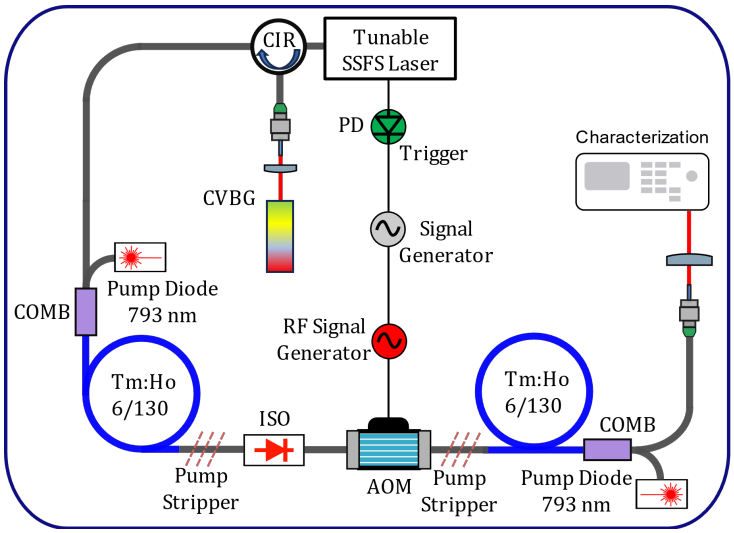

(a) Experimental setup for pre-amplification of the pulse-picked stretched ns pulses.

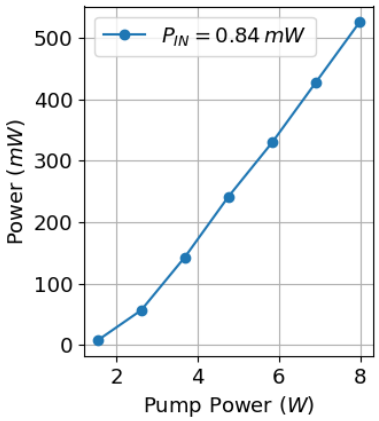

(b) Measured power as function of pump power.

Figure 3.26: Experimental setup for pre-amplification of the pulse-picked stretched ns pulses and output power after amplification at $1\,MHz$

For $0.84\,mW$ input power $7.35\,W$ pump power was required to reach $487.5\,mW$ in the $3.6\,m$ long 6/130 Tm:Ho doped fiber which is beyond the estimated $300\,mW$ that has to be injected into the LMA fiber amplifier. There is margin to further increase the power if required by further pumping in case losses due to the subsequent passive optical components (isolator and Filter) are too high.

Regarding the measured optical spectra in Fig.3.27a and 3.27b, further spectral degradation can be observed forming fast modulations in the measured spectrum together with an increase in the ASE. The growth on the ASE can be seen in the linear scale around

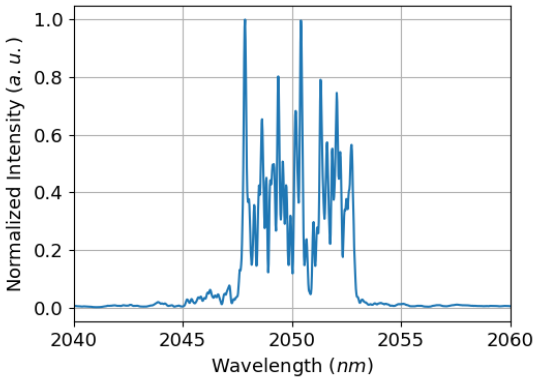

(a) Measured optical spectrum in linear scale for an output power of 487.5 mW.

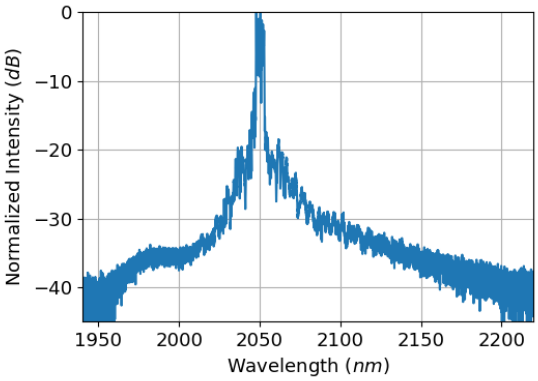

(b) Measured optical spectrum in logarithmic scale for an output power of 487.5 mW.

Figure 3.27: Measured spectrum at 1 MHz after amplification to 487.5 mW in linear and logarithmic scales.

2045 nm and 2055 nm with a relative intensity 20 dB below the main pulse. It is growing at around 1980 nm which comes from the Tm ions and at $\sim$ 2150 nm from the Ho ions. There is not much that can be done to minimize the ASE which grows due to the low injection into the amplifier however it was already anticipated in the design of the CPA by including a filter to remove the ASE and shape (apodize) the spectrum before further amplification.

Given the spectral degradation and the appearance of a pedestal and/or side pulses after pulse compression in both, the high average power and the high energy CPA, it was decided to investigate the Tm:Ho co-doped fiber amplifier in a wider variety of conditions to determine the origin of the observed phenomena before further power scaling. The objective is to isolate each of the involved components (the stretcher, the active fiber, the passive components and the compressor) to find the origin of the spectral and temporal degradation and to understand the amplification process in such complex gain medium that exhibits several cross-relaxation phenomena and energy transfer mechanisms.

Chapter 4

Amplification in the SWIR

The short wavelength infrared (SWIR) extends from $\sim 1400\,nm$ up to $\sim 2500\,nm$ and within the spectral region there are three main active elements that allows amplification of light. Those are Erbium (Er), Thulim (Tm) and Holmium (Ho). Among the three, only Thulium and Holmium are suitable to amplify light within the tunability range of the developed laser. In this chapter Tm and Ho are introduced including their spectroscopic properties when used as dopants in fused silica fibers.

4.1 Thulium Doped Fused Silica Fibers

Thulium is a rare earth element that has an atomic number of $\mathcal{Z} = 69$ and it belongs to the group of lanthanides. In its most common stable state it becomes a trivalent ion (Tm^{3+}) by loosing three electrons and its electronic configuration becomes [Xe] $4f^{12}$. Among all the elements used to amplify light, rare earth elements and more specifically lanthanides such as Er, Yb, Ho, Nd and Tm, are very convenient because in their trivalent state, transitions to the incomplete outermost electronic shell yield to meta-stable states. Whenever an electron is promoted to the metastable energy level, it will decay within hundreds of μs up to ms timescales depending on the glass composition. Such long radiative decay times allows to achieve population inversion and amplify light. The energy levels of trivalent atoms such as Tm, are subject to the interaction with neighbouring ions whenever they are introduced in a glass matrix such as fused silica. Due to the electric field of surrounding ions, the energy levels split producing multiplets (Stark effect) which combined with the vibrational interactions with the host glass, large and continuous absorption and emission bands are obtained (inhomogeneous broadening). This is of particular importance when it comes to ultrashort pulse amplification as tenths of nm are required to sustain fs pulses. The energy levels of Tm^{3+} ions in fused silica are shown in Fig.4.1.

The fundamental energy level or ground state is the $^3H_6$ and in order to excite the electrons and promote them to the excited states and achieve population inversion in Tm doped fibers two different approaches are used. The first one consists in using high power diodes at $\sim 790\,nm$ exciting the electrons to the $^3H_4$ energy level while the second relies on fiber lasers at $\sim 1600\,nm$ such as Er fiber lasers or Yb Raman shifted lasers to promote the electrons to the $^3F_4$ energy level. This pumping scheme is known as S-band pumping or in-band pumping [169, 170] as the pump light wavelength is very close to the emission wavelength of the Tm ions $\sim 1850 - 2050\,nm$. The lasing transition takes place between the $^3F_4$ and $^3H_6$ levels. Is it worth mentioning that Tm doped fibers exhibit a blue color due to the transition from $^1G_4$ to $^3H_6$ that manifest when inefficient depletion of the $^3H_4$

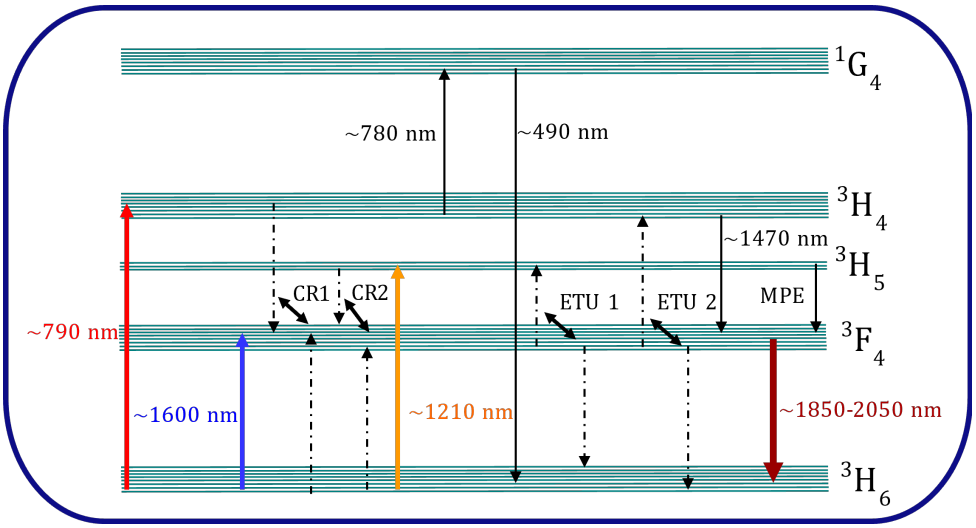

Figure 4.1: Tm energy levels and transitions in fused silica. CR: cross-relaxation, ETU: energy transfer upconversion and MPE: multi-phonon emission.

level. Pump photons can be absorbed promoting electrons from the $^3H_4$ to the $^1G_4$ in a process known as excited state absorption (ESA). A more detailed energy diagram for Tm can be found in [171, 172].

In principle, pumping at $\sim 790\,nm$ would not seem an attractive pumping scheme because of the expected quantum defect. For a laser at $1960\,nm$ wavelength, the quantum limit would be of $\sim 60\%$ limiting the efficiency of the laser or amplifier to the stokes limit of 40% which would be accompanied by a high thermal heat load. However, in Tm doped silica fibers, cross-relaxation processes (CR1 and CR2, see Fig.4.1) can take place allowing to surpass the stokes limit [173].

Cross-relaxation (CR) processes in Tm fibers are of paramount importance because they allow to obtain two excited photons per pump photon. This phenomena occurs between nearby surrounding Tm ions as energy transfers from one (the excited) to another. It turns out that the radiative decay from the $^3H_4$ to the lasing energy level $^3F_4$ can generate a photon which can promote an electron from a surrounding ion from the $^3H_6$ to the $^3F_4$ obtaining the 2 for 1 photon. The CR phenomena allows to surpass the 100% quantum efficiency and the stokes limit reaching efficiencies above 60% with respect to the absorbed pump power [167, 174, 175, 176]. Among the two CR processes depicted in Fig.4.1, the CR1 is the dominant one.

On the other side, there is also the opposite phenomena to cross-relaxation which is known as energy transfer up-conversion (ETU). In this situation, two nearby excited ions can exchange energy so that one of them decays to a lower energetic level while the other is excited to a higher energetic level. There are two energy transfer up-conversions mechanisms, ETU1 and ETU2, and they are depicted in Fig.4.1. ETU becomes more and more important as the Tm ions are closer together forming clusters of ions instead of being randomly spread along the fiber which can decrease the gain and efficiency of the laser. As for the case of CR, ETU1 is the dominant compared to ETU2 [173].

From a chemical point of view, CR and ETU processes are strongly dependent on the fiber composition, that is the Tm ions concentration and the co-dopants that enhance CR while reducing or keeping ETU low. The inclusion of Al ions prevents the clustering effect which limits ETU ensuring an homogeneous distribution of Tm ions along the fiber. There has been work on the proper Tm to Al ratio in silica doped fibers and it turns out to

be approximately 10:1 or bigger. At the same time, if efficient cross-relaxation needs to be achieved, higher doping concentrations of the order of 2% *w.t.* [177] of Tm is required which comes accompanied with a large heat load as the absorption increases reducing the length of the active fibers. This is beneficial for reducing NL effects however it is problematic with doped ions that exhibit such high quantum defect. In fact, high temperature is detrimental as it increases absorption at the signal wavelength and therefore affects the emission cross-section of the gain medium and can limit the NL effects in the system due to mode shrinking and transverse mode instability degrading the beam quality [178, 92]. It is also important to note that due to the three-level system behaviour that Tm exhibits, re-absorption takes place which worsens as the temperature of the fiber increases. Re-absorption in combination with fused silica losses as the wavelength approaches the $2\,\mu m$ due to OH ions limit the efficiencies of Tm doped fibers. This is usually referred as background losses and is an ongoing field of investigation to improve fused silica Tm doped fibers [179].

Provided that the doped fiber has the right composition in terms of Tm concentration and Tm to Al ratio, the cross relaxation effect is maximised when the fiber amplifier and pump diode are cooled down, the medium is strongly pumped and the fiber is seeded with high power. The cross relaxation rate in Tm fibers is [171]:

$$CR = k_{3101} N_0 N_3 - k_{1310} N_1^2 \tag{4.1}$$

Where N_0 is the population of the $^3H_6$, N_1 is the population of the $^3F_4$, N_3 is the population of $^3H_4$ and k_{3101} and k_{1310} are the cross-relaxation energy transfer and energy transfer up-conversion coefficients respectively. According to the equation, high pump intensity and low inversion is desired however this is counter-intuitive for pulsed laser systems which aim for high gain and short fibers lengths which implies less CR, that is why strongly seeding the amplifier will strongly depopulate the energy level $^3F_4$ enhancing the CR in the fiber amplifier or laser. It is then clear that efficient CR is not compatible with reduced non-linearities due to the high input powers in the fibers well beyond the saturation power of the amplifiers.

The Tm absorption and emission cross-sections are depicted in Fig.4.1. As can be seen three absorption peaks located at $\sim 790\,nm$, $1200\,nm$ and $\sim 1650\,nm$ allow for three different pumping schemes at different wavelengths. The absorption cross-section at $\sim 790\,nm$ consist of a narrow peak with a value about 2.5 times higher compared to the broad peak at $\sim 1650\,nm$. This plays an important role on the pump laser diodes which are designed at $793\,nm$ wavelength slightly off peak. It is also well known that as the diode temperature increases, the wavelength shifts towards longer wavelengths hence the absorption in the Tm fiber can substantially drop if the temperature of the diodes is not properly maintained. In an ideal situation, by cooling down the diode the emission wavelength is blue shifted so that the emission spectra of the diode is centered with the absorption peak of Tm ions. The main limitation on the wavelength shift is the operation temperature of the laser diode and the environmental conditions which can produce condensation and fatal damage on the pump diodes. The absorption peak at $\sim 1650\,nm$ is broadband and allows for pumping either using Er lasers or Ramans shifted lasers [170]. Due to pumping with high brightness single-mode lasers, core pumping is a more suitable strategy allowing for very high absorption. The emission cross section is very broad and extends from $1700\,nm$ up to $2050\,nm$ offering a large BW suitable for ultrashort pulse amplification yet in practice Tm fibers are used between $1900\,nm$ and $2000\,nm$. This is because emitting light in the short wavelength region require large population inversions

that are usually achieved with high pumping and short low doped active fibers. On the other hand, emitting beyond 2000 nm is complex due to the required long fibers and low emission cross-section which makes the whole process inefficient. Finally, pumping at 1200 nm can also be implemented. Yet the lack of suitable high power laser sources at this wavelength and the fact that it does not offer any advantage compared to 793 nm as there is no CR or to $\sim$ 1650 nm which exhibits a lower quantum defect, makes it an unpractical approach. In addition, this pumping scheme suffers from ESA depleting the available gain. Maximum efficiencies in Tm doped fibers are usually obtained between $\sim$ 1940 nm and $\sim$ 1980 nm yet it has been demonstrated amplification at shorter wavelengths even below 1800 nm and up to $\sim$ 2050 nm. Longer wavelengths are usually targeted with Ho or Tm:Ho co-doped fibers.

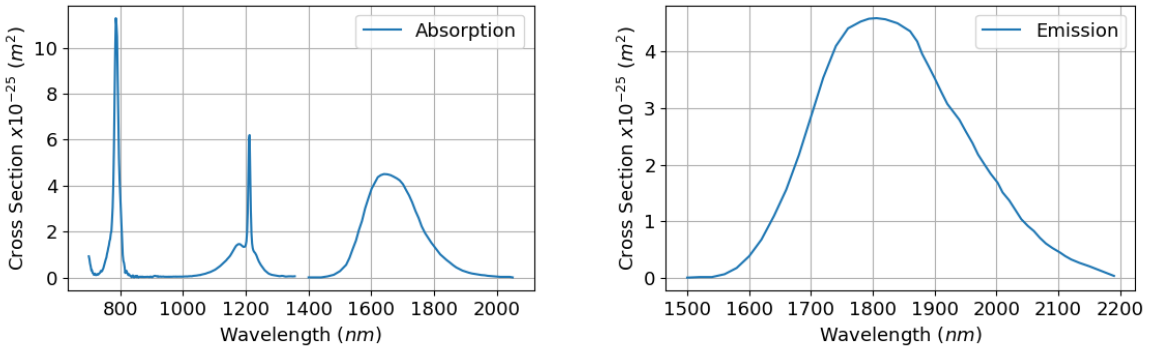

(a) Tm absorption cross section.

(b) Tm emission cross-sections.

Figure 4.2: Tm absorption and emission cross-sections in fused silica fibers.

4.2 Holmium Doped Fused Silica Fibers

Holmium is a rare earth element that has an atomic number $\mathcal{Z} = 67$ and it belongs to the group of lanthanides. In its most common stable state it becomes a trivalent ion (Ho^{3+}) by loosing three electrons and its electronic configuration becomes [Xe] $4f^{10}$. A simplified energy level diagram for Ho^{3+} ions which behave as a three-level system is shown in Fig.4.3a.

The ground energy level is the $^5I_8$ and lasing takes place from the excited state $^5I_7$ to the ground state. Compared to Tm ions, Ho exhibits an emission bandwidth shifted towards longer wavelengths and is usually used as gain medium for lasers emitting from 2000 nm up to 2200 nm wavelength (see Fig.4.3b). As for Tm, Ho also offers a large emission BW suitable for ultrashort pulse amplification. The main pumping mechanism of Ho doped fibers is through Tm lasers emitting at $\sim$ 1950 nm wavelength yet atoms can be excited to the $^5I_6$ energy level by pumping at 1150 nm. As for the case with Tm ions, there is no efficient pump sources at this wavelength and neither efficient commercially available pump diodes at $\sim$ 1950 nm hence Tm doped fiber lasers which provide high power single mode beams are used. A detailed energy level diagram for Ho in fused silica fibers can be found in [180]. If clad pumping is desired, the geometry of the fiber has to be modified as a fused silica clad is not an option because the polymer coating that surrounds the fused silica cladding strongly absorbs light in the 2 μm region heating up the fiber and quickly damaging it. That is why Ho doped fibers incorporate a fluoride

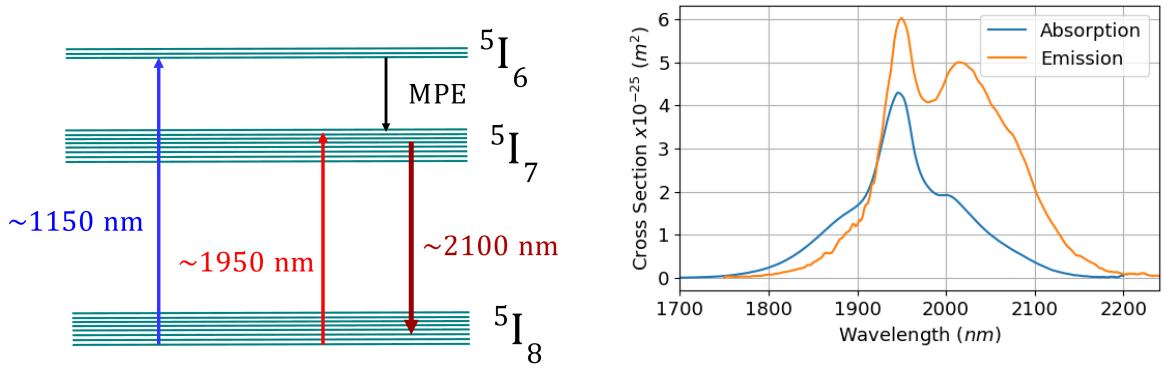

(a) Ho energy levels.

(b) Ho emission and absorption cross-sections in fused silica fibers.

Figure 4.3: Ho energy levels and emission and absorption cross-sections. MPE:multi-phonon emission.

cladding or a triple cladding structure with fluorine to avoid heating of the fiber in clad pumping configuration for power scaling.

In principle, due to the low quantum defect, very high efficiencies above 85% are expected however, efficiencies well below ($\sim 65-70\%$) have been recently obtained [181, 182]. Ho doped fibers are limited by the effect of active ion clustering which increases with the concentration of Ho in the fiber leading to ETU. This is reduced by using smaller dopant concentrations leading to longer fibers and potentially increased losses (background losses) or by increasing the concentration of Al doping to prevent clustering [183, 180]. At present, low doping concentration of Ho doped fibers yield to better performances due to reduced clustering effect which is the barrier for high power amplifiers and lasers. For clad pumping, high absorption is achieved by increasing the concentrations of active ions which in fact is limited by the present technology due to low slope efficiencies as a result of the mentioned clustering effect. Alternative approaches to keep a low concentration yet increase absorption is to play with the ratio core to clad, enhancing absorption or to use single mode Tm pump lasers to directly pump the fiber core.

The main issue in the $2\,\mu m$ spectral region is the lack of suitable pump sources and more specifically pump laser diodes. For Tm doped fibers, thanks to cross-relaxation effects, pumping is possible at $793\,nm$ allowing the combination of double clad fibers with high power pump diodes. For Ho doped fiber, there is no suitable diode pump laser hence double/triple clad fibers, which are a must for high power scaling, do not benefit from suitable pump sources. In order to circumvent this problem, Tm:Ho co-doping is used.

4.3 Tm:Ho Co-doped Fused Silica Fibers

Tm:Ho co-doped fibers take advantage of the pumping schemes for Tm and benefit from the long emission wavelengths from Ho. By pumping either using pump diodes at $793\,nm$ exploiting CR effects or in-band pumping, the Tm ions can be excited from $^3H_6$ energy level to the $^3F_4$ followed by an energy transfer from Tm to Ho ions exciting Ho from $^5I_8$ to $^5I_7$ allowing lasing in the $2-2.2\,\mu m$ wavelength. This process is illustrated in Fig.4.4 where a simplified energy level diagram for both Tm and Ho has been included. A more detailed energy level diagram can be found in [184].

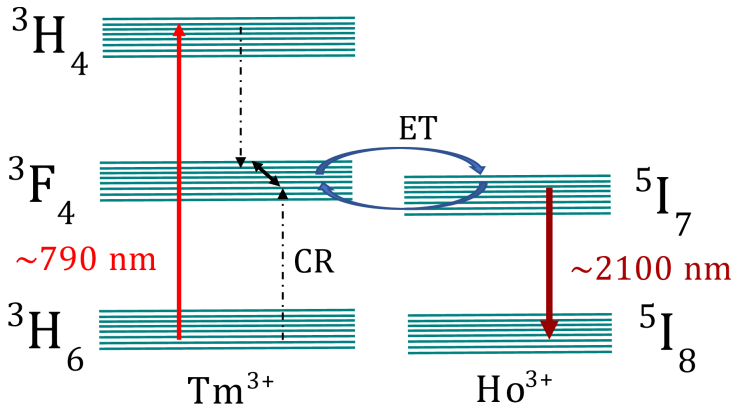

Figure 4.4: Energy transfer in Tm:Ho co-doped fused silica fibers.

Due to the pumping and emission wavelengths, a larger quantum defect of about $\sim$ 65 % is expected increasing the thermal load compared to Tm doped fibers which forces cooling of the fiber and pump diodes.

From a fiber composition point of view, the balance between Tm, Ho and Al ions need to be achieved for optimal performance. High Tm doping levels are required to achieve CR and high Al doping levels are also required to avoid Tm clustering and Ho clustering. At the same time, the good ratio between Tm and Ho ions will ensure proper energy transfer from one to another. This makes the fiber and the dynamics more complex compared to Tm or Ho fused silica fibers. It has all the complexity of Tm plus the energy transfer mechanisms that can go both ways. There has already been some work around the fiber composition of the co-doped fibers and the required concentration for Tm should be $\sim 5\% \, w.t.$ with donor-acceptor ratios between 10 : 1 and 20 : 1 [185]. For an accurate modelling of Tm:Ho co-doped fibers a larger amount of transitions need to be taken into account however from the simplified model valuable information can already be extracted to achieve optimal performance of the laser or amplifier systems.

An investigation of the commercially available PM Tm:Ho co-doped fibers performance was carried out when the fibers are used in a clad-pumped co-propagation amplifier scheme. This included testing the 6/130 (6 μm core diameter, 7.37 μm MFD @2 μm and 0.21 NA), the 20/300 (20 μm core diameter, 17.6 μm MFD @2 μm, and 0.09 NA) and the 25/300 (25 μm core diameter, 21.6 μm MFD @2 μm, and 0.09 NA) doped fibers. Due to limitations in the available components regarding power handling such as isolators (5 W @1960 nm) and the AOM (0.45 W @2050 nm) used in the CPA laser systems optimization of the fiber length for the 6/130 active fiber was done such that the pulse wavelength does not shift in the active fiber due to re-absorption while delivering up to 0.5 W of power into the AOM rather than focusing on extracting maximum efficiency out of the system. For the LMA fibers, the limitation was the available fiber length so that a spare amplifier in case of damaging or q-switching could be produced which resulted in too short active fiber length. Nevertheless, the investigation of the CR effect as function of the seed power and the influence of the fiber and diode temperature on the amplifier efficiency already gives useful information on how these fibers should be employed. The experimental setup used to study the fiber amplifiers is shown in Fig.4.5.

The seed used was the developed tunable laser with stretched pulses up to hundreds of ps to avoid NL effects during pulse amplification. A set of amplifiers (either 1 or 2) were included before the test fiber to evaluate its performance as the seed power was increased. All amplifiers including the fiber under study were cooled by placing them

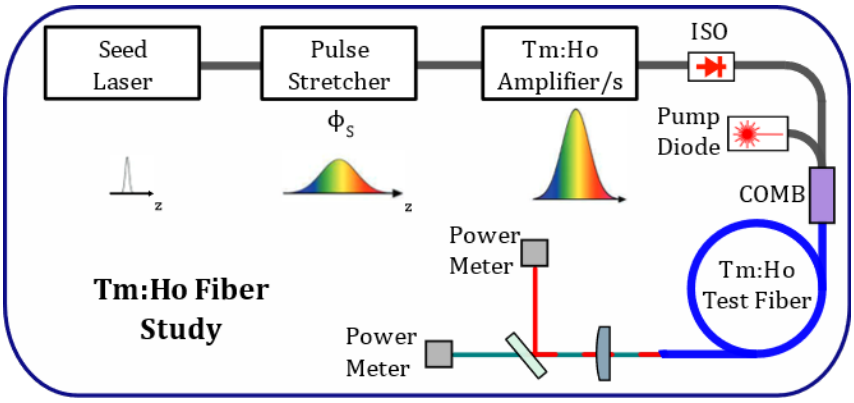

Figure 4.5: Experimental setup to test the Tm:Ho fibers in amplifier configuration.

in a water cooled plate with either graphite or thermal paste for improved contact and heat exchange. The active fiber performance when cooled down to different temperatures could be studied by adjusting the water temperature. The available pump powers were $16\,W$ for the Tm:Ho 6/130 and $50\,W$ for the Tm:Ho 25/300 and the pump diodes were cooled down using thermoelectric coolers (TECs). The non-absorbed pump and output power were collimated using an uncoated lens and the powers were measured after the dichroic used to separate both beams.

Since the most interesting process during amplification is the cross-relaxation effect, $3.6\,m$ of 6/130 active fiber were tested with $22.4\,mW$ input power and $\sim 200\,ps$ long pulses. The idea is to use this first amplifier to adjust the input power into the subsequent fibers under study, either the 6/130 or the LMA fibers and observe how the efficiency increases or decreases due to CR. The measured output power as function of the pump power is shown in Fig.4.6.

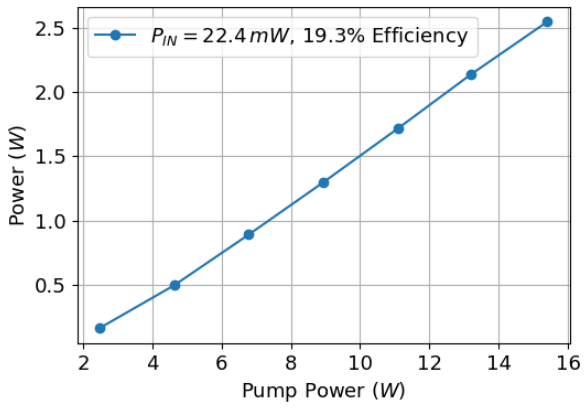

Figure 4.6: Measured output power out of the Tm:Ho 6/130 doped fiber for $22.4\,mW$ input power.

A maximum output power of $2.55\,W$ was obtained for $15.4\,W$ of pump at $793\,nm$. The measured efficiency with respect to the pump power was 19.3% which is quite low but it may be associated to the actual fiber length and to a limited input power to achieve cross-relaxation. The power does not exhibit any roll-over effect suggesting that a higher output can be achieved if the pump is increased which is possible by the addition of a second pump diode. This amplifier was used to study the 6/130 active fiber in the exact same configuration, co-propagation, clad pumping and same fiber length. Afterwards,

both amplifiers were used to test the LMA fibers. Results are summarised in Fig.4.7 and Fig.4.8.

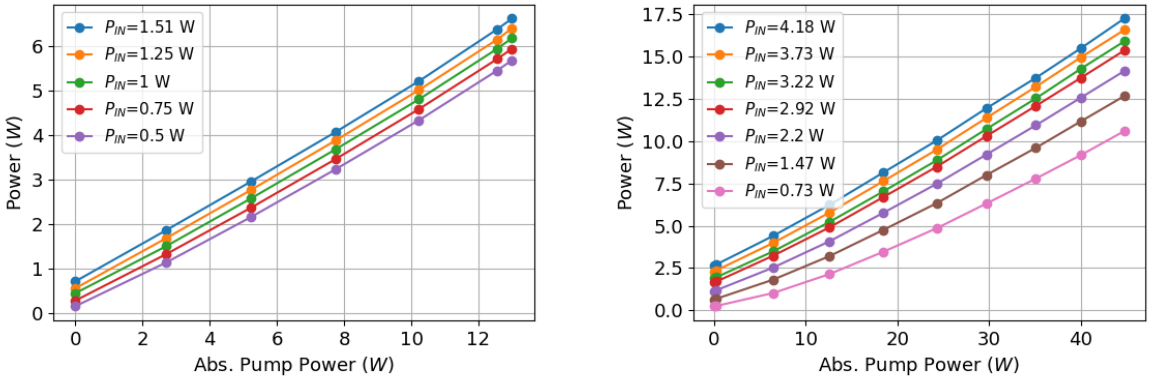

(a) Output power in Tm:Ho 6/130 for different injected powers P_{IN}.

(b) Output power in Tm:Ho 25/300 for different injected powers P_{IN}.

Figure 4.7: Output power in Tm:Ho fused silica fibers in clad-pumped co-propagation scheme.

In Fig.4.7a the output power from the 6/130 active fiber is depicted as function of the absorbed pump as the seed signal input is increased from $0.5\,W$ up to $1.5\,W$. In a saturated amplifier, the output power is linear with respect to the absorbed pump and for a fixed pump power, the maximum output increases with the injected signal yet the efficiency of the amplifier remains constant. This is true as long as there are no energy transfer phenomena however, this is not the case for Tm and Tm:Ho doped fibers as they exhibit CR and ETU. The slope efficiency with respect to the absorbed pump increased by 2.5% when the seed power was increased from $0.5\,W$ to $1.5\,W$. This can be explained by a further depopulation of the $^5I_7$ energy level in Ho ions favouring energy transfer from Tm to Ho depleting the $^3F_4$ in Tm ions and increasing the cross-relaxation process. The efficiency as a function of the absorbed pump and total pump power are shown in Fig.4.8b. Under strong seeding, the efficiency as function of the pump power has increased by more than 15% compared to the amplification in the first scenario were $22.4\,mW$ were injected into the system and this is exclusively attributed to the cross-relaxation process. No roll-over was observed suggesting that for the tested configuration the output power is limited by the available pump. By adding a second pump diode, the pump power could be increased up to $\sim 32\,W$ and the output powers reached were beyond $10\,W$ for the 6/130 Tm:Ho doped without exhibiting any roll-over effect.

Regarding the performance of the fiber with temperature, cooling of the diode and cooling of the fiber were investigated with very little improvement on the efficiency of the fiber amplifier. The effect on the pump diode temperature by cooling it using a TEC down to 15^o showed an improvement of $\sim 3\%$ with respect to the pump power which is linked to an increase on pump absorption due to shifting the diode emission wavelength closer to the absorption peak at $793\,nm$. If the fiber amplifier is cooled down from room temperature to 15^o, a slight improvement in efficiency was obtained of $\sim 2\%$. Even thought the performance improved in both situations, cooling the fiber and the diode had the same issue which was water condensation on the laser diode and on top of the cooling plate. This can cause fatal damage on the pump diode which which is why it was decided to maintain the TEC temperature at $\sim 25^o$ and the cooling plate temperature at 20^o .

The Tm:Ho 25/300 LMA fiber output power was investigated as a function of the pump power for input signal power P_{IN} varying from $0.73\,W$ up to $4.18\,W$. The results are summarised in Fig.4.7b and Fig.4.8b. A maximum output power of $17.5\,W$ was obtained for $50\,W$ pump and $4.18\,W$ input signal. Regardless of the injection, more than $10\,W$ power were obtained even for $0.73\,W$ input signal which is promising for power scaling the high energy CPA system up to $10\,W$ level with low seed power. As for the 6/130 active fiber, an increase in the input seed power improves the efficiency up to slightly above 30% and up to 33% when estimated with respect to the absorbed pump. There was no evidence of any roll-over effect meaning that further power scaling can be achieved by increasing the pump power and by optimising the fiber length with a longer piece which unfortunately was not possible due to lack of fiber.

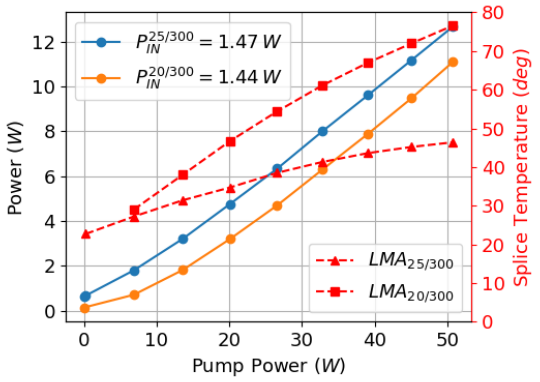

(a) Comparison between Tm:Ho 20/300 and Tm:Ho 25/300 in terms of output power and splice temperature.

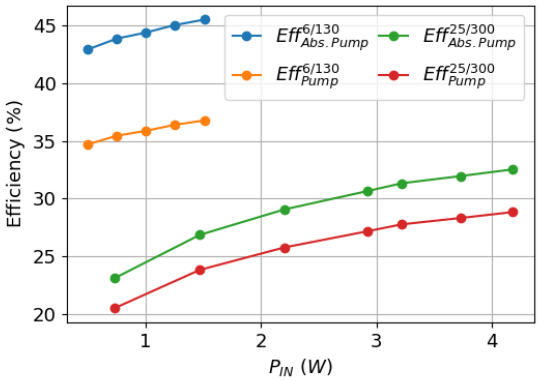

(b) Measured efficiencies in Tm:Ho co-doped fibers.

Figure 4.8: Tm:Ho LMA fiber performance comparison and measured efficicies for Tm:Ho fused silica fibers.

Among the LMA Tm:Ho fibers, the 25/300 was chosen because of its bigger MFD which is beneficial for power scaling with reduced non-linearities. The 20/300 fiber was tested as well however the combiner used was matched to the 25/300 fiber geometry and higher losses for the signal were expected in the splice. This can be seen on Fig.4.8a where the splice temperature was measured as a function of the pump. For the 20/300 LMA fiber, the splice reached a temperature of $\sim 75^o$ compared to the $\sim 48^o$ for the 25/300 at $50\,W$ pump. The reason why the splice temperature is higher is the miss-match between the combiner and the active fiber which leaks a portion of the signal power into the clad and the low index polymer causing heating on the splice. At the same time, due to the high pump power at the input of the fiber there is high absorption and not enough power to deplete the inverted population further heating the fiber. It is important to recall that the low index polymer is transparent for the pump wavelength at $793\,nm$ and highly absorbing at $2\,\mu m$ which can cause the polymer to suffer from thermally induced darkening worsening the transparency of the polymer further heating the splice causing further darkening in a cascaded process until the splice burns. Because of the above mentioned reasons, the use of the 20/300 fiber was avoided. Regarding the 25/300 fiber, the combiner and splice performance were characterised and $\sim 10\%$ losses were obtained on the combiner. From the remaining signal, about $\sim 5\%$ of it was located in the fiber cladding which makes a total loss of $\sim -0.68\,dB$ at the combiner. The splice losses were as

well characterised by cutting the first few cm of optical fiber after the slice and measuring the power assuming there is no absorption. About $\sim 12\%$ of signal is lost at the combiner to active fiber splice which corresponds to $\sim -0.55\,dB$. To further reduce the present heat load on the fiber, the splice was directly performed on top of the water cooled plate to maximise the heat exchange. The contact with the cooling plate was improved with the use of graphite and thermal paste. In terms of output power, it is not possible to really compare both LMA fiber due to not having optimised the amplifiers fiber lengths for each particular geometry.

Based on the results obtained, is it possible to further increase the output power out of the Tm:Ho 6/130 and Tm:Ho 25/300 fibers by increasing the pump power and optimising the fiber lengths however this could not be done due to lack of active fiber. The amplified spectrum was also measured and behaved as observed during the development of the CPA lasers. The observed modulations increased frequency and contrast as the power out of the amplifier was increased and pulses were further amplified in subsequent amplifiers as shown in Fig.4.9.

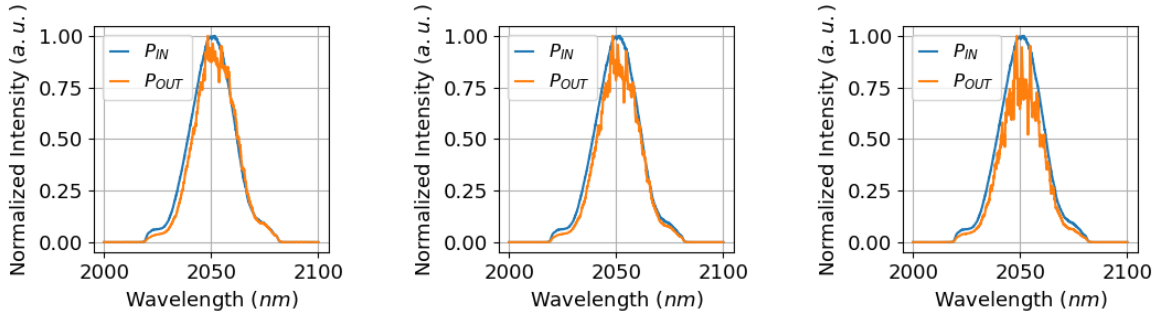

(a) Measured optical spectrum out of first Tm:Ho preamplifier. $P_{IN} = 22.4\,mW$ and $P_{OUT} = 0.359\,W$

(b) Measured optical spectrum out of first Tm:Ho preamplifier. $P_{IN} = 22.4\,mW$ and $P_{OUT} = 0.547\,W$

(c) Measured optical spectrum out of first Tm:Ho preamplifier. $P_{IN} = 22.4\,mW$ and $P_{OUT} = 1.143\,W$

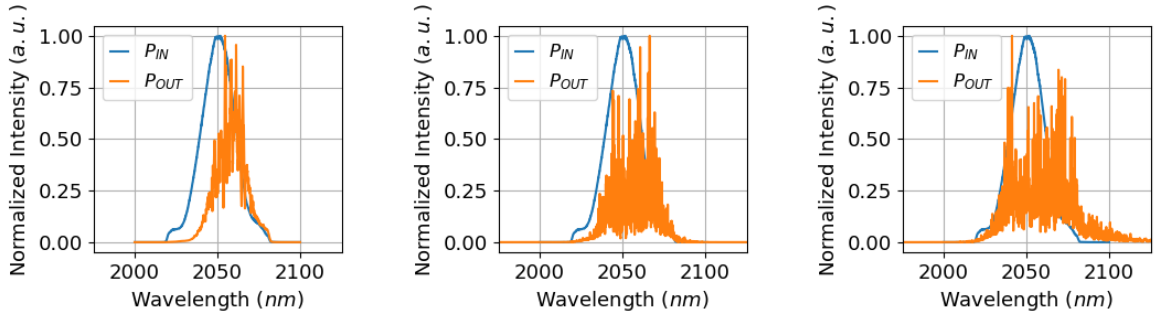

(d) Measured optical spectrum out second Tm:Ho preamplifier without pumping. $P_{IN} = 1.143\,W$ and $P_{OUT} = 0.56\,W$.

(e) Measured optical spectrum out of first Tm:Ho premplifier. $P_{IN} = 1.143\,W$ and $P_{OUT} = 5.66\,W$

(f) Measured optical spectrum out of first Tm:Ho preamplifier. $P_{IN} = 1.143\,W$ and $P_{OUT} = 10.12\,W$

Figure 4.9: Measured optical specra at high power out of Tm:Ho first and second pre-amplifiers, both use the 6/130 Tm:Ho active fibers.

As the output power increases out of the first pre-amplifier, the degradation of the spectra can be observed due to the high frequency modulations developing. The effect becomes even worse as the amplification takes place in the subsequent amplifiers completely scrambling the optical spectrum for powers above $\sim 5\,W$. For the worst case, a second

pump diode was added to increase the output power to $\sim 10\,W$, the calculated NL phase for $\sim 200\,ps$ long pulses is $4.5\,rad$ reaching peak powers as high as $1.3\,kW$. The NL phase starts to be substantial and it can affect pulse compression however, it shouldn't be enough to really affect the spectrum or ACT. Even if amplification doesn't take place and pulses are propagated in the active medium without pump (see Fig.4.9d), the spectrum worsens meaning that the problem should not come from NL effects. The modulations are similar to those that can be observed when broadband pulses excite the fundamental and higher order modes in LMA optical fibers. However, given the fiber characteristics ($6\,\mu m$ core, $7.4\,\mu m$ MFD and 0.21 NA) the fiber is single mode specially at such long wavelengths. Fast modulations are also obtained in spectral interferometry due to the interference of two delayed pulses yet the envelope of the pulses' optical spectrum is maintained. If a pair of delayed pulses with different intensities are amplified, the contrast between them is kept more or less constant when amplification takes place in non-saturated amplifiers. However if the amplifier is saturated which is the case for the second Tm:Ho amplifier, one pulse will experience higher gain compared to the second one worsening the contrast which can as well explain the degradation of the optical spectrum.

To evaluate the temporal pulse shape, compression was performed using the pair of broadband CVBGs to stretch and compress ($2050\,nm$ wavelength, $\sim 62\,nm$ BW, $\sim 90\,\%$ reflectivity and stretching factor of $\sim 8\,ps/nm$ and $\phi_3 \sim 0.22\,ps^3$ and $0.23\,ps^3$) ignoring the phase miss-match between them and the dispersion added by the fiber amplifiers leading to partially compressed pulses as shown in Fig.4.10.

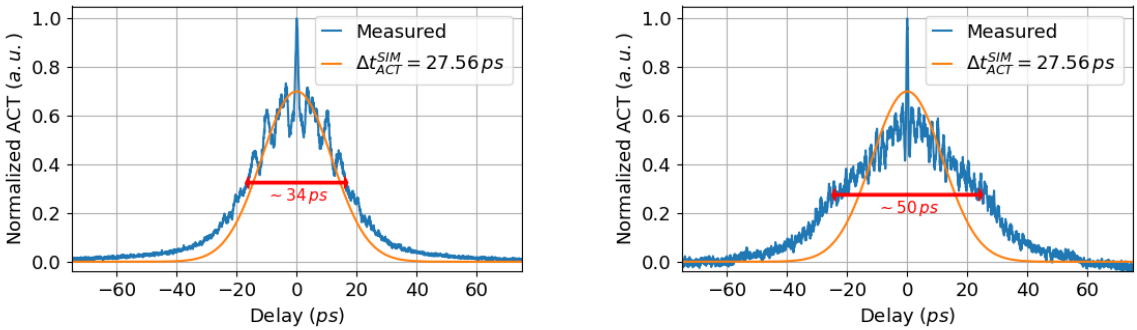

(a) Measured ACT for $P_{OUT} \sim 6\,W$.

(b) Measured ACT for $P_{OUT} \sim 10\,W$.

Figure 4.10: Measured ACT out of the second Tm:Ho 6/130 pre-amplifier. Dispersion missmatch between CVBGs and dispersion due to fiber amplifiers have not been compensated with PM2000D fiber.

A clear degradation can also be observed on the measured ACT which shows as a modulated ACT with a coherence peak on top of it. The higher the power the faster the modulations on the ACT. The expected pulse duration with the partially compressed pulses should be $\Delta t_{ACT}^{SIM} = 27.56\,ps$ which is quite close to the measured ACT for $6\,W$ output power. It is strange that by increasing the pump power of the second 6/130 pre-amplifier, the ACT is broadened to $\sim 50\,ps$ which is hard to understand as the dispersion has not changed and the NL effects are not playing an important role during amplification. As for the case of the measured optical spectrum, modulations on the ACT appear if a pair of delayed pulses with different relative intensities are measured provided that they overlap in time to some extent. This may explain the change in shape on the ACT shape. If the contrast between the pulses worsens, the modulation becomes deeper.

This is illustrated in the simulations below by computing the spectrum and ACT of two identically chirped pulses ($\lambda = 2050\,nm$, $\Delta\lambda_{FWHM} = 24\,nm$, $\Delta t_{ACT} = 27.5\,ps$ which corresponds to $\Delta t_{FWHM} = 19.4\,ps$, $\phi_1 = 0\,fs$ and $\phi_2 = 1.81\,ps^2$) with different relative intensities as can be seen in Fig.4.11.

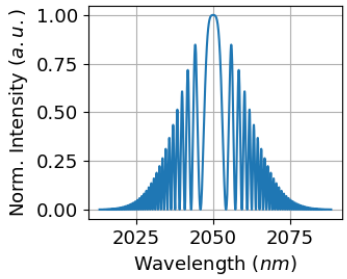

(a) Simulated spectrum of a pair of pulses with equal intensity.

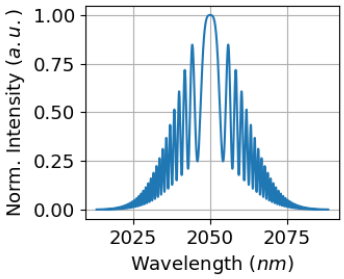

(b) Simulated spectrum of a pair of pulses with 10% relative intensity.

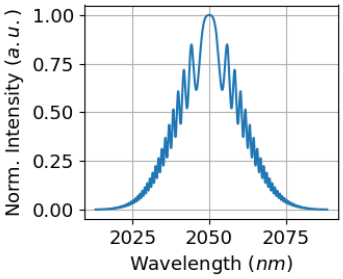

(c) Simulated spectrum of a pair of pulses with 1% relative intensity.

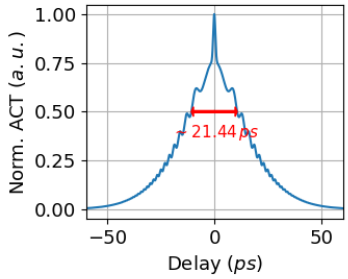

(d) Simulated ACT of a pair of pulses with equal intensity.

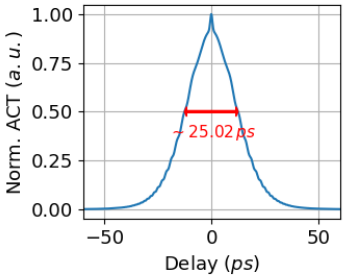

(e) Simulated ACT of a pair of pulses with 10% relative intensity.

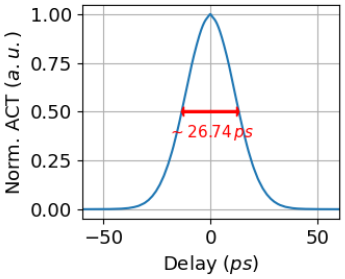

(f) Simulated ACT of a pair of pulses with 1% relative intensity.

Figure 4.11: Influence of the relative intensity between a pair of identical pulses in the spectrum and ACT. Pulse parameters: $\lambda = 2050\,nm$, $\Delta\lambda_{FWHM} = 24\,nm$, $\phi_2 = 1.81\,ps^2$ and $\phi_1 = 0\,fs$ which corresponds to $\Delta t_{ACT} = 27.5\,ps$ and $\Delta t_{FWHM} = 19.4\,ps$.

Regardless the relative intensity of the pair of pulses, the modulations that the ACT and the spectrum exhibit are not periodic, they exhibit a frequency chirp which is linked to the chirped nature of the pulses ϕ_2. As the modulations in the spectrum move away from the pulse wavelength $\lambda = 2050\,nm$ their frequency increases and the same happens in the ACT as the modulations move away from $\Delta t = 0$. In particular, the ACT exhibits a sharp peak at $\Delta_t = 0$ which tends to disappear as the contrast between pulses increases (the relative intensity decreases) as can be seen in Fig.4.11d, 4.11e and 4.11f. An increase on the contrast is also seen as a decrease on the modulation depth on the simulated spectrum for the pair of pulses as shown in Fig.4.11a, 4.11b and4.11c. The relative intensity between pulses, is not the only factor that can affect the measured spectrum and ACT, the delay between the pulses has an important effect too.

The spectrum and ACT of a pair of identical pulses ($\lambda = 2050\,nm$, $\Delta\lambda_{FWHM} = 24\,nm$, $\phi_2 = 1.81\,ps^2$ which corresponds to $\Delta t_{ACT} = 27.5\,ps$, and $\Delta t_{FWHM} = 19.4\,ps$) with increasing delays ($\phi_1 = 4, 8$ and $12\,ps$) is shown in Fig.4.12. Note that for $\phi_1 = 0$ is shown in Fig.4.11a and 4.11d. As the delay increases, the frequency of the modulations in the spectrum increase yet they still exhibit a frequency chirp. For $\phi_1 > 0$, higher modulation

frequencies are obtained for $\lambda < 2050\,nm$ and the other way around for $\phi_1 < 0$, higher modulation frequencies are obtained for $\lambda > 2050\,nm$. On the time domain, as the delay increases the modulations on the ACT smoothen out, yet maintaining a sharp peak at $\Delta t = 0$. This is because there is less overlap of the pulses in time therefore the modulations depth needs to decrease as the delay between the pulses increases.

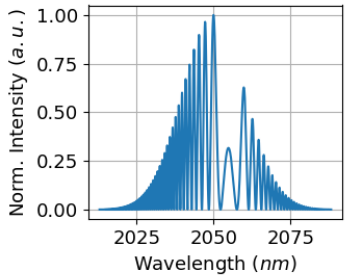

(a) Simulated spectrum of a pair of identical pulses with delay $\phi_1 = 4\,ps$

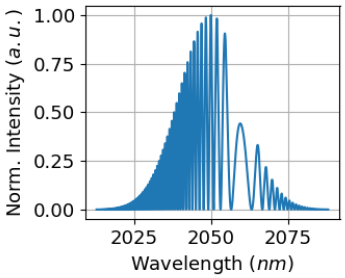

(b) Simulated spectrum of a pair of identical pulses with delay $\phi_1 = 8\,ps$

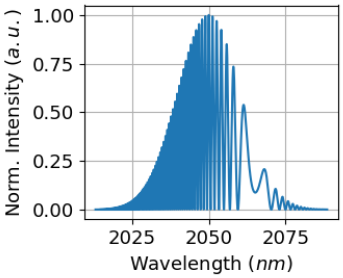

(c) Simulated spectrum of a pair of identical pulses with delay $\phi_1 = 12\,ps$

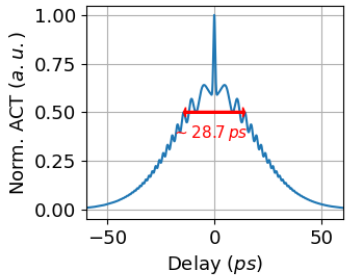

(d) Simulated ACT of a pair of identical pulses with delay $\phi_1 = 4\,ps$

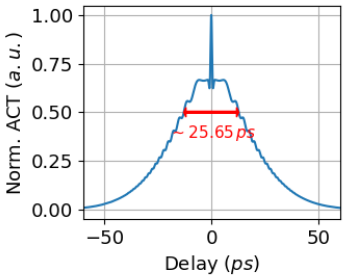

(e) Simulated ACT of a pair of identical pulses with delay $\phi_1 = 8\,ps$

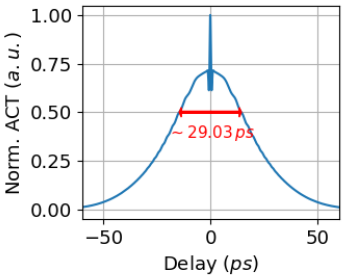

(f) Simulated ACT of a pair of identical pulses with delay $\phi_1 = 12\,ps$

Figure 4.12: Influence of the delay ϕ_1 between a pair of identical pulses in the spectrum and ACT. Pulse parameters: $\lambda = 2050\,nm$, $\Delta\lambda_{FWHM} = 24\,nm$, $\phi_2 = 1.81\,ps^2$ which corresponds to $\Delta t_{ACT} = 27.5\,ps$ and$\Delta t_{FWHM} = 19.4\,ps$.

The origin of the modulations was uncertain as they can be originated from any place along the laser system. At first one can consider that they come from the seed laser that is delivering a main pulse followed by one or multiple small pulses however this was not observed when characterising the seed laser. Neither FROG nor ACT showed multi-pulsing of the seed and repetition rate of the laser was constant and stable during operation. In addition, SSFS is a self-cleaning process, in the temporal and spectral domain, and the fact that same results were obtained either with our developed laser or the MIRPULSE indicates that the problem may not be coming from the seed source. Another physical phenomena linked to the seed lasers due to the SSFS is the loss of coherence due to quantum pick-up noise [131, 168]. This can be verified by replacing the seed laser by a highly coherent laser source such as a mode-locked oscillator at $2.05\,\mu m$. Partially coherent laser ACT slowly converges towards the measured ACT shown in Fig.4.10 and the simulated ones in Fig.4.12f which makes quite hard to distinguish if the origin is multi-pulsing or a loss of coherence of the source [186].

Working with optical components that are off-wavelength can also have an effect on the

system due to reflections in isolators or circulators for example. Polarization can also play a role if bad splicing takes place between fibers generating a pair of pulses delayed by the group velocity from one axis to the other. The polarization properties of the seed lasers and amplifiers was verified and was fixed by the isolators used ($\sim 20\,dB$) and nothing unusual was observed during the development of the fiber amplifiers. The stretching devices (CVBGs) are not standard and may have some unexpected behaviour as well that cannot be observed at low power but manifests as pulses are amplified. Fiber splicing can also be problematic specially with these fibers that have high doping concentration hence splicing the combiner to the active fiber and the active fiber to the mode stripper can be more subtle than expected. The problem can also be linked to the Tm:Ho co-doped fiber as their use is not widely spread and for instance, only CW and Q-switched operation is reported in literature with the LMA Tm:Ho fibers investigated [187, 188] while small core Tm:Ho co-doped fibers found in literature are usually non-pm or in-house fabricated. When the 6/130 Tm:Ho fibers were replaced by Tm doped fibers to test exclusively the first pre-amplifier, the same behaviour was obtained (modulations on the measured optical spectrum) similar to those shown previously.

The laser being a CPA doesn't make debugging of the system easier as it is not possible to evaluate the system with stretched pulses in the temporal domain which adds more complexity. This is mainly because of the available fast photodiodes which don't provide high resolution in the temporal domain. Amplification of the pulses always needs to be performed due to losses in the passive components and dispersion miss-match between the CVBGs which doesn't allow to test component by component as compression without amplification cannot be really observed on the ACT. In the temporal domain, a pedestal was observed in the previous chapters which can obscure small secondary pulses over the time span of the pedestal, specially if the pulses are not fully compressed. In order to debug the system, a set of experiments were designed to isolate each possible situation one by one and try to find the origin of the spectrum and ACT scrambling focusing on the Tm:Ho amplifiers (splicing and polarization) and on the stretching device as are the most likely components responsible of worsening the laser performance.

4.3.1 Tm:Ho ASE Source and Amplification

At first, in order to debug and try to find the origin of the modulations on the spectrum and on the measured ACT, the Tm:Ho amplifiers were tested as amplified ASE laser sources. Both pre-amplifiers were tested, the first one had isolators at the input and output operating at $2\,\mu m$ wavelength and the second one consisted exclusively of the combiner, active fiber and mode stripper with both ends terminated with angled connectors (FC/APC). By testing the amplifiers as ASE sources parasitic reflections or Fabry-Perot cavity within the amplifier can be observed on the measured ASE spectrum while ignoring any issue in polarization as the ASE is not polarised and exclusively excites the fundamental mode of the optical fiber. The measured optical spectra of both amplifiers for different output powers are shown in Fig.4.13.

As the pump increases the ASE shifts to shorter wavelengths which is linked to less re-absorption along the fiber. Pretty much identical results have been obtained for both amplifiers mainly due to having almost identical active fiber lengths. No periodic modulations on the optical spectrum could be observed neither when the FT of the measured optical spectra was computed.

Afterwards, the first Tm:Ho amplifier was used as ASE source to be amplified by the second one. To make sure that the behaviour observed is not exlusively associated

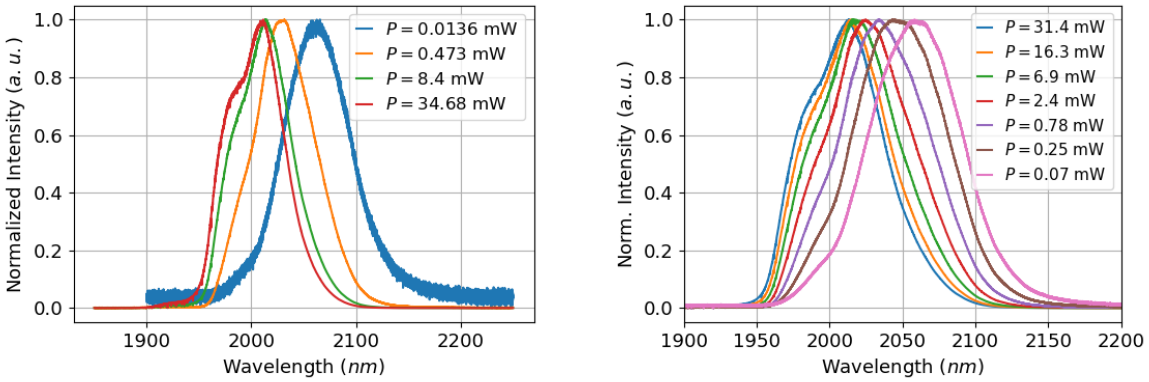

(a) ASE out of Tm:Ho first preamplifier.

(b) ASE out of Tm:Ho second preamplifier.

Figure 4.13: Measured amplified spontaneous emission out of the Tm:Ho preamplifiers for different pump powers.

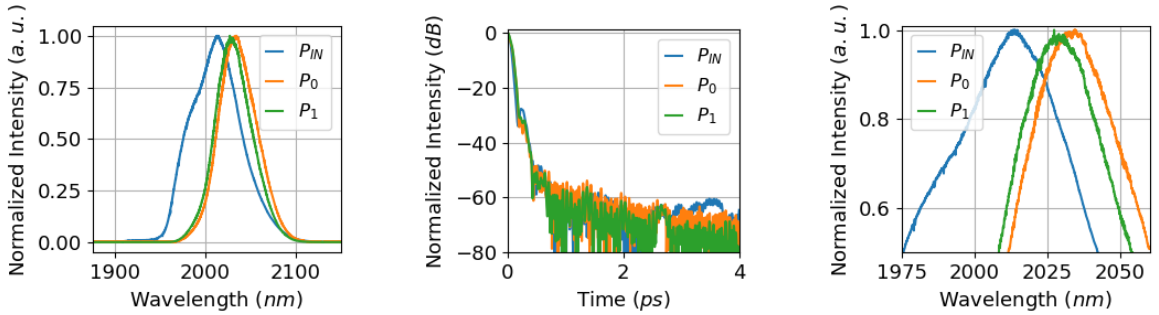

(a) Measured amplified ASE in the Tm:Ho 6/130 doped fiber amplifier.

(b) FFT of the measured amplified ASE in Tm:Ho 6/130 doped fiber amplifier for time scale below 4 ps

(c) Measured amplified ASE zoomed image.

Figure 4.14: Measured amplified ASE in the Tm:Ho 6/130 doped fiber amplifier and computed FFT for different output powers. $P_{IN} = 34.68\,mW$, $P_0 = 161\,mW$ and $P_1 = 550\,mW$

to Tm:Ho fibers, amplification of the ASE source was also performed in a Tm amplifier with 6/130 fiber and same pump combiner to make sure the conditions are as identical as possible. The Tm double clad fiber had a $6\,\mu m$ core, $0.21\,NA$ and was from the same provider as the Tm:Ho fiber. The results are shown in Fig.4.14 for the amplification in the Tm:Ho amplifier and in Fig.4.15 for amplification in the Tm amplifier.

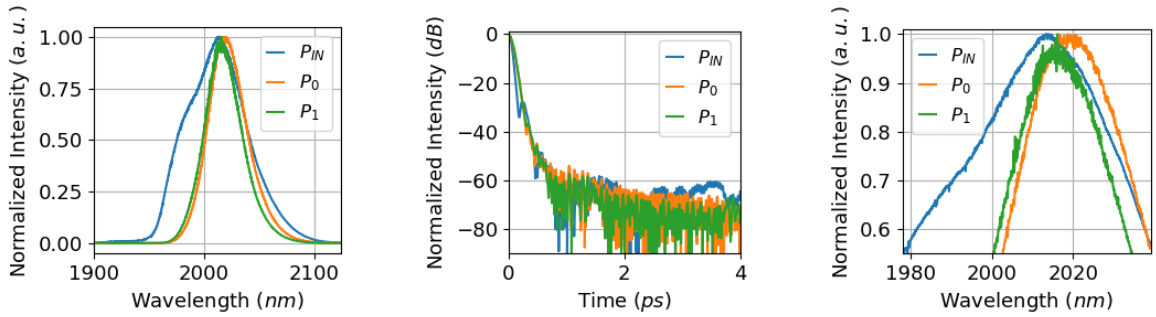

(a) Measured amplified ASE in Tm 6/130 doped fiber amplifier.

(b) FFT of the measured amplified ASE in Tm 6/130 doped fiber amplifier for time scale below $4\,ps$

(c) Measured amplified ASE zoomed image.

Figure 4.15: Measured amplified ASE in a Tm 6/130 doped fiber amplifier and computed FFT for different output powers. $P_{IN} = 34.68\,mW$, $P_0 = 459\,mW$ and $P_1 = 1200\,mW$

Amplification of the ASE source yields to very similar results either when using the Tm or the Tm:Ho amplifiers, there is no apparent important spectral degradation. Tiny oscillations start to appear on top of the measured amplified spectra which cannot be appreciated on the Tm:Ho amplified spectra yet they grow with the pump power. The difference from one to another may be linked to the output power which is two times higher for the Tm amplified ASE. The FT of the measured spectra was computed to try to observe any periodic pattern but it didn't reveal any information for times below $4\,ps$ and neither for longer timescales as the signal is already below $-60\,dB$ compared to the main peak at $0\,ps$. Even though both amplifiers seem to be working properly, both of them showed the same behaviour when tested in pulsed operation configuration.

4.3.2 Amplification of fs up to few ps Pulses

The main issue to debug the CPA laser is that it is not possible to study component by component as stretching needs to be performed before amplification and sometimes they need to be compressed as well to obtain information on the temporal domain. The tested CVBGs have a non-uniform diffraction efficiency across their surface which makes them more sensitive to alignment. For the broadband CVBGs, this is not a problem as their clear apperture is small ($5\,mm$ by $5\,mm$) and a more uniform pattern was imprinted in the glass which translated in a smooth optical spectrum after stretching. However, this is not the case for the narrowband CVBG whose surface had to be scanned with the beam in order to find a region with maximum diffraction efficiency and uniform spectrum after stretching. Since the use of $2\,\mu m$ CVBGs is not widely spread and they are usually found in research environments it was decided to investigate if the modulations on the spectrum were due to the stretching devices. By replacing the CVBGs with a gold mirror or with a low dispersion CFBG, amplification was tested with fs up to few ps pulses.

This allowed to amplify either in the high-nonlinear regime with fs pulses or with long enough ps pulses to avoid non-linearites and pulse compression as few ps pulses ACTs can be directly measured. The experimental setup is shown in Fig.4.16a.

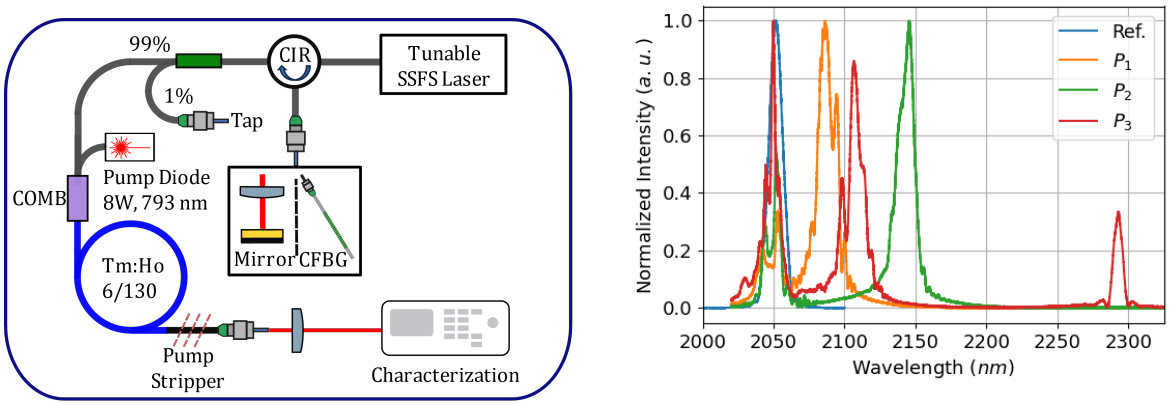

(a) Experimental setup with CFBG and gold mirror to test the Tm:Ho amplifier.

(b) Measured optical spectra when seeded with fs pulses.

Figure 4.16: Experimental setup to test the Tm:Ho amplifier with fs up to few ps long pulses and measured optical spectra for the amplified fs soliton pulses.

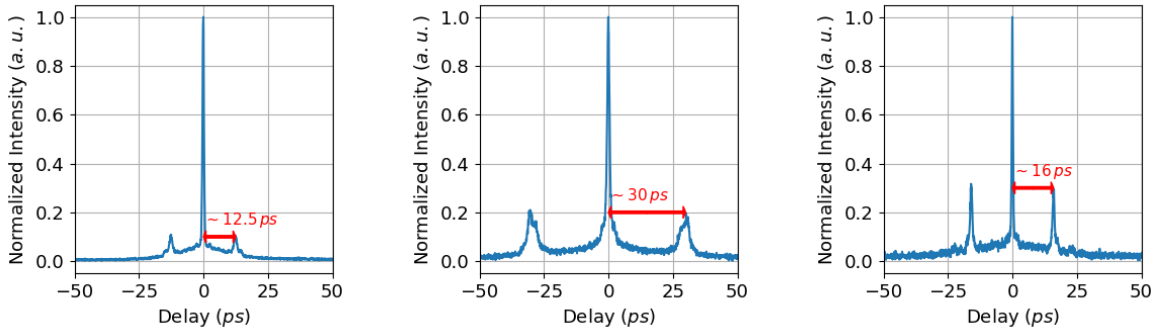

(a) Measured ACT for a pump power P_0

(b) Measured ACT for a pump power P_1

(c) Measured ACT for a pump power P_2

Figure 4.17: Measured optical spectra and ACT out of the Tm:Ho amplifier for different pump powers ($P_0 < P_1 < P_2$).

When the gold mirror is used and the fs pulses are amplified, the SSFS regime is reached very fast. The input pulses experienced amplification and shift in wavelength up to $\sim 2.3\,\mu m$ with smooth spectra and ACTs without evidence of multi-pulsing (see Fig.4.16b). This is because the SSFS effect is self-cleaning and as the pulse shifts, only the amount of light that suffers from Raman scattering will shift and the seed pulses and solitons will separate not only spectrally but also temporally due to different group velocities. As the pump power increases more and more solitons were generated and the power level at signal wavelength at which the spectral modulations started to develop ($\sim 0.5\,W$) was not reached. No information on the amplifier performance could really be extracted from the depleted seed pulse neither from the generated the solitons. On the measured ACT (see Fig.4.17), two pulses were observed which corresponded to the input

pulse and the shifted soliton. The separation in time between the two pulses increased with the pump power as the soliton is generated earlier in the fiber amplifier therefore reaching longer wavelengths and increasing the delay with the seed pulse at $2050\,nm$. To set the experimental conditions in a more similar situation to the use of CVBGs, a CFBG was used instead.

The CFBG was centered at $2050\,nm$ wavelength, had a FWHM of $14.62\,nm$ at $3\,dB$, a reflectivity of 37.6% and normal dispersion equal to $\beta_2 = 1.25\,ps^2$ with $\beta_3 = 0$. The use of the CFBG allows to have a fully fibered stretcher and compared to CVBGs, the inscription of gratings into fibers is a way more developed technology therefore çshould be in principle more reliable stretcher. The spectrum and pulse duration was analysed while the output power was increased.

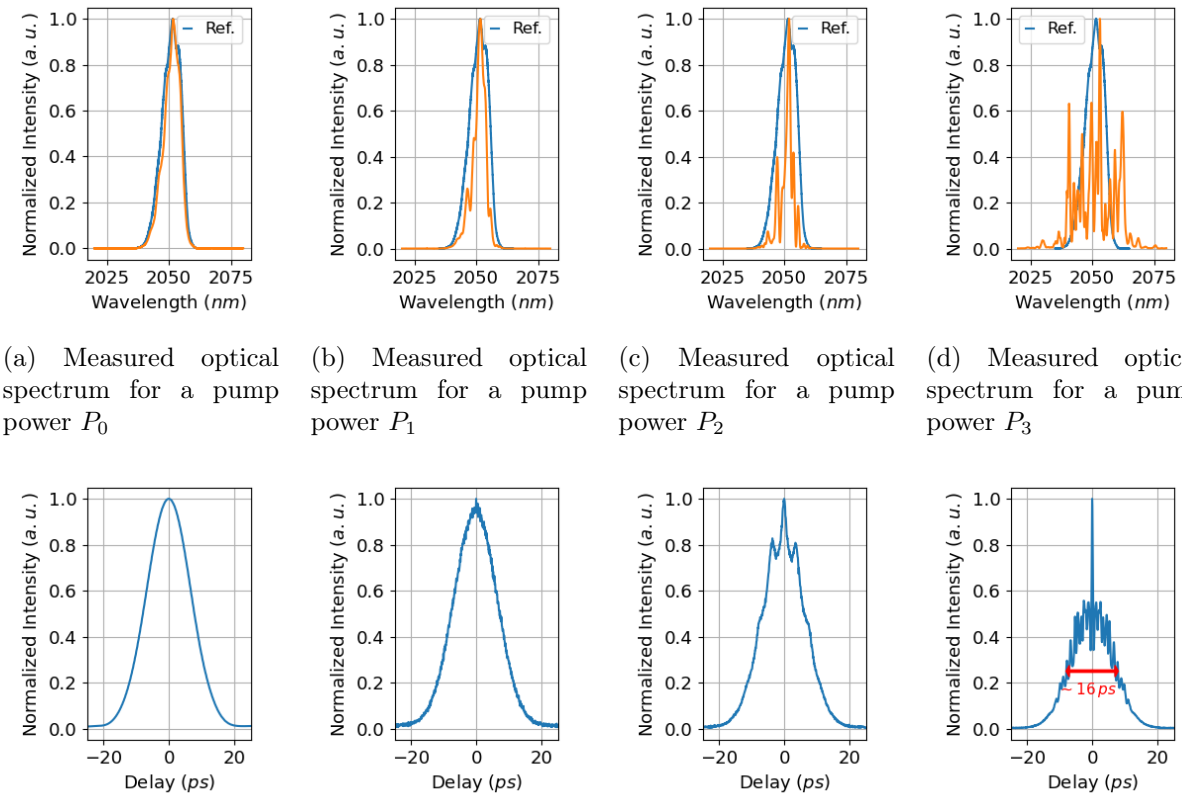

(a) Measured optical spectrum for a pump power P_0

(b) Measured optical spectrum for a pump power P_1

(c) Measured optical spectrum for a pump power P_2

(d) Measured optical spectrum for a pump power P_3

(e) Measured ACT for a pump power P_0

(f) Measured ACT for a pump power P_1

(g) Measured ACT for a pump power P_2

(h) Measured ACT for a pump power P_3

Figure 4.18: Measured optical spectra and ACT out of the Tm:Ho amplifier for different pump powers ($P_0 < P_1 < P_2 < P_3$). The CFBG was used pulse stretcher and Ref. states for the input spectrum to be amplified.

The few ps amplified pulses exhibited the same phenomena as when pulses were stretched using the CVBGs, that is modulations on the optical spectrum and on the ACT which become worse as pulses are further amplified (see Fig.4.18). Pulses were amplified up to $P_3 = 475\,mW$ which is almost the same power level used while studying pulse compression in the CPA laser. Observing the same phenomena means that the observed modulations are not originated or linked to the CVBGs. The combiner and the Tm:Ho active fiber could also be the responsible of the modulations. The combiner used is not matched to the active fiber and is slightly bigger as the input and output fiber was

the PM-GDF-10/130-2000-M, slightly bigger than the 6/130 Tm:Ho active. Excitation of the cladding modes in the fiber may be amplified and mixed with the fundamental mode scrambling the pulses in the time and frequency domains.

To avoid this problem, one can use the amplifier in contra-propagation scheme with the PM1950 or PM1550XP fibers which are single-mode and have a MFD closer to that of the active fiber reducing the supposed effect of cladding excitation. The same results were obtained meaning that this was not the problem. As final test, the 6/130 Tm:Ho fiber was tested in free space configuration. This will provide information on the quality of the splices between the active fiber, the combiner and the mode stripper and reveal if the fiber is suitable for amplification of broadband pulses.

4.3.3 Free Space Tm:Ho Fiber Ampilfier

The behaviour of the 6/130 Tm:Ho doped fiber was investigated in free space configuration to evaluate how sensitive the fiber is to polarization which will tell the accuracy required for the splicing with the combiner. If polarization axis are well aligned, amplification of broadband pulses can be tested and if successful (no modulations observed), it would mean that the splicing parameters need to be adjusted. Free space seeding of the active fiber has the advantage that all the optical components that are out off the operation wavelength of the laser can be avoided. The experimental setup is illustrated in Fig.4.19a. The MIRPULSE laser (120 fs soliton pulses at 2050 nm, $\sim$ 36 nm BW and $\sim$ 48 mW average power) in combination with an injection system were used to seed the Tm:Ho fiber in free space. A PBS and a half-waveplate were included to ensure linearly polarised light and to choose whether light is injected on the fast, slow or a combination of both axis of the active fiber. Pulses were stretched before injection using the broadband CVBGs and a circulator. The fiber could also be tested with fs pulses by removing the circulator and CVBG replacing them with an isolator to directly inject the solitonic pulses. The pump was injected in contra-propagation. The WincamD-IR-BB camera was used to image the fiber and optimize the injected signal into the fiber core as can be seen in Fig.4.19b.

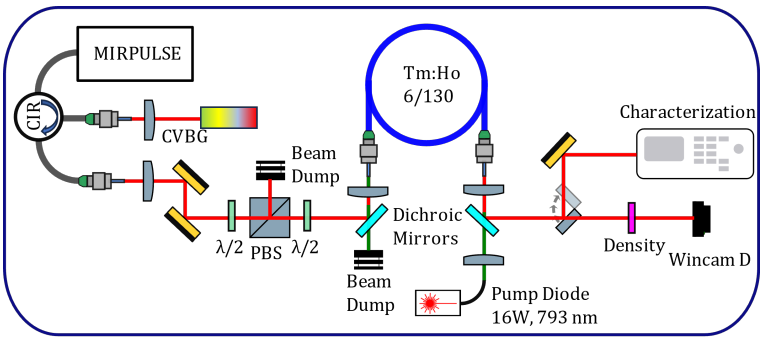

(a) Experimental setup to test the Tm:Ho fibers in free space configuration.

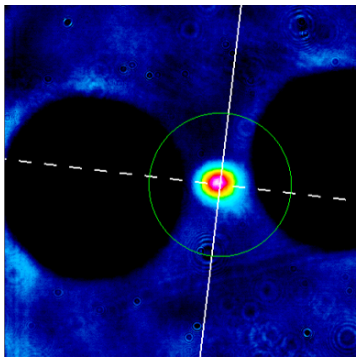

(b) Image of the injected Tm:Ho 6/130 active fiber.

Figure 4.19: Experimenatl setup to test the Tm:Ho active fibers in free space configuration and image of the seeded active fiber.

At first an isolator designed at the operation wavelength was used to test the sensitivity to polarization of the fiber with fs pulses. The doped fiber was pumped enough to slightly amplify the pulses yet below the limit at which NL effects such as SPM and SSFS started to develop. The sensitivity to polarization was evaluated by rotating the half waveplate

after the PBS cube. The output pulses were characterised using the OSA in two different configurations: free space injected using steering mirrors and with a passive SM fiber as transport fiber. Pulses in the temporal domain were characterised using the FROG technique.

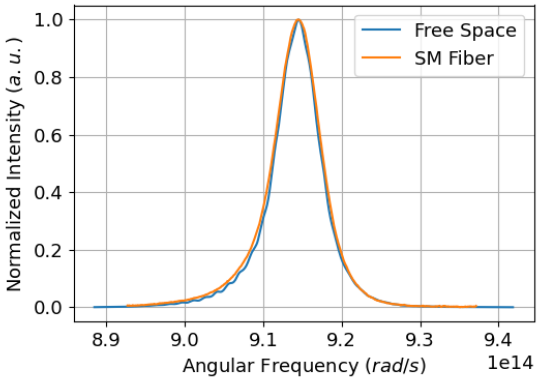

(a) Measured optical spectrum. $\Theta_{\lambda/2} = 0^o$

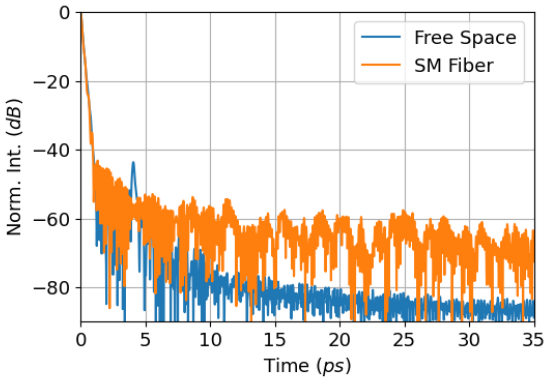

(b) Fourier transform of the measured optical spectrum.$\Theta_{\lambda/2} = 0^o$

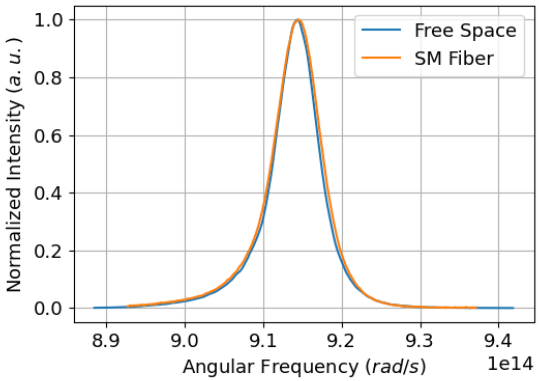

(c) Measured optical spectrum. $\Theta_{\lambda/2} = 45^o$

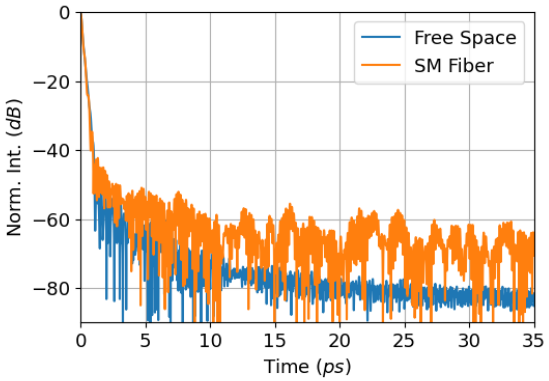

(d) Fourier transform of the measured optical spectrum.$\Theta_{\lambda/2} = 90^o$

Figure 4.20: Measured optical spectra and computed Fourier transforms for the fast and slow axis of the Tm:Ho 6/130 doped fiber for low amplification.

In Fig.4.20 the measured spectra have been included for both axes, fast and slow with the computed Fourier transform for low amplification to avoid NL effects. Due to the use of thin-film waveplates with unlabelled axes, it was not possible to identify whether light was injected into the fast or slow axis of the active fiber. This is not a problem provided that injection into one of the axis is verified which can be done by analysing the PER of the output light which should be maximum when well aligned. Then by rotating the waveplate 45^o injection into the other axis is achieved. Therefore, since the axis cannot be identified, each axis has been assigned a reference angle with respect to the waveplate angle $\Theta_{\lambda/2} = 0^o$ and $\Theta_{\lambda/2} = 45^o$. Regardless of the tested fiber axis the spectrum was almost identical independently of the injection mechanism into the OSA (SM fiber or free space injection). Minor differences can be observed when the FT is computed from the free space or SM fiber injected spectrum however better contrast is obtained when free space injection is used as more light is injected into the OSA. It is worth mentioning the appearance of a peak at $4\,ps$ in the FT for $\Theta_{\lambda/2} = 0^o$ axis $40\,dB$ below the main peak

at $0\,ps$. The origin of the peak can be understood when the waveplate angle is scanned while the measured spectrum is recorded and the FT of the spectrum is calculated. This is illustrated in Fig.4.21.

As the waveplate is scanned, the recorded spectrum changes, a set of well spaced modulations appear only visible when pulses are injected free space. The recorded spectrum when using the SM transport fiber broadens compared to the fast and slow axis ($\Theta_{\lambda/2} = 0^o$ and $\Theta_{\lambda/2} = 45^o$) and follows the envelope of the measured free space spectrum. This is because the SM fiber is not polarization maintaining and is mixing light in both axes hence it is not possible to observe the generated interference pattern. The maximum modulation depth is obtained for $\Theta_{\lambda/2} = 22^o$. This is because the polarization of the light is almost exactly between the fast and slow axis and in principle the modulation depth should reach 0. The reason why this is not happening is because the fast and slow axes have different MFDs and they are not being equally seeded. This implies that gain may be slightly different from one axis to the other which combined with the fact that the OSA relies on diffraction gratings which have different diffraction efficiencies depending on the polarization of the light, maximum modulation depth cannot be achieved. This was verified by injecting at $\Theta_{\lambda/2} = 45^o$ and adding a waveplate before the OSA to find the two maxima in signal which were significantly different. The modulation pattern depends on the delay between pulses and their chirp. TL pulses exhibit periodic modulations while chirped pulses exhibit a frequency chirp on the modulation observed in the optical spectrum. On the computed FT, a peak at $\sim 4\,ps$ has grown in intensity reaching a maximum for $\Theta_{\lambda/2} = 22^o$. This means that there is a second pulse which is delayed about $\Delta t \sim 4\,ps$ with respect to the main pulse. The delay is linked to the fiber birefringence Δn and the fiber length L ($\Delta t = \delta nL/c$) where c is the speed of light. For $\sim 3.6\,m$ of fiber, and Δt of $4\,ps$, the birefringence gives $3.3 * 10^{-4}$ above the value given by the provider of $> 2 * 10^-4$. The fiber was very sensitive to angle miss-alignment such that with variations on 1^o on the waveplate angle, small modulations on the measured optical spectrum could already be observed which then result in the peak at $4\,ps$ in the Fourier transform of the spectrum. In fact, for the recorded optical spectrum at $\Theta_{\lambda/2} = 0^o$ it was not possible to obtain good suppression of the peak at $4\,ps$ as can be seen on Fig.4.20. This suggests that active fiber splicing (splicing while seeding the fiber and/or pumping) should be tried when splicing the active fiber to the combiner or mode stripper fiber if after amplification periodic modulations appear on the spectrum. This can be done by core pumping while splicing the fiber to have some signal on the OSA and manually adjust the fiber angles if the splicing machine is not properly aligning the fibers.

The modulations observed when developing the CPA lasers were much faster and less periodic which suggests that the origin must be different or a combination of few effects. In addition, when the power was above $100\,mW$ the optical spectrum was measured using the SM fiber which is not sensitive to polarization. Maximum contrast is achieved for $\Theta_{\lambda/2} = 22^o$ and the measured PER was few dB as a result of having almost equal amount of light on both axes. When building the CPA, the PER was always at least above $\sim 14\,dB$ being the worst case when amplifying in non-saturated amplifiers as the ASE worsened the PER to $14\,dB$. The measured ACT and spectrograms as the wavelength was scanned have also been included in Fig.4.22 for $\Theta_{\lambda/2} = 0^o$ and $\Theta_{\lambda/2} = 22.5^o$.

The ACT of a single pulse is smooth however if a pair of pulses that can interfere are measured, modulations can be observed in the ACT which in addition has broadened due to the delay between the pulses. The measured pulse duration for the ACT exhibiting modulations is not accurate as the fitting is done to the envelope of the signal and the FROG technique, due to having such a complex ACT trace, was not converging. That is

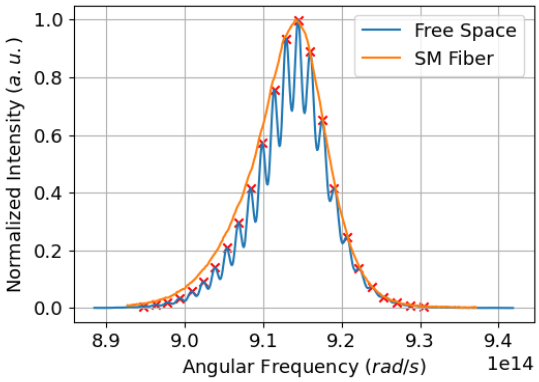

(a) Measured optical spectrum. $\Theta_{\lambda/2} = 17^o$

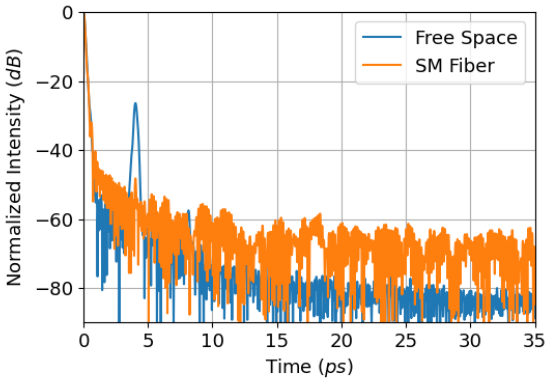

(b) Fourier transform of the measured optical spectrum.$\Theta_{\lambda/2} = 17^o$

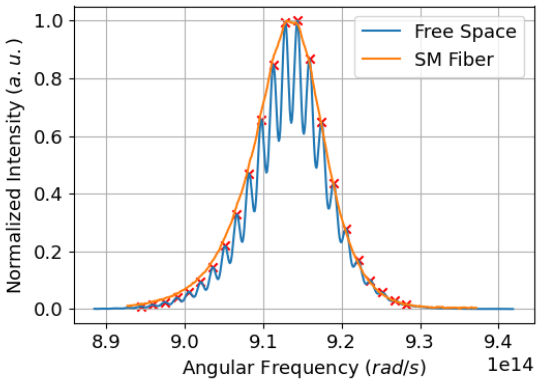

(c) Measured optical spectrum. $\Theta_{\lambda/2} = 22^o$

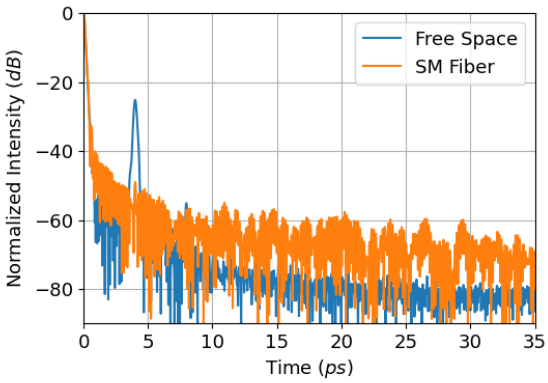

(d) Fourier transform of the measured optical spectrum.$\Theta_{\lambda/2} = 22^o$

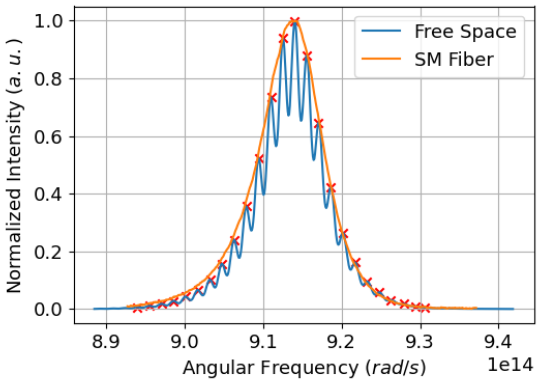

(e) Measured optical spectrum. $\Theta_{\lambda/2} = 31^o$

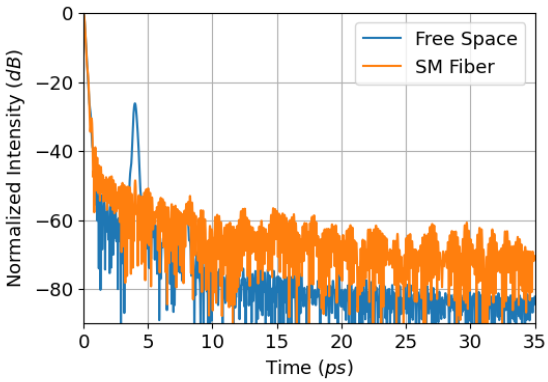

(f) Fourier transform of the measured optical spectrum.$\Theta_{\lambda/2} = 31^o$

Figure 4.21: Measured optical spectra and computed Fourier transforms when scanning the injected polarization axis in the Tm:Ho 6/130 doped fiber.

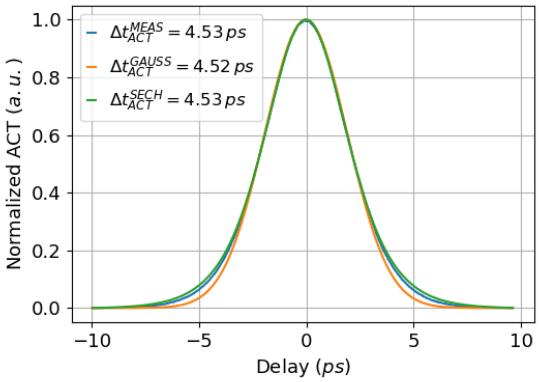

(a) Measured ACT trace. $\Theta_{\lambda/2} = 0^o$

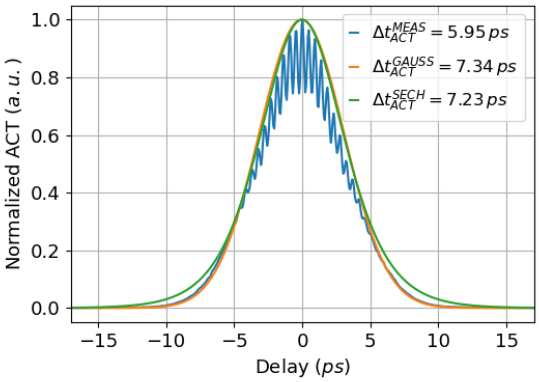

(b) Measured ACT trace. $\Theta_{\lambda/2} = 22.5^o$

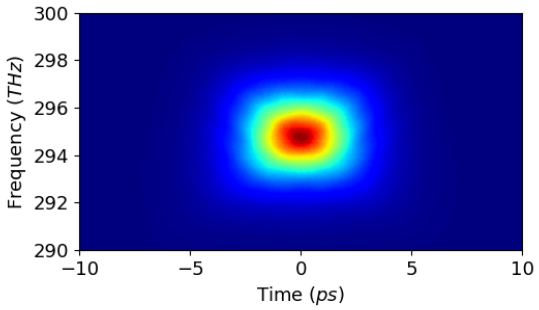

(c) Measured spectrogram. $\Theta_{\lambda/2} = 0^o$

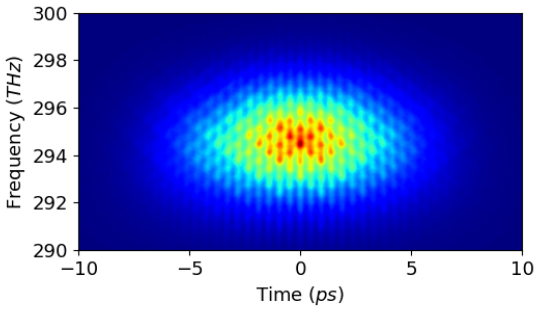

(d) Measured spectrogram. $\Theta_{\lambda/2} = 22.5^o$

Figure 4.22: Measured ACT and spectrogram for $\Theta_{\lambda/2} = 0^o$ and $\Theta_{\lambda/2} = 22.5^o$.

why only the measured spectrograms for both configurations have been included ($\Theta_{\lambda/2} = 0^o$ and $\Theta_{\lambda/2} = 22.5^o$).

If the isolator is removed and substituted by a circulator and a broadband CVBG (see Fig.4.19a) pulses can be stretched and amplified to W level to try to observe if the modulations develop as it was the case in the Tm:Ho fully spliced amplifier. The measured spectra are shown in Fig.4.23.

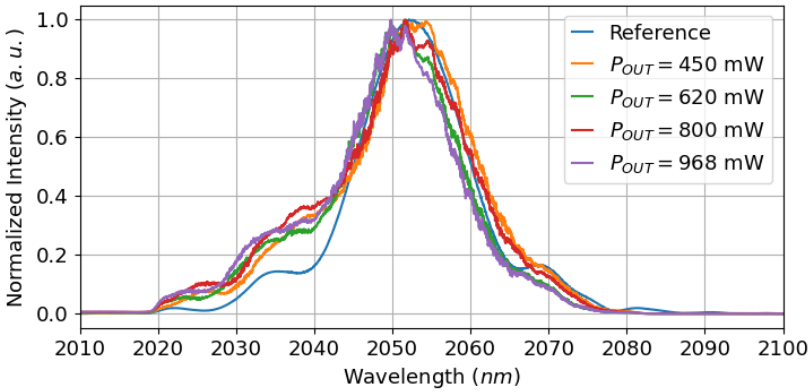

Figure 4.23: Measured optical spectra as function of the output power out of the free-space injected Tm:Ho 6/130 active fiber.

When the power is scaled in free space configuration, the measured optical spectrum maintains its shape without producing the fast modulations encountered during the development of the CPA laser systems for an output power of $0.5\,W$. This means that the active fiber is suitable for the amplification of broadband chirped pulses and that the problem is linked either to the splicing between the combiner and the active fiber or to the combiner itself. The main difference when splicing Tm or Tm:Ho fused silica doped fibers compared to Er or Yb doped fibers is the dopant concentration required to achieve optimal performance (cross-relaxation). The high doping levels may require a more accurate control on the splicing that expected to avoid undesired diffusion of the dopants during the arc process which turns out to be important not only for LMA fibers but also for small core size fibers. Due to the discovery of the splicing issue in the very end of the thesis, the complete development of the CPA lasers could not be achieved.

Conclusions

The objective of the thesis was the development of femtosecond laser sources in the $2\,\mu m$ spectral region and more specifically the development of CPA architectures, with high power and high energy. The research was motivated by the potential $2\,\mu m$ lasers have to overcome the well established Yb technology thanks to reduced non-linear effects which permit higher peak powers in the gain meda, the use of bigger LMA fibers operating in single mode regime enabling higher power scaling and the cross-relaxation effects in Tm and Tm:Ho doped fibers for efficient amplification. At the same time, long operation wavelengths opens a wide variety of applications including the generation of light in the mid IR through DFG, OPO architectures or to be used as pump laser for OPCPA taking advantage of the high efficiency of oxide non-linear crystals. This is of paramount importance for the strong-field physics research field and for spectroscopy as the IR is the molecular fingerprint spectral region.

At first, we have developed an all-fiber PM laser tunable over $170\,fs$ via SSFS delivering sub-100 fs pulses with central wavelength ranging from $1880\,nm$ up to $2050\,nm$. The Er mode-locked oscillator and the Er amplifier in combination with the non-linear fiber to trigger SSFS is an efficient approach to generate pulses in the $2\,\mu m$ spectral region where optical fibers and components are not so mature. Then, spectral broadening and NL pulse compression allows to generate the required bandwidth and to compress the pulses to sub-100 fs duration with powers ranging from $18\,mW$ up to $34\,mW$. Simulations on the post-compression stage showed that the system is very versatile as it allows customization in terms of pulse duration either at a particular wavelength or over the tunability range just by adjusting the fiber lengths involved in the post-compression stage. The present laser system is a convenient alternative to Tm, Ho and Tm:Ho oscillators as seed source for amplified laser architectures.

On the second part of the thesis we have demonstrated pulse stretching up to hundreds of ps and pulse compression down to $400\,fs$ of broadband pulses at $2.05\,\mu m$ wavelength. The effect of gain narrowing and the accumulated non-linear phase computed with the beta integral β_I with a distributed approach have been observed and taken into account when designing the CPA lasers. We have highlighted the importance of matching the stretching and compressor devices specially for broadband pulses with large stretching/compression factors as high order dispersion terms start to become very important if highly dispersive gratings are used. The lack of suitable stretchers (CFBGs and CVBGs with adjusted ϕ_3) suggests modifying the compressor to the available stretchers components by increasing the gratings size with reduced dispersion (less lines/mm) on expenses of the compressor size and operation angle.

Pulse stretching and compression of narrowband pulses ($\sim 6\,nm$ BW) down to $2\,ps$ duration has as well been demonstrated. Narrowband pulses are less sensitive to high order and uncompensated dispersion and therefore easier to achieve optimal pulse compression. Nevertheless, TL duration of $1.67\,ps$ is only achievable if the dispersion of the amplification

chain is also compensated. To reduce the repetition rate of the system, pulse picking was applied to go from $40\,MHz$ down to $1\,MHz$ with high contrast and $0.84\,mW$ output power by properly adjusting synchronization with the seed laser, gate length, delay and suitable choice of the RF signal generator. Further reduction of the repetition rate is not possible due to the high losses of the system ($10\,dB$ insertion losses) yet amplification of pulses to $\sim 0.5\,W$ level, the power level required to seed the LMA fiber amplifier.

On the last part of this thesis the performance of PM Tm:Ho co-doped fibers for pulse amplification was investigated. The cross-relaxation effect is of paramount importance to achieve efficient amplification and it has been demonstrated that it is strongly dependent on the input power. Signal to pump efficiencies vary from 19.3% up to 36.5% when the amplifiers are strongly seeded at the expense of increasing the accumulated NL phase on the amplifier. LMA fibers were as well tested with efficiencies below 30% reaching powers between $10\,W$ and $35\,W$ depending on the injection level and with potential to improve by optimizing the fiber length and increasing the pump power. The fibers were tested in a wide variety of conditions: with fs pulses which produced further SSFS up to $2.3\,\mu m$ and with few ps up to hundreds of ps for amplification with or without reduced non-linearities. An important pulse degradation the temporal and spectral domains was found when an all-fibered architecture with stretched pulses was employed compared to when the fiber was injected in free space. This suggest that splicing of the fiber is complex which may be linked to the high dopant concentration required to achieve sufficient cross-relaxation and efficient energy transfer from Tm to Ho ions.

Perspectives

The completion of the CPA is mainly limited by the spectral and temporal degradation of the amplified pulses either in high average power or high energy configuration. Few experiments to further study the seed laser and the amplifier can be performed to unravel the phenomena.

Replacing the seed laser by a mode-locked oscillator would be beneficial to test if the coherence of the seed source is responsible for the fast oscillation in the temporal and spectral domain. It has been shown that SSFS lasers can loose coherence due to quantum pick-up noise. Hence, random phase from pulse to pulse can degrade the amplification and compression of pulses. Even though we have tested our developed SSFS laser and the MIRPULSE laser, both of them rely on the SSFS effect hence using a highly coherent source such as a mode-locked oscillator would eliminate all doubts on the performance of the seed laser sources.

Amplification of pulses in the $2\,\mu m$ spectral region is usually done with Tm doped fibers and a large amount of work has been reported in the amplification of fs pulses and CPA architectures at slightly shorter wavelengths $\sim 1.96\,\mu m$. Even if the efficiency of Tm doped fibers decreases as the wavelength approaches $2.05\,\mu m$, testing amplification and compression with Tm fibers would provide information on whether the Tm:Ho fibers are suitable or not for an all-fibered configuration based on the performance of the Tm amplifier. So far, Tm:Ho fibers seem to be working properly when free space injected.

Finally, few changes could improve the performance of the high energy CPA laser system specially because of the low efficiencies and high non-linearities in the amplifiers. Efficiencies can be improved and non-linearities reduced simultaneously by core pumping the Tm:Ho 6/130 amplifiers. In-band core pumping with Er CW lasers allows for lower quantum defects, lower heat loads and higher efficiencies while reducing the active fiber length hence reducing simultaneously the non-linearities (non-linear phase). In addition, if a contra-propagation scheme is applied, gain distribution along the active fiber further reduces the non-linearities during amplification maybe even allowing higher output powers for the same non-linear phase. This would be as well beneficial for seeding the LMA fiber as higher injection powers will lead to higher efficiencies due to an enhanced cross-relaxation effect. The high energy CPA laser system would be then tested as seed laser in a multipass Ho:YLF amplifiers for further energy scaling.

Bibliography

[1] M. Gebhardt, C. Gaida, P. Kadwani, A. Sincore, N. Gehlich, C. Jeon, L. Shah, and M. Richardson, "High peak-power mid-infrared zngep 2 optical parametric oscillator pumped by a tm: fiber master oscillator power amplifier system," *Optics Letters*, vol. 39, no. 5, pp. 1212–1215, 2014.

[2] J.-Y. Huang, L.-Z. Guo, J.-Z. Wang, T.-C. Li, H.-J. Lee, P.-K. Chiu, L.-H. Peng, and T.-M. Liu, "Fiber-based 1150-nm femtosecond laser source for the minimally invasive harmonic generation microscopy," *Journal of Biomedical Optics*, vol. 22, p. 1, Mar. 2017.

[3] B. Li, M. Wang, K. Charan, M.-j. Li, and C. Xu, "Investigation of the long wavelength limit of soliton self-frequency shift in a silica fiber," *Optics Express*, vol. 26, p. 19637, July 2018.

[4] M. Tokurakawa, H. Sagara, and H. Tünnermann, "All-normal-dispersion nonlinear polarization rotation mode-locked tm: Zblan fiber laser," *Optics express*, vol. 27, no. 14, pp. 19530–19535, 2019.

[5] Z. Zhu, H. Zhang, M. Wang, R. Wei, Z. Zheng, P. Yan, S. Ruan, J. Wang, T. Hasan, and Z. Sun, "Soliton mode-locked large-mode-area tm-doped fiber oscillator," *IEEE Photonics Technology Letters*, vol. 32, no. 2, pp. 117–120, 2019.

[6] F. Haxsen, D. Wandt, U. Morgner, J. Neumann, and D. Kracht, "Monotonically chirped pulse evolution in an ultrashort pulse thulium-doped fiber laser," *Optics letters*, vol. 37, no. 6, pp. 1014–1016, 2012.

[7] Y. Meng, Y. Li, Y. Xu, and F. Wang, "Carbon nanotube mode-locked thulium fiber laser with 200 nm tuning range," *Scientific reports*, vol. 7, no. 1, p. 45109, 2017.

[8] K. Wei, H. Zhang, K. Yang, H. Zhu, P. Yan, S. Ruan, and J. Wang, "Tunable thulium-doped mode-locked fiber laser with watt-level average power," *Optics Letters*, vol. 47, no. 6, pp. 1545–1548, 2022.

[9] G. Soboń, T. Martynkien, K. Tarnowski, P. Mergo, and J. Sotor, "Generation of sub-100 fs pulses tunable from 1700 to 2100 nm from a compact frequency-shifted Er-fiber laser," *Photonics Research*, vol. 5, p. 151, June 2017.

[10] T. Karpate, G. Stepniewski, D. Pysz, A. Rampur, Y. Stepanenko, R. Buczynski, and M. Klimczak, "Soliton detuning of 68.5thz in the near-infrared in a highly nonlinear suspended core tellurite fiber," *J. Opt. Soc. Am. B*, vol. 37, pp. 1502–1509, May 2020.

[11] H. Delahaye, G. Granger, D. Gaponov, L. Lavoute, S. Aleshkina, M. Salganskii, A. Hideur, M. Likhachev, and S. Février, "Megawatt solitons generated above 2000 nm in Bragg fibers," *Optics Letters*, vol. 44, p. 2713, June 2019.

[12] N. Nishizawa and T. Goto, "Widely wavelength-tunable ultrashort pulse generation using polarization maintaining optical fibers," *IEEE Journal of selected topics in quantum electronics*, vol. 7, no. 4, pp. 518–524, 2001.

[13] P. Wang, H. Shi, F. Tan, and P. Wang, "Enhanced tunable Raman soliton source between 19 and 236 Mm in a Tm-doped fiber amplifier," *Optics Express*, vol. 25, p. 16643, July 2017.

[14] N. Nishizawa, R. Okamura, and T. Goto, "Simultaneous generation of wavelength tunable two-colored femtosecond soliton pulses using optical fibers," *IEEE Photonics Technology Letters*, vol. 11, pp. 421–423, Apr. 1999.

[15] K. S. Abedin and F. Kubota, "Widely tunable femtosecond soliton pulse generation at a 10-ghz repetition rate by use of the soliton self-frequency shift in photonic crystal fiber," *Optics letters*, vol. 28, no. 19, pp. 1760–1762, 2003.

[16] Y. Matsuo, N. Nishizawa, M. Mori, and T. Goto, "Characteristics of wavelength tunable femtosecond soliton pulse generation using femtosecond pump laser and polarization maintaining fiber," *Optical review*, vol. 7, pp. 309–316, 2000.

[17] Lou Yang and Wei Yizhen, "Widely tunable ultrashort soliton source with enhanced SSFS," in *2016 15th International Conference on Optical Communications and Networks (ICOCN)*, (Hangzhou, China), pp. 1–3, IEEE, Sept. 2016.

[18] M. Yu. Koptev, E. A. Anashkina, A. V. Andrianov, V. V. Dorofeev, A. F. Kosolapov, S. V. Muravyev, and A. V. Kim, "Widely tunable mid-infrared fiber laser source based on soliton self-frequency shift in microstructured tellurite fiber," *Optics Letters*, vol. 40, p. 4094, Sept. 2015.

[19] T. N. Nguyen, K. Kieu, D. Churin, T. Ota, M. Miyawaki, and N. Peyghambarian, "High power soliton self-frequency shift with improved flatness ranging from 1.6 to 1.78 μm," *IEEE Photonics Technology Letters*, vol. 25, no. 19, pp. 1893–1896, 2013.

[20] P. Morin, S. Boivinet, J.-P. Yehouessi, T. Berberian, F. Druon, S. Vidal, G. Machinet, F. Guichard, Y. Zaouter, and J. Boullet, "Sub-150 fs all-fiber polarization maintaining tunable laser in the mid-infrared," in *Fiber Lasers XVII: Technology and Systems*, vol. 11260, pp. 210–215, SPIE, 2020.

[21] A. Grande, D. Darwich, V. Freysz, J. Boullet, and E. Cormier, "Sub-100 fs all-fiber polarization maintaining widely tunable laser at 2 μm," *Optics Letters*, vol. 48, no. 20, pp. 5237–5240, 2023.

[22] B. Sun, J. Luo, J. Ji, X. Jin, and X. Yu, "Generation of 65-fs pulses at 2 μm in an all-fiber laser," in *CLEO: Science and Innovations*, pp. SM2I–6, Optica Publishing Group, 2017.

[23] W. Yao, M. Khalili, Y. Wang, M. Hoffmann, M. van Delden, T. Musch, and C. J. Saraceno, "Ghz repetition rate, sub-100-fs ho: Calgo laser at 2.1 um with watt-level average power," *arXiv preprint arXiv:2310.13928*, 2023.

[24] W. Yao, Y. Wang, S. Tomilov, M. Hoffmann, S. Ahmed, C. Liebald, D. Rytz, M. Peltz, V. Wesemann, and C. J. Saraceno, "8.7-w average power, in-band pumped femtosecond ho: Calgo laser at 2.1 μm," *Optics Express*, vol. 30, no. 23, pp. 41075–41083, 2022.

[25] W. Yao, Y. Wang, S. Ahmed, M. Hoffmann, M. van Delden, T. Musch, and C. J. Saraceno, "Low-noise, 2-w average power, 112-fs kerr-lens mode-locked ho: Calgo laser at 2.1 μm," *Optics Letters*, vol. 48, no. 11, pp. 2801–2804, 2023.

[26] Y. Wang, Y. Zhao, P. Loiko, Z. Pan, W. Chen, M. Mero, X. Xu, J. Xu, X. Mateos, A. Major, *et al.*, "52-fs sesam mode-locked tm, ho: Calgo laser," in *Advanced Solid State Lasers*, pp. AM3A–7, Optica Publishing Group, 2019.

[27] Y. Wang, Y. Zhao, Z. Pan, S. Suomalainen, A. Härkönen, M. Guina, U. Griebner, L. Wang, P. Loiko, X. Mateos, *et al.*, "73-fs sesam mode-locked tm, ho: Cngg laser at 2061 nm," in *Solid State Lasers XXIX: Technology and Devices*, vol. 11259, pp. 426–431, SPIE, 2020.

[28] Z. Pan, Y. Wang, Y. Zhao, M. Kowalczyk, J. Sotor, H. Yuan, Y. Zhang, X. Dai, H. Cai, J. E. Bae, *et al.*, "Sub-80 fs mode-locked tm, ho-codoped disordered garnet crystal oscillator operating at 2081 nm," *Optics letters*, vol. 43, no. 20, pp. 5154–5157, 2018.

[29] A. Suzuki, C. Kränkel, and M. Tokurakawa, "Sub-6 optical-cycle kerr-lens mode-locked tm: Lu 2 o 3 and tm: Sc 2 o 3 combined gain media laser at 2.1 μm," *Optics Express*, vol. 29, no. 13, pp. 19465–19471, 2021.

[30] A. Suzuki, Y. Wang, S. Tomilov, Z. Pan, and C. J. Saraceno, "Diode-pumped 88-fs sesam mode-locked tm, ho: Clngg laser at 2090 nm," *arXiv preprint arXiv:2311.11613*, 2023.

[31] S. Liu, P. Wang, K. Li, J. Lv, Y. Jin, X. Xu, Z. Wang, J. Liu, J. Liu, and Y. Zhao, "Sub-60-fs mode-locked tm, ho: Caylualo 4 laser at 2.05 μm," *Optics Express*, vol. 32, no. 5, pp. 7513–7519, 2024.

[32] Y. Zhao, Y. Wang, X. Zhang, X. Mateos, Z. Pan, P. Loiko, W. Zhou, X. Xu, J. Xu, D. Shen, *et al.*, "87 fs mode-locked tm, ho: Cayalo4 laser at similar to 2043 nm,"

[33] Z. Pan, L. Wang, J. E. Bae, F. Rotermund, Y. Wang, Y. Zhao, P. Loiko, X. Mateos, U. Griebner, V. Petrov, *et al.*, "Swcnt-sa mode-locked tm, ho: Lclngg laser," *Optics Express*, vol. 29, no. 24, pp. 40323–40332, 2021.

[34] F. Fusari, A. Lagatsky, G. Jose, S. Calvez, A. Jha, M. Dawson, J. Gupta, W. Sibbett, and C. Brown, "Femtosecond mode-locked tm 3+ and tm 3+-ho 3+ doped 2 μm glass lasers," *Optics Express*, vol. 18, no. 21, pp. 22090–22098, 2010.

[35] L. Wang, W. Chen, Y. Zhao, P. Loiko, X. Mateos, M. Guina, Z. Pan, M. Mero, U. Griebner, and V. Petrov, "Sub-50 fs pulse generation from a sesam mode-locked tm, ho-codoped calcium aluminate laser," *Optics Letters*, vol. 46, no. 11, pp. 2642–2645, 2021.

[36] G. Sobon, J. Sotor, I. Pasternak, A. Krajewska, W. Strupinski, and K. M. Abramski, "260 fs and 1 nj pulse generation from a compact, mode-locked tm-doped fiber laser," *Optics Express*, vol. 23, no. 24, pp. 31446–31451, 2015.

[37] H. Jeong, S. Y. Choi, M. H. Kim, F. Rotermund, Y.-H. Cha, D.-Y. Jeong, S. B. Lee, K. Lee, and D.-I. Yeom, "All-fiber tm-doped soliton laser oscillator with 6 nj pulse energy based on evanescent field interaction with monoloayer graphene saturable absorber," *Optics Express*, vol. 24, no. 13, pp. 14152–14158, 2016.

[38] Q. Zhang, X. Jin, G. Hu, M. Zhang, Z. Zheng, and T. Hasan, "Sub-150 fs dispersion-managed soliton generation from an all-fiber tm-doped laser with bp-sa," *Optics Express*, vol. 28, no. 23, pp. 34104–34110, 2020.

[39] W. Lai, H. Zhang, Z. Zhu, P. Yan, S. Ruan, Z. Sun, and J. Wang, "Sub-200 fs, 344 mhz mode-locked tm-doped fiber laser," *Optics Letters*, vol. 45, no. 19, pp. 5492–5495, 2020.

[40] B. Sun, J. Luo, B. P. Ng, and X. Yu, "Dispersion-compensation-free femtosecond tm-doped all-fiber laser with a 248 mhz repetition rate," *Optics Letters*, vol. 41, no. 17, pp. 4052–4055, 2016.

[41] J. Jiang, A. Ruehl, I. Hartl, and M. E. Fermann, "Tunable coherent raman soliton generation with a tm-fiber system," in *CLEO: Science and Innovations*, p. CThBB5, Optica Publishing Group, 2011.

[42] J. Wang, X. Liang, G. Hu, Z. Zheng, S. Lin, D. Ouyang, X. Wu, P. Yan, S. Ruan, Z. Sun, *et al.*, "152 fs nanotube-mode-locked thulium-doped all-fiber laser," *Scientific reports*, vol. 6, no. 1, p. 28885, 2016.

[43] G. Sobon, J. Sotor, T. Martynkien, and K. M. Abramski, "Ultra-broadband dissipative soliton and noise-like pulse generation from a normal dispersion mode-locked tm-doped all-fiber laser," *Optics Express*, vol. 24, no. 6, pp. 6156–6161, 2016.

[44] M. Wang, H. Zhang, R. Wei, Z. Zhu, S. Ruan, P. Yan, J. Wang, T. Hasan, and Z. Sun, "172 fs, 24.3 kw peak power pulse generation from a ho-doped fiber laser system," *Optics Letters*, vol. 43, no. 19, pp. 4619–4622, 2018.

[45] M. Pawliszewska, T. Martynkien, A. Przewłoka, and J. Sotor, "Dispersion-managed ho-doped fiber laser mode-locked with a graphene saturable absorber," *Optics Letters*, vol. 43, no. 1, pp. 38–41, 2018.

[46] A. Wienke, F. Haxsen, D. Wandt, U. Morgner, J. Neumann, and D. Kracht, "Ultrafast, stretched-pulse thulium-doped fiber laser with a fiber-based dispersion management," *Optics letters*, vol. 37, no. 13, pp. 2466–2468, 2012.

[47] N. Stevenson, C. Brown, J.-M. Hopkins, M. Dawson, C. Kränkel, and A. Lagatsky, "Diode-pumped femtosecond tm 3+-doped lusco 3 laser near 2.1 μm," *Optics Letters*, vol. 43, no. 6, pp. 1287–1290, 2018.

[48] C. Gao, Z. Wang, H. Luo, and L. Zhan, "High energy all-fiber tm-doped femtosecond soliton laser mode-locked by nonlinear polarization rotation," *Journal of Lightwave technology*, vol. 35, no. 14, pp. 2988–2993, 2017.

[49] P. Li, A. Ruehl, U. Grosse-Wortmann, and I. Hartl, "Sub-100 fs passively mode-locked holmium-doped fiber oscillator operating at 2.06 μm," *Optics letters*, vol. 39, no. 24, pp. 6859–6862, 2014.

[50] R. Sharp, D. Spock, N. Pan, and J. Elliot, "190-fs passively mode-locked thulium fiber laser with a low threshold," *Optics letters*, vol. 21, no. 12, pp. 881–883, 1996.

[51] B. Ren, C. Li, T. Wang, K. Guo, and P. Zhou, "All-polarization-maintaining figure-9 mode-locked tm-doped fiber laser with amplitude noise and timing jitter suppression," *Journal of Lightwave Technology*, vol. 41, no. 2, pp. 733–738, 2022.

[52] B. Ren, C. Li, T. Wang, K. Guo, and P. Zhou, "Stable noise-like pulse generation from a nalm-based all-pm tm-doped fiber laser," *Optics Express*, vol. 30, no. 15, pp. 26464–26471, 2022.

[53] D. Strickland and G. Mourou, "Compression of amplified chirped optical pulses," *Optics communications*, vol. 55, no. 6, pp. 447–449, 1985.

[54] C. Gaida, M. Gebhardt, T. Heuermann, F. Stutzki, C. Jauregui, and J. Limpert, "Ultrafast thulium fiber laser system emitting more than 1 kw of average power," *Optics letters*, vol. 43, no. 23, pp. 5853–5856, 2018.

[55] S. A. Rezvani, M. Suzuki, P. Malevich, C. Livache, J. V. De Montgolfier, Y. Nomura, N. Tsurumachi, A. Baltuška, and T. Fuji, "Millijoule femtosecond pulses at 1937 nm from a diode-pumped ring cavity tm: Yap regenerative amplifier," *Optics Express*, vol. 26, no. 22, pp. 29460–29470, 2018.

[56] U. Elu, T. Steinle, D. Sánchez, L. Maidment, K. Zawilski, P. Schunemann, U. Zeitner, C. Simon-Boisson, and J. Biegert, "Table-top high-energy 7 μm opcpa and 260 mj ho: Ylf pump laser," *Optics letters*, vol. 44, no. 13, pp. 3194–3197, 2019.

[57] P. Wan, L.-M. Yang, and J. Liu, "156 micro-j ultrafast thulium-doped fiber laser," in *Fiber Lasers X: Technology, Systems, and Applications*, vol. 8601, pp. 455–461, SPIE, 2013.

[58] T. Heuermann, Z. Wang, M. Lenski, M. Gebhardt, C. Gaida, M. Abdelaal, J. Buldt, M. Müller, A. Klenke, and J. Limpert, "Ultrafast tm-doped fiber laser system delivering 1.65-mj, sub-100-fs pulses at a 100-khz repetition rate," *Optics Letters*, vol. 47, no. 12, pp. 3095–3098, 2022.

[59] L. von Grafenstein, M. Bock, D. Ueberschaer, A. Koç, U. Griebner, and T. Elsaesser, "2.05 μm chirped pulse amplification system at a 1 khz repetition rate—2.4 ps pulses with 17 gw peak power," *Optics Letters*, vol. 45, no. 14, pp. 3836–3839, 2020.

[60] P. Gierschke, C. Grebing, M. Abdelaal, M. Lenski, J. Buldt, Z. Wang, T. Heuermann, M. Mueller, M. Gebhardt, J. Rothhardt, *et al.*, "Nonlinear pulse compression to 51-w average power gw-class 35-fs pulses at 2-μm wavelength in a gas-filled multipass cell," *Optics Letters*, vol. 47, no. 14, pp. 3511–3514, 2022.

[61] C. Gaida, F. Stutzki, M. Gebhardt, T. Heuermann, S. Breitkopf, T. Eidam, J. Rothhardt, and J. Limpert, "Long-term-stable thulium-doped fiber cpa with> 100w average power and> 1gw peak power," in *International Conference on Ultrafast Phenomena*, pp. W2A–6, Optica Publishing Group, 2020.

[62] R. A. Sims, P. Kadwani, A. S. L. Shah, and M. Richardson, "1 μj, sub-500 fs chirped pulse amplification in a tm-doped fiber system," *Optics Letters*, vol. 38, no. 2, pp. 121–123, 2013.

[63] J. Černohorská, M. Písařík, P. Peterka, J. Aubrecht, R. Amani, O. Novák, M. Smrž, M. Jelínek, A. Lucianetti, A. Endo, *et al.*, "High-energy subpicosecond 2-um fiber laser," in *Fiber Lasers and Glass Photonics: Materials through Applications*, vol. 10683, pp. 161–166, SPIE, 2018.

[64] M. Gebhardt, C. Gaida, T. Heuermann, F. Stutzki, C. Jauregui, J. Antonio-Lopez, A. Schulzgen, R. Amezcua-Correa, J. Limpert, and A. Tünnermann, "Nonlinear pulse compression to 43 w gw-class few-cycle pulses at 2 μm wavelength," *Optics letters*, vol. 42, no. 20, pp. 4179–4182, 2017.

[65] C. Gaida, M. Gebhardt, F. Stutzki, C. Jauregui, J. Limpert, and A. Tünnermann, "Thulium-doped fiber chirped-pulse amplification system with 2 gw of peak power," *Optics letters*, vol. 41, no. 17, pp. 4130–4133, 2016.

[66] M. Gebhardt, C. Gaida, F. Stutzki, S. Hädrich, C. Jauregui, J. Limpert, and A. Tünnermann, "High average power nonlinear compression to 4 gw, sub-50 fs pulses at 2 μm wavelength," *Optics letters*, vol. 42, no. 4, pp. 747–750, 2017.

[67] M. Hemmer, D. Sánchez, M. Jelínek, V. Smirnov, H. Jelinkova, V. Kubeček, and J. Biegert, "2-μm wavelength, high-energy ho: Ylf chirped-pulse amplifier for mid-infrared opcpa," *Optics letters*, vol. 40, no. 4, pp. 451–454, 2015.

[68] L. von Grafenstein, M. Bock, G. Steinmeyer, U. Griebner, and T. Elsaesser, "Taming chaos: 16 mj picosecond ho: Ylf regenerative amplifier with 0.7 khz repetition rate," *Laser & Photonics Reviews*, vol. 10, no. 1, pp. 123–130, 2016.

[69] L. von Grafenstein, M. Bock, U. Griebner, and T. Elsaesser, "High-energy multi-kilohertz ho-doped regenerative amplifiers around 2 μm," *Optics express*, vol. 23, no. 11, pp. 14744–14752, 2015.

[70] P. Kroetz, A. Ruehl, G. Chatterjee, A.-L. Calendron, K. Murari, H. Cankaya, P. Li, F. X. Kärtner, I. Hartl, and R. D. Miller, "Overcoming bifurcation instability in high-repetition-rate ho: Ylf regenerative amplifiers," *Optics letters*, vol. 40, no. 23, pp. 5427–5430, 2015.

[71] L. von Grafenstein, M. Bock, and U. Griebner, "Bifurcation analysis in high repetition rate regenerative amplifiers," *IEEE Journal of Selected Topics in Quantum Electronics*, vol. 24, no. 5, pp. 1–13, 2018.

[72] K. Murari, H. Cankaya, P. Kroetz, G. Cirmi, P. Li, A. Ruehl, I. Hartl, and F. X. Kärtner, "Intracavity gain shaping in millijoule-level, high gain ho: Ylf regenerative amplifiers," *Optics letters*, vol. 41, no. 6, pp. 1114–1117, 2016.

[73] K. Murari, H. Cankaya, P. Li, A. Ruehl, I. Hartl, and F. X. Kärtner, "1.2 mj, 1 khz, ps-pulses at 2.05 μm from a ho: fibre/ho: Ylf laser," in *Europhoton Conference*, 2014.

[74] L. Von Grafenstein, M. Bock, D. Ueberschaer, U. Griebner, and T. Elsaesser, "Ho: Ylf chirped pulse amplification at kilohertz repetition rates–4.3 ps pulses at 2 μm with gw peak power," *Optics Letters*, vol. 41, no. 20, pp. 4668–4671, 2016.

[75] L. von Grafenstein, M. Bock, D. Ueberschaer, U. Griebner, and T. Elsaesser, "Picosecond 34 mj pulses at khz repetition rates from a ho: Ylf amplifier at 2 μm wavelength," *Optics Express*, vol. 23, no. 26, pp. 33142–33149, 2015.

[76] P. Malevich, T. Kanai, H. Hoogland, R. Holzwarth, A. Baltuška, and A. Pugžlys, "Millijoule 1-ps pulses from a khz ho: Yag regenerative amplifier seeded with a tm, ho-fiber laser," in *CLEO: Science and Innovations*, pp. SM1P–4, Optica Publishing Group, 2015.

[77] K. Murari, H. Cankaya, B. Debord, P. Li, G. Cirmi, G. Rossi, S. Fang, O. Muecke, P. Kroetz, G. Stein, *et al.*, "Sub-300 fs, 0.5 mj pulse at 1khz from ho: Ylf amplifier and kagome pulse compression," in *2015 Conference on Lasers and Electro-Optics (CLEO)*, pp. 1–2, IEEE, 2015.

[78] P. Kroetz, A. Ruehl, G. Chatterjee, P. Li, K. Murari, H. Cankaya, A.-L. Calendron, F. X. Kärtner, I. Hartl, and R. D. Miller, "Ho: Ylf regenerative amplifier with 6.9 mj at 1 khz overcoming bifurcation instability," in *Advanced Solid State Lasers*, pp. ATh3A–4, Optica Publishing Group, 2015.

[79] L. von Grafenstein, M. Bock, U. Griebner, and T. Elsaesser, "8 mj, 1 khz, picosecond ho: Ylf regenerative amplifier," in *Advanced Solid State Lasers*, pp. AW4A–8, Optica Publishing Group, 2015.

[80] F. Zhou, A. Cintron, Y. Wu, and Z. Chang, "Enhancement of gain and efficiency of an ho: Ylf energy booster through deep thermoelectric cooling," *Optics Continuum*, vol. 1, no. 5, pp. 1060–1066, 2022.

[81] T. Nagy, L. von Grafenstein, D. Ueberschaer, and U. Griebner, "Femtosecond multi-10-mj pulses at 2 μm wavelength by compression in a hollow-core fiber," *Optics Letters*, vol. 46, no. 13, pp. 3033–3036, 2021.

[82] I. Astrauskas, T. Flöry, A. Pugžlys, and A. Baltuška, "Ho: Yag amplifier with dispersion control and spectral shaping in a single volume bragg grating," in *The European Conference on Lasers and Electro-Optics*, p. ca_9_5, Optica Publishing Group, 2019.

[83] M. Hinkelmann, D. Wandt, U. Morgner, J. Neumann, and D. Kracht, "High repetition rate, μj-level, cpa-free ultrashort pulse multipass amplifier based on ho: Ylf," *Optics Express*, vol. 26, no. 14, pp. 18125–18130, 2018.

[84] M. Hinkelmann, B. Schulz, D. Wandt, U. Morgner, M. Frede, J. Neumann, and D. Kracht, "Millijoule-level, kilohertz-rate, cpa-free linear amplifier for 2 μm ultrashort laser pulses," *Optics Letters*, vol. 43, no. 23, pp. 5857–5860, 2018.

[85] P. Malevich, G. Andriukaitis, T. Flöry, A. Verhoef, A. Fernández, S. Ališauskas, A. Pugžlys, A. Baltuška, L. Tan, C. Chua, *et al.*, "High energy and average power femtosecond laser for driving mid-infrared optical parametric amplifiers," *Optics Letters*, vol. 38, no. 15, pp. 2746–2749, 2013.

[86] M. Duda, L. Von Grafenstein, M. Bock, D. Ueberschaer, P. Fuertjes, L. Roškot, M. Smrž, O. Novák, and U. Griebner, "10-μj few-cycle 12-μm source based on difference-frequency generation driven by a 1-khz mid-wave infrared opcpa," *Optics Letters*, vol. 47, no. 11, pp. 2891–2894, 2022.

[87] L. von Grafenstein, M. Bock, D. Ueberschaer, E. Escoto, A. Koç, K. Zawilski, P. Schunemann, U. Griebner, and T. Elsaesser, "Multi-millijoule, few-cycle 5 μm opcpa at 1 khz repetition rate," *Optics Letters*, vol. 45, no. 21, pp. 5998–6001, 2020.

[88] P. Malevich, T. Kanai, H. Hoogland, R. Holzwarth, A. Baltuška, and A. Pugžlys, "Broadband mid-infrared pulses from potassium titanyl arsenate/zinc germanium phosphate optical parametric amplifier pumped by tm, ho-fiber-seeded ho: Yag chirped-pulse amplifier," *Optics Letters*, vol. 41, no. 5, pp. 930–933, 2016.

[89] T. Kanai, P. Malevich, S. S. Kangaparambil, K. Ishida, M. Mizui, K. Yamanouchi, H. Hoogland, R. Holzwarth, A. Pugzlys, and A. Baltuska, "Parametric amplification of 100 fs mid-infrared pulses in zngep 2 driven by a ho: Yag chirped-pulse amplifier," *Optics letters*, vol. 42, no. 4, pp. 683–686, 2017.

[90] P. Kroetz, A. Ruehl, G. Chatterjee, A.-L. Calendron, K. Muraria, H. Cankaya, F. X. Kärtnera, I. Hartl, and R. D. Miller, "High energetic and highly stable pulses from a ho: Ylf regenerative amplifier," in *Solid State Lasers XXV: Technology and Devices*, vol. 9726, pp. 135–144, SPIE, 2016.

[91] A. Wienke, D. Wandt, U. Morgner, J. Neumann, and D. Kracht, "700 mw peak power of a 380 fs regenerative amplifier with tm: Yap," *Optics Express*, vol. 23, no. 13, pp. 16884–16889, 2015.

[92] A. V. Smith and J. J. Smith, "Mode instability thresholds for tm-doped fiber amplifiers pumped at 790 nm," *Optics Express*, vol. 24, no. 2, pp. 975–992, 2016.

[93] D. Marcuse, "Gaussian approximation of the fundamental modes of graded-index fibers," *Journal of The Optical Society of America*, vol. 68, pp. 103–109, Jan. 1978.

[94] K. W. DeLong, R. Trebino, J. Hunter, and W. E. White, "Frequency-resolved optical gating with the use of second-harmonic generation," *Journal of the Optical Society of America B: Optical Physics*, vol. 11, pp. 2206–2215, Nov. 1994.

[95] G. P. Agrawal, "Nonlinear fiber optics," in *Nonlinear Science at the Dawn of the 21st Century*, pp. 195–211, Springer, 2000.

[96] D. Marcuse, "Light transmission optics," *New York*, 1982.

[97] J. A. Buck, *Fundamentals of optical fibers*, vol. 50. John Wiley & Sons, 2004.

[98] R. W. Boyd, *Nonlinear optics*. Academic press, 2020.

[99] D. Milam, "Review and assessment of measured values of the nonlinear refractive-index coefficient of fused silica," *Appl. Opt.*, vol. 37, pp. 546–550, Jan 1998.

[100] D. N. Christodoulides, I. C. Khoo, G. J. Salamo, G. I. Stegeman, and E. W. Van Stryland, "Nonlinear refraction and absorption: mechanisms and magnitudes," *Advances in Optics and Photonics*, vol. 2, no. 1, pp. 60–200, 2010.

[101] R. H. Stolen, J. P. Gordon, W. Tomlinson, and H. A. Haus, "Raman response function of silica-core fibers," *JOSA B*, vol. 6, no. 6, pp. 1159–1166, 1989.

[102] J. Sotor and G. Sobon, "24 fs and 3 nj pulse generation from a simple, all polarization maintaining er-doped fiber laser," *Laser Physics Letters*, vol. 13, no. 12, p. 125102, 2016.

[103] W. Tomlinson, R. Stolen, and C. Shank, "Compression of optical pulses chirped by self-phase modulation in fibers," *JOSA B*, vol. 1, no. 2, pp. 139–149, 1984.

[104] M. Müller, J. Buldt, H. Stark, C. Grebing, and J. Limpert, "Multipass cell for high-power few-cycle compression," *Optics Letters*, vol. 46, no. 11, pp. 2678–2681, 2021.

[105] T. Li, *Optical fiber communications: fiber fabrication*. Elsevier, 2012.

[106] T. Heuermann, C. Gaida, M. Gebhardt, and J. Limpert, "Thulium-doped nonlinear fiber amplifier delivering 50 fs pulses at 20 W of average power," *Optics Letters*, vol. 43, p. 4441, Sept. 2018.

[107] M. Gebhardt, C. Gaida, S. Hädrich, F. Stutzki, C. Jauregui, J. Limpert, and A. Tünnermann, "Nonlinear compression of an ultrashort-pulse thulium-based fiber laser to sub-70 fs in kagome photonic crystal fiber," *Optics letters*, vol. 40, no. 12, pp. 2770–2773, 2015.

[108] L. F. Mollenauer, R. H. Stolen, and J. P. Gordon, "Experimental observation of picosecond pulse narrowing and solitons in optical fibers," *Physical Review Letters*, vol. 45, no. 13, p. 1095, 1980.

[109] M. Bass, E. W. Van Stryland, D. R. Williams, and W. L. Wolfe, *Handbook of optics*, vol. 2. McGraw-Hill New York, 1995.

[110] J. P. Gordon, "Theory of the soliton self-frequency shift," *Optics Letters*, vol. 11, p. 662, Oct. 1986.

[111] F. M. Mitschke and L. F. Mollenauer, "Discovery of the soliton self-frequency shift," *Optics Letters*, vol. 11, p. 659, Oct. 1986.

[112] P. Beaud, W. Hodel, B. Zysset, and H. Weber, "Ultrashort pulse propagation, pulse breakup, and fundamental soliton formation in a single-mode optical fiber," *IEEE journal of quantum electronics*, vol. 23, no. 11, pp. 1938–1946, 1987.

[113] J. M. Dudley, G. Genty, and S. Coen, "Supercontinuum generation in photonic crystal fiber," *Reviews of modern physics*, vol. 78, no. 4, p. 1135, 2006.

[114] O. Szewczyk, K. Tarnowski, A. Głuszek, D. Szulc, K. Stefańska, P. Mergo, and G. Soboń, "All-normal dispersion supercontinuum vs frequency-shifted solitons pumped at 1560 nm as seed sources for thulium-doped fiber amplifiers," *Optics Express*, vol. 29, p. 18122, June 2021.

[115] Y. Tang, L. G. Wright, K. Charan, T. Wang, C. Xu, and F. W. Wise, "Generation of intense 100 fs solitons tunable from 2 to 43 Mm in fluoride fiber," *Optica*, vol. 3, p. 948, Sept. 2016.

[116] J. Takayanagi, T. Sugiura, M. Yoshida, and N. Nishizawa, "1.0–1.7-μm Wavelength-Tunable Ultrashort-Pulse Generation Using Femtosecond Yb-Doped Fiber Laser and Photonic Crystal Fiber," *IEEE Photonics Technology Letters*, vol. 18, pp. 2284–2286, Nov. 2006.

[117] S. Kelly, "Characteristic sideband instability of periodically amplified average soliton," *Electronics Letters*, vol. 28, no. 8, p. 806, 1992.

[118] N. Smith, K. Blow, and I. Andonovic, "Sideband generation through perturbations to the average soliton model," *Journal of Lightwave Technology*, vol. 10, pp. 1329–1333, Oct. 1992.

[119] M. Dennis and I. Duling, "Experimental study of sideband generation in femtosecond fiber lasers," *IEEE Journal of Quantum Electronics*, vol. 30, pp. 1469–1477, June 1994.

[120] F. Liu, J. Li, H. Luo, Q. Wu, X. Wu, F. Ouellette, and Y. Liu, "Study on soliton self-frequency shift in a Tm-doped fiber amplifier seeded by a Kelly-sideband-suppressed conventional soliton," *Optics Express*, vol. 29, p. 6553, Mar. 2021.

[121] R. Guan, F. Zhu, Z. Gan, D. Huang, and S. Liu, "Stress birefringence analysis of polarization maintaining optical fibers," *Optical Fiber Technology*, vol. 11, pp. 240–254, July 2005. https://web.archive.org/web/20211125215718/https://www.sciencedirect.com/science/article/ab

[122] H. Renner, "Bending losses of coated single-mode fibers: a simple approach," *Journal of Lightwave technology*, vol. 10, no. 5, pp. 544–551, 1992.

[123] D. N. Payne, A. J. Barlow, and J. R. Hansen, "Development of low-and high-birefringence optical fibers," *IEEE Transactions on microwave theory and techniques*, vol. 30, no. 4, pp. 323–334, 1982.

[124] J. Luo, B. Sun, J. Ji, E. L. Tan, Y. Zhang, and X. Yu, "High-efficiency femtosecond Raman soliton generation with a tunable wavelength beyond 2 Mm," *Optics Letters*, vol. 42, p. 1568, Apr. 2017.

[125] J. Wang, S. Lin, X. Liang, M. Wang, P. Yan, G. Hu, T. Albrow-Owen, S. Ruan, Z. Sun, and T. Hasan, "High-energy and efficient Raman soliton generation tunable from 198 to 229 Mm in an all-silica-fiber thulium laser system," *Optics Letters*, vol. 42, p. 3518, Sept. 2017.

[126] S. Kivisto, T. Hakulinen, M. Guina, and O. G. Okhotnikov, "Tunable Raman Soliton Source Using Mode-Locked Tm–Ho Fiber Laser," *IEEE Photonics Technology Letters*, vol. 19, pp. 934–936, June 2007.

[127] G. Imeshev and M. E. Fermann, "230-kW peak power femtosecond pulses from a high power tunable source based on amplification in Tm-doped fiber," *Optics Express*, vol. 13, no. 19, p. 7424, 2005.

[128] F. L. Galeener, J. Mikkelsen, J. C., R. H. Geils, and W. J. Mosby, "The relative Raman cross sections of vitreous SiO2, GeO2, B2O3, and P2O5," *Applied Physics Letters*, vol. 32, pp. 34–36, 08 2008.

[129] Y. Li, T. Du, B. Xu, H. Xu, Z. Cai, V. M. Mashinsky, and Z. Luo, "Compact all-fiber 2.1-2.7 μ m tunable Raman soliton source based on germania-core fiber," *Optics Express*, vol. 27, p. 28544, Sept. 2019.

[130] E. A. Anashkina, A. V. Andrianov, M. Yu. Koptev, S. V. Muravyev, and A. V. Kim, "Generating femtosecond optical pulses tunable from 2 to 3 Mm with a silica-based all-fiber laser system," *Optics Letters*, vol. 39, p. 2963, May 2014.

[131] G. Soboń, T. Martynkien, D. Tomaszewska, K. Tarnowski, P. Mergo, and J. Sotor, "All-in-fiber amplification and compression of coherent frequency-shifted solitons tunable in the 1800–2000 nm range," *Photonics Research*, vol. 6, p. 368, May 2018.

[132] H. Delahaye, G. Granger, J.-T. Gomes, L. Lavoute, D. Gaponov, N. Ducros, and S. Fevrier, "Generation of 35 kW peak power 80 fs pulses at 29 Mm from a fully fusion-spliced fiber laser," *Optics Letters*, vol. 44, p. 2318, May 2019.

[133] M. Louisy, C. Guo, L. Neoričić, S. Zhong, A. L'Huillier, C. L. Arnold, and M. Miranda, "Compact single-shot d-scan setup for the characterization of few-cycle laser pulses," *Appl. Opt.*, vol. 56, pp. 9084–9089, Nov 2017.

[134] P. Ciąćka, A. Rampur, A. Heidt, T. Feurer, and M. Klimczak, "Dispersion measurement of ultra-high numerical aperture fibers covering thulium, holmium, and erbium emission wavelengths," *JOSA B*, vol. 35, no. 6, pp. 1301–1307, 2018.

[135] W. Yang, B. Zhang, K. Yin, X. Zhou, and J. Hou, "High power all fiber mid-ir supercontinuum generation in a zblan fiber pumped by a 2 μm mopa system," *Opt. Express*, vol. 21, pp. 19732–19742, Aug 2013.

[136] P. Hlubina, M. Kadulová, and D. Ciprian, "Spectral interferometry-based chromatic dispersion measurement of fibre including the zero-dispersion wavelength," *Journal of the European Optical Society-Rapid publications*, vol. 7, 2012.

[137] S. Kane and J. Squier, "Grism-pair stretcher–compressor system for simultaneous second-and third-order dispersion compensation in chirped-pulse amplification," *JOSA B*, vol. 14, no. 3, pp. 661–665, 1997.

[138] O. Martinez, J. Gordon, and R. Fork, "Negative group-velocity dispersion using refraction," *JOSA A*, vol. 1, no. 10, pp. 1003–1006, 1984.

[139] N. Cassinerio, P. Laporta, and G. Galzerano, "Single-clad tmho: fiber amplifier for high-power sub-100-fs pulses around 1.9 μm," *Opt. Letters*, vol. 38, pp. 2757–2759, 2013.

[140] A. M. Weiner, "Femtosecond pulse shaping using spatial light modulators," *Review of scientific instruments*, vol. 71, no. 5, pp. 1929–1960, 2000.

[141] N. Thiré, R. Maksimenka, B. Kiss, C. Ferchaud, G. Gitzinger, T. Pinoteau, H. Jousselin, S. Jarosch, P. Bizouard, V. D. Pietro, E. Cormier, K. Osvay, and N. Forget, "Highly stable, 15 w, few-cycle, 65 mrad cep-noise mid-ir opcpa for statistical physics," *Opt. Express*, vol. 26, pp. 26907–26915, Oct 2018.

[142] R. Kashyap, *Fiber bragg gratings*. Academic press, 2009.

[143] T. Erdogan, "Fiber grating spectra," *Journal of lightwave technology*, vol. 15, no. 8, pp. 1277–1294, 1997.

[144] J. Thomas, C. Voigtlaender, R. G. Becker, D. Richter, A. Tuennermann, and S. Nolte, "Femtosecond pulse written fiber gratings: a new avenue to integrated fiber technology," 2012.

[145] L. Glebov, "Fluorinated silicate glass for conventional and holographic optical elements," in *Window and Dome Technologies and Materials X*, vol. 6545, pp. 67–75, SPIE, 2007.

[146] L. Glebov, V. Smirnov, E. Rotari, I. Cohanoschi, L. Glebova, O. Smolski, J. Lumeau, C. Lantigua, and A. Glebov, "Volume-chirped bragg gratings: monolithic components for stretching and compression of ultrashort laser pulses," *Optical Engineering*, vol. 53, no. 5, pp. 051514–051514, 2014.

[147] O. Andrusyak, L. Canioni, I. Cohanoshi, M. Delaigue, E. Rotari, V. Smirnov, and L. Glebov, "Sectional chirped volume bragg grating compressors for high-power chirped-pulse amplification," in *Solid State Lasers XIX: Technology and Devices*, vol. 7578, pp. 313–323, SPIE, 2010.

[148] E. Popov, L. Tsonev, and D. Maystre, "Gratings—general properties of the littrow mounting and energy flow distribution," *Journal of Modern Optics*, vol. 37, no. 3, pp. 367–377, 1990.

[149] C. Palmer and E. G. Loewen, "Diffraction grating handbook," 2005.

[150] E. Treacy, "Optical pulse compression with diffraction gratings," *IEEE Journal of quantum Electronics*, vol. 5, no. 9, pp. 454–458, 1969.

[151] G. R. Harrison, "The production of diffraction gratings: Ii. the design of echelle gratings and spectrographs1," *JOSA*, vol. 39, no. 7, pp. 522–528, 1949.

[152] E. G. Loewen and E. Popov, *Diffraction gratings and applications*. CRC Press, 2018.

[153] J. Neauport, E. Lavastre, G. Razé, G. Dupuy, N. Bonod, M. Balas, G. De Villele, J. Flamand, S. Kaladgew, and F. Desserouer, "Effect of electric field on laser induced damage threshold of multilayer dielectric gratings," *Optics Express*, vol. 15, no. 19, pp. 12508–12522, 2007.

[154] N. Bonod and J. Neauport, "Diffraction gratings: from principles to applications in high-intensity lasers," *Advances in Optics and Photonics*, vol. 8, no. 1, pp. 156–199, 2016.

[155] S. Kane and J. Squier, "Grating compensation of third-order material dispersion in the normal dispersion regime: sub-100-fs chirped-pulse amplification using a fiber stretcher and grating-pair compressor," *IEEE journal of quantum electronics*, vol. 31, no. 11, pp. 2052–2057, 1995.

[156] S. Kane and J. Squier, "Fourth-order-dispersion limitations of aberration-free chirped-pulse amplification systems," *JOSA B*, vol. 14, no. 5, pp. 1237–1244, 1997.

[157] O. Martinez, "Design of high-power ultrashort pulse amplifiers by expansion and recompression," *IEEE Journal of Quantum Electronics*, vol. 23, no. 8, pp. 1385–1387, 1987.

[158] A. Offner, "New concepts in projection mask aligners," *Optical Engineering*, vol. 14, no. 2, pp. 130–132, 1975.

[159] B. Lemoff and C. Barty, "Quintic-phase-limited, spatially uniform expansion and recompression of ultrashort optical pulses," *Optics letters*, vol. 18, no. 19, pp. 1651–1653, 1993.

[160] R. L. Fork, C. B. Cruz, P. Becker, and C. V. Shank, "Compression of optical pulses to six femtoseconds by using cubic phase compensation," *Optics letters*, vol. 12, no. 7, pp. 483–485, 1987.

[161] Y. Chiba, H. Takada, K. Torizuka, and K. Misawa, "65-fs yb-doped fiber laser system with gain-narrowing compensation," *Optics express*, vol. 23, no. 5, pp. 6809–6814, 2015.

[162] Z. Zhong, W. Gong, H. Jiang, H. Gu, X. Chen, and S. Liu, "Investigation of spatial chirp induced by misalignments in a parallel grating pair pulse stretcher," *Applied sciences*, vol. 10, no. 5, p. 1584, 2020.

[163] K. Osvay, A. P. Kovács, Z. Heiner, G. Kurdi, J. Klebniczki, and M. Csatári, "Angular dispersion and temporal change of femtosecond pulses from misaligned pulse compressors," *IEEE Journal of selected topics in quantum electronics*, vol. 10, no. 1, pp. 213–220, 2004.

[164] D. N. Schimpf, J. Limpert, and A. Tünnermann, "Controlling the influence of spm in fiber-based chirped-pulse amplification systems by using an actively shaped parabolic spectrum," *Optics express*, vol. 15, no. 25, pp. 16945–16953, 2007.

[165] D. N. Schimpf, T. Eidam, E. Seise, S. Hädrich, J. Limpert, and A. Tünnermann, "Circular versus linear polarization in laser-amplifiers with kerr-nonlinearity," *Optics express*, vol. 17, no. 21, pp. 18774–18781, 2009.

[166] D. Schimpf, E. Seise, T. Eidam, J. Limpert, and A. Tünnermann, "Control of the optical kerr effect in chirped-pulse-amplification systems using model-based phase shaping," *Optics letters*, vol. 34, no. 24, pp. 3788–3790, 2009.

[167] C. Gaida, M. Gebhardt, T. Heuermann, F. Stutzki, C. Jauregui, and J. Limpert, "Ultrafast thulium fiber laser system emitting more than 1 kw of average power," *Opt. Lett.*, vol. 43, pp. 5853–5856, Dec 2018.

[168] G. Soboń, T. Martynkien, P. Mergo, L. Rutkowski, and A. Foltynowicz, "High-power frequency comb source tunable from 2.7 to 4.2 μm based on difference frequency generation pumped by an yb-doped fiber laser," *Optics letters*, vol. 42, no. 9, pp. 1748–1751, 2017.

[169] P. Peterka, B. Faure, W. Blanc, M. Karasek, and B. Dussardier, "Theoretical modelling of s-band thulium-doped silica fibre amplifiers," *Optical and Quantum Electronics*, vol. 36, pp. 201–212, 2004.

[170] M. Lenski, T. Heuermann, M. Gebhardt, Z. Wang, C. Gaida, C. Jauregui, and J. Limpert, "Inband-pumped, high-power thulium-doped fiber amplifiers for an ultrafast pulsed operation," *Optics Express*, vol. 30, no. 24, pp. 44270–44282, 2022.

[171] S. D. Jackson and T. A. King, "Theoretical modeling of tm-doped silica fiber lasers," *Journal of lightwave technology*, vol. 17, no. 5, p. 948, 1999.

[172] M. Kamrádek, J. Aubrecht, P. Vařák, J. Cajzl, V. Kubeček, P. Honzátko, I. Kašík, and P. Peterka, "Energy transfer coefficients in thulium-doped silica fibers," *Optical Materials Express*, vol. 11, no. 6, pp. 1805–1814, 2021.

[173] S. D. Jackson, "Cross relaxation and energy transfer upconversion processes relevant to the functioning of 2 μm tm3+-doped silica fibre lasers," *Optics Communications*, vol. 230, no. 1-3, pp. 197–203, 2004.

[174] D. Darwich, R. Dauliat, R. Jamier, A. Benoit, J.-L. Auguste, S. Grimm, J. Kobelke, A. Schwuchow, K. Schuster, and P. Roy, "50.4% slope efficiency thulium-doped large-mode-area fiber laser fabricated by powder technology," *Optics letters*, vol. 41, no. 2, pp. 384–387, 2016.

[175] K. Yin, R. Zhu, B. Zhang, G. Liu, P. Zhou, and J. Hou, "300 w-level, wavelength-widely-tunable, all-fiber integrated thulium-doped fiber laser," *Optics express*, vol. 24, no. 10, pp. 11085–11090, 2016.

[176] A. Sincore, J. D. Bradford, J. Cook, L. Shah, and M. C. Richardson, "High average power thulium-doped silica fiber lasers: review of systems and concepts," *IEEE Journal of Selected Topics in Quantum Electronics*, vol. 24, no. 3, pp. 1–8, 2017.

[177] S. D. Jackson and S. Mossman, "Efficiency dependence on the tm 3+ and al 3+ concentrations for tm 3+-doped silica double-clad fiber lasers," *Applied optics*, vol. 42, no. 15, pp. 2702–2707, 2003.

[178] C. Gaida, M. Gebhardt, T. Heuermann, Z. Wang, C. Jauregui, and J. Limpert, "Transverse mode instability and thermal effects in thulium-doped fiber amplifiers under high thermal loads," *Optics Express*, vol. 29, no. 10, pp. 14963–14973, 2021.

[179] M. P. Buckthorpe and W. A. Clarkson, "Simple method for determining quantum efficiency and background propagation loss in thulium-doped fibres," *Applied Physics B*, vol. 129, no. 9, p. 142, 2023.

[180] J. Wang, N. Bae, S. B. Lee, and K. Lee, "Effects of ion clustering and excited state absorption on the performance of ho-doped fiber lasers," *Optics Express*, vol. 27, no. 10, pp. 14283–14297, 2019.

[181] A. Sincore, L. Shah, V. Smirnov, and M. Richardson, "Comparison of in-band pumped tm: fiber and ho: fiber," in *Fiber Lasers XIII: Technology, Systems, and Applications*, vol. 9728, pp. 163–169, SPIE, 2016.

[182] E. J. Friebele, C. G. Askins, J. R. Peele, B. M. Wright, N. J. Condon, S. O'Connor, C. G. Brown, and S. R. Bowman, "Ho-doped fiber for high energy laser applications," in *Fiber Lasers XI: Technology, Systems, and Applications*, vol. 8961, pp. 382–390, SPIE, 2014.

[183] A. S. Kurkov, E. M. Sholokhov, A. V. Marakulin, and L. Minashina, "Effect of active-ion concentration on holmium fibre laser efficiency," *Quantum electronics*, vol. 40, no. 5, p. 386, 2010.

[184] D. Kirsch, S. Chen, R. Sidharthan, Y. Chen, S. Yoo, and M. Chernysheva, "Short-wave ir ultrafast fiber laser systems: Current challenges and prospective applications," *Journal of Applied Physics*, vol. 128, no. 18, 2020.

[185] N. Ramírez-Martínez, M. Núñez-Velázquez, and J. Sahu, "Study on the dopant concentration ratio in thulium-holmium doped silica fibers for lasing at 2.1 μm," *Optics Express*, vol. 28, no. 17, pp. 24961–24967, 2020.

[186] N. Valero, D. Marion, J. Lhermite, J.-C. Delagnes, W. Renard, R. Royon, and E. Cormier, "High-power amplified spontaneous emission pulses with tunable coherence for efficient non-linear processes," *Scientific Reports*, vol. 11, no. 1, p. 4844, 2021.

[187] N. Dalloz, T. Robin, B. Cadier, C. Kieleck, M. Eichhorn, and A. Hildenbrand-Dhollande, "55 w actively q-switched single oscillator tm 3+, ho 3+-codoped silica polarization maintaining 2.09 μm fiber laser," *Optics express*, vol. 27, no. 6, pp. 8387–8394, 2019.

[188] A. Motard, C. Louot, T. Robin, B. Cadier, I. Manek-Hönninger, N. Dalloz, and A. Hildenbrand-Dhollande, "Diffraction limited 195-w continuous wave laser emission at 2.09 μm from a tm 3+, ho 3+-codoped single-oscillator monolithic fiber laser," *Optics Express*, vol. 29, no. 5, pp. 6599–6607, 2021.